

**EXAMINATION OF DEFORMATION IN MAGNESIUM USING
INSTRUMENTED SPHERICAL INDENTATION**

by

Ghazal Nayyeri

B.Sc., University of Tehran, 2007

M.Sc., University of Tehran, 2009

A THESIS SUBMITTED IN PARTIAL FULFILLMENT OF THE
REQUIREMENTS FOR THE DEGREE OF

DOCTOR OF PHILOSOPHY

in

THE FACULTY OF GRADUATE AND POSTDOCTORAL STUDIES

(Materials Engineering)

THE UNIVERSITY OF BRITISH COLUMBIA
(Vancouver)

April 2016

© Ghazal Nayyeri, 2016

Abstract

This investigation examines the use of instrumented indentation to extract information on the deformation behaviour of commercial purity magnesium, AZ31B (Mg-2.5Al-0.7Zn), and AZ80 (Mg-8Al-0.5Zn). In particular, indentation was conducted with spherical indenter using a range of spherical indenter tip radii of $R = 1 \mu\text{m}$ to $250.0 \mu\text{m}$. A detailed examination has been conducted for the load-displacement data combined with three-dimensional electron backscatter diffraction (3D EBSD) characterization of the deformation zone under the indenter after the load has been removed.

It was proposed that the initial deviation of the load-depth data from the elastic solution of Hertz is associated with the point when the critical resolved shear stress (CRSS) for basal slip is reached. Also, it was observed that reproducible large discontinuities could be found in the loading and the unloading curves. It is proposed that these discontinuities are related to the nucleation and growth of $\{10\bar{1}2\}$ extension twins during loading and their subsequent retreat during unloading. For the case of c-axis indentation, 3D EBSD studies showed that the presence of residual deformation twins depended on the depth of the indent. Further, a detailed analysis of the residual geometrically necessary dislocation populations in the deformation zone was conducted based on the EBSD data. It was found that residual basal $\langle a \rangle$ dislocations were dominant in the deformation zone. This was consistent with crystal plasticity finite element method calculations where only basal slip was allowed albeit with some differences that can be rationalized by the presence of $\{10\bar{1}2\}$ extension twins in the experiments. Using different spherical diamond tips, it was concluded that the quantitative values for the $RSS_{0.1\% \text{ offset}}$ for basal slip of magnesium obtained from the indentation test is indentation size dependent and it increases linearly with the inverse square root of the misorientation gradient under the indent. Finally, effects of chemistry on the CRSS for basal slip was also successfully measured by conducting the indentation tests on AZ31B and AZ80 alloys. It was shown that the CRSS of basal slip increases linearly with $c^{1/2}$, where c is the concentration of Al.

Preface

The majority of this work was conducted and completed by Ghazal Nayyeri at the University of British Columbia. All three dimensional electron back-scattered diffraction (3D EBSD) tests were completed at the Max-Planck Institute for Iron Research (MPIE) in Dusseldorf, Germany and were conducted by Ghazal Nayyeri under the supervision of Dr. Stefan Zaeferrer. Figures 5.39b and c and Figure 4.8 were also provided Dr. Zafferrer. Geometrically necessary dislocation (GND) calculations were done using QUBE, a software developed by P.J. Konijnenberg. Figures 5.9 and 5.10 were therefore constructed using this software by Dr. Stefan Zaeferrer. Finally, crystal plasticity finite element modelling (CPFEM) was performed by Dr. Claudio Zambaldi at the MPIE and the analysis presented in this work in Figure 5.12 was done by the author.

Table of Contents

Abstract	ii
Preface	iii
Table of Content	iv
List of Tables	ix
List of Figures	xi
List of Symbols	xx
List of Abbreviation	xxii
Acknowledgements	xxiii
1 Introduction	1
2 Literature Review	3
2.1 Introduction	3
2.2 Deformation of magnesium	3
2.2.1 Elastic deformation in magnesium	3
2.2.2 Slip modes in magnesium	4
2.2.3 Twin modes in magnesium	6
2.3 Indentation test	9

2.3.1	Analysis of instrumented indentation test data	10
2.3.2	Indentation stress and strain	12
2.3.3	Zero-load and zero-displacement	15
2.3.4	Pop-in and pop-out events during indentation test	15
2.4	Influence of orientation on deformation behaviour of pure magnesium using instrumented indentation technique	19
2.5	Indentation size effect	22
2.6	Effect of composition on the mechanical properties of magnesium	24
2.7	Conclusion	25
3	Scope and Objectives	26
4	Materials and Methodology	28
4.1	Initial material	28
4.2	Material characterization: sample preparation and tools	29
4.3	Processing of initial material	30
4.3.1	Heat treatment of the as-received material	31
4.4	Mechanical property testing, using instrumented indentation testing	33
4.5	Microstructure and texture characterization	38
4.5.1	Electron backscatter diffraction-based orientation microscopy (EBSD)	38

4.5.2	Geometrically necessary dislocations (GND) calculations	39
4.6	Crystal plasticity finite element simulation of indentation in magnesium ..	39
5	The Effect of Crystallographic Orientation on the Local Mechanical Properties of Commercially Pure Magnesium	41
5.1	Introduction	41
5.2	Spherical indentation with direction close to [0001]	41
5.2.1	Microstructural analysis before and after the spherical indentation	41
5.2.2	Indentation load-depth curves	44
5.2.3	3D EBSD Maps	49
5.2.4	Analysis of stress field under indent using Hertzian elastic contact mechanics	54
5.2.5	Crystal plasticity finite element simulation results	55
5.2.6	Stress-strain curve	58
5.3	Spherical indentation on commercially pure Mg with loading nearly perpendicular to the c-axis	63
5.3.1	Microstructural analysis before and after the spherical indentation	63
5.3.2	Analysis of stress field under indent using Hertzian elastic contact mechanics	66
5.3.3	Indentation load-depth curves	69
5.3.4	3D EBSD Maps	73

5.4	Spherical indentation with direction 54° away from c-axis	76
5.4.1	Microstructural analysis before and after the spherical indentation	76
5.4.2	Analysis of stress field under indent using Hertzian elastic contact mechanics.....	77
5.4.3	Indentation load-depth curves	79
5.4.4	3D EBSD Maps	83
5.5	Discussion	84
5.5.1	Proposed sequence of events during loading and unloading	84
5.5.2	Detailed observations on the residual deformation zone	90
5.6	Summary	99
6	The Effect of Tip Radius on the Local Mechanical Properties of Pure Magnesium	101
6.1	Introduction	101
6.2	Load-depth curve	101
6.3	Indentation stress-strain curve	113
6.4	Discussion	116
6.5	Conclusion	121
7	The Effect of Composition on the Local Mechanical Properties of Commercially Pure Magnesium	122
7.1	Introduction	122

7.2	Load-depth curves	122
7.3	Stress-strain curve	126
7.4	Discussion	127
7.5	Conclusions	130
8	Conclusions and Future Work	131
8.1	Conclusion	131
8.2	Future work	132
	References	133
	Appendix A 3D-EBSD Measurements of Commercially Pure Magnesium	146

List of Tables

Table 2.1: Characteristics of slip modes in pure magnesium single crystals	6
Table 2.2: Projected areas for various types of indenters. The semi-angles given for the pyramidal indenters are the angles between the face with the central axis of the indenter [56]. These angles are defined in Figure 2.5	12
Table 4.1: Chemical composition of investigated of as-received materials (in weight percent)	28
Table 5.1: List of normalized RSS (τ_{rss}/p_m) for the basal, prismatic, and pyramidal slip planes	55
Table 5.2: List of normalized RSS (τ_{rss}/p_m) for 6 extension twins	55
Table 5.3: Critical resolved shear stress values obtained from indentation test for the basal planes for the selected grain	62
Table 5.4: Critical resolved shear stress values obtained from indentation test for the extension twin planes for the selected grain	62
Table 5.5: List of normalized RSS (τ_{rss}/p_m) for the basal, prismatic, and pyramidal slip planes	69
Table 5.6: Critical resolved shear stress values obtained from indentation test for the basal planes for the selected grain	73
Table 5.7: Critical resolved shear stress values obtained from indentation test for the extension twin planes for the selected grain	73
Table 5.8: List of maximum normalized RSS (τ_{rss}/p_m) for bas slip and 6 extension twins on a grain which was oriented such that the indentation direction was 54 degrees away from the c-axis	79
Table 5.9: Critical resolved shear stress values obtained from indentation test for the basal planes for the selected grain	82

Table 5.10: Critical resolved shear stress values obtained from indentation test for the extension twin planes for the selected grain	82
Table 5.11: Summary of the critical resolved shear stress for bas slip and 6 extension twins for three different studied orientations	99
Table 6.1: Summary of EBSD and indentation tests results for indent depth of 500 nm	111
Table 6.2: Summary of EBSD and indentation tests results for indent depth of 3500 nm	112
Table 6.3: List of normalized RSS, yield strength, and the $RSS_{0.1\% \text{ offset}}$ of the basal slip for five indenters	114
Table 6.4: List of normalized RSS (τ_{rss}/p_m), yield strength, and the apparent CRSS of the extension twin plane for five indenters	115
Table: 6.5: The misorientation gradient ($d\theta/dx$) for all five indenters	118
Table 7.1: List of normalized RSS (τ_{rss}/p_m), yield strength, and the $RSS_{0.1\% \text{ offset}}$ for the basal slip using 13.3 micron indent	127
Table 7.2: List of normalized $RSS_{0.1\% \text{ offset}}$ for the basal slip for commercially pure Mg, AZ31B, and AZ80 alloys	128

List of Figures

Figure 2.1: Anisotropy of Young's modulus in magnesium. The xy-plane corresponds to the basal plane, and z-axis corresponds to the c-axis in an HCP crystal. $C_{11} = 33.5$ GPa, $C_{12} = 49.9$ GPa, $C_{13} = 20.8$, $C_{33} = 61.0$ GPa, and $C_{44} = 16.6$ GPa were used for plotting the figure [11]	4
Figure 2.2: Demonstrates the basal and non-basal slip systems (both $\langle a \rangle$ and $\langle c+a \rangle$ types) in HCP magnesium. The Burgers vector of the dislocation is given by the solid arrow	5
Figure 2.3: Schematic re-orientation of the $\langle c \rangle$ axis which results from a) $\{10\bar{1}2\}$ extension and b) $\{10\bar{1}1\}$ contraction twinning in magnesium [32]	7
Figure 2.4: A schematic representation of load versus indenter displacement data for an indentation experiment. P_{\max} is the peak indentation load, h_{\max} is the maximum displacement at peak load, h_e is the elastic indentation depth, and h_f is the final depth of the contact impression after unloading	11
Figure 2.5: Schematic figures of various types of indenters: (a) Berkovich, (b) Vickers, and (c) Knoop indenter tips [56]	12
Figure 2.6: The predicted load–displacement curves and stress contours in the finite element simulations with the two selected material properties: (a) aluminum and (b) tungsten. The indentation zone in both cases extends approximately to a depth of about $2.4a$ [68]	14
Figure 2.7: A schematic figure of pop-in	16
Figure 2.8: (a) The unloading segment of the load-displacement curve (b) and its corresponding derivative. The occurrence of the pop-out can be observed [99]	17
Figure 2.9: Indentation load-displacement and indentation stress-strain curves for mechanically polished and electropolished samples of (a) Al and (b) W using $1 \mu\text{m}$ spherical indenter [102]	18
Figure 2.10: Schematic figure shows the favourable positions under the indent for extension twin activity for the case of indentation (a) parallel and (b) perpendicular to the c-axis [103]	20

Figure 2.11: Optical micrographs of indentation (a) on $\{10\bar{1}0\}$ plane, and (b) $\{0001\}$ plane of single crystal of magnesium [104]	21
Figure 2.12: Model of geometrically necessary dislocations for a conical indenter [116]	23
Figure 2.13: Geometrically necessary dislocations for a spherical indenter [130]	23
Figure 2.14: The Vickers hardness vs. Al content. The error bars show the standard deviations [139]	25
Figure 4.1: a) An optical micrograph showing the grain structure of the as-received magnesium sheet, b) and c), respectively show the EBSD measured $\{0001\}$ and $\{10\bar{1}0\}$ pole figures (stereographic), representing the texture of the same material. The RD, TD and ND correspond to rolling direction, transverse direction and normal direction of the sample, respectively. The intensity colour scale is given in multiples of a random distribution (m.r.d)	30
Figure 4.2: Mg-Al binary equilibrium phase diagram	31
Figure 4.3: Optical micrographs of the annealed materials (a) commercially pure Mg, (b) ZE10, (c) AZ31B, and (d) AZ80	32
Figure 4.4. (a) Schematic drawings illustrating the orientation of the grains in the sheet sample	33
Figure 4.5: Instrumented-indentation machine	34
Figure 4.6: Schematic figure of instrumented-indentation machine	34
Figure 4.7: The load-displacement curves obtained from nanoindentation tests on one grain	35
Figure 4.8: A schematic figure of the sample preparation for 3D-EBSD using the lift-out method	39

Figure 5.1: (a) Inverse pole figure map of the studied grains before indentation tests, (b) optical micrograph after spherical indentation	42
Figure 5.2: Indentation load-displacement curves for three different indent depths: 500 nm, 1500 nm, and 3500 nm	42
Figure 5.3: (a, b, and c) EBSD image quality maps and (d, e, and f) {0001} pole figure maps for three different indent depths: 500 nm, 1500 nm, and 3500 nm. The white arrows on the EBSD maps show the indentation areas (the dark roughly circular areas). Note, the sample reference direction for A1 is close to $[11\bar{2}0]$, A2 is close to $[10\bar{1}0]$, and A3 is perpendicular to the surface (parallel to indentation direction)	43
Figure 5.4: load-displacement curve for three indentation tests (labelled test 1, test 2 and test 3). All three tests were conducted with the same condition, i.e. indentation depth of 500 nm to illustrate the reproducibility of the measurements. In order to make the comparison of the data easier, the curves of tests 2 and 3 were shifted by an offset of 2 mN and 4 mN in load	44
Figure 5.5: Load-displacement curves for four grains made within the same grain showing the loading-unloading behavior for indent depths of (a) 35nm, (b) 40 nm, (c) 100 nm, and (d) 250 nm. Also, the prediction from Hertzian contact theory [65] (the red line) is shown for comparison	46
Figure 5.6: (a, c, e) Unloading curves for 35, 100, and 500 nm displacements, (b,d,f) and the derivative curves for the corresponding displacements	48
Figure 5.7: Observations on the deformation zone under the centre of the indenter for the 500 nm indent, a) point to origin misorientation angle magnitude map (origin denoted by the point “a”) with image quality superimposed, b) misorientation profiles for the horizontal lines (i) to (iv) in a) and c) 0001 and $11\bar{2}0$ pole figures for line (iii) in figure b). Note, the sample reference direction for A1 is close to $[11\bar{2}0]$, A2 is close to $[10\bar{1}0]$, and A3 is perpendicular to the surface (parallel to indentation direction)	50

Figure 5.8: Observations on the deformation zone under the centre of the indenter for the 1500 nm indent, a) point to origin misorientation angle magnitude map (origin denoted by the point “a”) with image quality superimposed, b) misorientation profiles for the horizontal lines (i) to (iv) in a) and c) 0001 and $11\bar{2}0$ pole figures for line (iii) in figure b). Note, the sample reference direction for A1 is close $[11\bar{2}0]$, A2 is close to $[10\bar{1}0]$, and A3 is perpendicular to the surface (parallel to indentation direction)	52
Figure 5.9: 3D reconstructed microstructure for the volume under the 1500 nm indent from EBSD maps, a) inverse pole figures and image quality surface at depth of 2 μm and b) only twins highlighted	53
Figure 5.10: 3-dimensional maps of GND densities for the 1500 nm indent, (a) $\langle a \rangle$ basal edge, (b) $\langle a \rangle$ basal screw, (c) $\langle a \rangle$ prismatic edge (d) all $\langle c+a \rangle$ type dislocations	53
Figure 5.11: Distribution of normalized resolved shear stress (t_{rss}/p_m) below the spherical indenter for (a) basal slip, (b) 2 nd order pyramidal slip and (c) extension twin	55
Figure 5.12: (a) The results for a map of local misorientation under the indent obtained from the crystal plasticity finite element method calculations. The $\langle a \rangle$ type basal slip was the only deformation mode allowed, the loading direction was parallel to the c-axis and the simulated indentation depth is 3500 nm. (b) The misorientation profile of four normalized distance under the indent ($z/a = 0.25, 0.5, 0.75,$ and 1) were extracted	56
Figure 5.13: (a) The maximum amplitude of the misorientation as a function of normalized indenter depth (h/a), and (b) Maximum misorientation obtained from experiments and CPFEM for $z/a = 0.25 - 4.0$	57
Figure 5.14: The identification of the effective zero-point using the method described in section 2-3-3	59
Figure 5.15: The measured load–displacement curves	59
Figure 5.16: The measured indentation stress–strain curves for high purity Al	60
Figure 5.17: Comparison between the data obtained in this work and reported in the literature [68] for high purity Al	60

Figure 5.18. The measured indentation stress–strain curves for commercially pure magnesium for the studied grain	61
Figure 5.19: (a) Inverse pole figure map of the studied grains before spherical indentation tests, (b) optical micrograph after spherical indentation	63
Figure 5.20: Load-displacement curve for three indentation tests (labelled test 1, test 2 and test 3). All three tests were conducted with the same condition, i.e. indentation depth of 500 nm to illustrate the reproducibility of the measurements. In order to make the comparison of the data easier, an offset of 2 mN and 4 mN in load was added to these tests for test 2 and test 3, respectively, i.e the load displacement was shifted vertically to avoid overlap of the data points	64
Figure 5.21: (a, b, and c) IPF maps, and (d, e, and f) IPF maps rotated 90° around axis 2 (the magnified view of Figure 5.21f can also be seen), (g, h, and i) {0001} pole figures after indentation for three different indent depths: 500 nm, 1500 nm, and 3500 nm. Note, the sample reference direction for A1 is close to [0001], A2 is close to [10 $\bar{1}$ 0], and A3 is perpendicular to the surface (parallel to indentation direction)	65
Figure 5.22: Distribution of normalized resolved shear stress (τ_{rss}/p_m) below the spherical indenter on (a, and b) extension twin planes and (c) basal slip plane for indentation perpendicular to c-axis	67
Figure 5.23: Distribution of normalized resolved shear stress (τ_{rss}/p_m) below the spherical indenter on (a, and b) extension twin planes and (c) basal slip plane. The angle between the indentation direction and c-axis is 80°	68
Figure 5.24: (a) Load-displacement curve for 3500 nm displacement. The magnified view of the load-displacement curve up to (b) 500 nm, and (c) 1500 nm	70
Figure 25: (a, c, e) Unloading curves for 500, 1500, and 3500 nm displacements, (b,d,f) and the derivative curves for the corresponding displacements	71
Figure 5.26: The measured indentation stress–strain curves for high purity magnesium for the case of indentation nearly perpendicular to the c-axis	72

Figure 5.27: (a) The EBSD map of the indentation area, (b) the combined image quality/IPF map of the same area shown in (a), and (c) the combined image quality/inverse pole figure map of the centre cross-section. The section shown is perpendicular to the surface of the sample and the location of it is shown by dashed lines in (b). The white arrows show the six different extension twin variants under the indent. The black arrow in Figure (a) shows the basal slip trace. Note, the sample reference direction for A1 is close to $[\bar{1}\bar{1}20]$, A2 is close to $[\bar{1}100]$, and A3 is perpendicular to the surface (parallel to indentation direction) 74

Figure 5.28: (a) The EBSD map of the indentation area, (b) the combined image quality/IPF map of the same area shown in (a), and (c) the combined image quality/inverse pole figure map of the centre cross-section. The section shown is perpendicular to the surface of the sample and the location of it is shown by dashed lines in (b). The white arrows show the six different extension twin variants under the indent. Note, the sample reference direction for A1 is close to $[\bar{1}2\bar{1}0]$, A2 is close to $[\bar{1}100]$, and A3 is perpendicular to the surface (parallel to indentation direction) 75

Figure 5.29: Inverse pole figure map before indentation tests, and (b) optical microscopy map after spherical indentation 76

Figure 5.30: (a, b, and c) Combined image quality/IPF maps of the indented areas for three different indent depths: 500 nm, 1500 nm, and 3500 nm, respectively, and (d, e, and f) magnified view of the IPF maps of the same areas shown in (a, b, and c), and (g, h, and i) the corresponding $\{0001\}$ pole figures of the IPF maps 77

Figure 5.31: Distribution of normalized resolved shear stress (τ_{rss}/p_m) below the spherical indenter for basal slip for indentation along a direction 54 degrees away from c-axis 78

Figure 5.32: The EBSD map and the load-displacement curve after the indentation on a grain which is 54 degrees off from $[0001]$ direction. Five extension twins around the indent are shown by white arrows. The presence of five extension twins (labelled 1 to 5) can be seen around the indent. The black arrow shows the basal slip trace 80

Figure 5.33: (a) Unloading curve for 3500 nm displacement, (b) and the derivative curve for the corresponding displacement 81

Figure 5.34. The measured indentation stress–strain curves for high purity magnesium for the case of indentation nearly perpendicular to the c-axis 82

Figure 5.35: (a) The combined image quality/IPF map of the indentation area, (b) the magnified view of the IPF map of the same area shown in (a), and (c) the IPF map of a section which is 5 micron away from the centre cross-section. This section is perpendicular to the surface of the sample and the location of it is shown by dashed line in Figure 5.35b	83
Figure 5.36: A set of schematic diagrams to illustrate the proposed sequence of events under the indenter. (a) The contact is elastic at this point. In the background of the figure the contour plot for the resolved shear stress (RSS) on the basal slip plane is shown. (b) The RSS on the basal slip plane reaches the CRSS for basal slip and plastic deformation is initiated. (c) The twins will form at those places where the RSS exceeds the CRSS for twinning. The distribution of the resolved shear stress on the extension twin habit planes derived from the Hertzian stress field is plotted as a background image. (d) The sample is unloaded and most of the twins will de-twin due to the elastic forces acting in their surrounding and due to the ease of movement of extension twin boundaries	85
Figure 5.37: (a) Inverse pole figures (IPF) map and (b) its corresponding {0001} pole figure map after indentation tests on ZE10 alloy. Six variants of {10 $\bar{1}$ 2} extension twins can be observed around the indent. Note, the sample reference direction for A1 is close to $[\bar{1}2\bar{1}0]$, A2 is close to $[10\bar{1}0]$, and A3 is perpendicular to the surface (parallel to indentation direction)	89
Figure 5.38: (a) Load-displacement curve of indentation test for ZE10, for indent depth of 3500 nm, and (b) An enlarged view of the loading curve, showing the occurrence of six similar	89
Figure 5.39: Characterization of rotations under the 1500 nm indent, a) schematic diagram of dislocation loops for different basal slip systems. Note, the black arrow is $[10\bar{1}0]$, and the orange dashed line is $[11\bar{2}0]$ b) experimental observation on rotation axis the of crystal with respect to the original orientation for a horizontal slice, 4 μ m below the surface and c) magnitude of the misorientation angle on the same slice as shown in b). Note, solid black lines in b) and c) are misorientations greater than 15 $^{\circ}$	92
Figure 5.40: (a) Schematic figure of indentation perpendicular to the c-axis, and (b) IPF EBSD image after indentation nearly perpendicular to the c-axis, for indentation of 3500 nm	94
Figure 5.41: Comparison between the indentation load-displacement curves for three orientations	97

Figure 5.42: Comparison between the indentation stress-strain curves for three orientations	98
Figure 6.1: Effect of tip radius on the load-displacement curves for commercial purity magnesium, (spherical indentation performed using spherical indenter tip radii of R= 1 μm , 3.69 μm , 13.3 μm , 50.0 μm , and 250.0 μm)	102
Figure 6.2: Inverse pole figures (IPF) maps and their corresponding {0001} pole figure maps after indentation tests using five different indenter tips (a, b, and c) R= 250 μm , and (d, e, and f) R= 50 μm , (g, h, and i) R= 13.3 μm , (j, k, and l) R= 3.9 μm , and (m, n, and o) R= 1 μm for two indentation depths; (a, d, g, j, and m) 500 nm indent depth, (b, e, h, k, and n) 3500 nm indent depth	103
Figure 6.3: Load-displacement curves for commercial purity magnesium using different spherical diamond tips, (a and b) R = 250 μm , (c and d) R = 50 μm , (e and f) R = 13.3 μm , (g and h) R = 3.6 μm , and (i and j) R = 1 μm , for 500 nm, and 3500 nm displacements	106
Figure 6.4: Magnified view of unloading curves, and Magnified view of the derivative curves for 500 nm depth using different spherical diamond tips, (a, b) R = 250 μm , (c, d) R = 50 μm , (e, f) R = 13.3 μm , (g, h) R = 3.6 μm , and (i, j) R = 1 μm	108
Figure 6.5: Magnified view of unloading curves, and Magnified view of the derivative curves for 3500 nm depth using different spherical diamond tips, (a, b) R = 250 μm , (c, d) R = 50 μm , (e, f) R = 13.3 μm , (g, h) R = 3.6 μm , and (i, j) R = 1 μm	111
Figure 6.6: Summary of number of twins appearing around the indent for three different indentation depths, (i.e. 500, 1500, and 3500 nm) using four indenters with radii of R = 50 μm , 13.3 μm , 3.5 μm , and 1 μm	113
Figure 6.7: Effect of tip radius on the stress-strain curves for commercial purity magnesium, spherical indentation was performed using a range of spherical indenter tip radius of R= 1, 3.69, 13.3, 50.0, and 250.0 μm	114
Figure 6.8: Effects of tip radius on the $\text{RSS}_{0.1\% \text{ offset}}$ for (a) basal slip for pure magnesium.....	115

Figure 6.9: Effects of tip radius on the apparent CRSS for extension twin for pure magnesium.....	116
Figure 6.10: The misorientation profile under the indent for 1500 nm indentation depth. The slope of the misorientation profile can be obtained by dividing θ_{\max} over half of the contact radius ($a/2$)	118
Figure 6.11: The critical resolved shear stress as a function of square root of misorientation gradient. A linear regression was used to fit to the data	119
Figure 6.12: The critical resolved shear stress as a function of inverse square root of indenter radius. A linear regression was used to fit to the data	120
Figure 7.1: Effect of composition on the load-displacement curves for commercial purity magnesium	123
Figure 7.2: (a) Indentation load-depth curve for pure Mg, AZ31B, and AZ80 alloys for 3500 nm displacement, and magnified view of unloading curves, and Magnified view of the derivative curves for (b and c) AZ31B, and (d and e) AZ80 alloys	124
Figure 7.3: (a) SEM image, (b) inverse pole figures (IPF) map and (c) its corresponding {0001} pole figure map after indentation tests on AZ80 alloy. The indent depth is 3500 nm, and the indenter diameter is 13.3 μm . Six variants of {10-12} extension twins can be observed around the indent. Note, the sample reference direction for A1 is close to $[\bar{1}2\bar{1}0]$, A2 is close to $[10\bar{1}0]$, and A3 is perpendicular to the surface (parallel to indentation direction)	125
Figure 7.4: Effect of aluminum additions on the stress-strain curves for commercial purity magnesium	126
Figure 7.5: ΔCRSS for basal slip activation vs. $c^{1/2}$ for Mg-(0, 3, and 8 wt.%)Al. Data by Jain [46] and Akhtar and Teghtsoonian [175] are included for comparison	130

List of Symbols

Symbol	Description
A	projected area of the elastic contact
a	contact radius
α	material constant
b	Burgers vector
C_{ij}	elastic constants
E_{eff}	effective Young's modulus
ε_{ind}	indentation strain
γ	shear strain
S	measured stiffness
h_c	contact depth
H	hardness
L	spacing between dislocations
M	Taylor factor
μ	shear modulus
P_{max}	peak indentation load
ρ_G	geometrically necessary dislocations (GND) density
p_m	mean contact pressure
R	indenter radius

σ_0 friction stress

σ stress

τ shear stress

List of Abbreviation

BCC	body-centered cubic
CA	confidence index
CRSS	critical resolved shear stress
CPFEM	crystal plasticity finite element modelling
CSM	continuous stiffness measurement
DSI	depth sensing indentation
EBSD	electro back-scattered diffraction
FCC	face-centered cubic
FIB	focus ion beam
GND	geometrically necessary dislocations
HCP	hexagonal closed packed
IPF	inverse pole figure
IQ	image quality map
ISE	indentation size effect
OIM	orientation imaging microscopy
SEM	scanning electron microscopy
TEM	transmission electron microscopy

Acknowledgments

I wish to thank first and foremost my advisers, Professor Warren Poole and Professor Chad Sinclair for the true research spirit that they showed me with patience. Without their constant support and guidance, I would never be able to finish this journey. I have been extremely lucky to have this chance to work under their supervision. I also wish to thank them for providing a respectful, warm, and supporting environment in which I can freely talk and discuss ideas. I would like to thank Prof. Warren Poole for supporting me to present my work at international conferences and also to give an incredible opportunity to spend a part of my PhD at the Max-Planck Institute in Dusseldorf, Germany. I would like to give special thanks to Prof. Stefan Zaefferer, Peter Konijnenberg, and Dr. Claudio Zambaldi for helping me with 3D-EBSD measurements and also for providing me with incredible ideas and advices at Max-Planck Institute. Working with such innovative and energetic people has been a unique experience in my professional life. I would like to gratefully thank Prof. Rizhi Wang for permission to use the indentation machine and help in training. Sincere thanks to all staff members of Materials Engineering Department at UBC (Ross Mcleod, David Torok, Carl Ng, Debbie Burgess, Mary Jansepar, Fiona Webster, Michelle Tierney, and Jacob Cable) for all their help on my research work. I would like to give my especial thanks to Dr. Hamid Azizi Alizamini, Dr. Alban de Vaucorbeil, Dr. Morteza Toloui, Dr. Tomas Garcin, and Dr. Elizabeth Sterling for all their assistance and advice and for being so friendly from the beginning of my PhD at UBC. I would specially like to thank Jingqi Chen for being so patient in answering all my never-ending questions.

Thanks to all my friends that supported me from the first moment I entered Canada. Special thanks to Yalda Hakki, who gave me my first ride in this country. I would like to thank my best friend ever, Mahsa Keyvani, for all her support and kindness and for being there whenever I needed help during the previous years. She taught me that you do not have to be birth sisters to feel that special sisterly bond. I wish to thank my two other best friends, Mina Vafaei and Nastaran Arianpoo for being so energetic, kind, and helpful, and for all the happy and sad moments we shared. They are friends who have become part of my family. Special thanks to Mina for editing this thesis and also for trying to solve all my problems in Canada and for never giving up on me. Also, Nastaran who was always trying to make me not to feel bored and alone specially during the time I was writing my thesis. I would like to thank Dr. Shima Karimi and her kind husband,

Dr. Hadi Mansoor for being there for me as friends and for all their supports, in particular when I had just arrived in Canada and I knew very few people.

Thanks to my friends who were not in Vancouver but never forgot me. Specially I wish to thank Melika Allami for being a wonderful friend who was always checking on me, encouraging me, and mentally supporting me. Also, I would like to thank Dr. Fatemeh Pishbin, who always supported me even from far away. Knowing them was enough for me not to feel lonely.

I wish to thank my fantastic mother, Soraya, and my amazing father, Hossein, for being so devoted, dedicated, and concerned about my future. Thanks to them for being so selfless to support me to migrate to Canada and to continue my studies, and for their unconditional and never-ending love. Their presence was always the most important reason for me not to give up. I wish to thank my uncle Dr. Alireza Chavoshian and my amazing aunt Dr. Minh Hoa Ta for all their support, help, love, and kindness from the time I came to Canada. I am thankful to them for coming to Vancouver each semester just to check on me and make sure I am doing fine. I would like to thank my brother, Dr. Amir Nayyeri, and my wonderful sister-in-law Dr. Parisa Hosseinzadeh, for all their love and support. Thanks, Amir, for always being a role model for me since my childhood. Without their sincere support I would not be able to make this journey.

CHAPTER 1 Introduction

The use of magnesium as a structural material has a long history. During World War I magnesium was one of the strategic aerospace construction metals which was used for German military aircraft. The production of magnesium dropped significantly after the First World War, but it increased again during the Second World War and weakened again after World War II. Recently, there has been considerable concern in the transportation sector about fuel economy and the need to reduce weight. Thus, a revised interest in developing magnesium and its alloys has developed. In addition to the low density of magnesium (i.e. the lowest density of all the structural metals), magnesium also exhibits excellent damping capacity, reasonable cost, good recyclability, and machinability [1,2].

Recently, magnesium usage has been increased in automobiles vehicles almost entirely as die castings [3,4]. However, the successful production of the Nd-containing alloy Elektron 717 prototype door inner panels, weighing 58% less than the original steel panels, represents a major step forward for magnesium forming technologies [5]. However, the key difference in the formation of magnesium compared to steel is that the deformation should be conducted at elevated temperatures (i.e. 200-250° in the case of the door inner panels) [5].

One of the most significant challenge for current applications of magnesium and its alloys is its low ductility at room temperature, and its highly anisotropic plastic response. To overcome these challenges, it is necessary to improve our knowledge on the plastic deformation of magnesium and its alloys. This will allow for magnesium to be more widely employed in various applications in industry, so that cost effective parts can be easily manufactured and the in-service performance meets the demands of the automotive sector [2].

According to the von-Mises criterion, five independent slip systems are required for a general homogeneous plastic deformation [6]. In contrast to body-centered cubic (BCC) and face-centered cubic (FCC) lattices, the hexagonal lattice does not provide a sufficient number of easily activated slip systems to satisfy the von-Mises criterion. To achieve this, more than one crystallographic slip mode and/or twin mode are required. This makes the mechanical response of hexagonal metals much more complex compared to BCC and FCC metals. Further, the stress to operate these deformation modes are widely different. For example, the critical resolved shear stress (CRSS) for basal slip measured from single crystals is of order 1 MPa and 5-50 times greater for non-basal

slip [7,8]. In principle, the various critically resolved shear stresses for slip and twinning could be measured from single crystals but this is difficult and time consuming. Therefore, it would be of interest to extract these fundamental properties from a local test, such as indentation test, that could be conducted on polycrystalline samples. The instrumented indentation test, which is a development of the traditional hardness test, has been finding increased applications for a broad range of materials with heterogeneous microstructures. This technique has the ability to probe local mechanical behavior of small material volumes (nm^3 - μm^3). In comparison with a traditional hardness test, an instrumented indentation test is able to measure load and displacement during the entire test [9].

Solid solution hardening of magnesium has been known for a long time. As mentioned before, the CRSS of high purity magnesium is 1 MPa. So, the strength of magnesium on its own is too low, and thus there is a need to develop alloys to take advantage of solid solution and/or precipitation hardening [10]. There are many potential alloys and only a few have been well characterized at the slip system level.

In this research, the mechanical response of individual grains in a fully annealed condition in polycrystalline high purity magnesium will be characterized using instrumented indentation test. This approach provides information on the heterogeneity of deformation as a function of the grain orientation with respect to the indentation axis. Furthermore, this work seeks to investigate the effect of solid solution hardening on the mechanical and deformation behavior of small materials volumes (grain size scale) by conducting the indentation test on individual grains on AZ magnesium alloys and comparing the obtained results with high purity magnesium.

This thesis begins with a review of literature on the deformation behaviour of magnesium and its alloys, and the use of indentation to study plasticity in magnesium. Having reviewed the current state of knowledge, the scope and objectives of the current work are presented in Chapter 3. Chapter 4 includes the experimental and modelling methodology, used to meet these objectives. Chapter 5 contains the experimental and simulation results obtained on the effect of crystallographic orientation for spherical indentation. Chapter 6 shows that the CRSS obtained by the indentation technique is size dependant. Finally, Chapter 7 describes the effect of composition on the CRSS of basal slip in high purity magnesium by presenting the experimental results obtained on AZ magnesium alloys, i.e. AZ31B (Mg-2.5Al-0.7Zn), and AZ80 (Mg-8Al-0.5Zn).

CHAPTER 2 Literature Review

2.1 Introduction

The literature review begins with a brief summary on the deformation of magnesium in which elastic and plastic anisotropy and slip modes/twin modes are considered. After that, instrumented indentation testing which can be utilized to investigate the local deformation behaviour of a material at small size scale (nano/micrometer length scale), will be introduced. Following this, a detailed review of the indentation studies conducted on magnesium using different shapes/sizes of indenters will be presented.

In the current study, the influence of crystal orientation, indentation size, and composition on the local deformation behaviour of magnesium has been studied. Therefore, the available literature in this area will be reviewed. These topics will be explored with the goal of examining the advantages and challenges of using the instrumented indentation test compared to the conventional mechanical testing methods.

2.2 Deformation of magnesium

2.2.1 Elastic deformation in magnesium

In order to characterise the elastic behaviour of the hexagonal closed pack (HCP) lattice, five elastic constants are required as shown in Equation (2.1) below [11]:

$$\begin{bmatrix} \sigma_1 \\ \sigma_2 \\ \sigma_3 \\ \sigma_4 \\ \sigma_5 \\ \sigma_6 \end{bmatrix} = \begin{bmatrix} c_{11} & c_{12} & c_{13} & 0 & 0 & 0 \\ c_{12} & c_{11} & c_{13} & 0 & 0 & 0 \\ c_{13} & c_{13} & c_{33} & 0 & 0 & 0 \\ 0 & 0 & 0 & c_{44} & 0 & 0 \\ 0 & 0 & 0 & 0 & c_{44} & 0 \\ 0 & 0 & 0 & 0 & 0 & (c_{11} - c_{12})/2 \end{bmatrix} \begin{bmatrix} \varepsilon_1 \\ \varepsilon_2 \\ \varepsilon_3 \\ \varepsilon_4 \\ \varepsilon_5 \\ \varepsilon_6 \end{bmatrix} \quad (2.1)$$

All HCP metals are elastically isotropic in the basal plane [12]; however, the elastic properties parallel to the c-axis can vary from those perpendicular to it, resulting in a pronounced elastic anisotropy. As a result of this, the way in which a particular grain elastically deforms when a polycrystalline aggregate is strained may depend on the crystallographic orientation of the grain with respect to the stress axes. Figure 2.1 shows how the Young's modulus of a magnesium single

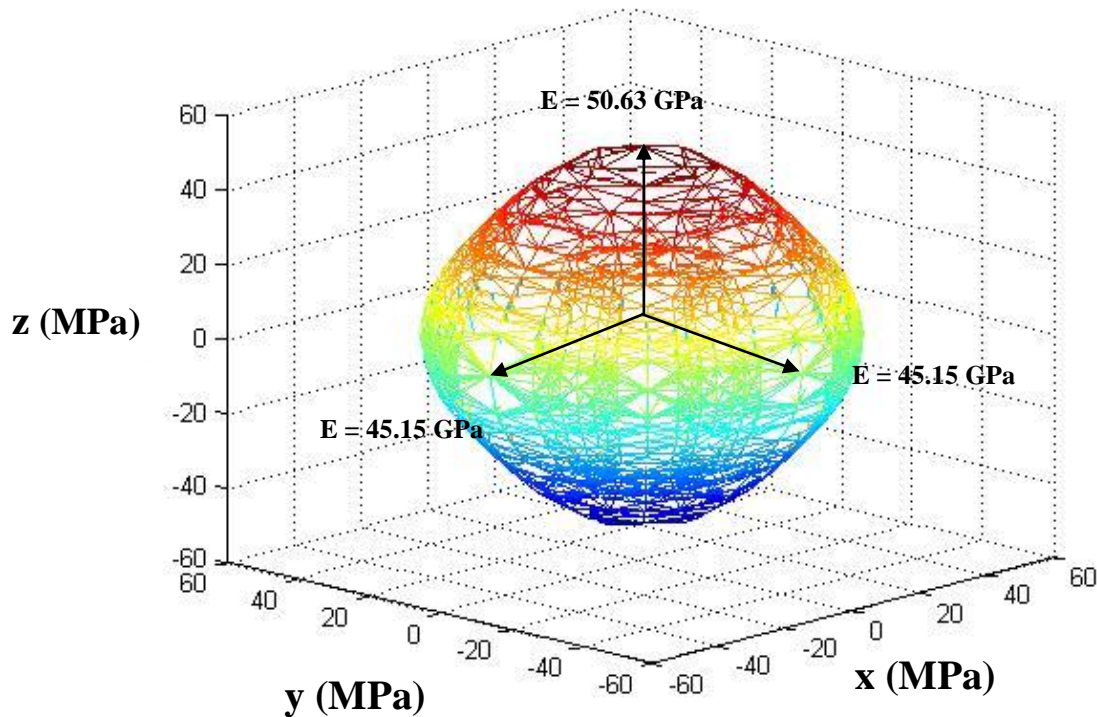


Figure 2.1: Anisotropy of Young's modulus in magnesium. The xy-plane corresponds to the basal plane, and z-axis corresponds to the c-axis in an HCP crystal. $C_{11} = 33.5$ GPa, $C_{12} = 49.9$ GPa, $C_{13} = 20.8$, $C_{33} = 61.0$ GPa, and $C_{44} = 16.6$ GPa were used for plotting the figure [11].

crystal varies with crystallographic direction in magnesium. As can be seen, magnesium shows low elastic anisotropy; the percentage differences between the modulus along the c-axis and perpendicular to it is only $\sim 10\%$.

2.2.2 Slip systems in magnesium

According to the von-Mises criterion [6], in polycrystalline metals, five independent slip/twinning systems are required in order to sustain a general homogeneous deformation. In magnesium, the possible slip systems are, basal (0001) , $\langle 11\bar{2}0 \rangle$ [10,13], prismatic $\{10\bar{1}0\}$, $\langle 11\bar{2}0 \rangle$ [14], 1st order pyramidal $\{1\bar{1}01\}$, $\langle 11\bar{2}0 \rangle$ [7,8] and 2nd order pyramidal $\{11\bar{2}2\}$, $\langle 11\bar{2}\bar{3} \rangle$ [15-17] as shown in Figure 2.2.

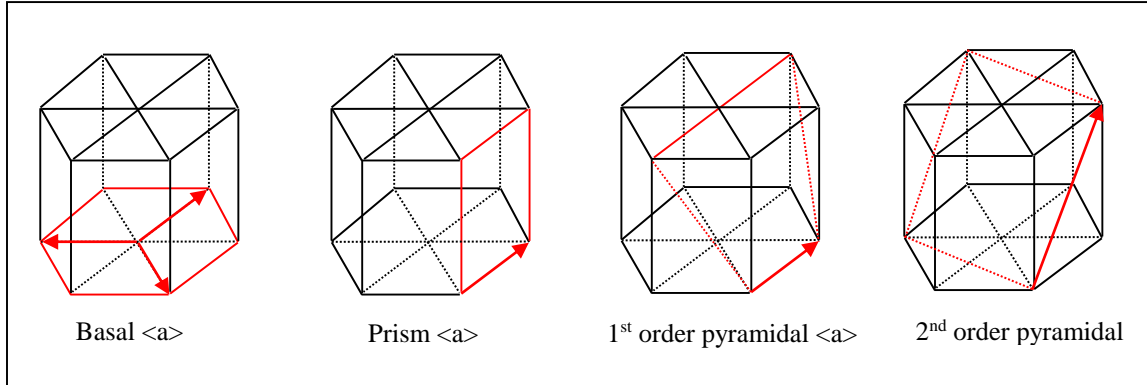


Figure 2.2: Demonstrates the basal and non-basal slip systems (both $\langle a \rangle$ and $\langle c+a \rangle$ types) in HCP magnesium. The Burgers vector of the dislocation is given by the solid arrow.

The characteristics of the slip systems are summarized in Table 2.1, including the critically resolved shear stress (CRSS) measured experimentally. Since the pyramidal slip system with $\langle a \rangle$ Burgers vector is crystallographic equivalent to the combination of basal and prismatic slip, a total number of four independent modes are provided by dislocations with an $\langle a \rangle$ Burgers vector. Furthermore, slip in the $\langle 11\bar{2}0 \rangle$ direction does not generate strain parallel to the $\langle c \rangle$ axis. The strain along the $\langle c \rangle$ axis can be accommodated either by twinning on $\{10\bar{1}2\}$ or $\{10\bar{1}1\}$ plane or by $\langle c+a \rangle$ slip on the 2nd order pyramidal plane ($\{11\bar{2}2\}$). The 2nd order pyramidal $\langle c+a \rangle$ slip alone can provide the essential five independent modes. However, the value of the critical resolved shear stress (CRSS) for the 2nd order pyramidal $\langle c+a \rangle$ slip shows a wide range magnitude but it is always higher than that of basal slip at room temperature [17-21].

In spite of the high values of CRSS for non-basal slip at room temperature, there are a number of research papers which report the activity of $\langle c+a \rangle$ slip in magnesium alloys at ambient temperature. Hauser et al. [22] and more recently Keshavarz and Barnett [23] have confirmed the significance of the non-basal slip at room temperature using slip trace analysis. Furthermore, recent dislocation observations [24-27] using transmission electron microscopy (TEM) provide further support for non-basal slip.

Table 2.1. Characteristics of slip modes in pure magnesium single crystals

Mode	Plane	Direction	Crystallographic elements (slip systems)	CRSS in MPa at room temperature	Number of independent modes
Basal	(0001)	$\langle 11\bar{2}0 \rangle$	$(0001)\langle 11\bar{2}0 \rangle$	0.49-0.8 ^[14,7]	2
Prismatic	$\{10\bar{1}0\}$	$\langle 11\bar{2}0 \rangle$	$\{10\bar{1}0\}\langle 11\bar{2}0 \rangle$	45 ^[14]	2
Pyramidal 1 st order	$\{1\bar{1}01\}$	$\langle 11\bar{2}0 \rangle$	$\{1\bar{1}01\}\langle 11\bar{2}0 \rangle$	-	4
Pyramidal 2 nd order <c+a>	$\{11\bar{2}2\}$	$\langle 11\bar{2}\bar{3} \rangle$	$\{11\bar{2}2\}\langle 11\bar{2}\bar{3} \rangle$	10 ^[18] , 42 ^[19] , 2.3 ^[20]	5

2.2.3 Twin modes in magnesium

Generally, two types of twins are observed in magnesium alloys: extension twins and contraction twins [28-30]. In magnesium, $\{10\bar{1}2\}$ twins are expected when a grain is expanded parallel to the $\langle c \rangle$ axis, while $\{10\bar{1}1\}$ and $\{10\bar{1}3\}$ twins are expected when a grain is contracted along the $\langle c \rangle$ axis. Deformation twinning on the $\{10\bar{1}2\}$ plane causes extension along the $\langle c \rangle$ axis (extension twin), and reorients the crystal by a rotation of 85.2° around the $\langle 11\bar{2}0 \rangle$ axis as illustrated in Figure 2.3a. Twinning on the $\{10\bar{1}1\}$ plane leads to contraction parallel to the $\langle c \rangle$ axis (contraction twin), and a reorientation of the crystal of 57° around the $\langle 1\bar{2}10 \rangle$ axis (Figure 2.3b).

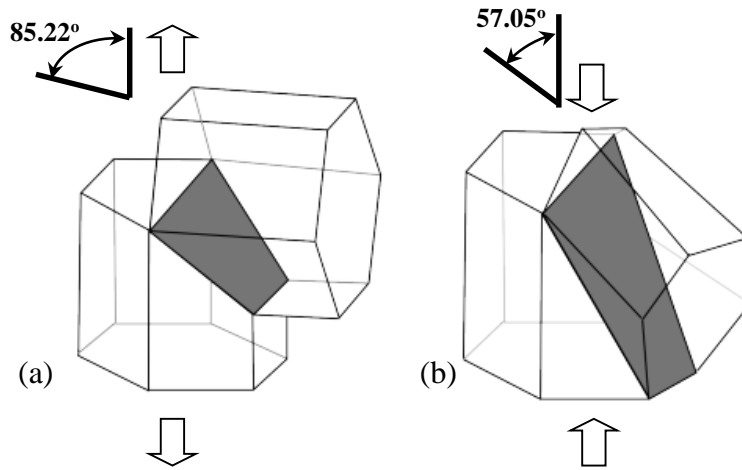


Figure 2.3: Schematic re-orientation of the $\langle c \rangle$ axis which results from a) $\{10\bar{1}2\}$ extension and b) $\{10\bar{1}1\}$ contraction twinning in magnesium [30].

The reorientation of grains after twinning can lead to an orientation that is more favourable for slip. Twinning may occur over a large fraction of a sample after only a small amount of deformation and leads to sudden change in the texture of the sample [31,32]. Researchers have modelled the deformation behavior of magnesium including twin activity [33-36]. It has been observed, to a first approximation, that the activation of twinning can be described by a CRSS criterion such as Schmid's law [37]. For the case of high purity Mg, the CRSS for extension twinning was determined as 2-10 MPa [7, 38], which shows its easy activation. However, for the contraction twinning the CRSS ranges from 76 to 153 MPa [39]. Gharghouri et al [40], studied the internal stresses in Mg-7.7 at.% Al alloy using in-situ neutron diffraction method. Their observations confirm the applicability of the critical resolved shear stress criteria for extension twinning. Also, Godet et al [41] conducted compression testing on an extruded AM30 alloy along the extrusion direction. Using EBSD analysis, they claimed that the extension twinning satisfied Schmid's law. Later, Park et al [32] performed tensile tests parallel to ND and also compression test parallel to RD on AZ31 alloy. EBSD analysis of the extension twin orientation supported the idea that among all deformation twinning planes the ones would activate which show the high value of Schmid factor. Finally, Jiang et al [42] have performed similar experiments on AZ31 and AM 30 alloys. Using X-ray and EBSD, they have also reported a correlation for the activation of twinning with the Schmid factor.

However, in contrast with these studies [32,39,40-42], some reports do not support the applicability of Schmid's law to predict the operation of twinning. Beyerlein et al [43], studied the

relationship between material microstructure and extension twinning in magnesium by conducting a systematic, statistical analysis on EBSD data. They demonstrated that extension twin variants which observed after the compression tests were not exclusively those which show the highest Schmid factor. In addition, Jiang et al [44] conducted compression test on rolled Mg–3%Al–1%Zn, and investigated the relationship between the original grain and the extension twinning variants nucleated in the parent grain using EBSP. In agreement with Beyerlein et al [43], they also confirmed that the Schmid factor parameter cannot always predict the activation of extension twinning. Also, Barnett et al [45] conducted tensile tests on an AZ31 alloy and found using EBSD analysis that the occurrence of twinning could not always be predicted based on Schmid's law. Moreover, in the case of polycrystal plasticity models, Agnew et al. [33] used the viscoplastic self-consistent model to interpret the differences in the mechanical behavior of pure Mg compared with Mg-Li and Mg-Y magnesium alloys. The VPSC simulations were utilized to model the plain strain compression textures of different magnesium alloys by varying the CRSS of the potential deformation modes (including basal, prismatic and $\langle c+a \rangle$ slip and extension twinning systems). They have mentioned that, similar to the slip systems, the twinning systems are also activated according to a CRSS criteria. In agreement with Agnew's primary work [33], Yi et al. [35] and later Jain and Agnew [34] have used the VPSC model to predict the deformation behaviour in AZ31 magnesium alloy and assumed that the extension twinning can be activated based on the CRSS criterion. Afterwards, Jain [46] showed that the CRSS criterion in the VPSC model was not sufficient to predict twinning activation. It has been observed that twinning is sensitive to microstructure [47]. Generally, twins nucleate at some preferential sites such as grain boundaries, twin interfaces etc. Therefore, in the case of polycrystal plasticity models, twinning makes the situation complex. Thus, a more sophisticated representation of twinning was required. Recently, there has been effort to improve the twinning model. Beyerlein et al [47] have proposed a new probabilistic theory for twin nucleation in HCP metals. They have utilized the proposed theory into a multi-scale constitutive model. This newly developed model was validated for zirconium.

Furthermore, secondary twinning can occur within the primary twin region [48]. Generally reported double twins are $\{10\bar{1}3\}$ - $\{10\bar{1}2\}$ and $\{10\bar{1}1\}$ - $\{10\bar{1}2\}$, which are normally characterized by 22.3° and 37.5° boundary misorientation around a $\langle 1\ \bar{2}\ 1\ 0 \rangle$ axis, respectively. Both classes of double twins lead to a contraction along the c-axis [37]. A number of researchers [49,50] have suggested that double twinning may lead to texture changes that reorient grains into softer

orientations so that easier modes of slip can be activated. Also, recently the presence of double extension twins (i.e. extension twins formed within extension twins) in an AZ80 alloy, compressed along the $\langle 11\bar{2}0 \rangle$ direction was reported [46].

In addition to primary twinning, de-twinning may also happen during unloading or reverse loading. De-twinning leads to shrinking of twins, and does not require nucleation. Cáceres et al. [51] and Mann et al. [52] observed the partial reversal of $\{10\bar{1}2\}$ extension twins in magnesium during unloading. According to their in-situ observations using Normarsky interference contrast [51], they found that the existing twins may completely disappear or become narrower under reverse loading or unloading. Gharghoury et al. [40] also reported the reversible movement of twins during cyclic tension and compression on high purity magnesium and Mg-8%Al alloy using in-situ neutron diffraction. Later, Lou et al. [53] found twinning during in-plane compression and de-twinning in the subsequent tension for high purity magnesium, and AZ31B alloy, using metallography, acoustic emission, and texture measurement. Also, Yasutomi and Enoki used in-situ acoustic emission to study the detwinning process during the tensile test. Based on their in-situ measurement results, they concluded that detwinning occurs during three stages which are as follow. In the first stage, the twin boundary starts to move, and then in the second stage the twin area shrinks, and finally in the last stage the twin area disappears. Their EBSD analysis were in good agreement with their in-situ measurements [54]. Thereafter, other researchers studied the de-twinning behaviour in magnesium with similar conclusions using conventional tensile/compression tests [55].

2.3 Indentation tests

Measuring mechanical properties for materials on a small scale, e.g. grain size scale, cannot be easily conducted using conventional tensile or compression tests. Consequently, techniques measuring material "hardness" by indenting a material with an impression have been developed to determine such properties [56]. The indentation test is quick and simple and requires only a small sample and can be considered as a non-destructive method [57-59]. This technique has been traditionally employed for characterizing the local hardness [17] using sharp indenters such as Vickers or Berkovich or Knoop [60,61]. However, during traditional hardness tests load-displacement data is not usually measured. The development of instrumented indentation machine primarily began in the late 1980's. In the early 1990's, a commercially instrumented indentation

machine, became available [60]. However, one of the challenges associated with instrumented indentation testing is the indirect measurement of the contact area, i.e. the area of contact between the indenter and the specimen [62-64]. In conventional indentation tests, the area of contact is calculated from direct measurements of the dimensions of the residual impression after the removal of load. This can be different from the contact shape under the load, as there may have been plastic deformation during unloading [56]. However, in an instrumented indentation test the area of contact is determined by measuring the depth of penetration of the indenter into the specimen surface. Because of this, instrumented indentation testing is occasionally called depth sensing indentation (DSI) [61,62, 65-72]. The test process, typically involves an elastic–plastic loading series followed by an unloading.

One of the important improvement in the instrumented indentation test compared with the traditional hardness test is the continuous stiffness measurement (CSM) technique. This technique allows direct measurement of the contact stiffness at any point during the loading and also unloading, and can be made at even a small volume of deformation.

2.3.1 Analysis of instrumented indentation test data

Estimates of both the elastic modulus and the hardness of a specimen can be obtained in an instrumented indentation test from the load versus displacement measurements. Rather than a direct measurement of the size of residual impressions, contact areas are instead calculated from depth measurements together with knowledge of the shape of the indenter. The stiffness of the material can be calculated from unloading data using the following equation [60]:

$$S = \frac{dP}{dh} \quad (2.2)$$

Here, S is the experimentally measured stiffness of the upper portion of the unloading data, indicated in Figure 2.4. In order to measure the effective Young's modulus during unloading, the following equation has been determined for the unloading data [60]:

$$E_{eff} = \frac{\sqrt{\pi}}{2} \frac{S}{\sqrt{A}} \quad (2.3)$$

' A ' is the projected area of the elastic contact which can be determined from the indenter tip calibration and is a function of the contact depth (h_c). The areas of contact as a function of the depth of penetration for different types of indenters are given in Table 2.2 [56]. Figure 2.5 shows schematic representation of different indenters. All variables that were used in Table 2.2, i.e. θ , θ_1 , and θ_2 , are defined in this figure.

In addition, the machine compliance should be considered and calibrated. During the instrumented indentation test, the machine frame is also being loaded. Therefore, the total stiffness obtained from the loading curve also includes very small elastic deformation of the machine frame. However, since the machine frame is usually very stiff, i.e. $> 10^6$ N/m, the effect of the machine compliance is only significant at relatively large loads. In order to calibrate the machine compliance, a large indentation is conducted on a soft reference material such as aluminum. Using a Berkovich indenter, the contact area can be approximated to $24.5h_c^2$ (Table 2.2). Therefore, the expected stiffness can be measured from Equation (2.3). The difference between the measured value of the stiffness from the upper portion of the unloading curve, and the expected value is related to compliance of the machine frame [73].

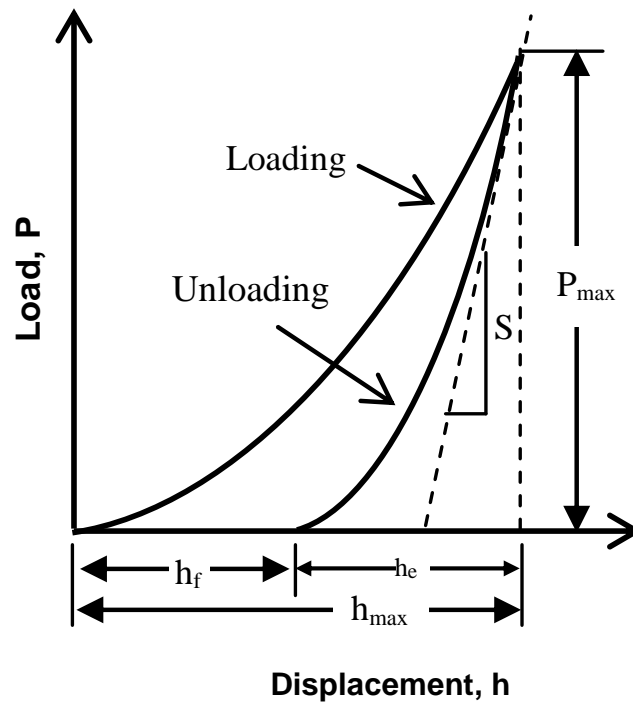


Figure 2.4. A schematic representation of load versus indenter displacement data for an indentation experiment. P_{max} is the peak indentation load, h_{max} is the maximum displacement at peak load, h_e is the elastic indentation depth, and h_f is the final depth of the contact impression after unloading.

Further, the hardness value can also be evaluated as:

$$H = \frac{P_{\max}}{A} \quad (2.4)$$

where P_{\max} is the peak indentation load and A is the projected area of the hardness impression.

Table 2.2. Projected areas for various types of indenters. The semi-angles given for the pyramidal indenters are the angles between the face with the central axis of the indenter [56]. These angles are defined in Figure 2.5

Indenter type	Projected area	Semi-angle θ (deg)
Sphere	$A = \pi 2R h_p$	N/A
Berkovich	$A = 3\sqrt{3} h_p^2 \tan^2 \theta$	65.30°
Vickers	$A = 4 h_p^2 \tan^2 \theta$	68°
Knoop	$A = 2 h_p^2 \tan \theta_1 \tan \theta_2$	$\theta_1 = 86.25^\circ, \theta_2 = 65^\circ$

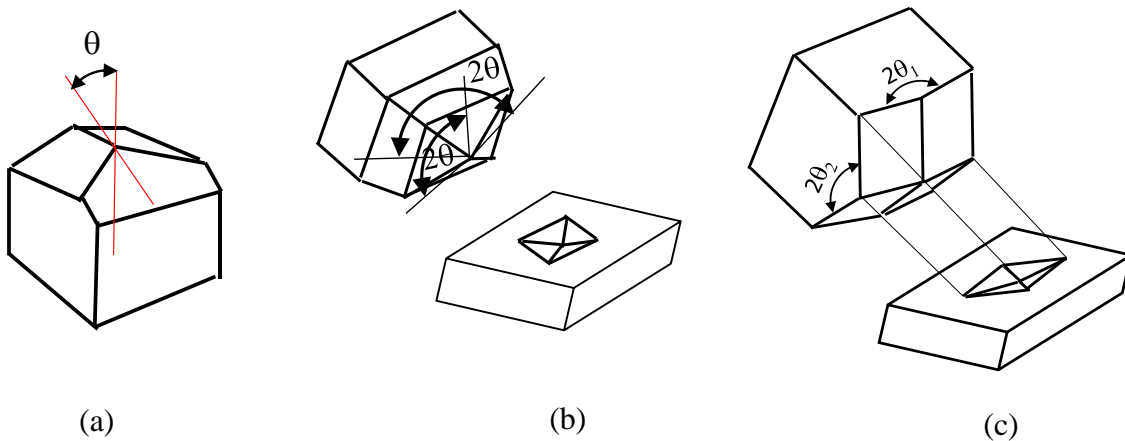


Figure 2.5. Schematic figures of various types of indenters: (a) Berkovich, (b) Vickers, and (c) Knoop indenter tips.

2.3.2 Indentation stress and strain

In addition to the measurement of hardness and Young's modulus, there is literature on extracting indentation stress-strain curves from the measured indentation load-displacement data using analytical methods [72-80]. In recent research it has been emphasized that the use of a

spherical indenter has unique advantages over sharp indentation [69,70], i.e. the stress singularity at the contact point is avoided and for the case of loading of elastically isotropic material, the complete stress field under the indenter can be calculated using Hertzian contact mechanics. The lack of a stress singularity under the indenter allows one to follow the elastic-plastic transition from the indentation load – displacement data [69,70]. Kalidindi et al. have suggested that extracting indentation stress–strain curves is more successful with spherical indenters [69,70] compared to sharp indenters.

According to Hertz theory for the case of spherical indentation [58,59], the indenter load P , is proportional to the effective radius R_{eff} , the elastic penetration depth h_{eff} , and the effective Young's modulus E_{eff} based on the equation below. E_{eff} can be derived from Equation (2.3).

$$P = \frac{4}{3} E_{eff} R_{eff}^{1/2} h_e^{3/2} \quad (2.5)$$

where R_{eff} can be expressed as:

$$\frac{1}{R_{eff}} = \frac{1}{R_i} + \frac{1}{R_s} \quad (2.6)$$

and subscripts s and i refer to specimen and indenter, respectively. For elastic loading of a flat sample, R_s approaches infinity, and therefore $R_{eff} = R_i$.

Furthermore, for elastic indentation, the above equation can be recast as:

$$\sigma_{ind} = E_{eff} \varepsilon_{ind} \quad (2.7)$$

$$\sigma_{ind} = \frac{P}{\pi a^2} \quad (2.8)$$

where a is the contact radius. A majority of studies have proposed a/R_{eff} or a/R_i as a measure of the indentation strain [70-74]. Recently Kalidindi et al [68] have shown that using a/R_{eff} or a/R_i as a measure of indentation strain lacks reasonable physical interpretation. They have proposed a new definition of the indentation strain based on experiments and finite element method simulations, and proposed the following simplified results:

$$\varepsilon_{ind} = \frac{4}{3\pi} \frac{h_e}{a} \approx \frac{h_e}{2.4a} \quad (2.9)$$

In order to evaluate the new definition of the indentation strain and the predicted stress and strain fields in the indented samples, finite element (FE) simulations of the spherical indentation using the commercial finite element code ABAQUS were conducted. The FE model which has been proposed by Kalidindi et al [68] is composed of two three-dimensional solids: (i) an elastic–plastic deformable sample with an initially flat surface and (ii) an elastic deformable hemi-spherical indenter. The contact between the indenter and the sample was assumed to be frictionless. The model was first utilized in order to predict the load–displacement curve in a purely elastic indentation. The results were compared against Hertz’s theory (Equation 2.5). The agreement with Hertz’s theory was within 3%. The predicted load–displacement curves and the stress fields in the aluminum and tungsten samples are shown in Figure 2.6.

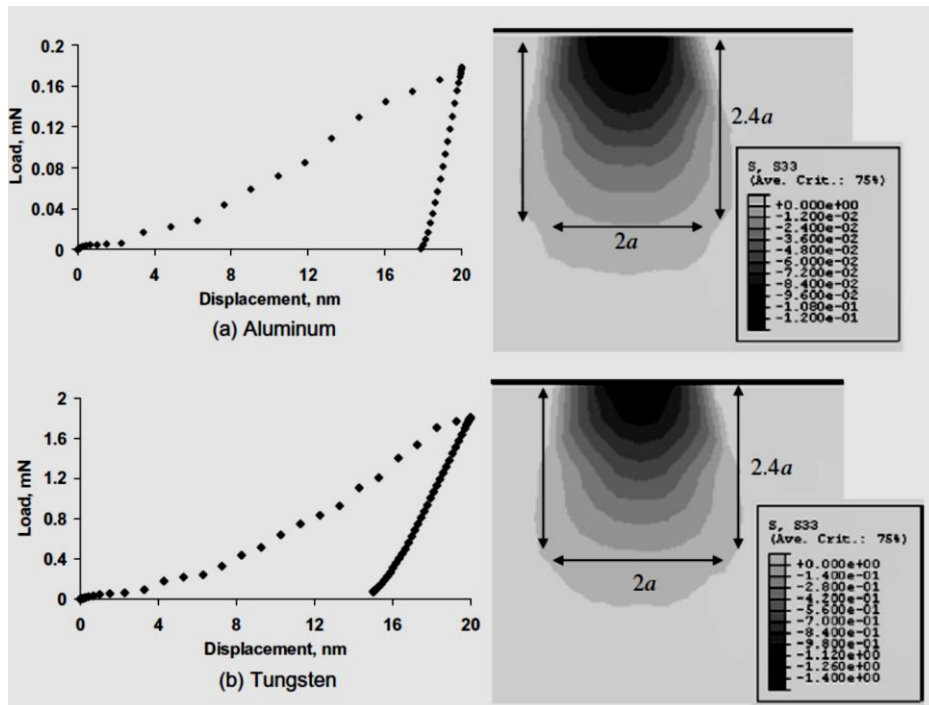


Figure 2.6. The predicted load–displacement curves and stress contours in the finite element simulations with the two selected material properties: (a) aluminum and (b) tungsten. The indentation zone in both cases extends approximately to a depth of about $2.4a$ [68].

2.3.3 Zero-load and zero-displacement

An accurate estimation of the point of initial contact must be obtained from the raw indentation data. The selection of the initial contact can significantly affect the estimation of the contact radius and, consequently, the values of the indentation stress and strain [68].

Several researchers have tried to develop methods to estimate the zero-point in the indentation test [81-74]. Kalidindi et al [68] have estimated the zero-point by conducting a regression analysis on the initial elastic loading segment in the measured load–displacement curve and fitting it to the expected relationships as predicted by the Hertz theory. They introduced \tilde{P} , \tilde{h}_e and S as the measured load signal, the measured displacement signal and the elastic stiffness signal in the initial elastic loading. According to Hertz theory [58], during the elastic loading, the three signals measured in spherical indentation should be related as:

$$S = \frac{3P}{2h_e} = \frac{3(\tilde{P} - P^*)}{2(\tilde{h}_e - h^*)} \quad (2.10)$$

where P^* and h^* indicate the values of the load and displacement signals at the actual point of initial contact. From the above equation, it can be concluded that a plot of $\tilde{P} - 2/3S\tilde{h}_e$ against S will produce a linear relationship whose slope is equal to $-2/3 h^*$ and the y-intercept is equal to P^* . Therefore, the initial contact point can be estimated using the above calculation.

2.3.4 Pop-in and pop-out events during indentation test

In addition to the material's mechanical properties mentioned thus far, such as hardness, Young's modulus, yield strength, it has been observed that an instrumented-indentation test can also be employed to examine defect nucleation and propagation events happening during loading and unloading. These events can be defined by sudden discontinuities in the load-displacement curve, as shown in Figure 2.7 [85]. In Figure 2.7, the discontinuity illustrates the transition from purely elastic behavior to plastic deformation and the formation of a permanent hardness impression [85].

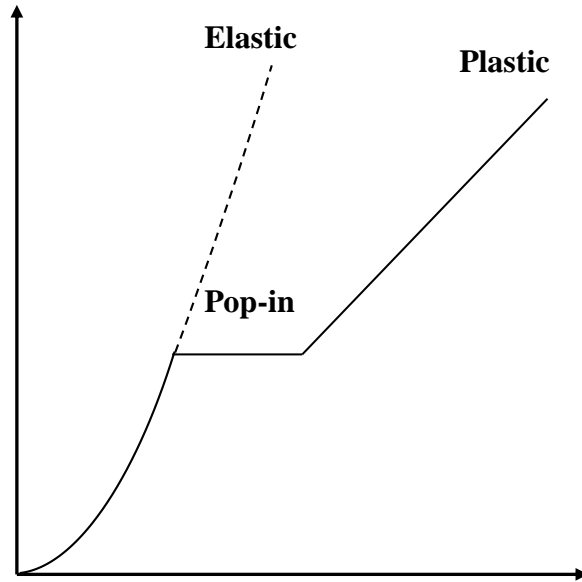


Figure 2.7. A schematic figure of pop-in.

Generally, the discontinuity occurs in the loading segment of load-displacement curve, called pop-in, may be ascribed to dislocation nucleation, or the sudden onset of plasticity [86]. It has also been reported that the discontinuities may also be associated with phase transformation [87] and mechanical twinning [88,89]. Further, there is some literature that suggests a phase transformation may happen during unloading giving rise to a discontinuity in the unloading curve, referred to as a pop-out [90-97]. For example, it has been reported that a material expansion due to a phase transformation in silicon may happen during unloading, causing the occurrence of a discontinuity in the unloading segment. Further, discontinuities may also be associated with dislocation motion or reverse plasticity of materials happening during unloading [98].

It has been illustrated for several materials that numerical first derivative analysis of load-displacement curves can be utilized to define the presence and the place that a discontinuity may occur during unloading in silicon [99]. Figure 2.8 shows the occurrence of a discontinuity happening in the unloading segment of the load-displacement curve (Figure 2.8a), and in its corresponding derivative (Figure 2.8b). This discontinuity which occurred during unloading is attributed to the phase transformation happening in silicon (from Si-I to Si-XII phase) [99].

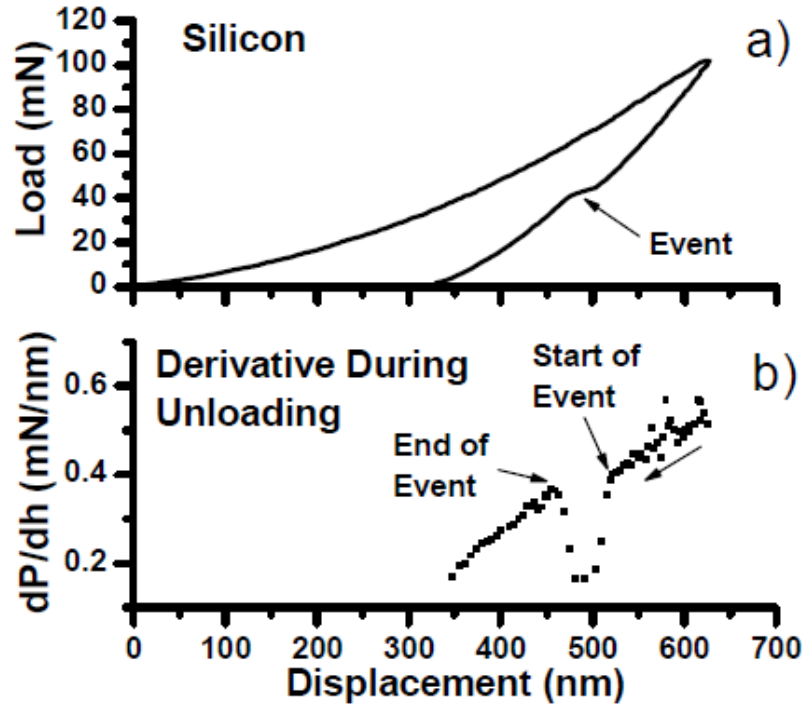


Figure 2.8: (a) The unloading segment of the load-displacement curve (b) and its corresponding derivative. The occurrence of the pop-out can be observed [99].

Catoor et al. [100] studied discontinuities in the load-displacement curve of high purity magnesium for the case of indentation parallel and perpendicular to the c-axis using a spherical indenter with a radius of $3.3 \mu\text{m}$. According to their post indentation TEM analysis and theoretical calculations, they proposed that the first discontinuity occurring in the loading segment of the indentation curve was due to the nucleation of $\langle a \rangle$ type dislocations. Later, Guo et al [101] showed that the occurrence of large pop-ins in the load-displacement curves during the indentation test is caused by twinning events rather than the nucleation of basal dislocations.

Furthermore, it has been shown by Pathak et al. [102] that the occurrence of pop-ins can be influenced by sample preparation. They have seen that a mechanically polished sample, which might have a layer which is severely deformed, could affect the pop-in behaviour. Recent research has illustrated that electropolishing can be used as a promising method to obtain reproducible results. However, electropolishing should be conducted for a sufficient time to ensure that the damaged layer is removed. Figure 2.9 shows the load-displacement data and indentation stress-strain curves obtained from the mechanically polished and electropolished samples of annealed (a) Al, and (b) W, using a $1 \mu\text{m}$ spherical indenter. As can be observed for the case of indentation on

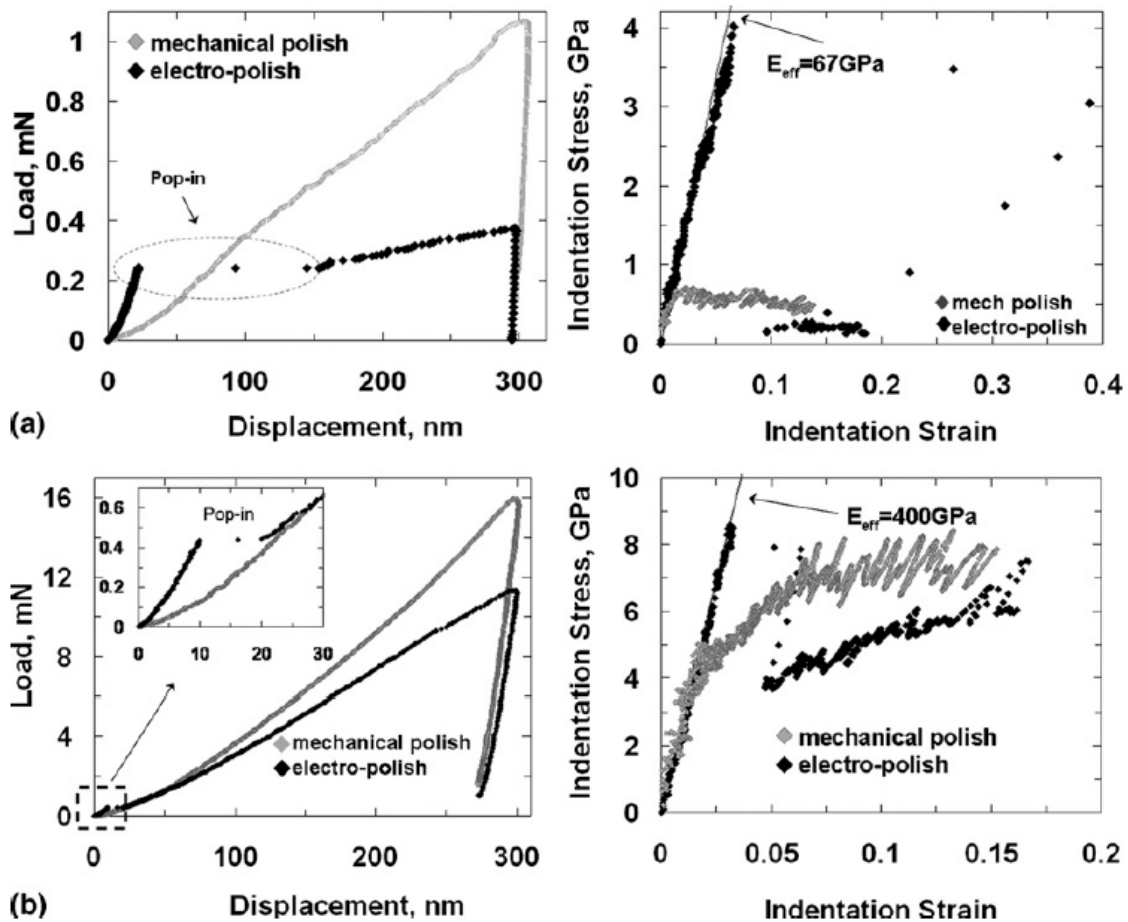


Figure 2.9: Indentation load-displacement and indentation stress-strain curves for mechanically polished and electropolished samples of (a) Al and (b) W using 1 μm spherical indenter [102].

mechanically polished sample, the pop-in events cannot be observed.

For the case of magnesium alloy, Guo [101] studied how the surface preparation affects the pop-in behavior in AZ31 alloy. She prepared two sets of samples of AZ31 alloy. For the first set, samples were mechanically polished and subsequently chemically polished using a solution of 60 % ethanol, 20 % distilled water, 5 % nitric acid and 15 % acetic acid. However, for the second set, in addition to mechanical and chemical polishing, the samples were polished by 50 nm colloidal silica (OPS). According to her observations, the loads and displacements at which the pop-ins occurred were repeatable for samples which were subsequently polished by OPS.

2.4 Influence of orientation on deformation behaviour of pure magnesium using instrumented indentation technique

As mentioned in Section 2.2.2, magnesium deforms on a number of slip and twin systems. However, the activation stresses for these systems are significantly different. This results in the plastic behaviour of magnesium being strongly asymmetric and anisotropic [7,8]. In addition, the activity of each type of slip and twin mode is dependent on parameters such as temperature, stress-state, alloying, and crystallographic texture. Consequently, in order to predict the mechanical response and texture evolution of magnesium and its alloys accurately, knowledge of the active deformation mechanisms and the variation in their relative contribution as a function of these variables is necessary.

To study the influence of the grain orientation with respect to the indentation loading axis on the mechanical response of magnesium, a number of studies have been conducted for different crystallographic orientations of single crystals of magnesium using different shapes of indenters [103-105]. In contrast to the conventional compression test results on HCP crystals [30,32], reports from indentation tests on single crystals of magnesium parallel to the [0001] direction, do not show any evidence for $\{10\bar{1}1\}$ and $\{10\bar{1}3\}$ compression twins [103-105]. However, Shin et al. [103] reported the activation of $\{10\bar{1}2\} < 10\bar{1}1 >$ extension twins on a single crystal of magnesium indented along the c-axis and perpendicular to the c-axis, using a combination of a Berkovich type indenter and transmission electron microscopy observations. They observed that in the case of indentation parallel to the c-axis, the extension twin was observed near the edge of the contact between the indenter and the surface. However, for the case of indentation perpendicular to the c-axis, extension twins are found under the indenter. Figure 2.10 shows schematically the favourable positions beneath the indent for extension twin activity for the case of indentation parallel and perpendicular to the c-axis [103]. As can be observed in Figure 2.10b, indentation parallel to c-axis induces compressive stress along the prismatic direction in the left and right side regions of the indenter. Therefore, the activation of extension twinning is expected at these two regions. However, for the case of indentation perpendicular to the c-axis (Figure 2.10c), the favourable location for tensile twinning is under the indent, where the indenter applies the compressive stress perpendicular to the c-axis.

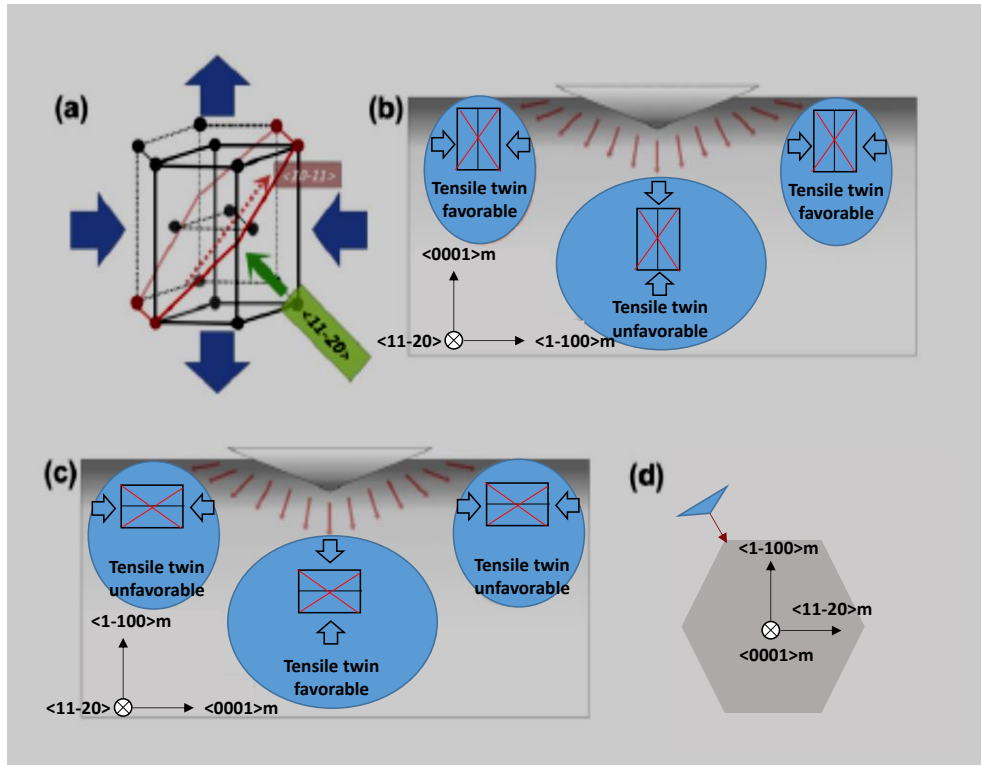


Figure 2.10: Schematic figure shows the favourable positions under the indenter for extension twin activity for the case of indentation (b) parallel and (c) perpendicular to the c-axis [103].

Recently, Kitahara et al. [104] employed a spherical indenter with a 500 μm radius on a single crystal of magnesium loaded parallel and perpendicular to the c-axis. They have used a combination of optical microscopy, EBSD orientation mapping and crystal plasticity finite element (CPFE) simulations to characterize the resulting deformation microstructures. Figure 2.11 shows the optical micrographs after the spherical indentation for the case of indentation parallel and perpendicular to the c-axis. For the case of indentation perpendicular to the c-axis, basal slip traces and extension twins were observed around the indenter, Figure 2.11a. However, for the case of indentation parallel to the c-axis, there was no evidence of slip traces or twins on the surface, Figure 2.11b. On the other hand, crystal plasticity analysis of indentation parallel to the c-axis predicted the activation of both $\langle a \rangle$ basal and $\langle c+a \rangle$ pyramidal slips systems under the indenter.

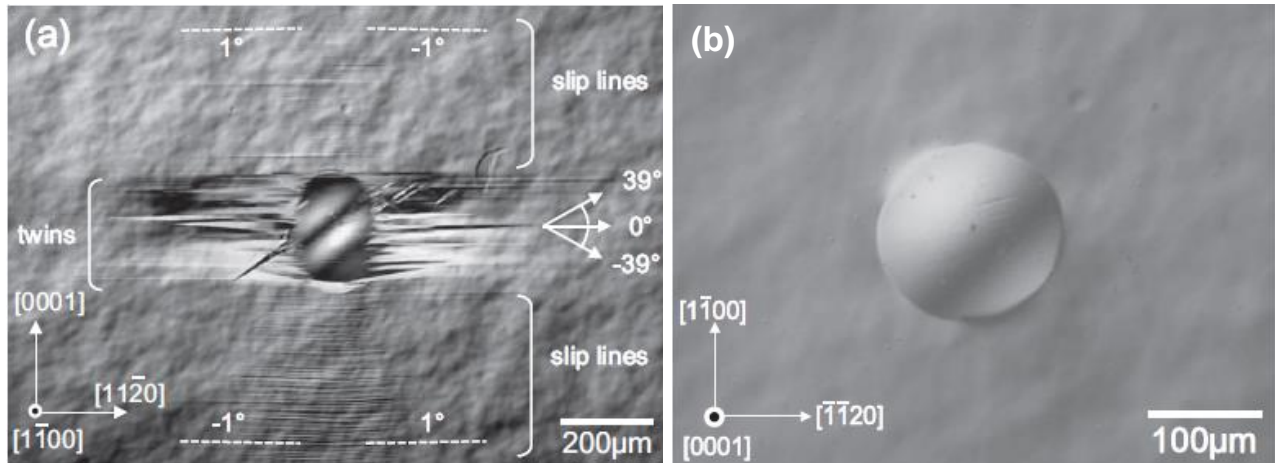


Figure 2.11: Optical micrographs of indentation (a) on $\{10\bar{1}1\}$ plane, and (b) $\{0001\}$ plane of single crystal of magnesium [104].

Further, the question of deformation modes under spherical indents has recently been considered by Catoor [100], Selvarajou [37], and Zambaldi [106]. Catoor et al. [100] impressed a spherical indenter with a radius of $3.3\ \mu\text{m}$ parallel and perpendicular to c -axis and of a magnesium single crystal. They have shown evidence for extension twins only in the case of spherical indentation conducted perpendicular to the c -axis. Using a spherical indenter with a radius of $663\ \text{nm}$ on a single crystal of high purity magnesium, Selvarajou et al [39] reported the occurrence of extension twinning under the indent in both the case of indentation along the c -axis and perpendicular to the c -axis, using TEM analysis in conjunction with crystal plasticity finite element modeling (CPFEM) results. Zambaldi et al [106] also studied the orientation dependant response of magnesium by using a spherical indenter with a radius of $1\ \mu\text{m}$. Grains with different crystallographic orientations with respect to specimen surface were studied in this work. They have used combined EBSD orientation mapping and three dimensional crystal plasticity finite element (CPFE) simulations to characterize the slip and twinning patterns around the indents. According to their experimental and model results, extension twins occur in magnesium crystal of any orientation. However, the twinning shapes around indentations are strongly dependant on the indented orientations. Finally, R. Sanchez-Martin et al. [107] conducted sphero-conical indentation on pure magnesium with a wide range of crystallographic orientations, and concluded that tensile twinning is a key deformation mode in magnesium. Sanchez-Martin reported that the observation of extension twins by EBSD on the surface around the indent for the case of

indentation parallel to the c-axis, depended on the size of the indent, i.e. twins were not observed for an indent of $\approx 2 \mu\text{m}$ but were found for indents of $\approx 4 \mu\text{m}$ or larger.

2.5 Indentation size effect

Material length scale and its influence on strength is a widely discussed topic. It has been observed [108] that the properties of materials become established at large scales, i.e. above $10 \mu\text{m}$. However, the mechanical properties may change significantly when the specimen is small or when a small volume is under deformation. For indentation tests, it has been observed that the measured hardness or yield strength increase drastically with decreasing the indentation size or the indenter size, this phenomenon is called the indentation size effect (ISE), [108-123].

In 1996, Poole et al [113] performed indentation tests using a Vickers hardness on annealed and working hardened poly-crystalline copper. They observed a size dependence of hardness in both work hardened and annealed copper, and explained this as a result of the presence of geometrically necessary dislocations due to the presence of strain gradients under the indent. Nix and Gao tried to bring a mechanistic theory to model the ISE [117], utilizing the Taylor dislocation model [122]. According to their model (Figure 2.12), as the indenter is pushed into the surface of a material, the geometrically necessary dislocations (GND) are required to accommodate the plastic deformation of the surface. Nix and Gao assumes that the indenter is conical, the angle between the undeformed surface and the indenter is θ , the contact radius is a , and the depth of indentation is h . They showed that the hardness can be expressed as a function of depth,

$$H = H_0 \sqrt{1 + \frac{h^*}{h_p}} \quad (2.11)$$

Where, $h^* = 3 \tan^2 \theta / 2b\rho_s$, is a length scale and $H_0 = 3 \sqrt{3} \alpha \mu b \sqrt{\rho_s}$ is the macroscopic hardness in the absence of GND.

Later Swadener et al [124] showed that the Nix and Gao's model can be extended for the case of a spherical indenter. Similar to the conical indenter, in the case of spherical indenter, it is assumed that the GNDs exist under the indent in a hemispherical region (Figure 2.13). For the conical indenter, the GND is inversely proportional to the indentation depth, h . However, for the

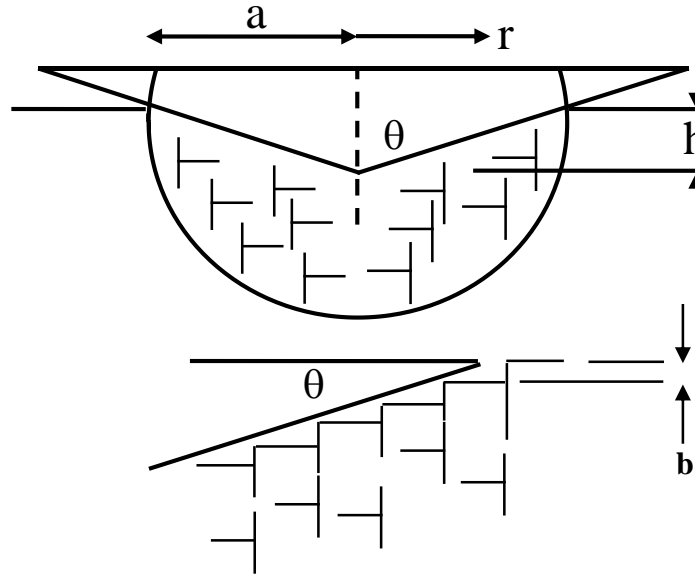


Figure 2.12: Model of geometrically necessary dislocations for a conical indenter.

case of spherical indenter, they have shown that the GND is inversely proportional to the indenter radius, R . Finally, Swadener et al. [124] illustrated that the hardness is inversely proportional to the square root of the indenter radius, and can be expressed as:

$$H = H_0 \sqrt{1 + \frac{R^*}{R_p}} \quad (2.12)$$

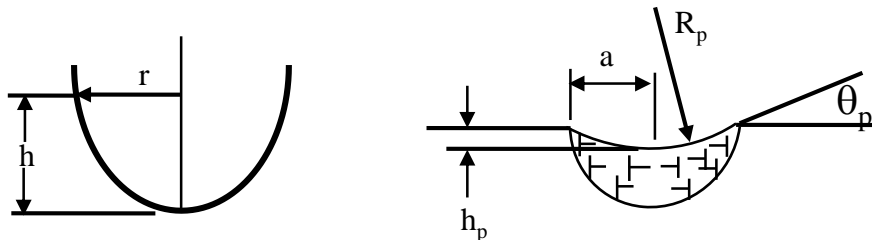


Figure 2.13: Geometrically necessary dislocations for a spherical indenter.

McElhaney et al. [125] and Ma and Clarke [126], conducted indentation using a Berkovich indenter on single crystal of Cu and Ag, respectively. They both illustrated that their experimental results are in good agreement with Nix and Gao's model. Later, Recent researches of Dust et al. [127-129] also confirms the displacement dependence of the hardness as proposed by Nix and Gao [116].

2.6 Effect of composition on the mechanical properties of magnesium

The systematic study of strengthening mechanisms of hexagonal closed packed materials is much more complex than for cubic metals [130]. Since, at least in principle, solute and precipitation hardening can affect the various deformation modes in different ways. Mg alloys have slower ageing kinetics compared to aluminum alloys and do not show natural ageing at room temperature [131].

Work on polycrystal and single crystal of high purity magnesium has shown that addition of alloying elements to magnesium, typically increases the hardness and the yield strength of the base material. Basically, the strengthening of the materials occurs by three different mechanisms, precipitation hardening, solid solution hardening, and grain refinement [133].

It has been reported that some elemental additions such as Zn, Al [134], and also rare earth alloying elements such as, Y, Ce, and Nd [135,136], result in solid solution strengthening in magnesium. Trinkle et al [137] used quantum-mechanical first-principles calculations to predict the chemical effects on strengthening of magnesium. They have used their model to predict solid solution strengthening of 29 different solutes in Mg. Also, their model was validated with the experimental data for the case of Zn and Al solutes in magnesium.

The seminal study on single crystals by Akhtar showed that [130] the CRSS for basal and prismatic slip in magnesium is controlled by solute addition. A variety of alloying additions including Zn [137,138], Al, In, Pb, Bi, Cd [137, 138], may lead to the solid solution hardening of basal slip in magnesium. The strengthening predominantly depends on the size misfit between the solute atoms and the matrix.

Among all studied solute atoms such as Pb, Cd, In, Bi etc [135-137], addition of Al and Zn to magnesium increases the CRSS for basal slip by an amount which is proportional to C^n , where C is the concentration of the solute, and n equals $\frac{1}{2}$ as described by Fleischer [140], or $\frac{2}{3}$ according to Labusch [141]. Cáceres and Rovera [139] have investigated the effect of Al additions on strengthening of Mg-Al alloys with Al contents ranging from 1 to 8 wt%. They observed that the more concentrated alloys show higher hardness which is due to the solid solution hardening effect. They showed that the hardness increase with the Al concentration as $H_{v10} \text{ (Kg mm}^{-2}\text{)} = 29 + 3 \text{ Al (wt\%)}$. Figure 2.14 shows how the Vickers hardness changes as a function of Al concentration.

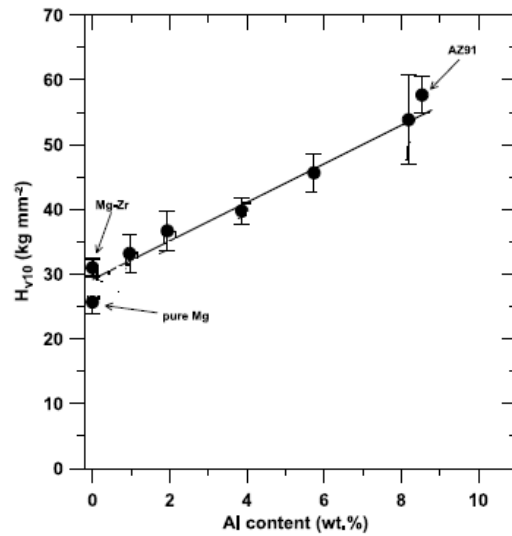


Figure 2.14: The Vickers hardness vs. Al content. The error bars show the standard deviations [139].

They concluded that in polycrystal of Mg-Al alloys, the strengthening of the basal plane controls the solid solution hardening.

2.7 Conclusion

As can be seen in this chapter, there is a variety of results in the literature for indentation of magnesium parallel and/or perpendicular to the c-axis with different indenter geometries (tip radius and shape). However, there is a lack of a consistent framework for understanding how plasticity occurs underneath the indenter and the interpretation of load-displacement measurements from instrumented indentation tests. Important questions remain such as how plasticity i) is initiated, ii) spreads and iii) how the penetration of a spherical indenter is accommodated by the operation of different deformation modes in the material under the indenter as a function of crystallographic orientations, composition, and indenter size.

CHAPTER 3 Scope and Objectives

The aim of this study is to demonstrate that instrumented spherical indentation can be used to measure basic information on plasticity in magnesium alloys particularly the critically resolved shear stress for basal slip and extension twinning from coarse grained polycrystalline samples. This requires detailed knowledge on the deformation behaviour under and around the indent for different loading directions with respect to the crystal axes. In this work, the indentation response of commercially pure magnesium, AZ31B and AZ80 alloys is investigated at room temperature using different indenters with indentation tip radii between 1 and 250 μm .

The following summarizes the specific objectives of the work:

- I. Experimentally characterize the deformation zone under the indenter, and identify the slip/twin activity in the deformation zone under the indent for different orientation relationships between the indenter and the grain. Three principle crystallographic orientations were studied, i.e. the indentation direction is approximately i) parallel to the c-axis, ii) basal plane inclined at 40° - 60° , and iii) perpendicular to the c-axis. The selected grains have a range of orientations that provide a reasonable coverage of the corners of the fundamental triangle in the inverse pole figure.
- II. Calculate the stress-state under the indent using Hertzian contact mechanics and subsequently characterize how stresses are resolved onto the various crystallographic slip/twin planes. This will help to understand how plasticity is initiated under the indenter for different crystallographic orientations.
- III. Measure the indentation size effect on the mechanical behaviour of magnesium. The purpose of this study is to determine the effect of tip radius on the yield strength and associated deformation mechanisms of magnesium with the goal of developing a model to convert CRSS's measured from a given indent radius to the macroscopic CRSS one would get on a single crystal.

IV. Examine the influence of solid solution hardening on the mechanical behaviour of magnesium using instrumented indentation. In particular, this study focuses on characterizing solid solution strengthening effects on critically resolved shear stress for basal slip of magnesium. AZ magnesium alloys are appropriate candidates to study solid solution strengthening, as there are existing results in the literature which can be compared to the results from the analysis of the indentation tests.

CHAPTER 4 Materials and Methodology

This chapter describes the experimental and modeling methods employed in this work. The organization of this chapter is as follows. First the details on the starting materials, processing of the as-received materials, and sample preparation techniques are described. Then, the instrumented indentation method is described in detail, and microstructure and texture characterization methods are explained. Finally, the methodology involved in three-dimensional crystal plasticity finite element (CPFE) simulations is described.

4.1 Initial material

As-cast commercially pure Mg was supplied by McMaster University. ZE10 alloy was cast by CANMET Materials Laboratory. The as-received commercially pure Mg, and ZE10 alloy were hot-rolled, and annealed by Guilhem Martin at the University of British Columbia [142]. AZ80 alloy was supplied by Timminco Inc. in the form of DC cast billets. AZ31B alloy was provided by Magnesium Elektron in the form of a sheet with an initial thickness of 6 mm. Table 4.1 shows the chemical composition of the investigated as-received materials.

Table 4.1: Chemical composition of investigated of as-received materials (in weight percent)

Element	Al	Zn	Mn	Si	Nd	Mg
Commercially pure	0.06	0.01	0.01	0.02	-	Bal.
AZ31B	2.5	0.7	0.2	-	-	Bal.
AZ80	8	0.5	0.2	-	-	Bal.
ZE10	-	1	-	-	0.5	Bal.

4.2 Material characterization: sample preparation and tools

Sample preparation for optical microscopy, scanning electron microscopy (SEM), electron backscatter diffraction (EBSD), and instrumented indentation was as follows. Samples were ground with 600, 800, 1200, 2400 grade SiC grinding papers, followed by diamond suspension polishing using 6 μ m, 1 μ m, and 0.05 μ m compound.

For the instrumented indentation test, it is crucial to have a very clean sample surface as, even very small polishing scratches or twins may significantly affect the final results [102]. It has been observed [143] that even a fine mechanical polish, using diamond particles of sizes ranging from 0.5–1 μ m, can result in a disturbed surface layer, the thickness of this layer being on the order of the diamond particle size. The initial elastic segment in a nanoindentation experiment typically covers the initial 10–20 nm of indentation. Therefore surface preparation can significantly affect the indentation load-displacement curve. Particularly, the critical load for the first discontinuity depends considerably on how much of the damaged surface is removed by electro polishing or chemical polishing [134]. In this study, the damaged layer results from the mechanical polishing. This layer was removed using a 10% nitric acid in 90% absolute ethanol chemical polishing solution and subsequent electropolishing. The sample was immersed in the solution for 5 minutes. After chemical polishing, an additional step of electropolishing was needed both for indentation tests and also for EBSD observation. The surface of the sample was examined by high resolution scanning electron microscopy (SEM) after the chemical polishing and subsequent electropolishing. There were not any scratches or twins visible on the surface of the sample. Electropolishing is performed at -20°C for 20 seconds using a stainless steel cathode and magnetic stirring. A voltage of 20-30V is used. A solution of 20% nitric acid in 80% absolute ethanol is used for electropolishing. After electro-polishing, samples were quickly rinsed with ethanol and dried under a blast of air.

For optical metallography, the polished surface was etched in an acetic-picric solution (4.2 g picric acid, 10 ml acetic acid, 10 ml water, 70 ml ethanol) to reveal the grain boundaries. The sample was immersed in the solution until its surface turned light orange (~ 45 s) and was then rinsed with ethanol and dried in a blast of air. A Nikon EPIPHOT 300 optical microscope was used to examine the initial microstructure of the investigated materials.

4.3 Processing of initial material

One of the significant concerns for investigating the local mechanical response of individual grains is that the selected grains should be large enough (of the order of hundreds of microns) [71], to reduce the chance of a grain boundary existing just below the surface of the indentation site. Figure 4.1a shows an optical micrograph from the as-received commercially pure magnesium sample. The material is fully recrystallized with an average grain size of $\approx 30 \mu\text{m}$. Figures 4.1b and 4.1c show the $\{0001\}$ and $\{10\bar{1}0\}$ pole figures (measured via EBSD from 5000 grains).

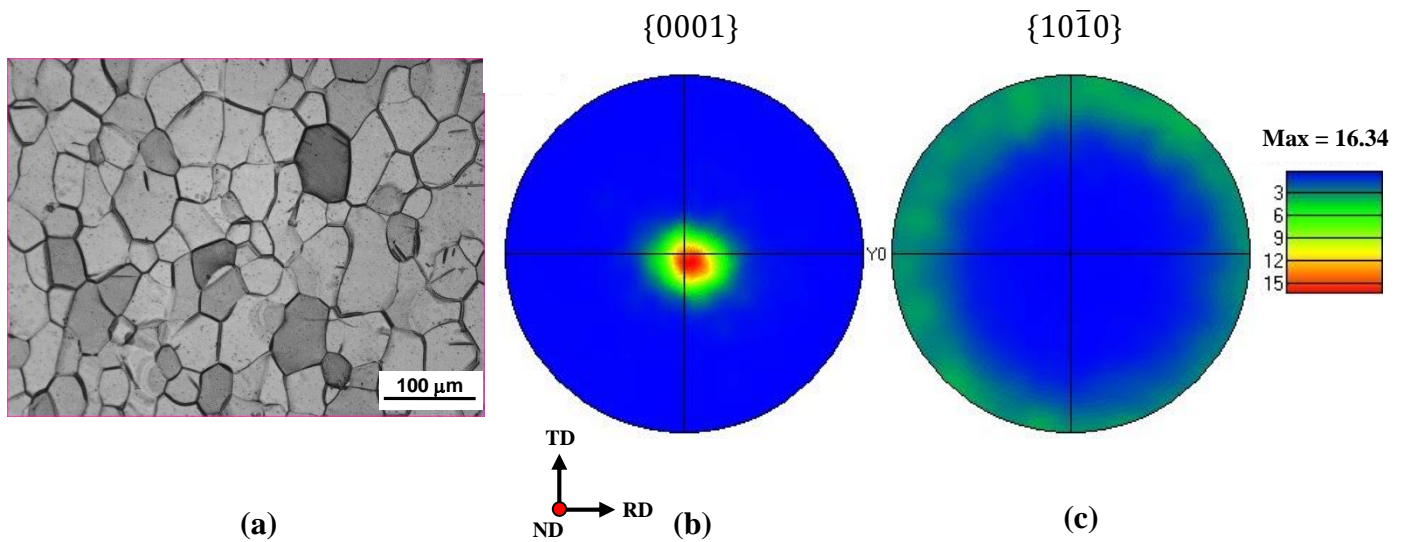


Figure 4.1: a) An optical micrograph showing the grain structure of the as-received magnesium sheet, b) and c), respectively show the EBSD measured $\{0001\}$ and $\{10\bar{1}0\}$ pole figures (stereographic), representing the texture of the same material. The RD, TD and ND correspond to rolling direction, transverse direction and normal direction of the sample, respectively. The intensity colour scale is given in multiples of a random distribution (m.r.d).

The average grain size of as-received ZE10, AZ31B, and AZ80 alloys were 20 μm , 8 μm , and 30 μm , respectively. Therefore, in order to have a material with a large grain size, a heat-treatment process was required on the as-received materials.

4.3.1 Heat treatment of the as-received material

The annealing time and the temperature of the investigated materials were selected according to the phase diagram. For commercially pure Mg, AZ31B, and ZE10, annealing was performed at 500 °C for 48 hours in a resistance furnace under an argon atmosphere. After the annealing, the material was quenched in water. For the AZ80 alloy, heat treatment was performed at 420 °C for 48 hours. This temperature was selected to ensure annealing occurred in the single phase region (Figure 4.2).

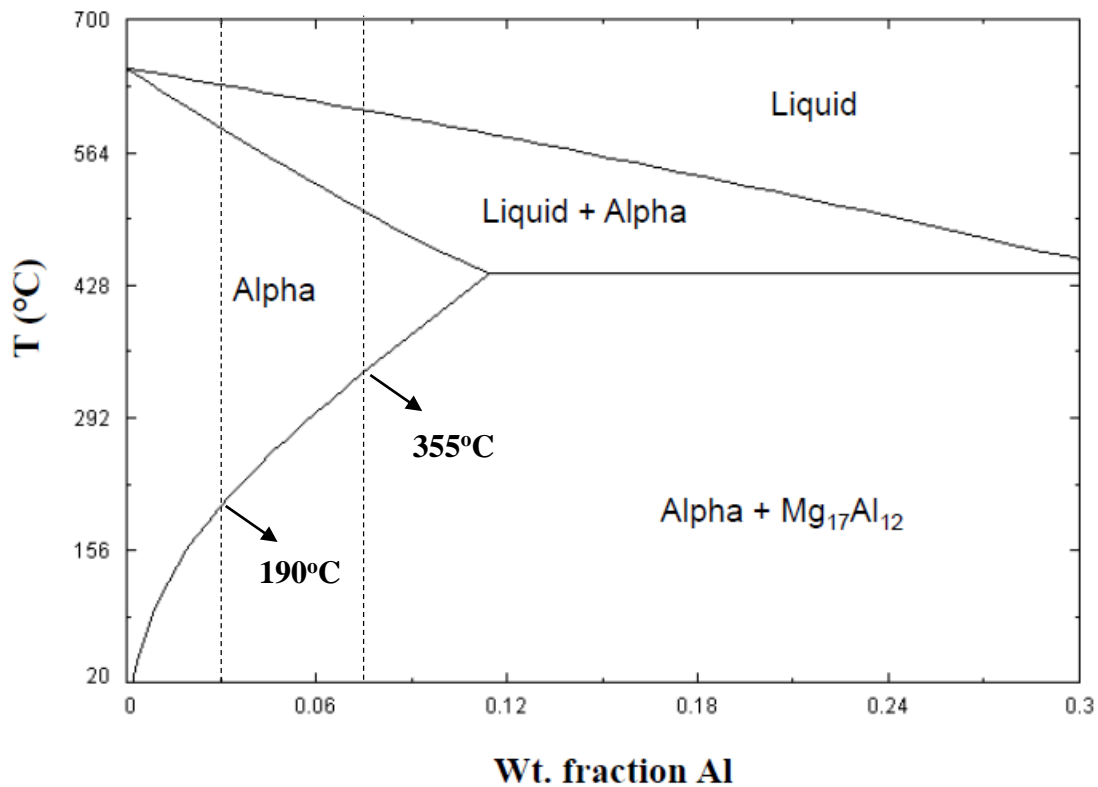


Figure 4.2: Mg-Al binary equilibrium phase diagram [144].

Figure 4.3a shows the optical micrographs of the annealed pure Mg. The abnormally large grains, illustrated by white arrows, were selected to perform the spherical indentation tests. Similarly, the micrographs of the annealed materials for ZE10, AZ31B, and AZ80 can be observed in Figures 4.3b, 4.3c, and 4.3d, respectively.

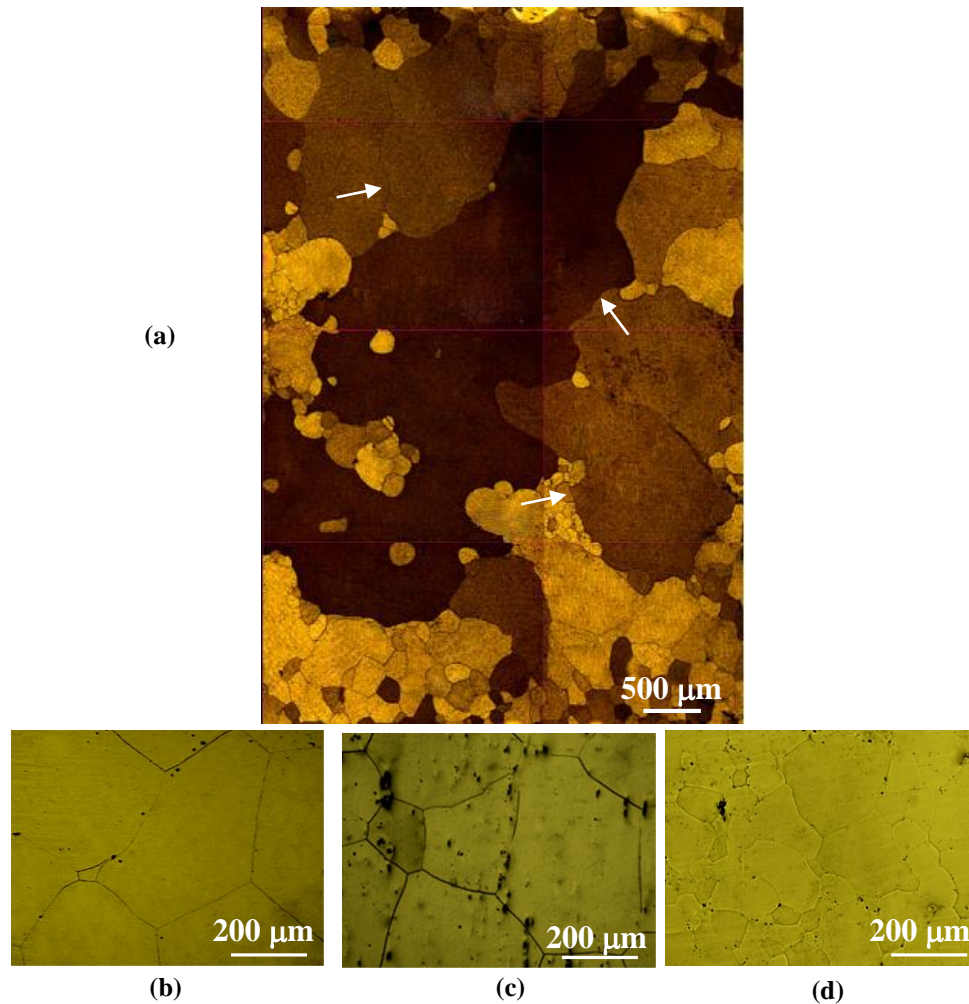


Figure 4.3: Optical micrographs of the annealed materials (a) commercially pure Mg, (b) ZE10, (c) AZ31B, and (d) AZ80.

Crystallographic orientations of selected grains were determined using EBSD. The inverse pole figure (IPF) in Figure 4.4 shows the crystallographic direction parallel to the normal direction of the sheet (the surface into which the indents are made) for several grains. The grain orientations are colour-coded to reflect their positions in the inverse pole figure (IPF) from an EBSD map. For example, the grains that have a (0001) crystallographic plane parallel to the sample surface are coloured red. The selected grains have orientations that provide three principle cases, i.e. the indentation direction is approximately i) parallel to the c-axis, ii) basal plane inclined at 40°-60°, and iii) perpendicular to the c-axis.

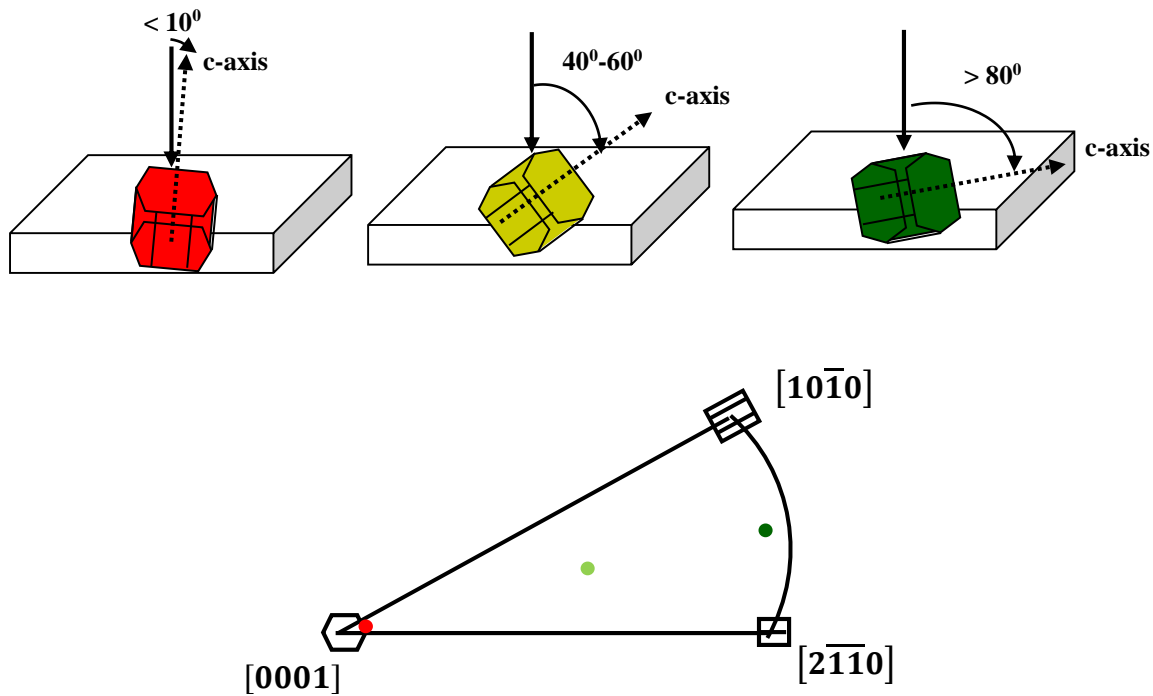


Figure 4.4. (a) Schematic drawings illustrating the orientation of the grains in the sheet sample.

4.4 Mechanical property testing, using instrumented indentation testing

Instrumented indentation was carried out using a MTS XP Nanoindentation System equipped with a continuous stiffness measurement (CSM) attachment as shown in Figure 4.5. A schematic figure of the nanoindenter is shown in Figure 4.6. The indenter shown in the schematic figure, can be changed based on experimental needs. In this work, 5 different spherical diamond tips with $1 \mu\text{m} \pm 0.2 \mu\text{m}$, $3.94 \mu\text{m} \pm 0.2 \mu\text{m}$, $13.3 \mu\text{m} \pm 0.5 \mu\text{m}$, $50.0 \mu\text{m} \pm 5.0 \mu\text{m}$, and $250.0 \mu\text{m} \pm 12.0 \mu\text{m}$ radii were used. The tips were produced by Synton Company¹ in Switzerland. All measurements were conducted overnight to minimize the variations from activity in the laboratory. Temperature in the laboratory is maintained at $21^\circ\text{C} \pm 0.5^\circ\text{C}$. Cube specimens were mounted on cylindrical holders designed for the indentation machine. The measurements were made at a loading rate of 5 mN/sec. The data acquisition rate was 15 Hertz. The tests were carried out under displacement control with a variety of indent depths ranging from 500 nm to 3500 nm.

¹ Synton-MDP LTD, Helmstrasse 1, 2560 Nidau, Switzerland, website: info@synton-mdp.ch, Phone: +41323329100, Fax: +41323329101



Figure 4.5. Instrumented-indentation machine.

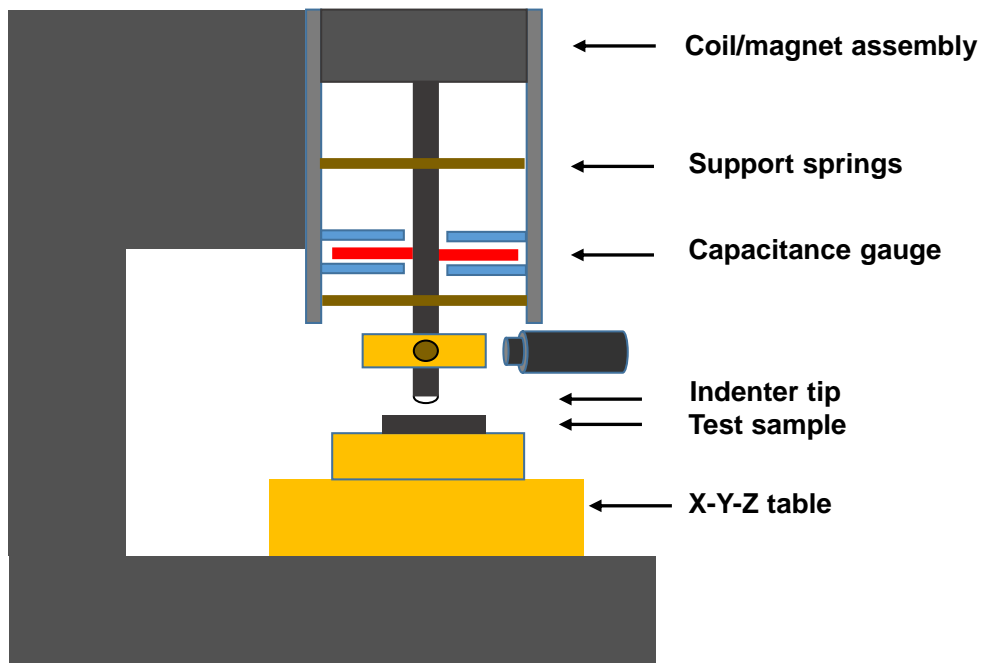


Figure 4.6: Schematic figure of instrumented-indentation machine.

The indentation test points were chosen in the middle of a grain, well away from the grain boundaries, to reduce the influence of grain boundaries on the test results. The orientation of each grain was measured once prior to and again after indentation using EBSD. The indentation tests were performed at least 20 times on a selected grain. For example, Figure 4.7 shows the load-displacement data for six indentation tests (Labelled Test 1 to Test 6) performed on the same grain to an indentation depth of 3500 nm. The maximum load for an indent of 3500 nm displacement is $128 \text{ mN} \pm 1 \text{ mN}$, i.e. a variation of less than 1%.

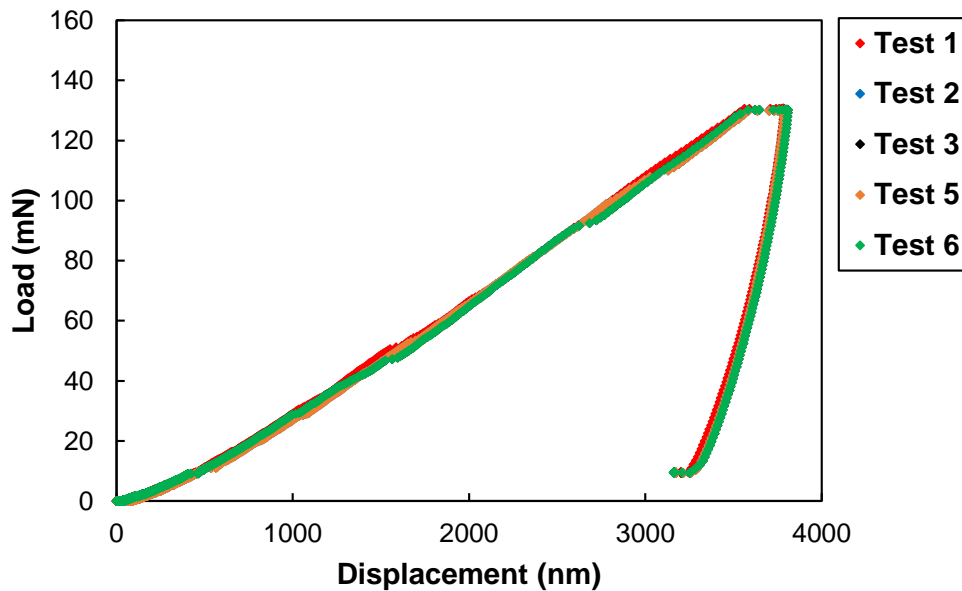


Figure 4.7: The load-displacement curves obtained from nanoindentation tests on one grain.

It was of interest to compare the elastic solution of Hertz for the load-displacement curve to the experimentally measured results, that can be done by using Equation (2.5) from Section (2.3.2) which shows the relationship between the indentation load (P) and the elastic indentation depth (h_e).

In order to characterize the discontinuities occurring during unloading, the unloading portions of the load-displacement curves were numerically differentiated. The first order derivative (dP/dh) at a depth $h=h_0$ was calculated as:

$$\left(\frac{dP}{dh}\right)_{h_0} = \frac{P_{h_0+\Delta h} - P_{h_0}}{\Delta h} \quad (4.1)$$

The (dP/dh) values were calculated for all points of the unloading segment without smoothing, and were plotted versus displacement. To identify the zero-load and zero-displacement point in the measured raw dataset, the approach of Kalidindi (Section 2.3.3) was followed [68].

Furthermore, a series of calculations were conducted using the Hertz solution for the complete elastic stress field under the indenter [56]. First, the normalized stress tensors (i.e. σ_r/ρ_m , σ_θ/ρ_m , σ_z/ρ_m , and τ_{rz}/ρ_m) beneath the indenter were calculated in the cylindrical coordinate system (r, θ, z) using the following equations [145]:

$$\frac{\sigma_r}{\rho_m} = \frac{3}{2} \left\{ \frac{1-2\nu}{3} \frac{a^2}{r^2} \left[1 - \left(\frac{z}{u^{1/2}} \right)^3 \right] + \left(\frac{z}{u^{1/2}} \right)^3 \frac{a^2 u}{u^2 + a^2 z^2} + \frac{z}{u^{1/2}} \left[u \frac{1-\nu}{a^2 + u} + (1+\nu) \frac{u^{1/2}}{a} \tan^{-1} \left(\frac{a}{u^{1/2}} \right) - 2 \right] \right\} \quad (4.2)$$

$$\frac{\sigma_\theta}{\rho_m} = -\frac{3}{2} \left\{ \frac{1-2\nu}{3} \frac{a^2}{r^2} \left[1 - \left(\frac{z}{u^{1/2}} \right)^3 \right] + \frac{z}{u^{1/2}} \left[2\nu + u \frac{1-\nu}{a^2 + u} - (1+\nu) \frac{u^{1/2}}{a} \tan^{-1} \left(\frac{a}{u^{1/2}} \right) \right] \right\} \quad (4.3)$$

$$\frac{\sigma_z}{\rho_m} = -\frac{3}{2} \left(\frac{z}{u^{1/2}} \right)^3 \left(\frac{a^2 u}{u^2 + a^2 z^2} \right) \quad (4.4)$$

$$\frac{\tau_{rz}}{\rho_m} = -\frac{3}{2} \left(\frac{rz^2}{u^2 + a^2 z^2} \right)^3 \left(\frac{a^2 u^{1/2}}{a^2 + u} \right) \quad (4.5)$$

Where ρ_m is the mean contact pressure, a is the indent contact radius, ν is a Poisson's ratio, and u is obtained from the following equation,

$$u = \frac{1}{2} \left[(r^2 + z^2 - a^2) + \left[(r^2 + z^2 - a^2)^2 + 4a^2 z^2 \right]^{1/2} \right] \quad (4.6)$$

Later, the cylindrical coordinate system was converted to Cartesian coordinate system (x, y, z) using the following formulas,

$$r = \sqrt{x^2 + y^2} \quad (4.7)$$

$$\theta = \arctan \frac{y}{x} \quad (4.8)$$

$$z = z \quad (4.9)$$

Thus the six normalized stress tensor components beneath the indenter were obtained, i.e. σ_{xx}/p_m , σ_{yy}/p_m , σ_{zz}/p_m , τ_{xy}/p_m , τ_{yz}/p_m , and τ_{xz}/p_m . At each location under the indent, each component of the stress tensor was then resolved on the relevant crystallographic plane of interest for any given crystallographic loading direction using rotation matrices. The following rotation matrices can be used to rotate the normalized stress tensors under the indent counter-clockwise by any arbitrary angle θ about the x , y , or z axis, in three dimension,

$$R_x(\theta) = \begin{bmatrix} 1 & 0 & 0 \\ 0 & \cos \theta & \sin \theta \\ 0 & -\sin \theta & \cos \theta \end{bmatrix} \quad (4.10)$$

$$R_y(\theta) = \begin{bmatrix} \cos \theta & 0 & \sin \theta \\ 0 & 1 & 0 \\ -\sin \theta & 0 & \cos \theta \end{bmatrix} \quad (4.11)$$

$$R_z(\theta) = \begin{bmatrix} \cos \theta & \sin \theta & 0 \\ -\sin \theta & \cos \theta & 0 \\ 0 & 0 & 1 \end{bmatrix} \quad (4.12)$$

4.5 Microstructure and texture characterization

4.5.1 Electron backscatter diffraction-based orientation microscopy (EBSD)

A Zeiss Sigma VP Field Emission Scanning Electron Microscope equipped with the DigiView IV EBSD Camera and combined with the Orientation Imaging Microscopy (OIM) Data Analysis software version 7.01 was used to determine the crystal orientations of grains of the initial materials before indentation tests. The operating conditions were as follows: accelerating voltage 20 keV, sample tilt 70°, working distance 12 mm, step size 1 μm .

To experimentally characterize the deformation zone underneath the indent, 3D-EBSD at the Max-Planck Institute tests were performed on deformed samples using a Zeiss XB 1540 dual-beam high-resolution field emission scanning electron microscopy equipped with an Orsay Physics focused ion beam column. An EDAX/TSL EBSD system with a Hikari EBSD detector was used to perform EBSD mapping. Serial sectioning for 3D EBSD was done with a Ga^+ ion beam as described in [146]. Figure 4.8 provides a brief summary of the sample preparation for 3D EBSD using a lift-out method modified from methods described in [147]. First, the indent was covered with a protective platinum layer (1). Next, using focuses ion beam (FIB) trenches were cut at an angle of 45° with respect to the surface from both sides of the indent to create a wedge-shaped material block containing the indent (2). This block was attached to a nano-manipulator using a Pt-deposit. Finally it was cut free from the rest of the sample by cutting the front surfaces perpendicularly into the surface. This free standing block was then extracted from the sample and moved, using the manipulator to an edge of the sample (3). There, it was fixed using a Pt deposit and finally cut free from the manipulator. The block was then in an ideal position for 3D orientation microscopy. 3D EBSD was performed by milling the indent-containing block in grazing incidence parallel to the surface as indicated by the hatched lines (4). For EBSD the sample was tilted by 36° from the milling position (5) as described in detail in [146]. The milling for individual sections was performed for 360 seconds with a 500 pA Ga^+ ion beam accelerated at 30 kV. The acceleration voltage used for acquisition of EBSD data was 15kV. All orientation maps were processed with the EDAX/TSL OIM Data collection software version 7.01 using a batch processing operation. This operation allows one to apply the same set of analysis functions to several datasets. The 2D-EBSD maps were cleaned using a confidence index (CI) standardization and a CI neighbour

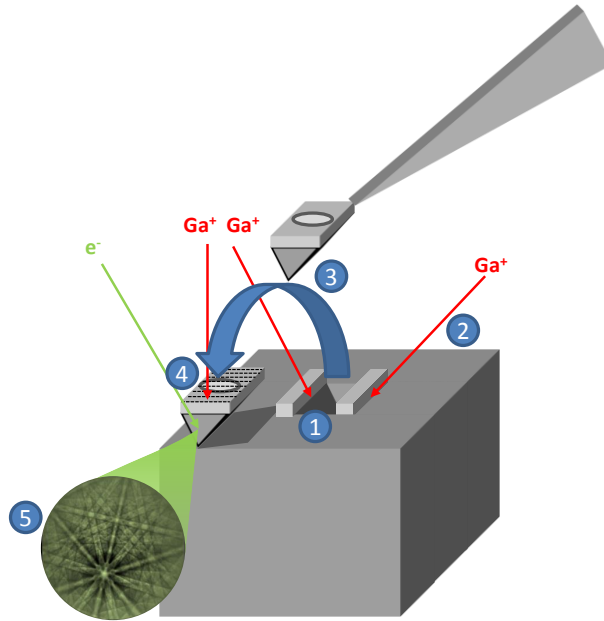


Figure 4.8: A schematic figure of the sample preparation for 3D-EBSD using the lift-out method.

correlation algorithm. Finally, the resulting datasets of 2D-EBSD maps were analyzed and joined together using the post-processing software QUBE [148].

4.5.2 Geometrically necessary dislocations (GND) calculations

In order to calculate the geometrically necessary dislocations (GND), we followed Demir's approach [149] for HCP crystals. GND are described by two vectors, the Burgers vector, b , indicating the slip direction, and the normalized tangent vector, t , representing the dislocation line direction. The $\langle a \rangle$ Burgers vector is 0.3196 nm, and the $\langle c+a \rangle$ Burgers vector is 0.6095 nm in the case of magnesium. Details of the analysis of GND from EBSD output data is reported elsewhere [149]. There are several sources of error that can influence the estimated GND density [149,150]. However, the orientation noise error is the most significant one [150]. Orientation noise represents a random background to the GND signal.

4.6 Crystal plasticity finite element simulation of indentation in magnesium

In order to support the analysis of the observed deformation patterns under the indent, three-dimensional crystal plasticity finite element (CPFE) simulations were performed by Dr. Claudio Zambaldi at the Max-Planck Institute for Iron Research. Zambaldi modeled a spherical tip with a

radius of 13.5 micron, the same tip geometry which was used in the experiments. The model was generated parametrically in the preprocessor software MSC Mentat by a set of Python routines which were used to generate Mentat procedure files.

An elasto-viscoplastic phenomenological crystal plasticity model was used in this simulation [151,152]. The specific implementation which we are applying here is explained elsewhere [153,154]. It is a predecessor of the DAMASK [155,156] code base and employs a user-defined material subroutine to interface the constitutive law with the finite element solver, here the material subroutine hypela2 of the commercial FEM system MARC.

In this model, only the three basal slip systems of type $\{0001\} \langle 1\bar{1}20 \rangle$, were allowed to operate, i.e, the prismatic $\langle a \rangle$ slip, pyramidal $\langle c+a \rangle$ slip, or any deformation twinning were not included. Based on previous work [103-105], the most probable slip systems observed during indentation on perpendicular to the (0001) plane was basal slip. Deformation twinning was also not accounted for in the simulations. In Chapter 5, it will be shown that including only basal slip in the model will help to clarify the source of deformation patterns under the indent. This will be done by comparing the 3D-EBSD results and CPFEM results.

The elastic constants $c_{11} = 58.0$ GPa, $c_{12} = 25.0$ GPa, $c_{13} = 20.8$ GPa, $c_{33} = 61.2$ GPa, $c_{44} = 16.6$ GPa and $c_{66} = 16.5$ GPa were used in the model [157]. According to extended Voce law [158], the evolution of the threshold stress with accumulated shear strain is expressed as:

$$\tau = \tau_0 + (\tau_s + a\varepsilon)(1 - \exp(-\varepsilon \frac{h_0}{\tau_s})) \quad (4.13)$$

An initial shear strength, τ_0 , of 10 MPa, a saturation shear strength, τ_s of 100MPa, an initial hardening slope parameter, h_0 , of 100MPa, and a saturation hardening exponent, a , of 2.0, were used for all simulations [154]. The reference shear rate was 10^{-3} s^{-1} and the latent hardening coefficients between all slip systems were arbitrarily set to 0.

CHAPTER 5 The Effect of Crystallographic Orientation on the Local Mechanical Properties of Commercially Pure Magnesium

5.1 Introduction

This chapter is concerned with a study of the effect of crystallographic orientation on the local mechanical properties of commercially pure magnesium using a spherical indentation. First the experimental results obtained on commercially pure Mg for indentation approximately parallel to the [0001] direction will be presented. In this case, the angle between the indentation loading direction and the c-axis is 9.3° . It will be shown that there is an advantage to choosing a grain oriented slightly off the ideal basal orientation. In Sections 5.3 and 5.4, the experimental results for two other crystallographic orientations, i.e. for the cases in which the angle between the indentation direction and the c-axis are 80° and 54° will also be presented. The results section includes optical microscopy, high resolution EBSD characterization, spherical indentation load-displacement data, and 3D-EBSD measurements using a combination of automated FIB serial sectioning and EBSD orientation mapping on the individual sections for each orientation. These results will be discussed in detail to provide a self-consistent view of the local mechanical behaviour of magnesium.

5.2 Spherical indentation with direction close to [0001]

5.2.1 Microstructural analysis before and after the spherical indentation

Figure 5.1a shows the inverse pole figure map and its corresponding {0001} pole figure which shows the orientation of the loading axis with respect to HCP c-axis. According to this map, for this studied case, the angle between the indentation direction and the c-axis is 9.3° . In the following the indented orientations are identified by an angle between the c-axis and the indentation direction ranges between 0 to 90 degrees.

A number of indentation tests with three different depths (500 nm, 1500 nm, and 3500 nm) were made on this grain, i.e. where the angle between the loading axis and c-axis is 9.3° . Figure 5.2 shows the load-displacement data for three indents of different depths. The corresponding

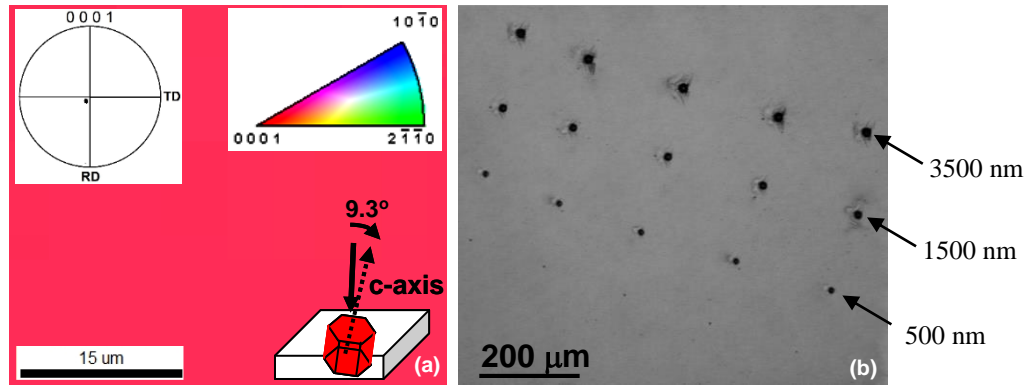


Figure 5.1: (a) Inverse pole figure map of the studied grains before indentation tests, (b) optical micrograph after spherical indentation.

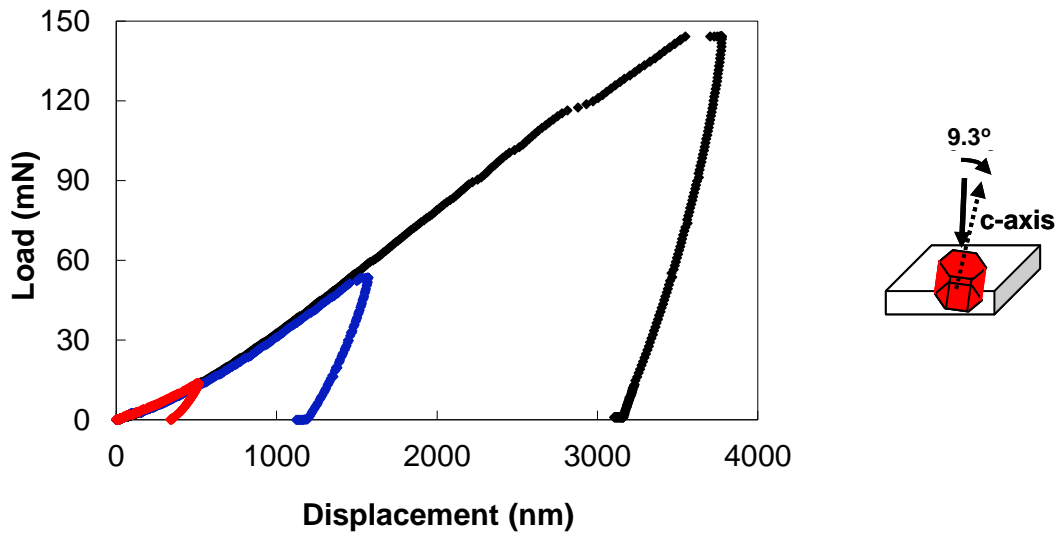


Figure 5.2: Indentation load-displacement curves for three different indent depths: 500 nm, 1500 nm, and 3500 nm.

depths are 500 (red curve), 1500 (blue curve), and 3500 nm (black curve). The maximum loads for these three indents are 13 mN, 56 mN, and 143 mN, respectively. Figure 5.3 shows the inverse pole figures (shortly named IPF map in the following) and the corresponding $\{0001\}$ pole figures for these indents.

The indentation areas (the dark roughly circular areas) are indicated by white arrows on the EBSD maps. In these regions the orientation could not be easily indexed with the EBSD software, possibly due to the fact that the surface is not flat where indentation has occurred. Figure 5.3a shows the IPF map of the smallest indent, i.e. a depth of 500 nm. The size of the residual impression on the surface is approximately $5.5\ \mu\text{m}$ in diameter. Figure 5.3d shows the corresponding pole

figure of the 500 nm indent where it can be seen that only one crystal orientation, i.e. the matrix, was found. This is consistent with the observation in Figure 5.3a that there is no evidence of other orientations in the IPF map. Figure 5.3b shows the IPF map of the 1500 nm indent, where the residual size of impression on the surface is now roughly 12.9 μm in diameter. In addition, it can be seen that an area of large misorientation can be observed around the indent. Figure 5.3e shows the corresponding pole figure of 1500 nm indent. According to this pole figure, an additional orientations are now present which has a misorientation of 86° with respect to the matrix. This is consistent with this area being variants of $\{10\bar{1}2\}$ extension twin. Finally, Figure 5.3c shows the IPF map of the 3500 nm indent, where the size of the residual impression is $\approx 19.1 \mu\text{m}$ in diameter. In this case, two different areas of large misorientation can be observed. The corresponding pole figure (Figure 5.3f) of the EBSD map shows that this would be consistent with two variants of $\{10\bar{1}2\}$ extension twins. This illustrates that the presence of deformation twins on the surface after unloading depends on the depth (or size) of the indent.

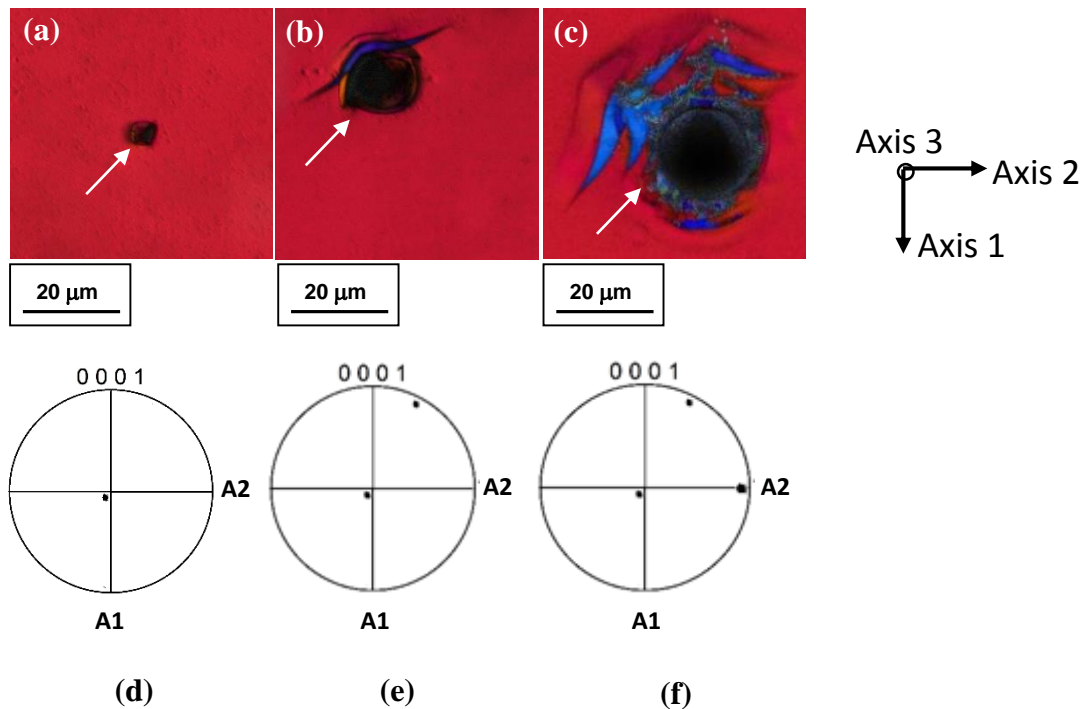


Figure 5.3: (a, b, and c) EBSD image quality maps and (d, e, and f) $\{0001\}$ pole figure maps for three different indent depths: 500 nm, 1500 nm, and 3500 nm. The white arrows on the EBSD maps show the indentation areas (the dark roughly circular areas). Note, the sample reference direction for A1 is close to $[11\bar{2}0]$, A2 is close to $[10\bar{1}0]$, and A3 is perpendicular to the surface (parallel to indentation direction).

5.2.2 Indentation load-depth curves

As mentioned in Section 4.4, spherical indentation was conducted 20 times on selected grains. Figure 5.4 shows the load-displacement ($P-h$) data for three representative indentation tests (labelled test 1, test 2 and test 3) conducted on the same grain to an indentation depth of 500 nm. In order to make the comparison of the data easier, an offset of 2 mN and 4 mN in load was added to these tests for test 2 and test 3, respectively, i.e the load displacement was shifted vertically to avoid overlap of the data points. It can be observed from this figure there are 6 discontinuities in each curve and the displacement at which these discontinuities occur is very reproducible, i.e. at loads of 1.9 ± 0.08 mN, 2.29 ± 0.17 mN, 2.64 ± 0.09 mN, 3.88 ± 0.04 mN, 4.44 ± 0.05 mN, and 9.53 ± 0.17 mN.

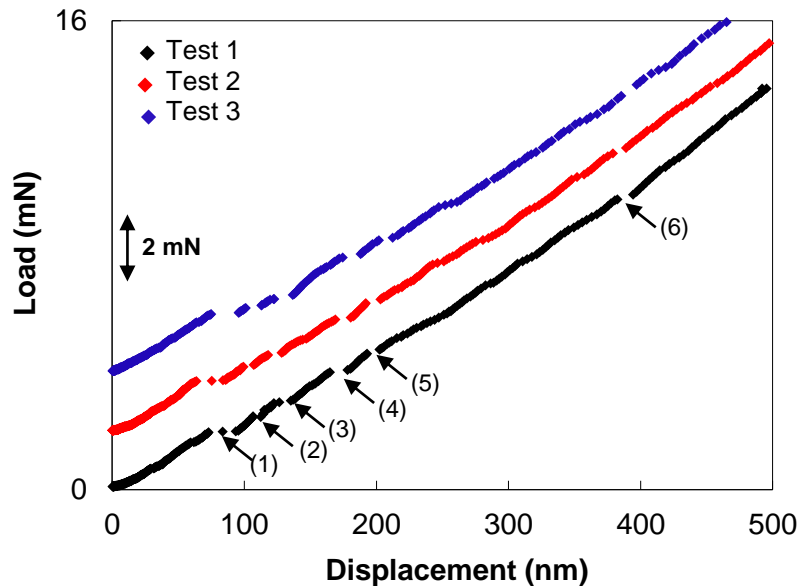


Figure 5.4: Load-displacement curve for three indentation tests (labelled test 1, test 2 and test 3). All three tests were conducted with the same condition, i.e. indentation depth of 500 nm to illustrate the reproducibility of the measurements. In order to make the comparison of the data easier, the curves of tests 2 and 3 were shifted by an offset of 2 mN and 4 mN in load.

To better understand the origin of these discontinuities, a set of indentation tests were conducted with different maximum displacements (from 30 nm to 500 nm). In our experiments, the displacements were chosen based on the location of the discontinuities in the load displacement curves of Figure 5.4. Figure 5.5 shows a subset of these indentation ($P-h$) curves (displacements of 30 nm, 40 nm, 100 nm, and 240 nm) which illustrate the main points. Each indent was conducted in the same grain separated by a suitable distance, i.e. a distance of three diameters from the center of one indentation to another, to ensure no interaction with the other indents. Figure 5.5a shows an indentation test which was conducted up to the load below which the first discontinuity occurred. In this Figure, the prediction from the Hertzian contact theory [65] (the red line) is shown for comparison, i.e. Equation (2.5). It can be observed that indentation up to a load of 1 mN followed by unloading leads to a very small level of residual plastic deformation. It is difficult to measure this precisely but there is only a minor hysteresis between the loading and unloading curve. The maximum difference in displacement at a given load is only 3-4 nm. This is interpreted as indicating that the contact is essentially elastic for this depth of indent. Moving to Figure 5.5b where the depth of the indent was increased to 40 nm, one can see that a significant deviation from the Hertzian contact occurs at a depth of ≈ 34 nm. Upon unloading, the hysteresis is now much larger (about 8 nm) suggesting that permanent deformation has occurred. The deviation from Hertzian contact at ≈ 26 nm is interpreted as being associated the transition from elastic to elastic-plastic deformation. If the depth of the indent is further increased to 100 nm as shown in Figure 5.5c, a large discontinuity is observed in the load displacement curve. At a load of 1.97 mN, the displacement jumps forward by 32 nm. Apparently, this happens very quickly as no data points can be observed during this step increase in displacement.

Upon unloading, there are two interesting observations. First, there appears to also be a discontinuity in the unloading curve and second, the residual depth at 0 load is now ≈ 43 nm or alternatively the elastic recovery is 57 nm or 57% of the total indent depth.

If the loading is continued to a displacement of 240 nm (as shown in Figure 5.5d) or 500 nm (see Figure 5.4), it was found that 5 or 6 discontinuities were observed in the loading segment, respectively. Further, the amount of elastic recovery as a percentage of the total indentation depth decreases to 39% and 31%, respectively. Although, it is not that clear in this figure (due to the large scale), there were a number of discontinuities in the unloading curve. This is further examined in Figure 5.6 for these four cases.

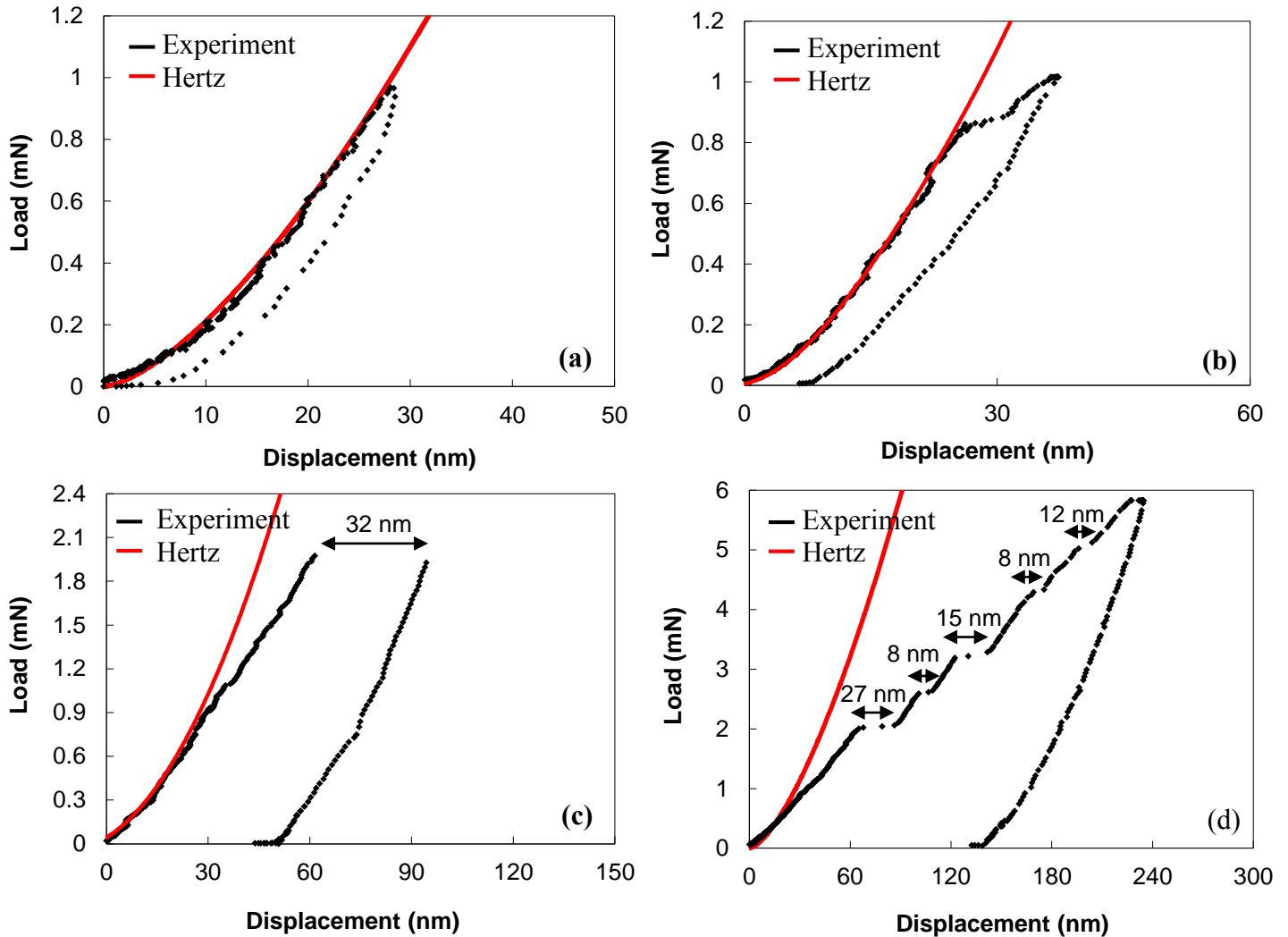


Figure 5.5: Load-displacement curves for four grains made within the same grain showing the loading-unloading behavior for indent depths of (a) 30 nm, (b) 40 nm, (c) 100 nm, and (d) 240 nm. Also, the prediction from Hertzian contact theory [65] (the red line) is shown for comparison.

Figure 5.6 shows an enlarged view of the unloading segment of the indentation curve (figures 5.6a, 5.6c, and 5.6e), and their corresponding derivatives (Figures 5.6b, 5.6d, and 5.6f) for displacements of 30 nm, 100 nm and 500 nm, respectively. Here it is of interest to quantify the discontinuities in the unloading curve which is not always clear visually. One way to differentiate these discontinuities is to calculate the derivative, (dP/dh) of the unloading data and plot it as a function of depth as described in Section 4.4. Figure 5.6a and 5.6b shows the unloading curve and

its corresponding derivative, respectively, for a displacement of 35 nm. In this case, there is no evidence of discontinuities during unloading. Further, the elastic modulus can be calculated from the initial linear region of the unloading curve, as explained in Section 2.3.1. The Young's modulus value obtained was 46 GPa which is in good agreement with the modulus of magnesium, i.e. 45 GPa. The deviation of the unloading curve at low loads has traditionally been interpreted as a result of the indenter peeling away from the surface and the resulting change in the true contact area [159]. However, in the cases of the larger indents shown in Figures 5.6c and 5.6d, measurable discontinuities can be observed in the unloading segment of the indentation curve. For the indent depths of 100 and 500 nm, one and six discontinuities are observed, respectively.

The occurrence of discontinuities during unloading has been previously reported in the literature [98]. Several possibilities have been proposed including dislocation motion or reverse plasticity during unloading [98]. As described in the literature review, observations exist for twinning and de-twinning after loading and then unloading in conventional tension and compression tests [51-54]. As such, it is worth examining whether the discontinuities observed in the current work would be consistent with reverse plasticity of the material during unloading as a result of de-twinning. We will not be able to prove this hypothesis definitively as there are no direct observations of the sample under load, but it will be shown to be consistent with the experimental observations.

For example, for an indent depth of 100 nm shown in Figure 5.5c, there is one discontinuity during loading and one during unloading (Figure 5.6c and 5.6d) while for an indent depth of 500 nm (Figure 5.4) one can observe six discontinuities in the loading curve and six discontinuities in the unloading curve (Figures 5.6e and 5.6f). It was found that for all other cases of indents at less than 500 nm in depth, the number of discontinuities in the loading curves and unloading curves matched. If it is assumed that the discontinuities during loading correspond to twinning and those occurring during unloading correspond to de-twinning, it would suggest that no twins are left around the indent after the load is removed. This is consistent with the observation in Figure 5.3a that no twins could be observed on the surface for an indent depth of 500 nm.

In order to investigate this hypothesis in more detail, the volume of material under the indent was investigated using 3D-EBSD measurements conducted on indented samples using a combination of automated FIB serial sectioning and EBSD orientation mapping on the individual sections as described in Section 4.5.

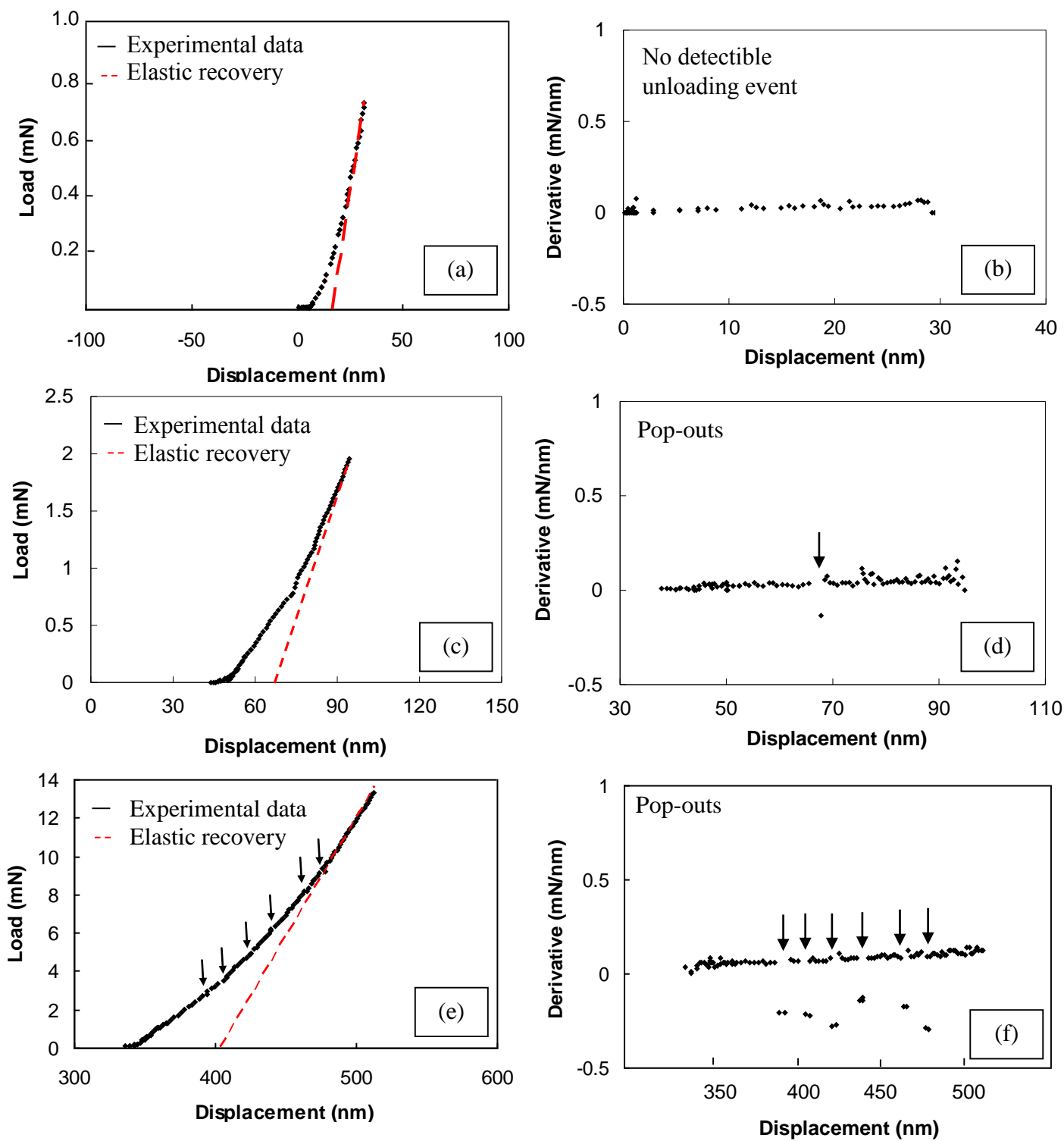


Figure 5.6: (a, c, e) Unloading curves for 30, 100, and 500 nm displacements, (b,d,f) and the derivative curves for the corresponding displacements.

5.2.3 3D EBSD maps

Figure 5.7 shows combined image quality/inverse pole figure maps for one section of the volume under the indent obtained from 3D-EBSD on an indent with a depth of 500 nm. The section shown is perpendicular to the surface of the sample and located at the centre of the indent. In this case, no twins could be found under the indent (Figure 5.7a) or in any of the total volume examined under the indent. This is consistent with the surface observations in Figure 5.3a where no twins were observed.

A careful examination of Figure 5.7a shows that there are two sharp boundaries; on the right side a yellow/green boundary and on the left side, a red/yellow boundary. These correspond to relatively sharp lines of low image quality can be observed, i.e. dark lines which run from top to bottom of the image inclined at an angle of $\approx 10^\circ$. The two lines appear to emanate from the boundary where the indenter was in contact with the material under load and presumably the angle of inclination corresponds to the angle between the indentation axis and the [0001] direction which was 9.3° . To investigate this further, a series of lines were drawn parallel to the surface at different depths (here reported in terms of the normalized depth, z/a , where the z is the depth below the surface and a is the diameter of the indent) and the point to origin misorientation along each line was plotted in Figure 5.7b. Several important observations can be made from this data. If one follows one of the lines from left to right, the misorientation is first low (i.e. the orientation corresponds to that of the parent grain), decreases quickly to a minimum when x/a is ≈ -1 (the edge of the contact zone on the left side), then increases continuously and with almost constant slope from one side of the indent to a maximum at $x/a \approx 1$ (the edge of the contact zone on the right side) and then rapidly decreases back to near zero, i.e. the orientation corresponds again to the orientation of the parent grain.

In order to examine the associated rotation axis, the orientation for points along the line at $z/a = 0.25$ were plotted as 0001 and $11\bar{2}0$ pole figures shown in Figure 5.7c. Here, it can be observed that the rotation axis corresponds to $[11\bar{2}0]$ which appears as a small point near the centre of the pole figure.

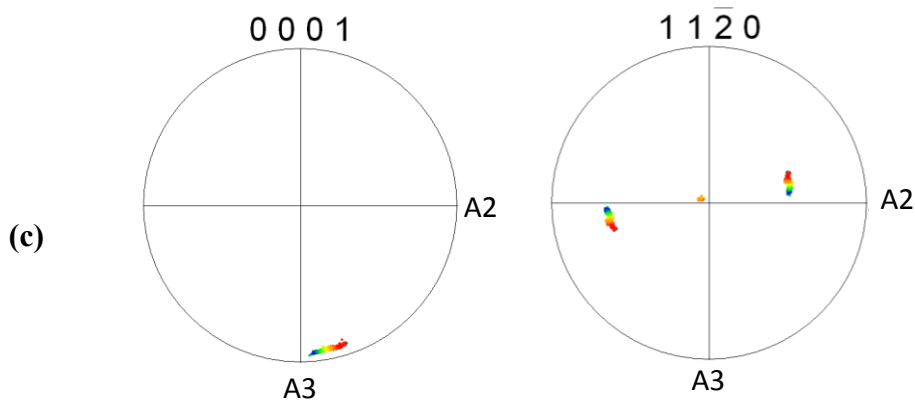
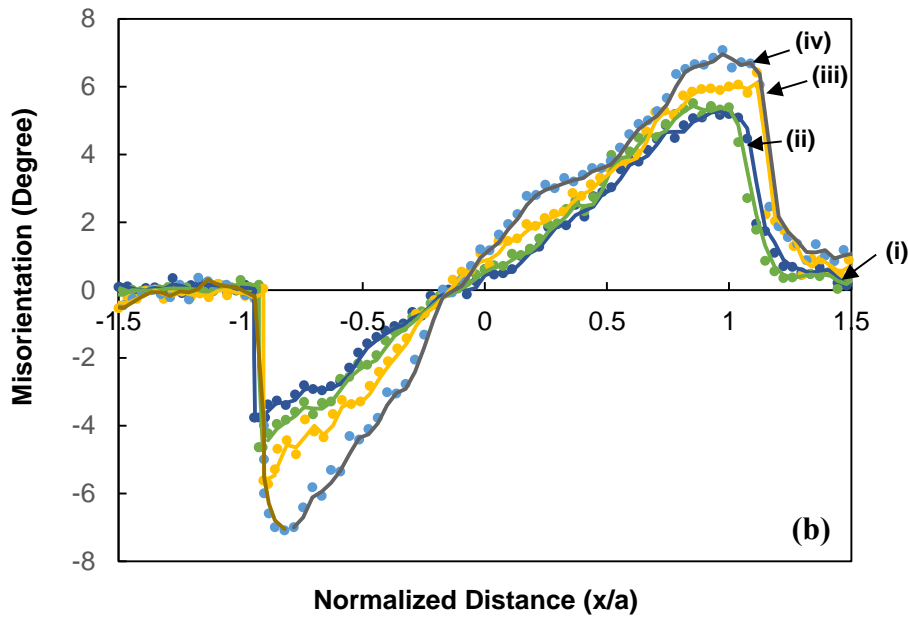
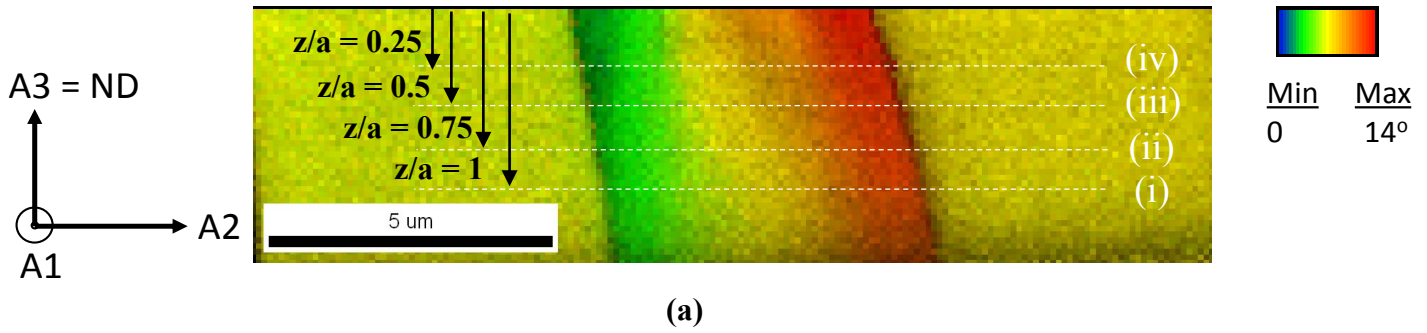


Figure 5.7: Observations on the deformation zone under the centre of the indenter for the 500 nm indent, a) point to origin misorientation angle magnitude map (origin denoted by the point “a”) with image quality superimposed, b) misorientation profiles for the horizontal lines (i) to (iv) in a) and c) 0001 and $11\bar{2}0$ pole figures for line (iii) in figure b). Note, the sample reference direction for A1 is close to $[11\bar{2}0]$, A2 is close to $[10\bar{1}0]$, and A3 is perpendicular to the surface (parallel to indentation direction).

Figure 5.8 illustrates the situation for the 1500 nm indent. In Figure 5.8a, similar to the 500 nm indent, there are two relatively sharp lines of low image quality can be observed, i.e. dark lines which run from top to bottom of the image inclined at an angle of $\approx 10^\circ$. Similar to the case of the 500 nm indent, plotting the orientations in 0001 and $11\bar{2}0$ pole figures shows that the rotation axis corresponds to $[11\bar{2}0]$ which appears as a small point near the centre of the pole figure. The only difference between the two cases is that the magnitude of the rotations is larger for the case of the 1500 nm indent compared to the 500 nm case.

To examine the 3D topology of the structure below the indent, Figure 5.9a illustrates an example of a plane below the surface at depth of 2 μm which comes from the 3D reconstruction of the EBSD images. Here, it can be observed that the sharp misorientation lines seen in Figure 5.8a correspond to a circular boundary under the indenter which is similar in diameter to the contact surface. Further, Figure 5.9b shows that the twins are outside of the indenter contact surface and their shape conforms to the circular shape of the indenter.

To obtain a better understanding of the deformation zone under the indent, the geometrically necessary dislocation (GND) densities have been calculated for the center cross-section of 1500 nm indent. Figure 5.10 illustrates the 3-dimensional distribution of GND's for $\langle a \rangle$ basal screw, $\langle a \rangle$ basal edge, $\langle c+a \rangle$ pyramidal edge, and all $\langle c+a \rangle$ type dislocations. It is clear in Figure 5.10a that there is a high density of basal edge dislocations ($>10^{15} \text{ m}^{-2}$) distributed homogeneously throughout the volume under the indent. Figure 5.8b shows that the density of basal screw dislocations is highest near the circular boundary under the indent which corresponds to the highest absolute value of the misorientation angles in Figure 5.7b and 5.8b. The density of prismatic edge dislocations (Figure 5.10c) is generally low, however, there is evidence for some prismatic dislocations near the indenter-sample interface and along the lines of high misorientation. Finally, Figure 5.10d shows that there appears to be measurable density of $\langle c+a \rangle$ dislocations in the volume under the indenter although it should be noted that the magnitude is at least an order of magnitude lower than that of the basal $\langle a \rangle$ dislocations.

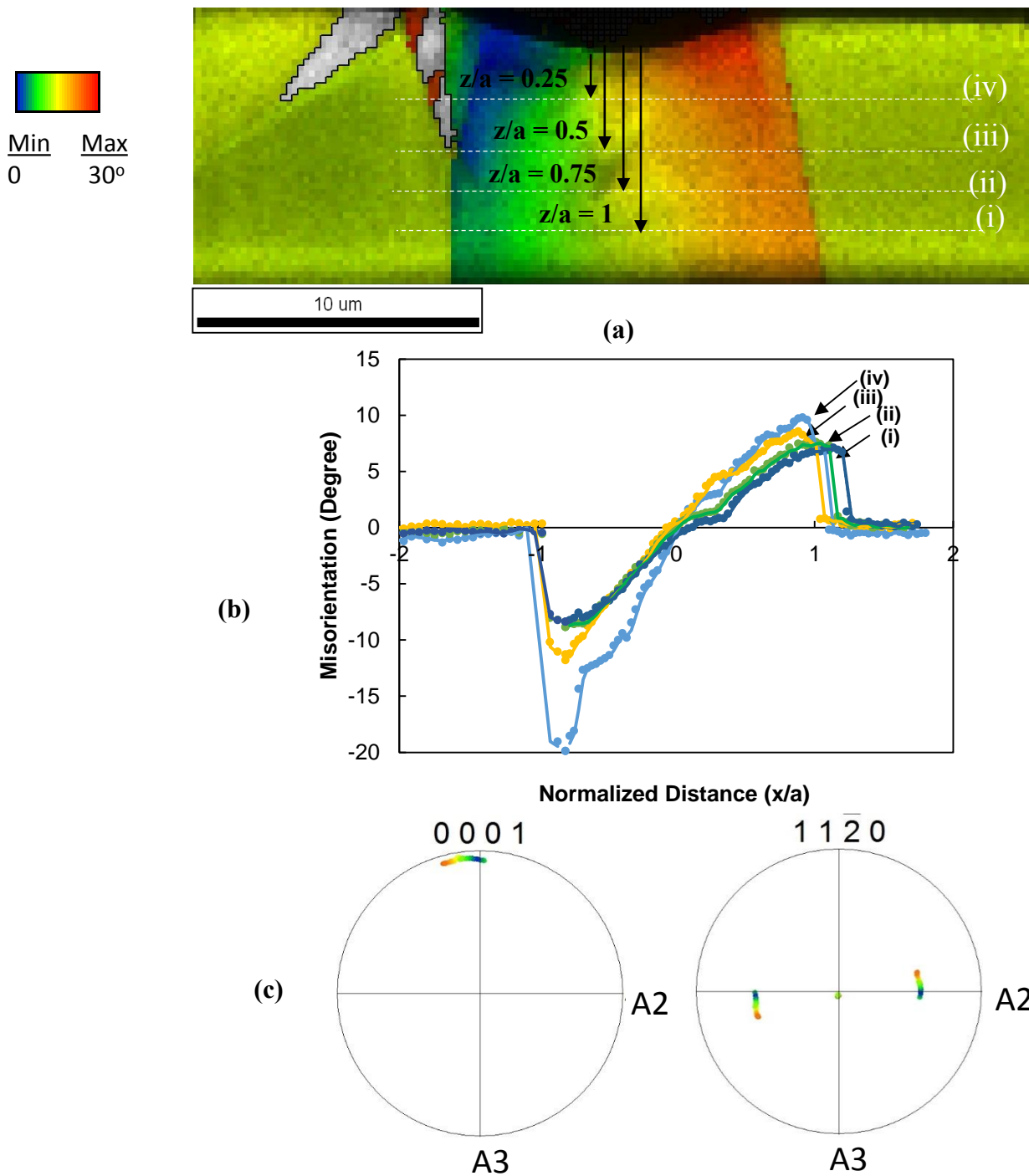


Figure 5.8: Observations on the deformation zone under the centre of the indenter for the 1500 nm indent, a) point to origin misorientation angle magnitude map (origin denoted by the point “a”) with image quality superimposed, b) misorientation profiles for the horizontal lines (i) to (iv) in a) and c) 0001 and $11\bar{2}0$ pole figures for line (iii) in figure b). Note, the sample reference direction for A1 is close $[11\bar{2}0]$, A2 is close to $[10\bar{1}0]$, and A3 is perpendicular to the surface (parallel to indentation direction).

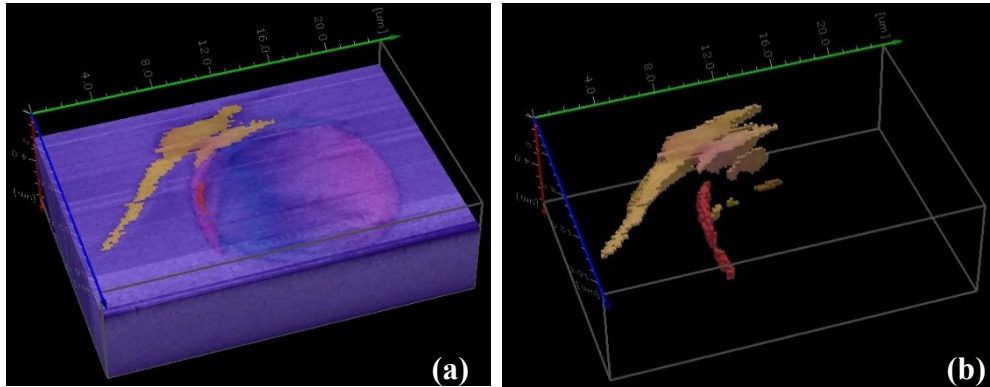


Figure 5.9: 3D reconstructed microstructure for the volume under the 1500 nm indent from EBSD maps, a) inverse pole figures and image quality surface at depth of 2 μm and b) only twins highlighted.

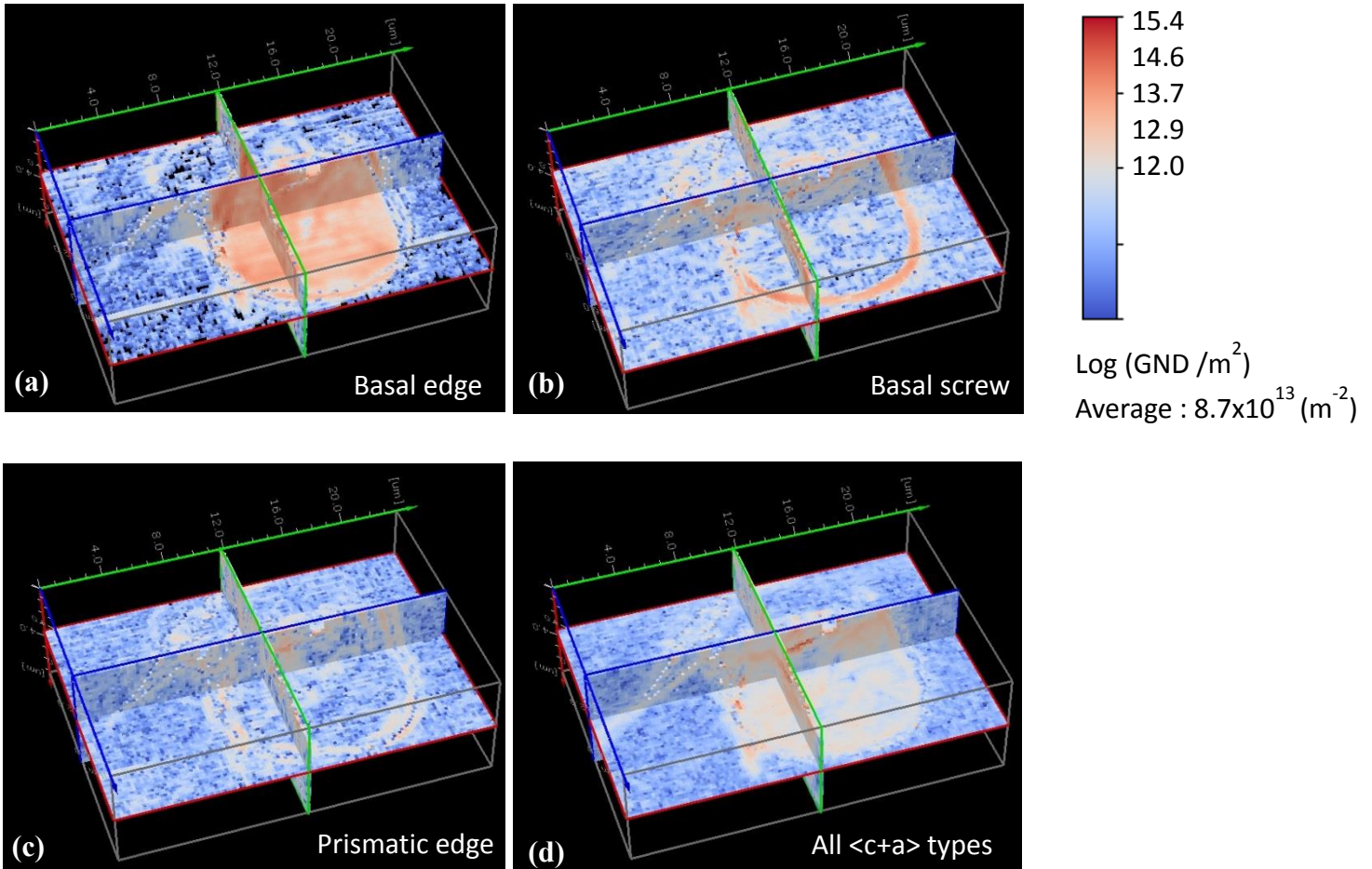


Figure 5.10: 3-dimensional maps of GND densities for the 1500 nm indent, (a) $\langle a \rangle$ basal edge, (b) $\langle a \rangle$ basal screw, (c) $\langle a \rangle$ prismatic edge (d) all $\langle c+a \rangle$ type dislocations.

5.2.4 Analysis of stress field under indent using Hertzian elastic contact mechanics

As noted in the literature review, magnesium shows large differences in the CRSS of different slip/twin systems. In order to examine how deformation initiates under the indent, the elastic stress field was calculated from the solution of Hertz and then the components of the stress tensor were resolved onto the slip systems of interest to determine the spatial variation of the resolved shear stress. Figure 5.11a illustrates the solution for the spatial distribution of resolved shear stress (RSS) on the basal plane normalized by the indentation pressure, p_m as a function of the normalized depth, z/a and the normalized length, x/a for indentation parallel to the c -axis. Here, one can observe that the normalized resolved shear stress on the basal plane at the centre of the indent is zero, i.e. the loading axis and the basal plane are almost at 90° and thus the Schmid factor is very low. However, as one moves away from the centreline, the normalized RSS on the basal plane increases raising the possibility for the initiation of basal slip when the RSS equals the critical resolved shear stress (CRSS). The maximum normalized RSS on the basal plane occurs below the surface near the edge of the contact between the indenter (at $\pm x/a = 1$) and has a value of 0.375, marked by the white arrows. In contrast, the normalized RSS on the 2nd order pyramidal slip system (Figure 5.11b) is maximum directly under the indenter and has a magnitude of 0.45. Finally, Figure 5.11c shows the map of the normalized RSS for one variant of the $\{10\bar{1}2\}$ extension twins. The maximum value of the normalized RSS for extension twinning is 0.16 and this occurs in the subsurface region outside of the contact zone.

Table 5.1 summarizes the maximum normalized RSS on the prismatic $\langle a \rangle$ and 2nd order pyramidal $\langle c+a \rangle$, and contraction twins, i.e. 0.08, 0.45, and 0.43, respectively. Table 5.2 summarizes the normalized RSS values for the 6 variants of the $\{10\bar{1}2\}$ extension twins (here only the RSS in the appropriate direction for the twin to operate were considered). It can be seen that these values range from 0.16 to 0.09, again much lower RSS values than for basal slip favouring basal slip.

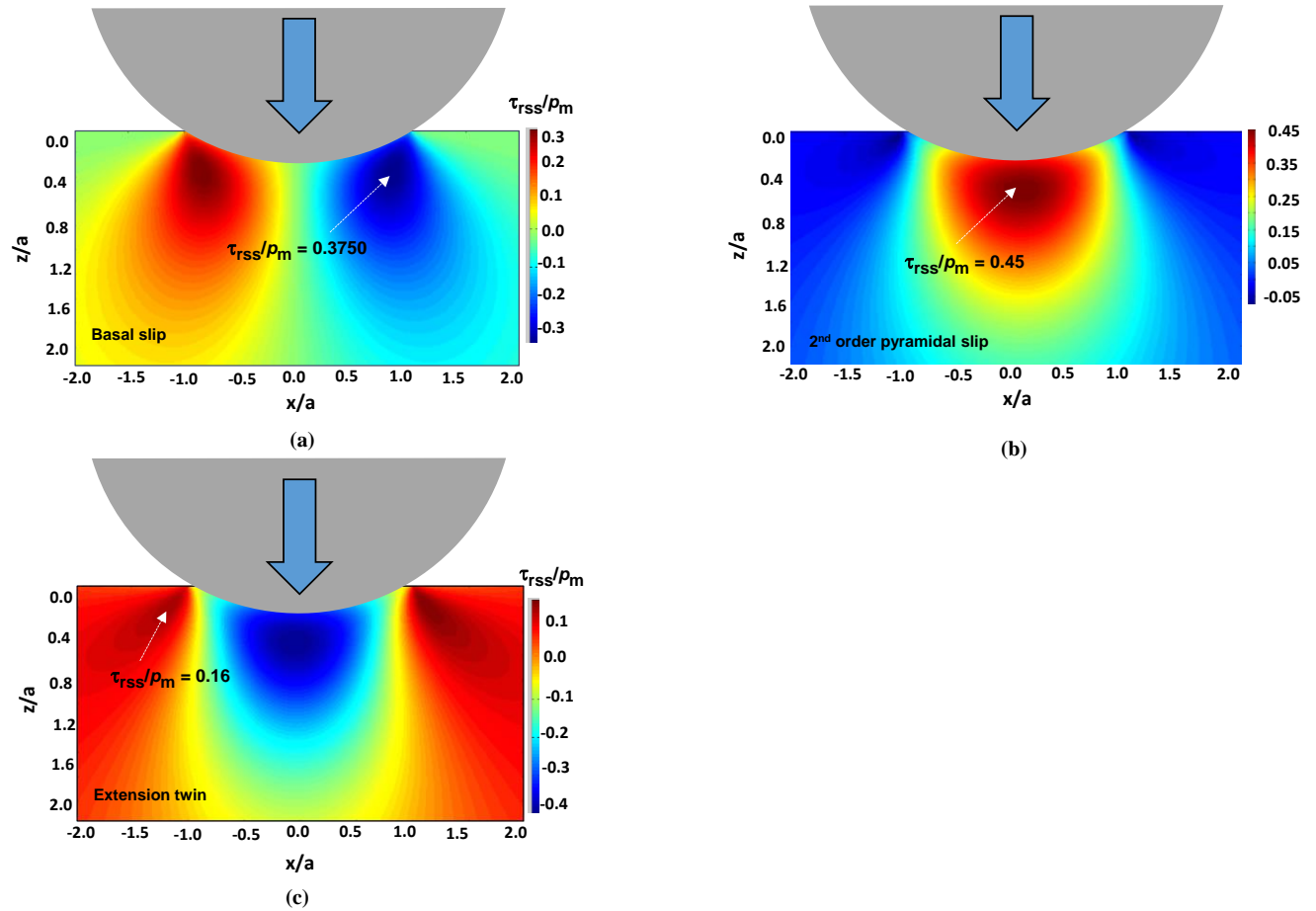


Figure 5.11: Distribution of normalized resolved shear stress (τ_{rss}/ρ_m) below the spherical indenter for (a) basal slip, (b) 2nd order pyramidal slip and (c) extension twin.

Table 5.1: List of normalized RSS (τ_{rss}/ρ_m) for the basal, prismatic, and pyramidal slip planes

Basal slip	Prismatic slip	2 nd order pyramidal <c+a>	Contraction twin
0.38	0.08	0.45	0.43

Table 5.2: List of normalized RSS (τ_{rss}/ρ_m) for 6 extension twins

First twin	Second twin	Third twin	Fourth twin	Fifth twin	Sixth twin
0.16	0.13	0.11	0.09	0.09	0.09

5.2.5 Crystal plasticity finite element simulation results

Crystal plasticity finite element modelling calculations were conducted to examine how the deformation zone under the indent develops as shown in Figure 5.12. In these simulations, <a> type basal slip was the only deformation mode allowed, the loading direction was parallel to the

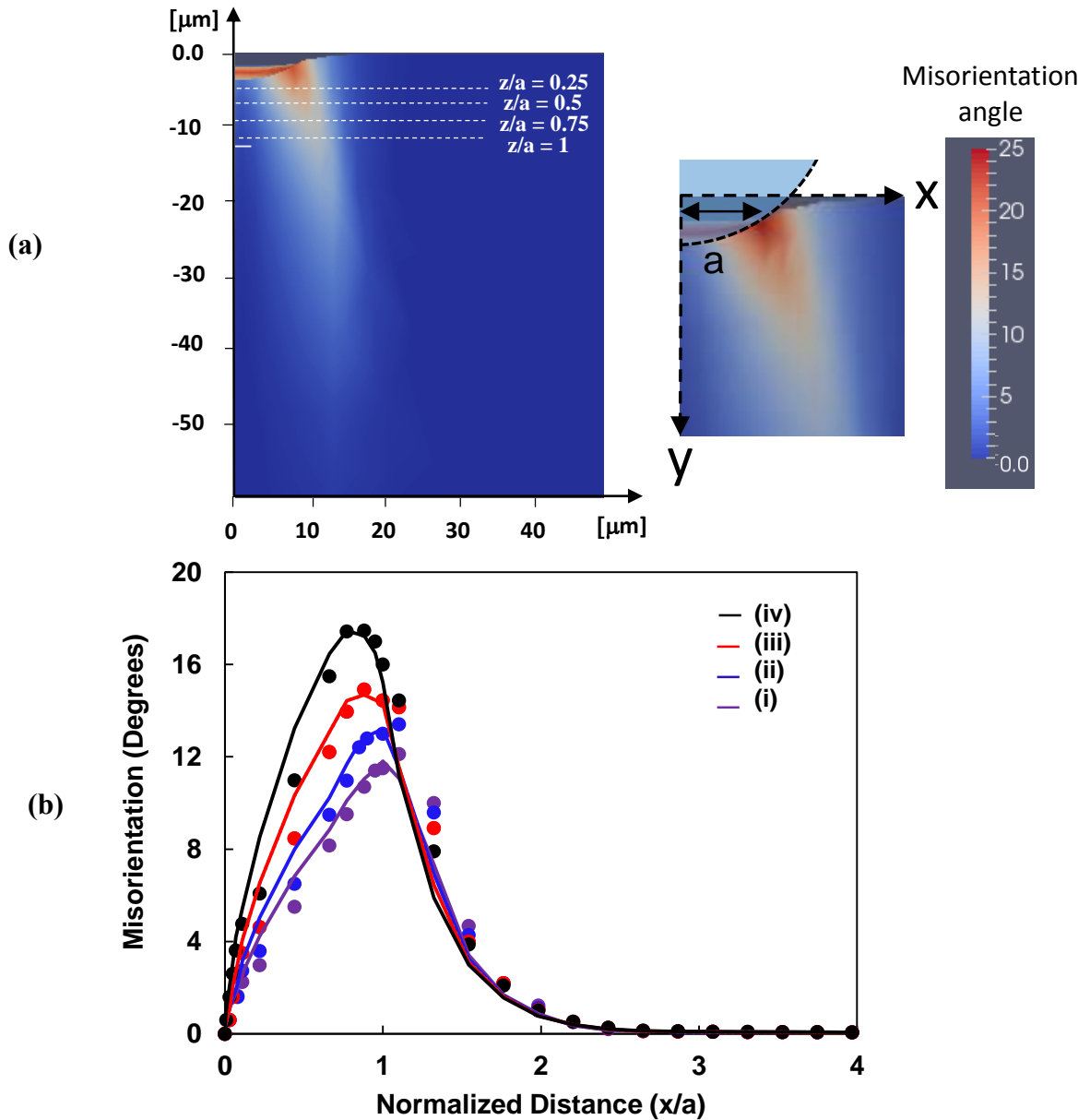


Figure 5.12: (a) The results for a map of local misorientation under the indent obtained from the crystal plasticity finite element method calculations. The $\langle a \rangle$ type basal slip was the only deformation mode allowed, the loading direction was parallel to the c -axis and the simulated indentation depth is 3500 nm. (b) The misorientation profile of four normalized distance under the indent ($z/a = 0.25, 0.5, 0.75,$ and 1) were extracted.

c -axis and the simulated indentation depth was 3500 nm. The misorientation profiles of four normalized distances under the indent ($z/a = 0.25, 0.5, 0.75,$ and 1) were extracted and are shown in Figure 5.12b. Here, similar to the experimental results, it can be observed that the misorientation angle zero under the centre of the indent, increases to a maximum near $x/a = 1$ and finally decreases

to zero outside the indent contact area. The location of the maximum misorientation is similar to the experimental observations and, in addition, the maximum value of misorientation decreases with depth below the surface, also consistent with the experiments. However, the rate of change of misorientation outside of the contact zone (i.e. for $x/a > 1$) is significantly lower than that of the experiment.

In order to compare all experimental and CPFEM results, the depth below the surface and the distance from the centre of the indent were normalized with respect to the indent contact radius, a . Figure 5.13a shows the resulting values for the maximum misorientation as function of the indent depth / contact radius (h/a) for both the CPFEM (red circles) and the experiments (triangles). It can be seen that the experimental results follow the same trend of increasing misorientation with increasing indentation depth but the experimental values are approximately 10-15% lower than the CPFEM results. Further, Figure 5.13b is a plot of the normalized maximum misorientation vs. normalized depth under the indent, z/a from the CPFEM (red circles) and the experiments (triangles) for different maximum indentations. It can be observed that the values obtained from the model are in good agreement with the experimental results for the 500 nm depth indent but they over-predict the misorientation for the larger 1500 and 3550 nm indents.

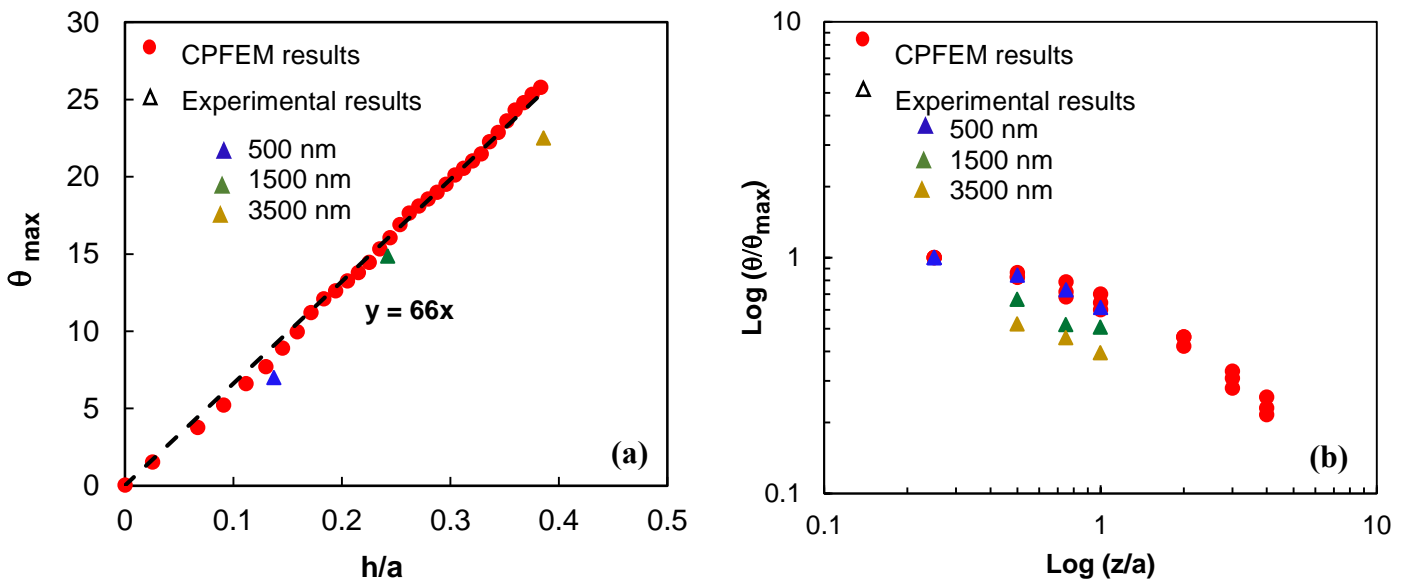


Figure 5.13: (a) The maximum amplitude of the misorientation as a function of normalized indenter depth (h/a), and (b) Maximum misorientation obtained from experiments and CPFEM for $z/a = 0.25 - 4.0$.

The model is also capable of predicting the maximum misorientation values for larger depths under the indent than what can be obtained experimentally (due to limited FIB milling time). As expected, the misorientation angle under the indent diminishes to zero at large depths, i.e. the deformation due to the indenter has a characteristic depth of approximately 3-4 the indenter radius.

5.2.6 Stress-strain curve

Transforming the measured load–displacement data from spherical indentation into indentation stress–strain curves allows a more transparent and efficient way of analyzing the local material behavior. These indentation stress–strain curves allow a better identification of the different stages of material behavior under contact loading, particularly during the loading segment of the indentation process. As explained previously in literature review (Section 2.3.2), extracting indentation stress–strain curves has been more successful with spherical indenters.

In order to be able to compare our results with literature [68], preliminary experiments have been performed on high purity aluminum. The first step in the analysis process is a clear identification of a zero-point that makes the measurements in the initial elastic loading segment consistent with the predictions of Hertz’s theory [65]. As discussed in Chapter 2, the zero-point can be conveniently determined using Equation 2.10 for the initial elastic segment in a frictionless, spherical indentation. The regression analysis performed on a typical dataset to identify the effective point of initial contact is shown in Figure 5.14. The points of initial contact, as identified by the default procedure in the MTS software (C_1) and by our analysis (C_2) for this dataset, are displayed in Figure 5.15. It is noted that the load signal had to be moved by about 0.093 mN and the displacement signal by about 15.4 nm with respect to C_1 to arrive at C_2 . After this small shift, the corrected load–displacement curve in the initial elastic loading segment is found. The indentation stress–strain curve for the selected data set, computed using Equations 2.8 and 2.9, is shown in Figure 5.16. The value of E was estimated from this data to be 71 GPa, which is with 1% of the value expected for aluminum [160]. When a yield point for a material cannot be defined based on the shape of the stress-strain curve, an offset yield point is arbitrary chosen. The offset is commonly specified 0.1 or 0.2% plastic strain [161]. The yield stress value obtained here using the 0.1% offset

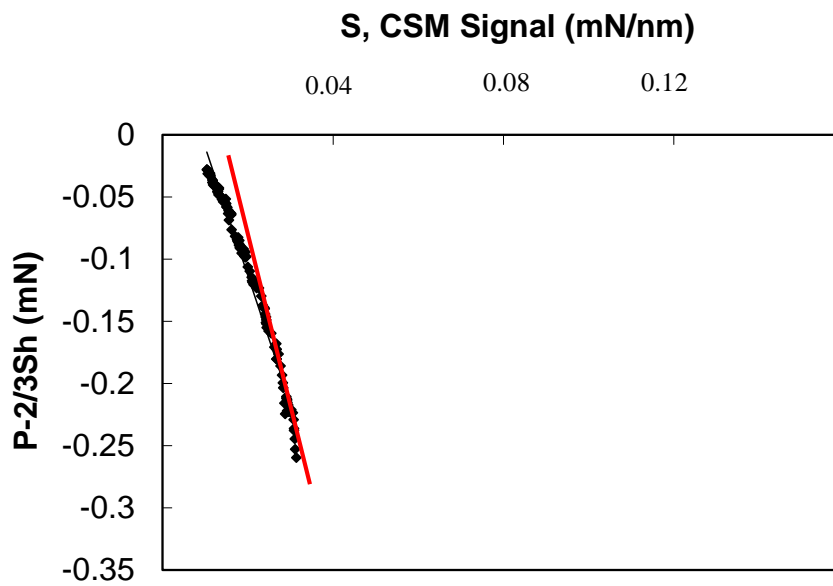


Figure 5.14: The identification of the effective zero-point using the method described in section 2-4-3.

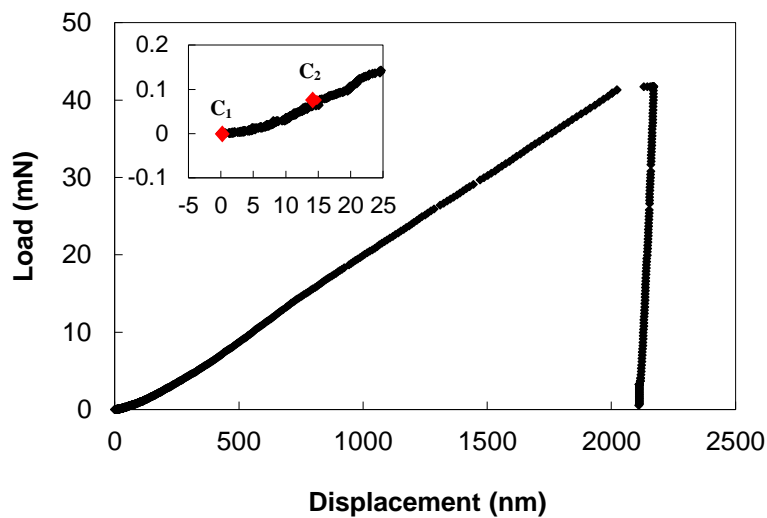


Figure 5.15: The measured load–displacement curves.

is 110 MPa, which is in good agreement with what has been derived for high purity aluminum in aluminum.

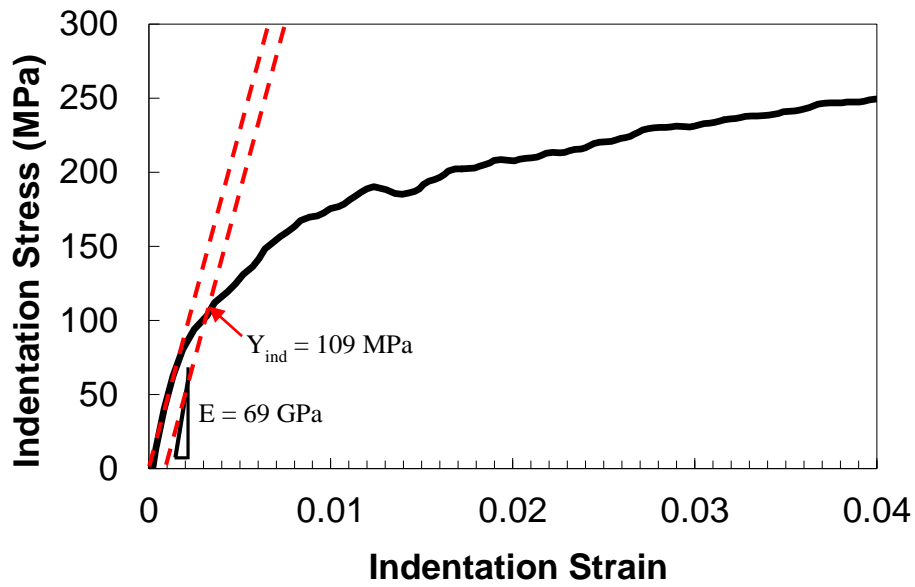


Figure 5.16: The measured indentation stress–strain curves for high purity Al.

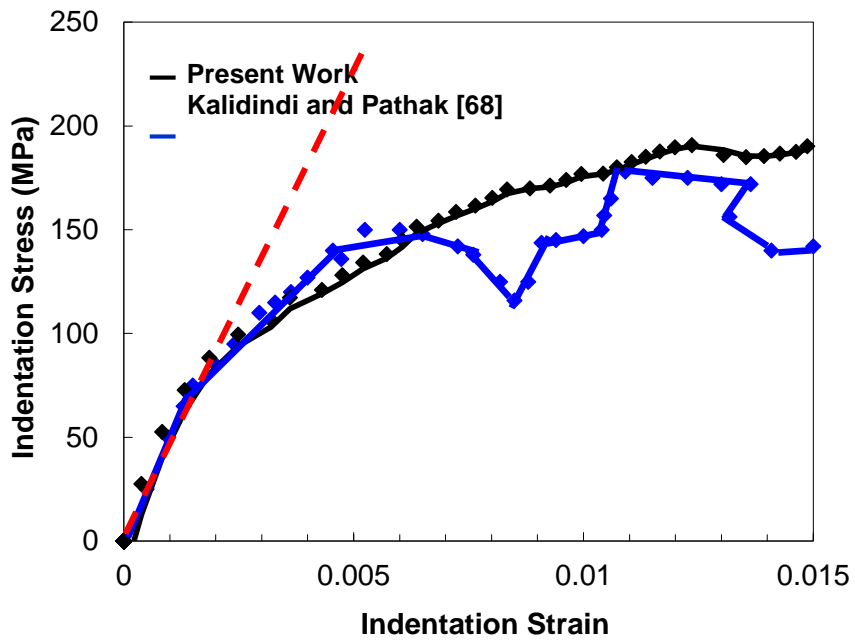


Figure 5.17: Comparison between the data obtained in this work and reported in the literature [68] for high purity Al.

It should be mentioned that the experimental condition of this work was similar to the Kalidindi's work, i.e. the same tip with the same indenter radius (13.5 micron) was used in the literature (i.e., 114 MPa) [68]. The yield strength was also calculated using 0.2% offset which is 135 MPa. This value is larger than the yield value reported in the previous work. In order to be consistent with the previous study [68], here 0.1% offset was chosen. Figure 5.17 shows the comparison of the present results with those reported by Kalidindi et al. [68] for high purity aluminum. As can be observed, the overall stress-strain curve obtained in this work (shown by black line) is in good agreement with the stress-strain response previously reported (shown by blue line), although with somewhat less scatter in the data.

Based on the success of the test on Al samples, the stress-strain curve was extracted from the load-displacement data for the studied orientation, i.e. indentation on a grain which is 9.3 degrees off from [0001] direction. Figure 5.18 shows the indentation stress-strain curves obtained from the selected grain. The obtained Young's modulus value of 45 GPa for this grain is in good agreement with the theoretical value of 46 GPa [160]. Table 5.3 shows the obtained values of Young's modulus and yield strength for these three grains. The 0.1% offset was chosen to define the yield stress in the indentation load-displacement curve.

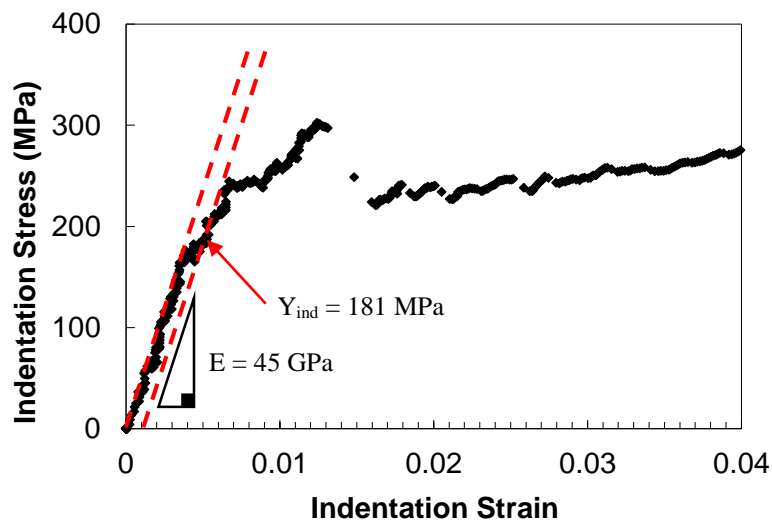


Figure 5.18. The measured indentation stress–strain curves for commercially pure magnesium for the studied grain.

Using normalized resolved shear stress values obtained from Hertzian contact theory described in Section 5.2.4 combined with yield strength obtained from indentation stress-strain curves (using the 0.1% offset), and assuming plasticity was initiated by basal slip (Section 5.2.4), the $RSS_{0.1\% \text{ offset}}$ values for basal slip were determined and shown in Table 5.3. Also, Table 5.4 summarizes the $RSS_{0.1\% \text{ offset}}$ values for the first variant of the $\{11\bar{2}0\}$ extension twins. This value was obtained using normalized resolved shear stress for the first variant of the $\{11\bar{2}0\}$ extension twins from Table 5.2 combined with the stress at which the first discontinuity occurs in the indentation stress-strain curve (i.e. 299 MPa). It should be mentioned that these results were obtained based on 20 spherical indentation tests conducted on the same grain. Thus, the $RSS_{0.1\% \text{ offset}}$ values shown in Table 5.3 and 5.4 are the mean of the 20 indentation tests plus/minus the standard deviation of the mean.

The $RSS_{0.1\% \text{ offset}}$ values obtained for commercially pure Mg is higher than what have been expected for magnesium from literature [14,162,163]. At room temperature, the CRSS of the basal slip in commercially pure magnesium is reported in the range of 0.45-0.81 MPa [14,160]. This discrepancy will be discussed in detail in Chapter 6.

Table 5.3: $RSS_{0.1\% \text{ offset}}$ values obtained from indentation test for the basal planes for the selected grain

Normalized RSS (τ_{rss}/p_m)	Yield stress (MPa)	$RSS_{0.1\% \text{ offset}}$ (MPa)
0.38	181 ± 5	68 ± 3

Table 5.4: Apparent critical resolved shear stress values obtained from indentation test for the extension twin planes for the selected grain

	Normalized RSS (τ_{rss}/p_m)	Pop-in stress (MPa)	Apparent CRSS (MPa)
First twin	0.16	299 ± 8	48 ± 3

5.3 Spherical indentation on commercially pure Mg with loading nearly perpendicular to the c-axis

5.3.1 Microstructural analysis before and after the spherical indentation

In this section, the focus will be on the response of commercially pure magnesium to spherical indentation with an indentation direction approximately perpendicular to the c-axis. Figure 5.19a shows the IPF map of the studied grain before the spherical indentation test. The indentation direction is 80° away from the c-axis and approximately parallel to $\langle 11\bar{2}0 \rangle$ direction in the basal plane. Figure 5.19b is an optical micrograph of the same grain after the spherical indentation.

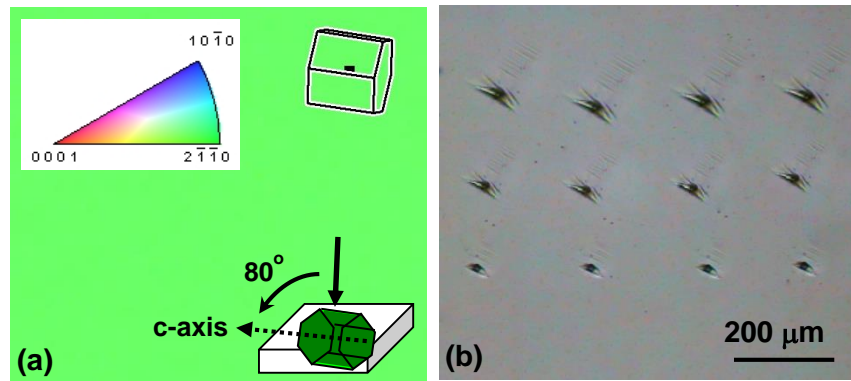


Figure 5.19: (a) Inverse pole figure map of the studied grains before spherical indentation tests, (b) optical micrograph after spherical indentation.

In order to check the repeatability and reproducibility of the indentation result, spherical indentation tests were performed 20 times on the selected grain with three different indentation depths, i.e. 500 nm, 1500 nm, and 3500 nm. Figure 5.20 shows the load-displacement ($P-h$) data for three representative indentation tests (labelled test 1, test 2 and test 3) conducted on the same grain to an indentation depth of 500 nm. An offset of 2 mN and 4 mN in load was added to these tests for test 2 and test 3, respectively, to make the comparison of the data easier. The existence of four discontinuities in each curve can be observed from this figure, and the displacement at which they occur is very reproducible i.e. at loads of 1.17 ± 0.05 mN, 2.51 ± 0.08 mN, 3.97 ± 0.09 mN, 4.606 ± 0.04 mN.

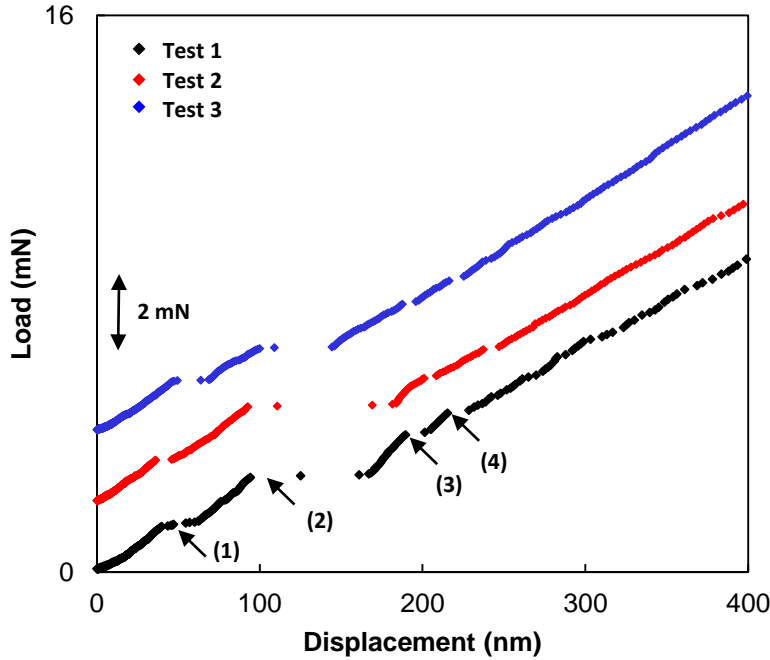


Figure 5.20: Load-displacement curve for three indentation tests (labelled test 1, test 2 and test 3). All three tests were conducted with the same condition, i.e. indentation depth of 500 nm to illustrate the reproducibility of the measurements. In order to make the comparison of the data easier, an offset of 2 mN and 4 mN in load was added to these tests for test 2 and test 3, respectively, i.e. the load displacement was shifted vertically to avoid overlap of the data points.

Figure 5.21 shows combined image quality/inverse pole figure maps and their corresponding $\{0001\}$ pole figures for spherical indentation of 500 nm, 1500 nm, and 3500 nm. The indentation areas (black regions) are indicated by white arrows on the EBSD maps (Figure 5.21a, 5.21b, and 5.21c). The size of residual impressions on the sample surfaces are approximately 5 μm , 10 μm , and 17 μm in diameter for 500 nm, 1500 nm, and 3500 nm indentation depths, respectively (Figures 5.19a, 5.19b, and 5.19c). In order to identify accurately the number of deformation twins which formed around the indent after unloading, the IPF maps have been rotated 30 degrees around axis 1 in the TSL software, and are shown in figures 5.21d, 5.19e, 5.21f. For all three indents, the presence of large misorientations around the indents can be observed. According to $\{0001\}$ pole figures (Figures 5.21g, 5.21h, and 5.21i), these areas have a misorientation of 86° with respect to the matrix and thus they are considered as $\{10\bar{1}2\}$ extension twins. In contrast to the results of Section 5.2 (i.e. for the case of indentation nearly along $[0001]$ direction), here it can be observed that the presence of deformation twins after unloading is observed for all three studied cases.

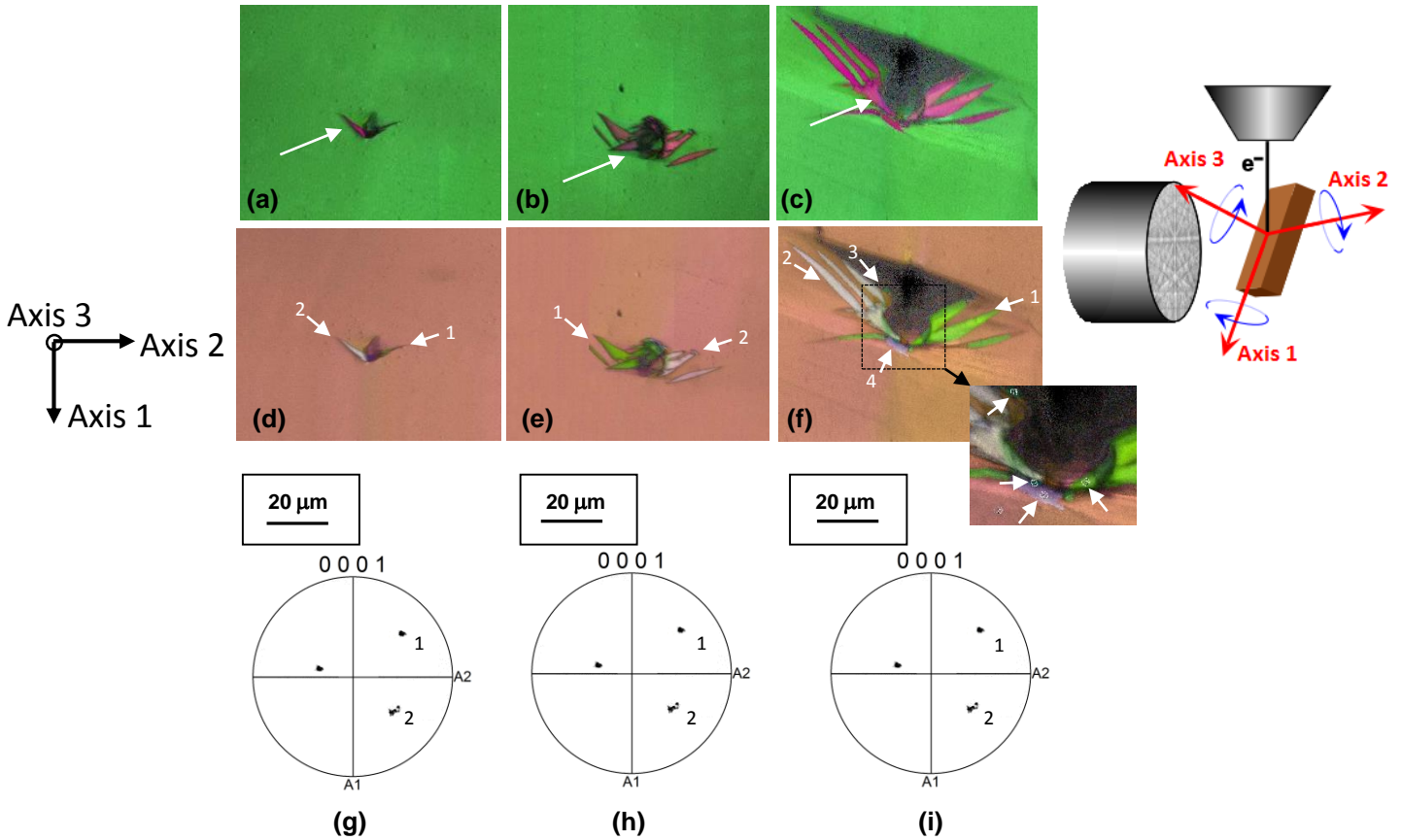


Figure 5.21: (a, b, and c) IPF maps, and (d, e, and f) IPF maps rotated 90° around axis 2 (the magnified view of Figure 5.21f can also be seen), (g, h, and i) $\{0001\}$ pole figures after indentation for three different indent depths: 500 nm, 1500 nm, and 3500 nm. Note, the sample reference direction for A1 is close to $[0001]$, A2 is close to $[10\bar{1}0]$, and A3 is perpendicular to the surface (parallel to indentation direction).

However, the number of deformation twin exists on the surface depends on the depth of the indent. For example, for the case of 500 nm and 1500 nm indent depths, two variants of $\{10\bar{1}2\}$ extension twin exist around the indent after unloading. This can be observed from the IPF maps (Figure 5.21d and 5.21e), labelled as twin numbers 1 and 2, and also their corresponding pole figures (Figure 5.21g and 5.21h). However, for the case of the 3500 nm indent, four variants of $\{10\bar{1}2\}$ extension twin exist around the indent after unloading. The white arrows in the magnified view of Figure 5.21f show the presence of four extension twins around the indent. The existence of two of the extension twins cannot be observed in the corresponding $\{0001\}$ pole figure of the IPF map (Figure 5.21i). This is due to the fact that these two extension twins are overlapping twins numbers 1 and 2, and thus they cannot be observed separately.

5.3.2 Analysis of stress field under indent using Hertzian elastic contact mechanics

In order to understand the material response to the applied stress for the case of indentation perpendicular to the c-axis, the complete stress field under the indenter was calculated using Hertzian contact mechanics for spherical indentation. As was explained earlier in Section 2.2.3, in magnesium, for uniaxial loading, $\{10\bar{1}2\}$ extension twins are expected when a grain is compressed perpendicular to the $\langle c \rangle$ axis, i.e. similar to the current loading axis. Figure 5.22 shows the solution for the spatial distribution of normalized RSS on the extension twin, and basal slip planes normalized by the indentation pressure, p_m as a function of the normalized depth, z/a and the normalized length, x/a . It can be observed that the maximum normalized RSS on four extension twin planes, i.e. $(01\bar{1}2)$, $(0\bar{1}12)$, $(\bar{1}012)$, and $(10\bar{1}2)$ planes, occurs under the indent at $x/a=0$, and have values of 0.34, marked by the white arrows. However, for the two other cases, i.e. $(1\bar{1}20)$, and $(\bar{1}\bar{1}02)$ extension twin planes, the normalized RSS values are zero under the indent. Therefore, these two twinning systems are expected to be inactive. On the other hand, Figure 5.22c shows the distribution of the normalized RSS on the basal plane. It can be observed that the maximum normalized RSS on the basal plane occurs underneath the surface at $\pm x/a = 1$ and has a value of 0.31. In our experiment, the angle between the c-axis of the HCP crystal and the indentation axis is 80 degrees. The normalized RSS of the basal slip, and extension twin planes for the studied grain is shown in Figure 5.23 which shows a slight asymmetry compared to the perfect orientation (Figure 5.22). Table 5.5 summarizes the normalized RSS values for the basal, prismatic, 2nd order pyramidal $\langle c+a \rangle$ slip, contraction twin, and the 6 variants of the $\{10\bar{1}2\}$ extension twins for indentation on the studied grain. It can be observed that the maximum normalized RSS on the prismatic $\langle a \rangle$ slip planes (i.e. 0.13), is much lower than the maximum normalized RSS on basal slip plane (i.e. 0.37). The maximum normalized RSS on the second order pyramidal slip and extension twins, shows higher values in comparison with the basal slip. However, based on the literature [21,100], the activation of these two deformation modes is not expected which might be due to the high CRSS for these two systems. For the case of extension twinning, these values, range from 0.34 to 0.39, for four extension twin variants (i.e. $(01\bar{1}2)$, $(0\bar{1}12)$, $(\bar{1}012)$, and $(10\bar{1}2)$).

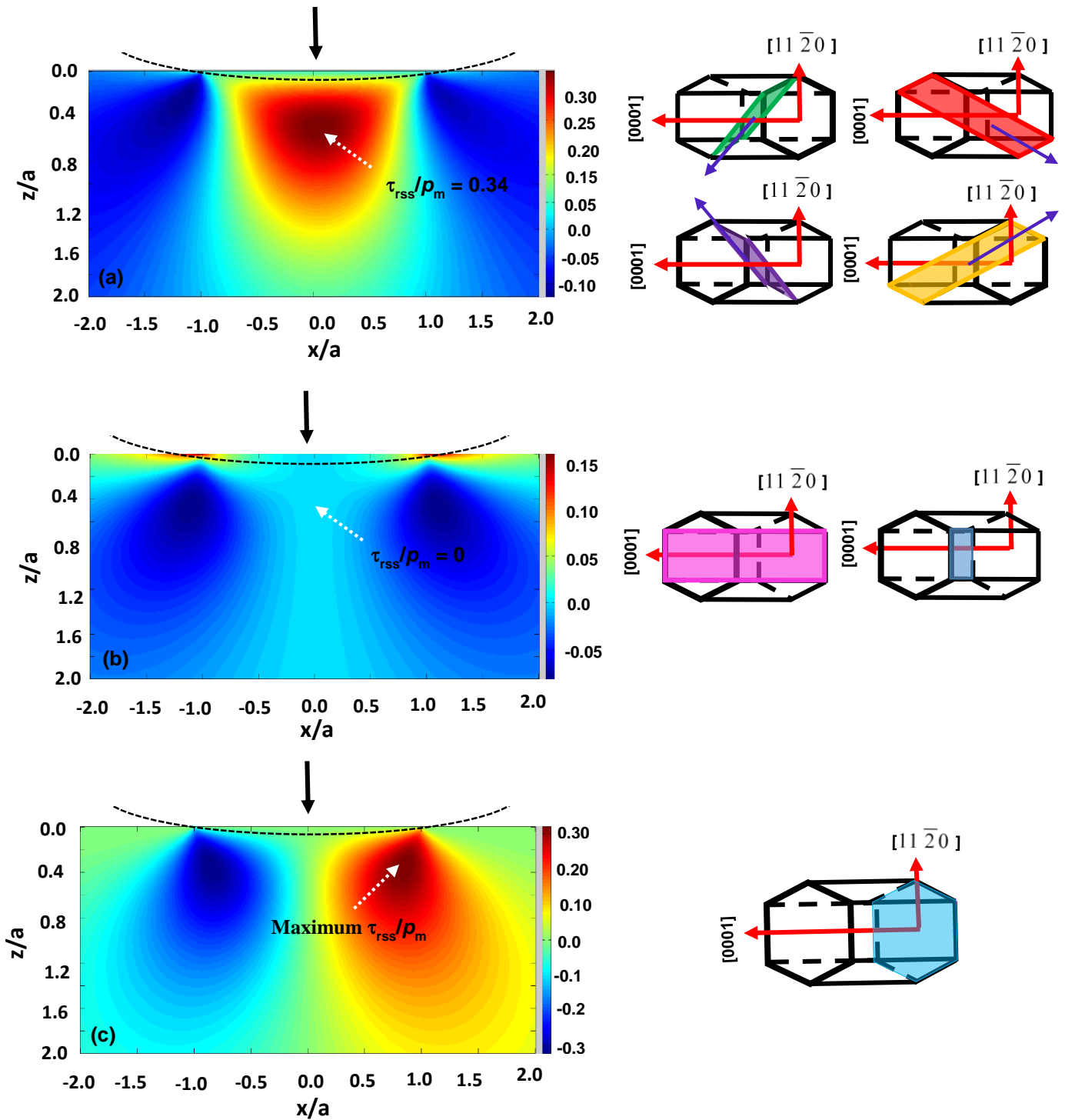


Figure 5.22: Distribution of normalized resolved shear stress (τ_{rss}/ρ_m) below the spherical indenter on (a, and b) extension twin planes and (c) basal slip plane for indentation perpendicular to c-axis.

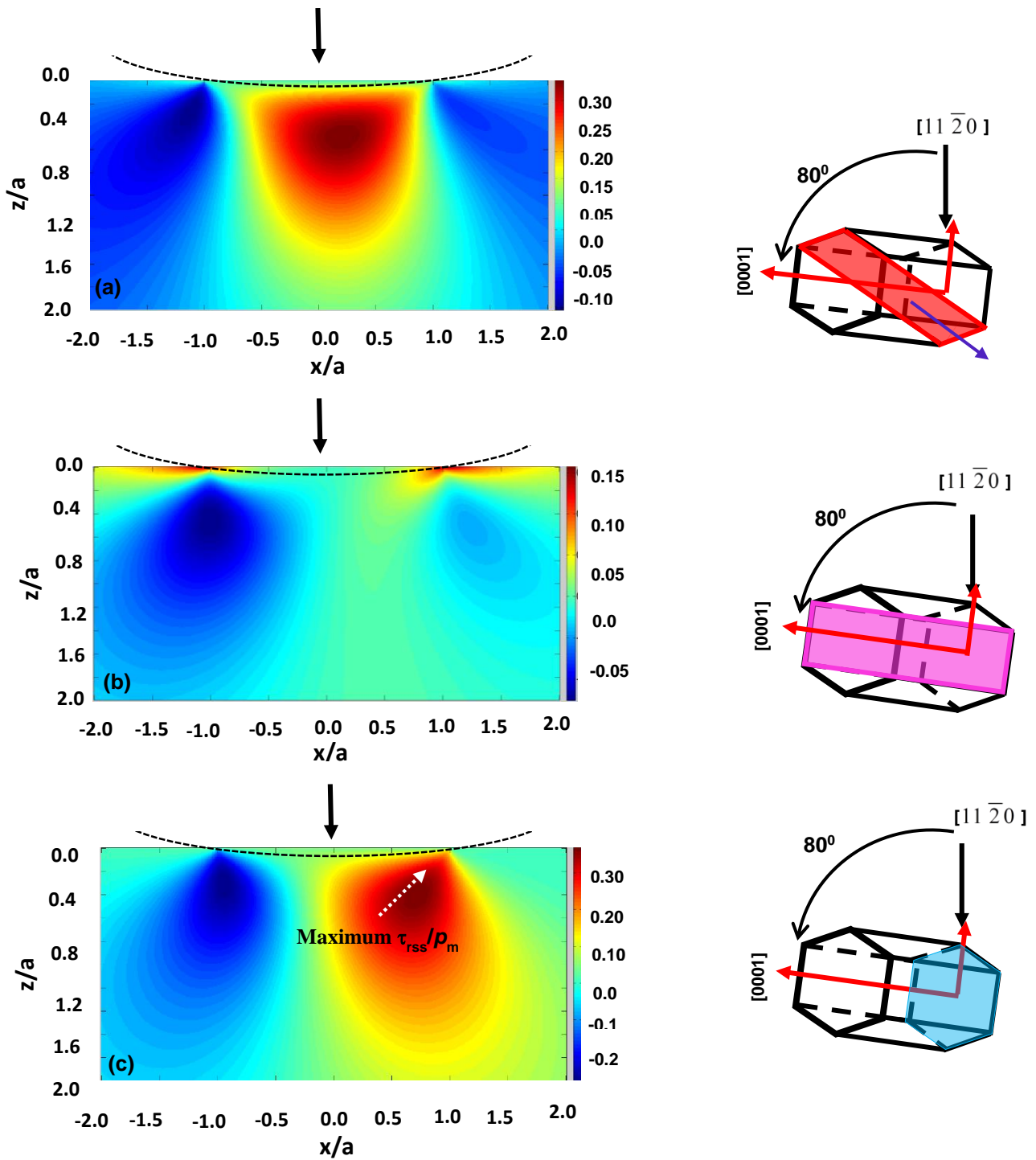


Figure 5.23: Distribution of normalized resolved shear stress (τ_{rss}/ρ_m) below the spherical indenter on (a, and b) extension twin planes and (c) basal slip plane. The angle between the indentation direction and c-axis is 80° .

Table 5.5: List of normalized RSS (τ_{rss}/ρ_m) for the basal, prismatic, and pyramidal slip planes

Deformation mode	Indentation Schmid factor (τ_{rss}/ρ_m)
	80 degrees from [0001]
Basal Slip	0.37
Prismatic Slip	0.14
2 nd order Pyramidal <c+a> Slip	0.45
Contraction twin	0.42
(0 $\bar{1}12$) twin plane	0.38
($\bar{1}012$) twin plane	0.34
(10 $\bar{1}2$) twin plane	0.34
(1 $\bar{1}20$) twin plane	0.16
(1 $\bar{1}02$) twin plane	0.15

Also, the maximum normalized RSS on basal slip plane (0.37) and extension twin plane (0.39) is nearly similar. Therefore, it is expected that it would be a competition between basal slip and extension twinning operations under the indent. In order to define which deformation system will operate first, it is needed to study the critical resolved shear stress (CRSS) for both basal slip and extension twinning. Later in the Section 5.5, this will be discussed in more detail.

5.3.3 Indentation load-depth curves

The load-displacement ($P-h$) data for spherical indentation on a studied grain for 500 nm, 1500 nm, and 3500 nm displacements was examined in detail. Figure 5.24a shows this data for indentation depth of 3500 nm. Also, in this figure, the prediction from Hertzian contact theory [65] (the red line) is shown for comparison. It can be observed that a significant deviation from Hertzian contact occurs at small loads. Also, the occurrence of some discontinuities can be seen in the loading segment in Figure 5.24a. However, the number of discontinuities and the loads at which they occur is not clear from this figure. In order to have a better view of these features, Figures 5.24b, and 5.24c show the enlarged view of loading segment of the indentation curve. In Figures 5.24b, and 5.24c, the occurrence of six discontinuities can be observed during loading at loads of 1.37 mN, 2.51 mN, 3.97 mN, 4.60 mN, 15.19 mN and 26.22 mN. As explained previously in Section 5.2, the occurrence of discontinuities during loading is proposed to be due to the twinning.

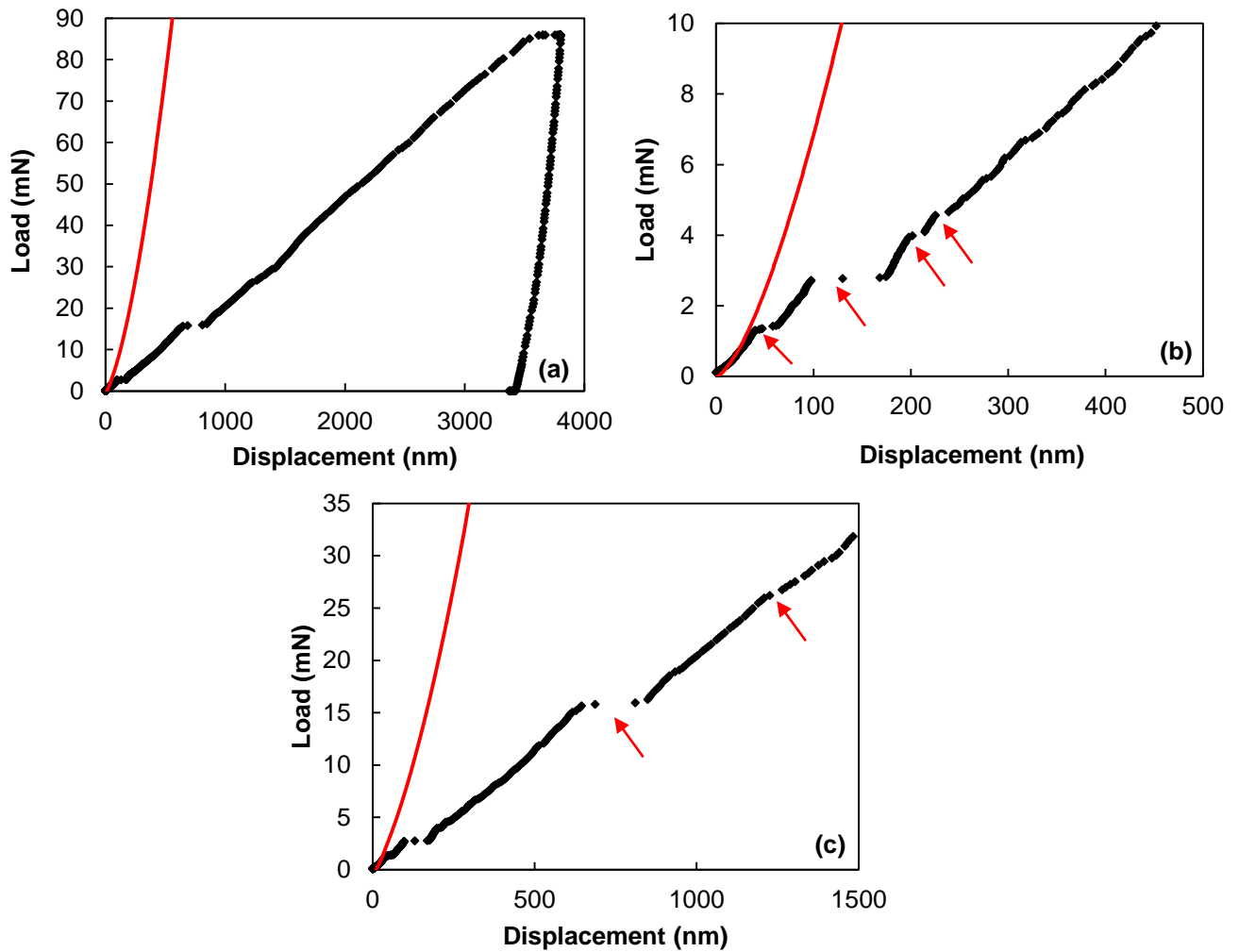


Figure 5.24: (a) Load-displacement curve for 3500 nm displacement. The magnified view of the load-displacement curve up to (b) 500 nm, and (c) 1500 nm.

Therefore, indentation up to 500 nm and 1500 nm depth, suggests the formation of 4 and 6 variants of deformation twins, respectively. However, this result is in contrast with our EBSD observations (Figure 5.21), which shows the presence of two extension twins for the case of 500 nm and 1500 nm indent depth, and 4 extension twins for the case of 3500 nm indent. In order to study the possible reasons for this result, 3D-EBSD measurements were conducted on magnesium samples indented for 500 nm and 1500 nm depths, using a combination of automated FIB serial sectioning and EBSD orientation mapping on the individual sections.

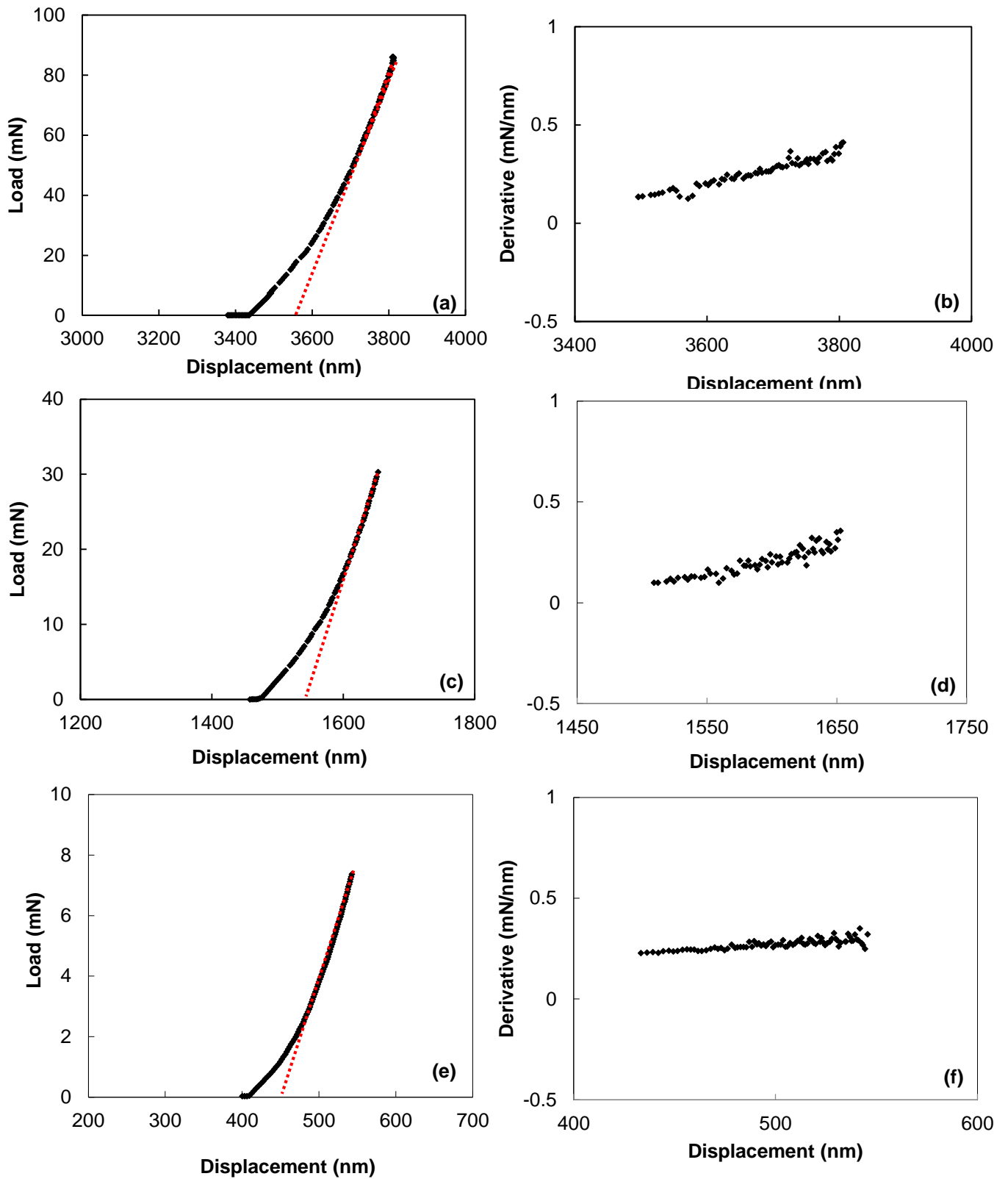


Figure 25: (a, c, e) Unloading curves for 500, 1500, and 3500 nm displacements, (b,d,f) and the derivative curves for the corresponding displacements.

In addition, the unloading curves of the load-displacement data have been investigated in detail. An enlarged view of the unloading segment of the indentation curve (Figures 5.25a, 5.25c, and 5.21e), and their corresponding derivatives (Figures 5.25b, 5.25d, and 5.25f) were studied for displacements of 500 nm, 1500 nm and 3500 nm, respectively. In contrast to the results for the case of loading nearly parallel to the *c*-axis (section 5.2), here there is no evidence of a detectible discontinuities during unloading in both the unloading curves and their corresponding derivatives, i.e. detwinning does not seem to occur in this case.

Figure 5.26 shows the indentation stress-strain curves obtained from the selected grain. Similar to the previous studied orientation, for this studied case, the 0.1% offset was chosen to define the yield stress in the indentation load-displacement curve. The Young's modulus obtained is 45 GPa which is in good agreement with the theoretical value, i.e. 46 GPa [160]. It can be observed that the deviation from elasticity occurs at stress of 178 MPa, which is lower than the stress at which the first discontinuity occurs, i.e. 203 MPa. Also, there are four discontinuities in the indentation stress-strain curves which are proposed to be related to extension twinning.

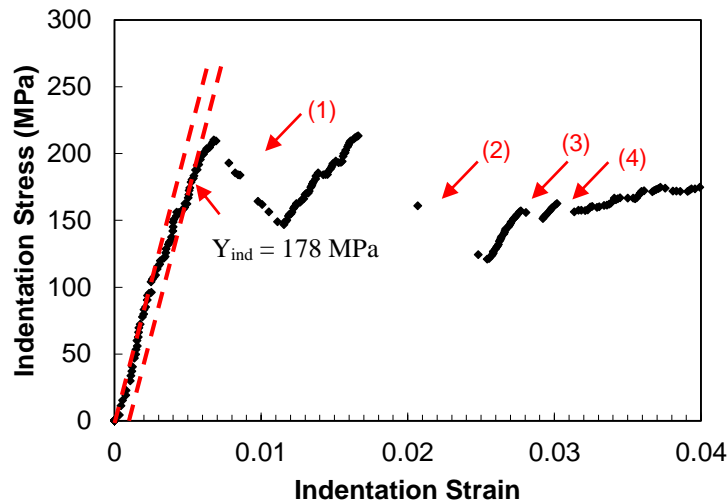


Figure 5.26. The measured indentation stress–strain curves for high purity magnesium for the case of indentation nearly perpendicular to the *c*-axis.

If it is assumed that the presence of large discontinuities in indentation stress-strain curve, are related to extension twin operation, it can be concluded that the deviation from elasticity is due to the basal slip operation (considering the low value of normalized RSS of prismatic and $\langle c+a \rangle$ slip from Table 5.4). Using normalized RSS values obtained from Hertzian contact theory for basal

slip operation, i.e. 0.37 from Table 5.5, combined with yield strength obtained from indentation stress-strain curves (178 MPa), the $RSS_{0.1\% \text{ offset}}$ values for basal slip were determined and shown in Table 5.6. Also, Table 5.7 summarizes the apparent CRSS values for the first variants of the $\{10 \bar{1} 2\}$ extension twins. This value was obtained using normalized resolved shear stress for the first variants of the $\{10 \bar{1} 2\}$ extension twins from Table 5.5 combined with the stresses at which the discontinuity occur in the indentation stress-strain curves (Figure 5.26).

Table 5.6: $RSS_{0.1\% \text{ offset}}$ values obtained from indentation test for the basal planes for the selected grain

Normalized RSS (τ_{rss}/ρ_m)	Yield stress (MPa)	$RSS_{0.1\% \text{ offset}}$ (MPa)
0.37	178 ± 5	66 ± 3

Table 5.7: Apparent critical resolved shear stress values obtained from indentation test for the extension twin planes for the selected grain

	Normalized RSS (τ_{rss}/ρ_m)	Pop-in stress (MPa)	Apparent CRSS (MPa)
First twin	0.39	205 ± 7	79 ± 4

5.3.4 3D EBSD maps

The results from 3D-EBSD tests for 1500 nm indent can be observed in Figure 5.27. Figure 5.27a shows an EBSD map of the indentation area, which illustrates the presence of basal slip traces around the indent. Figure 5.27b shows the combined image quality/inverse pole figure map of the same area shown in Figure 5.27a. Figure 5.27c shows the combined image quality/inverse pole figure map of the centre cross-section. This section is perpendicular to the surface of the sample and the location of it is shown by a dashed line in Figure 5.27b. As explained previously in Figure 5.21, two twin variants were observed on the indented surface. However, looking at the IPF map of the center cross-section slice (Figure 5.27c), one observes the existence of six variants of the extension twins under the indent. This is consistent with the load-displacement data (Figure 5.24c) which shows six discontinuities during loading, and also with Figure 5.25b which illustrates the occurrence of no discontinuity during unloading.

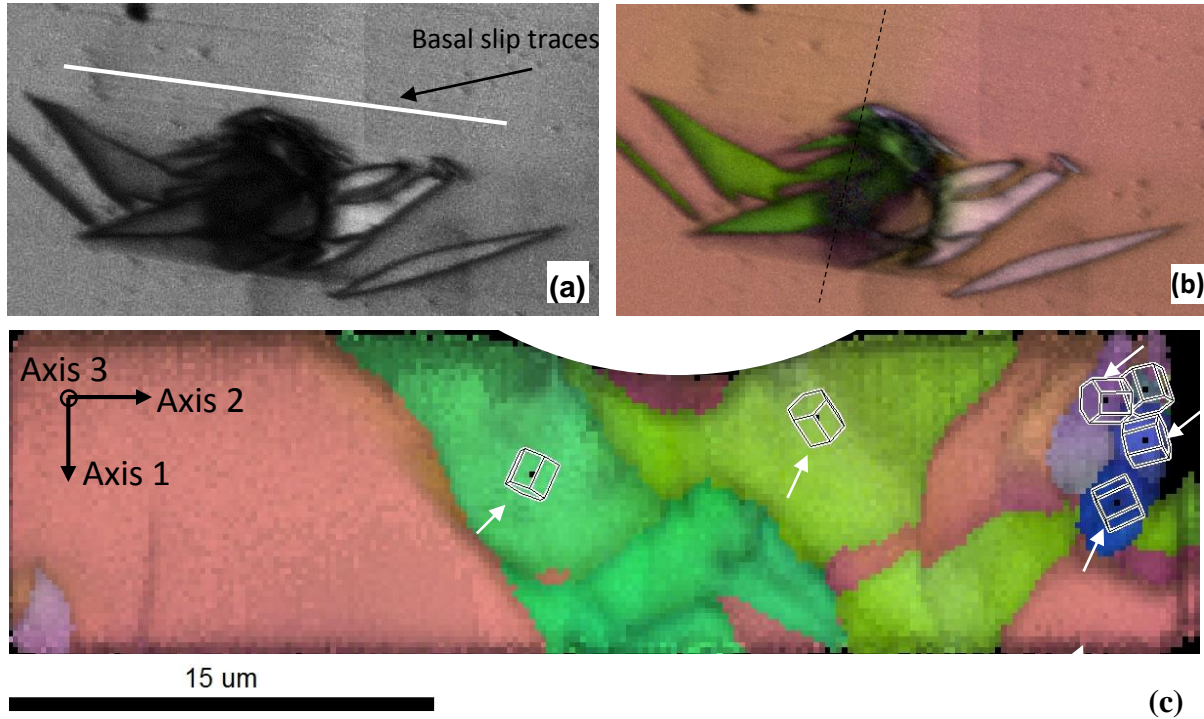


Figure 5.27: (a) The EBSD map of the indentation area, (b) the combined image quality/IPF map of the same area shown in (a), and (c) the combined image quality/inverse pole figure map of the centre cross-section. The section shown is perpendicular to the surface of the sample and the location of it is shown by dashed lines in (b). The white arrows show the six different extension twin variants under the indent. The black arrow in Figure (a) shows the basal slip trace. Note, the sample reference direction for A1 is close to $[\bar{1}\bar{1}20]$, A2 is close to $[\bar{1}100]$, and A3 is perpendicular to the surface (parallel to indentation direction).

Figure 5.28a shows the EBSD map of the surface of the sample indented for 500 nm depth. Figure 5.28b shows the combined image quality/inverse pole figure map of the same area. 3D-EBSD test has been conducted on this sample. Figure 5.28c shows a combined image quality/inverse pole figure maps of the centre cross-section. The section shown is perpendicular to the surface of the sample and the location of it is shown by dashed lines in Figure 5.27b. Figure 5.27c, shows the existence of two extension twin variants under the indent on centre cross-section. However, this result is in contrast with the load-displacement data (Figure 5.24b) which shows the occurrence of four discontinuities during loading, and also with Figure 5.25e which illustrates the occurrence of no discontinuities during unloading.

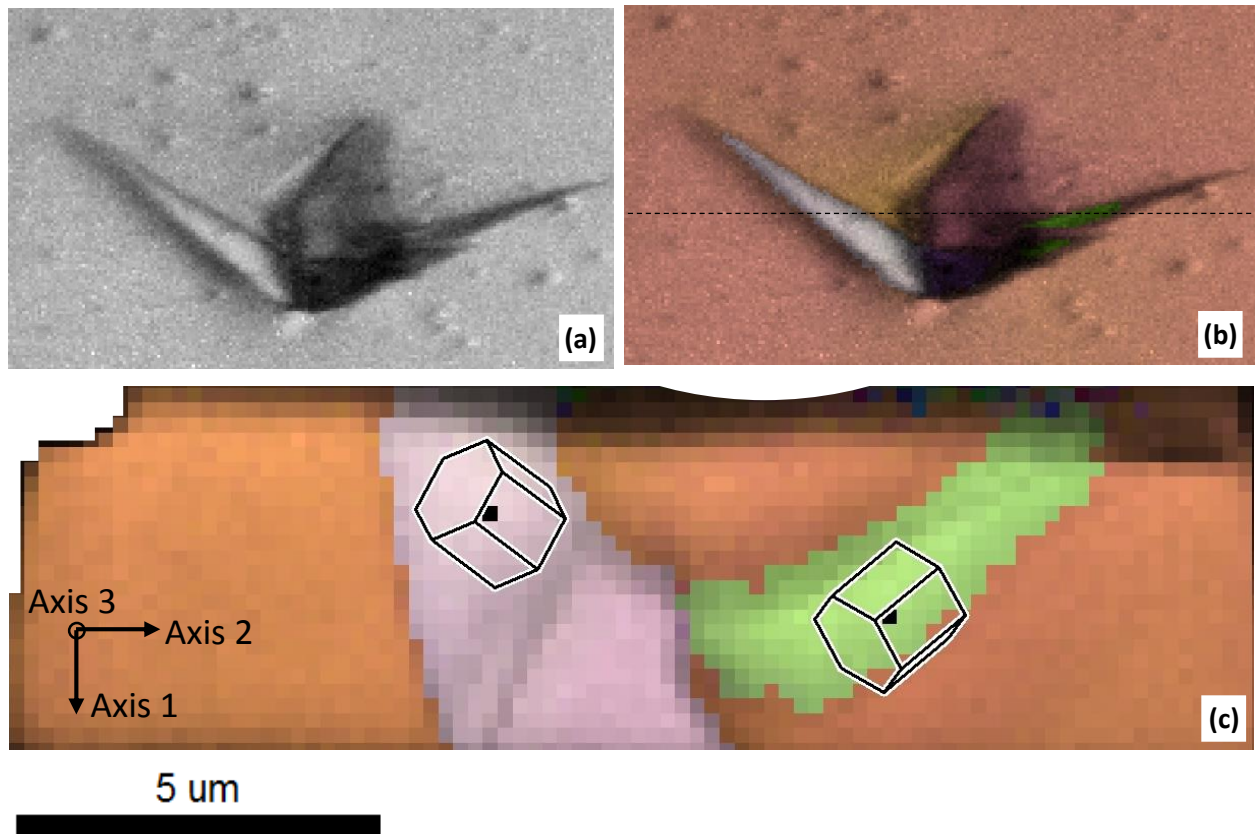


Figure 5.28: (a) The EBSD map of the indentation area, (b) the combined image quality/IPF map of the same area shown in (a), and (c) the combined image quality/inverse pole figure map of the centre cross-section. The section shown is perpendicular to the surface of the sample and the location of it is shown by dashed lines in (b). Note, the sample reference direction for A1 is close to $[\bar{1}120]$, A2 is close to $[\bar{1}100]$, and A3 is perpendicular to the surface (parallel to indentation direction).

However, looking at Figure 5.28c, one might see that the extension twins extended much deeper distances under the indent than can be practically obtained (limited by FIB time). (Note: the sample extracted by FIB had a thickness of 5 micron, and presumably the deformation twins propagated much deeper than the sample thickness). Therefore, one possibility is that there might be more extension twins which nucleate and propagate under the indent, but it was not possible to detect them in the IPF map due to the FIB sample size limit.

5.4 Spherical indentation with direction 54° away from c-axis

5.4.1 Microstructural analysis before and after the spherical indentation

The last loading direction which was selected for this study is shown in Figure 5.29a. In this case, the spherical indentation was made on a grain which was oriented such that the indentation direction was 54 degrees away from the c-axis. Several arrays of indents were performed on the selected grain with three different indentation depths (500 nm, 1500 nm, and 3500 nm). Figure 5.29b shows the optical micrograph of the tested sample after the spherical indentation. Generally the presence of twinning and slip traces can be seen around the indentation areas. These features will be studied in detail in the following.

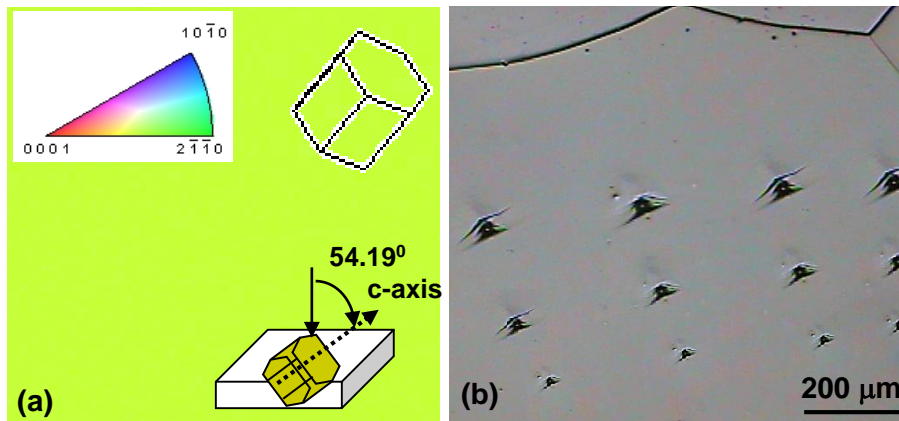


Figure 5.29: Inverse pole figure map before indentation tests, and (b) optical microscopy map after spherical indentation

Figures 5.30a, 5.30b, and 5.30c show combined image quality/inverse pole figure maps for spherical indentation of 500 nm, 1500 nm, and 3500 nm, respectively. The corresponding $\{0001\}$ pole figures are shown in Figures 5.30g, 5.30h, and 5.30i. The indentation areas (black regions) are indicated by white arrows on the EBSD maps and the impressions have approximate diameters of 7 μm , 14 μm , and 20 μm for depths of 500 nm, 1500 nm, and 3500 nm, respectively. Figures 5.30d, 5.30e, and 5.30f show the magnified view of the IPF maps of the same areas shown in Figure 5.30a, 5.30b, and 5.30c. According to the IPF map (Figure 5.30d) and its corresponding pole figure map (Figure 5.30g), for the case of 500 nm indent, two variants of $\{10\bar{1}2\}$ extension twins can be observed on the surface after the unloading (labelled twin number 2 and 3). For two other cases, i.e. 1500 nm and 3500 nm indent depths (Figures 5.30e and 5.30f), four variants of

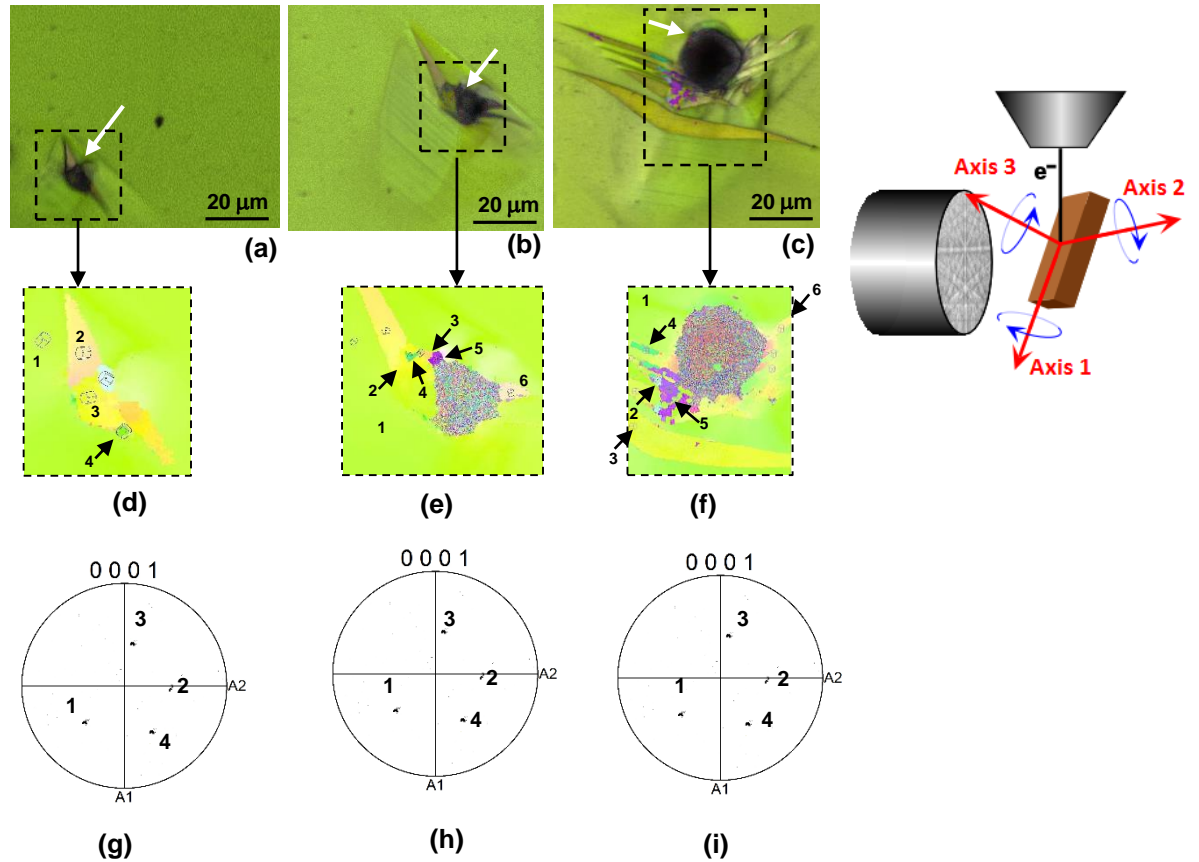


Figure 5.30: (a, b, and c) Combined image quality/IPF maps of the indented areas for three different indent depths: 500 nm, 1500 nm, and 3500 nm, respectively, and (d, e, and f) magnified view of the IPF maps of the same areas shown in (a, b, and c), and (g, h, and i) the corresponding {0001} pole figures of the IPF maps.

extension twin exist around the indent. Besides $\{10\bar{1}2\}$ extension twins, there is another misoriented area around the indent for all three studied indentation depths. This area (labelled 4) is shown with green color in the IPF maps (Figures 5.30d, 5.30e, and 5.30f), and has misorientations of 86° with extension twins number 3 (Figures 5.30g, 5.30h, and 5.30i).

5.4.2 Analysis of stress field under indent using Hertzian elastic contact mechanics

In this section, similar to Sections 5.3.2 and 5.2.2, the stress field under the indenter was calculated for indentation with direction 54° away from c-axis using Hertzian contact theory. This helps us to define the type of slip/twin systems which shows relatively higher value of normalized RSS and consequently is more probable to activate under the indent. Figure 5. 31 shows the

solutions for the spatial distribution of resolved shear stress (RSS) on the basal slip plane normalized by the indentation pressure, p_m as a function of the normalized depth, z/a and the normalized length, x/a . It can be observed that the maximum normalized resolved shear stress for basal slip, occurs under the indent at approximately $x/a=0$, and has a value of 0.46, marked by the white arrows. It should be noted that in our experiment, the angle between the c-axis and the indentation direction is 54° , and thus a slight asymmetry in this figure can be seen (note: the RSS should be symmetrical around axis x/a , i.e. there should be a mirror plane at $x/a = 0$, for a case in which the indentation direction is 45° away from c-axis). The maximum normalized RSS for basal slip, prismatic slip, pyramidal $\langle c+a \rangle$ slip, and extension twin planes were also calculated and summarized in Table 5.8. According to this Table, the maximum normalized RSS on the prismatic $\langle a \rangle$, 2nd order pyramidal $\langle c+a \rangle$ slip planes, and contraction twin, i.e. 0.34, 0.41, and 0.4, respectively, are still lower than that for basal slip (0.46). Therefore, it is expected that basal slip operates first under the indent. Also, the normalized RSS for extension twinning ranges from 0.32 to 0.28 for four extension twin variants, i.e. $(01\bar{1}2)$, $(0\bar{1}12)$, $(\bar{1}012)$, and $(10\bar{1}2)$. However, for the two other cases, i.e. $(1\bar{1}20)$, and $(1\bar{1}02)$, the maximum normalized RSS shows considerably lower values, i.e. 0.13.

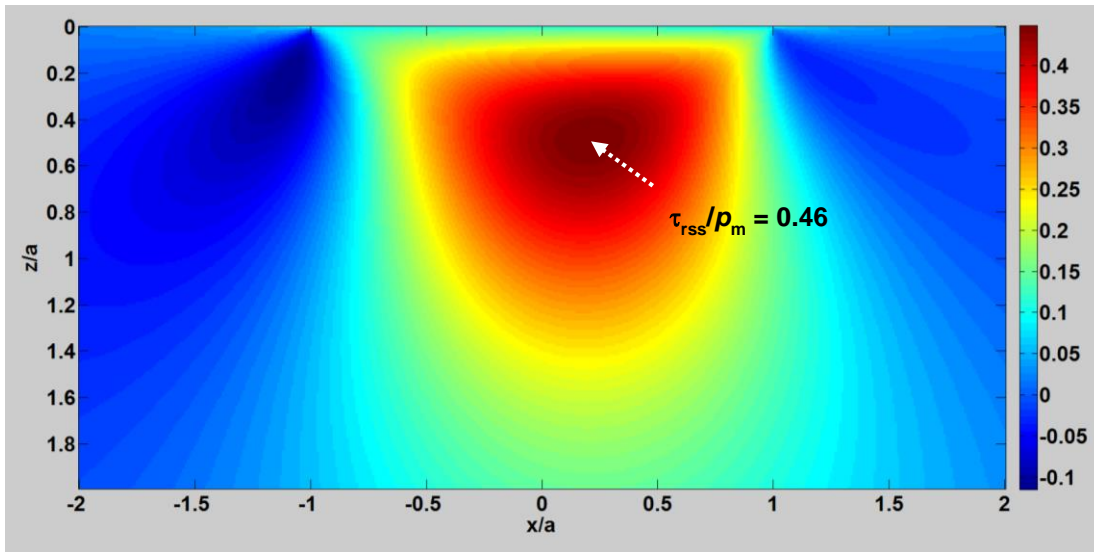


Figure 5.31: Distribution of normalized resolved shear stress (τ_{rss}/ρ_m) below the spherical indenter for basal slip for indentation along a direction 54 degrees away from c-axis.

Table 5.8: List of maximum normalized RSS (τ_{rss}/ρ_m) for basal slip and 6 extension twins on a grain which was oriented such that the indentation direction was 54 degrees away from the c-axis

	Indentation Schmid factor (τ_{rss}/ρ_m)
	54 degrees off from [0001]
Basal Slip	0.46
Prismatic Slip	0.34
Pyramidal <c+a> Slip	0.41
Contraction twin	0.40
(01 $\bar{1}2$) twin plane	0.32
(0 $\bar{1}12$) twin plane	0.31
($\bar{1}012$) twin plane	0.28
(10 $\bar{1}2$) twin plane	0.27
(1 $\bar{1}20$) twin plane	0.13
(1 $\bar{1}02$) twin plane	0.13

5.4.3 Indentation load-depth curves

The load-displacement ($P-h$) data for spherical indentation for 500 nm, 1500 nm, and 3500 nm displacements was examined in detail. Figure 5.32a shows the magnified view of the loading segment up to 500 nm depth. Also, this figure illustrates the prediction from Hertzian contact theory [65] (red line) for comparison. It can be observed that a significant deviation from Hertzian contact occurs at load of 0.54 mN. As mentioned in Section 5.4.2 the deviation from elasticity may occur by basal slip initiation. Also, the occurrence of five large discontinuities can be seen in the loading segment at loads of 2.14 mN, 3.35 mN, 4.15 mN, 4.75 mN, and 5.10 mN. Figure 5.32b shows the combined image quality/IPF map of the indented sample for 3500 nm displacement which shows the presence of five extension twins around the indent. It can be seen that the number of discontinuities appears on the loading segment is consistent with the number of twins observed around the indent.

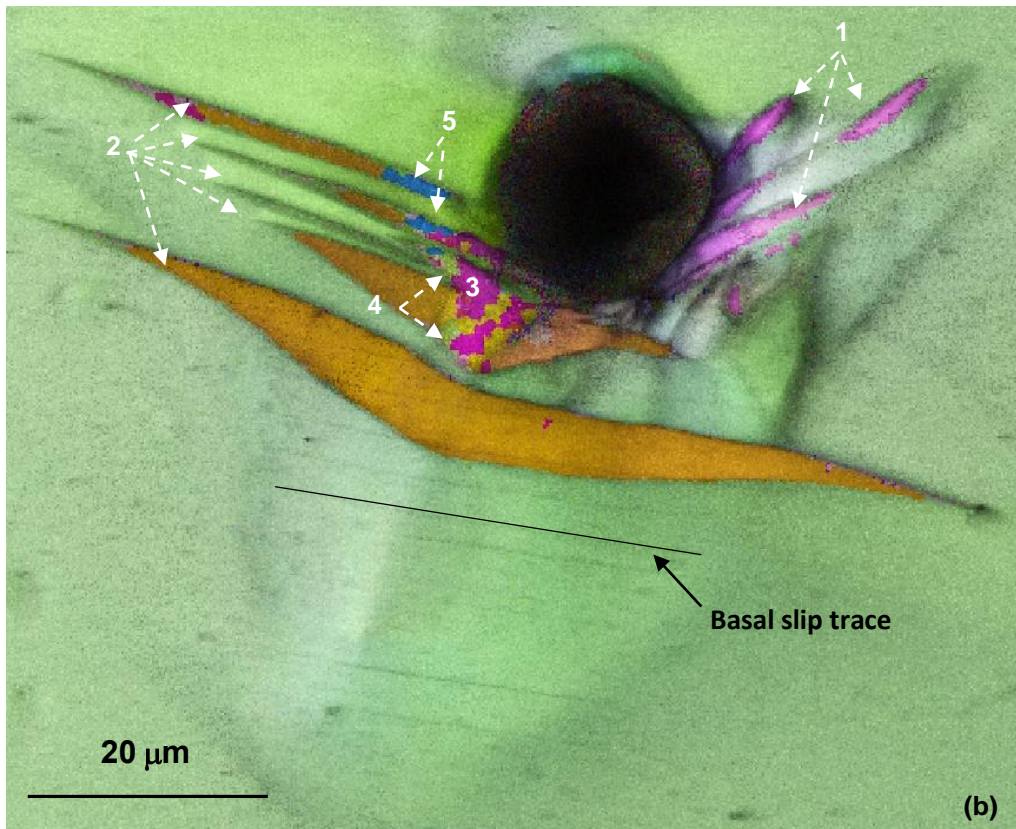
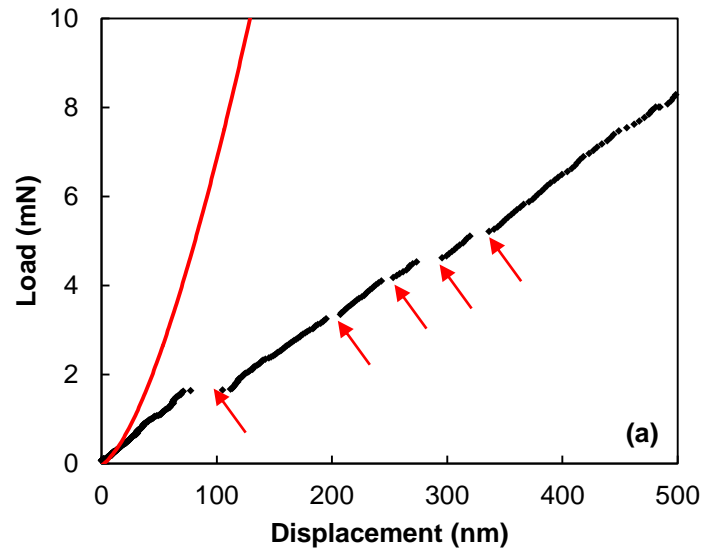


Figure 5.32: The EBSD map and the load-displacement curve after the indentation on a grain which is 54 degrees off from $[0001]$ direction. Five extension twins around the indent are shown by white arrows. The presence of five extension twins (labelled 1 to 5) can be seen around the indent. The black arrow shows the basal slip trace.

Furthermore, the unloading curves of the load-displacement data have been investigated in detail for all three indents, the results from the 3500 nm indents can be observed in Figure 5.33. Similar to the previous studied orientation (i.e. indentation nearly perpendicular to the c-axis), no evidence of discontinuities can be observed in the unloading curve (Figures 5.33a) and its corresponding derivative (Figures 5.33b) for this case. Therefore, the detwinning occurrence is not expected for this studied orientation.

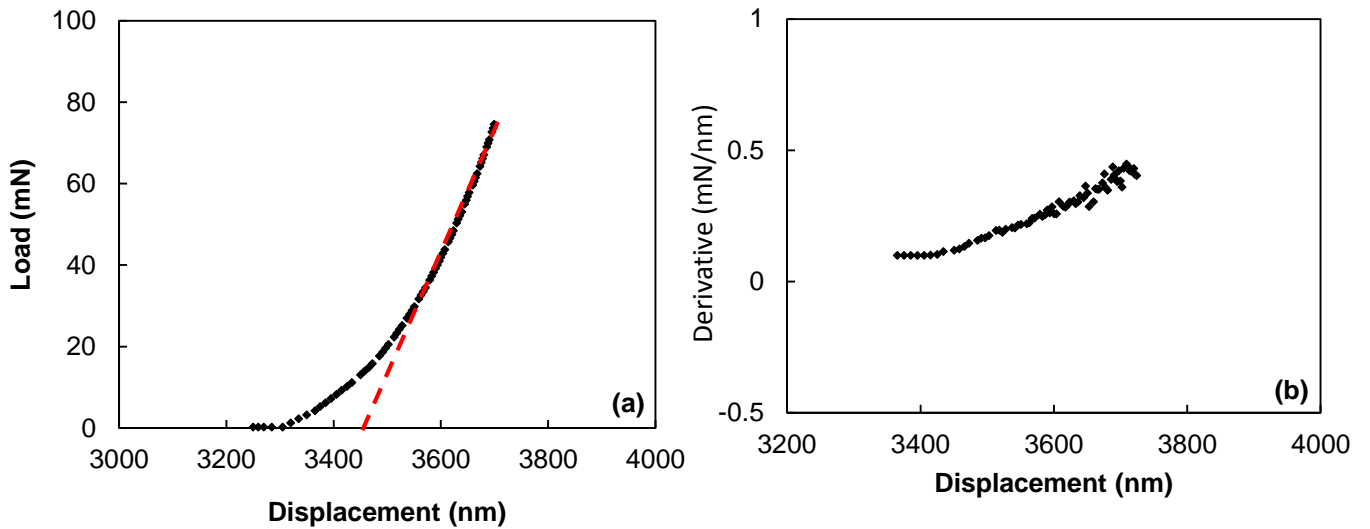


Figure 5.33: (a) Unloading curve for 3500 nm displacement, (b) and the derivative curve for the corresponding displacement.

The indentation stress-strain curve obtained from the load-displacement data is shown in Figure 5.34. The 0.1% offset was chosen to define the yield stress in the indentation load-displacement curve. The Young's modulus obtained is 45 GPa which is in good agreement with the theoretical value [160]. From the stress-strain curve, it can be observed that the deviation from elasticity occurs at a stress of 135 MPa. As explained in Section 5.4.2, it is expected that basal slip would operate first under the indenter. This is due to the large value of the maximum normalized RSS for basal slip operation, i.e. 0.46, in comparison with other slip systems. Therefore, the deviation in the stress-strain curve (at ~ 135 MPa), is proposed to be attributed to basal slip operation. Also, five significant discontinuities occur at loads of 248 MPa, 149 MPa, 161 MPa, 159 MPa, and 164 MPa, respectively, which are proposed to be related to extension twinning.

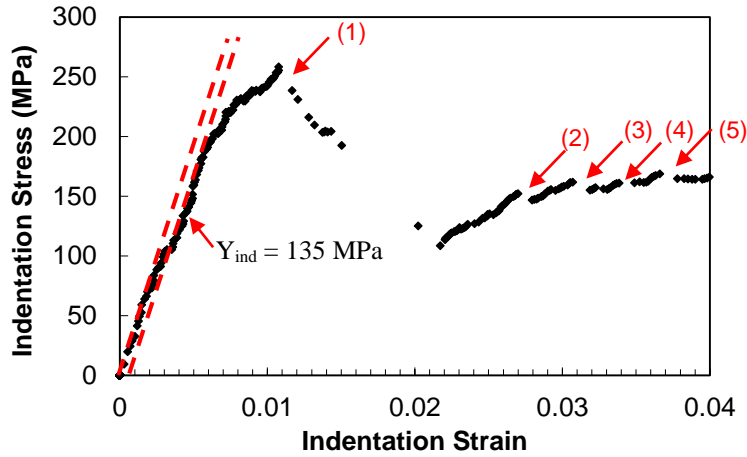


Figure 5.34. The measured indentation stress–strain curves for high purity magnesium for the case of indentation nearly perpendicular to the c-axis.

Using the normalized resolved shear stress value obtained from the Hertzian contact theory for basal slip operation (Table 5.8), combined with yield strength obtained from indentation stress-strain curves (135 MPa), the $RSS_{0.1\% \text{ offset}}$ values for basal slip were determined and shown in Table 5.9. In addition, Table 5.10 summarizes the apparent CRSS values for the first variant of the $\{10\bar{1}2\}$ extension twins. This value was obtained using normalized resolved shear stress for the first variant of the $\{10\bar{1}2\}$ extension twins from Table 5.8 combined with the stress at which the first discontinuity occurs in the indentation stress-strain curves (Figure 5.34). Note: these results were obtained based on 20 spherical indentation tests conducted on the same grain. Thus, the CRSS values shown in Table 5.3 and 5.4 are the mean of the 20 indentation tests plus/minus the standard deviation of the mean.

Table 5.9: $RSS_{0.1\% \text{ offset}}$ values obtained from indentation test for the basal planes for the selected grain

Normalized RSS (τ_{rss}/ρ_m)	Yield stress (MPa)	$RSS_{0.1\% \text{ offset}}$ (MPa)
0.46	135 ± 5	63 ± 3

Table 5.10: Apparent critical resolved shear stress values obtained from indentation test for the extension twin planes for the selected grain

	Normalized RSS (τ_{rss}/ρ_m)	Pop-in stress (MPa)	Apparent CRSS (MPa)
First twin	0.32	252 ± 7	81 ± 5

5.4.4 3D EBSD maps

3D-EBSD measurements were performed for a 1500 nm indent, the results being shown in Figure 5.35. Figure 5.35a shows a combined image quality/IPF map of the indentation area, which illustrates the presence of basal slip traces around the indent by a black line. Figure 5.35b shows the magnified view of the IPF map of the same area shown in Figure 5.35a. Figure 5.35c shows an IPF map of a section which is 5 μm away from the center slice. The section shown is perpendicular to the surface of the sample and location is shown by a dashed line in Figure 5.35b. Three variants of deformation twins can be observed in this section. According to the $\{0001\}$ pole figures (Figure 5.35d), twin number 4 shows 60 degrees misorientation with the matrix. However, twin number 4 shows 86° misorientation with twin number 3. Later, in the discussion section, the nature of twin number 4 will be discussed in more detail.

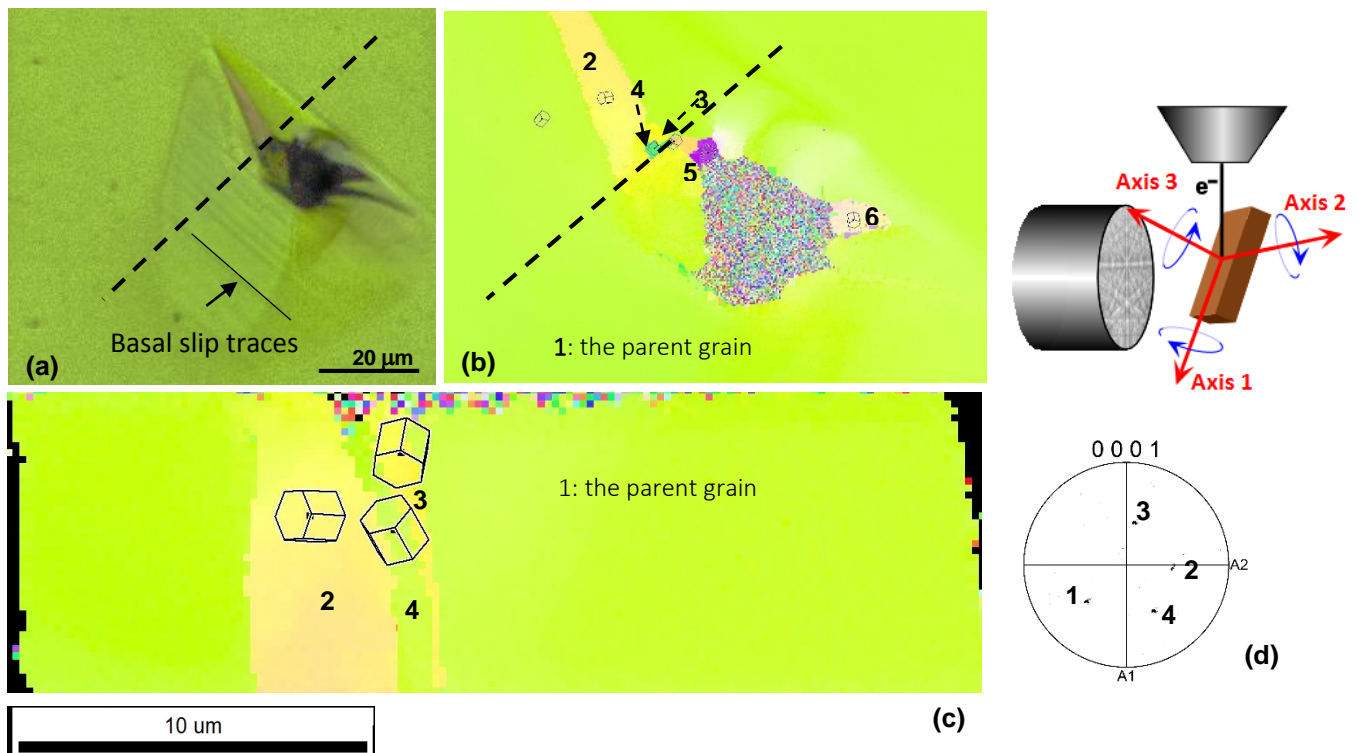


Figure 5.35: (a) The combined image quality/IPF map of the indentation area, (b) the magnified view of the IPF map of the same area shown in (a), and (c) the IPF map of a section which is 5 micron away from the centre cross-section. This section is perpendicular to the surface of the sample and the location of it is shown by dashed line in Figure 5.35b. (d) shows the corresponding $\{0001\}$ pole figure of the IPF maps.

5.5 Discussion

The problem of how materials flow under an indenter has a long history. Continuum plasticity approaches such as slip field or upper bound solutions show that during indentation the material under the indenter forms a dead zone pushing material perpendicular to the indentation direction and then flowing up to the free surface. The “pileup” of material around the indent ensures that volume is conserved. The role of the restriction of slip to specific crystal planes and directions in crystalline materials has been studied in detail recently by Kalidindi [164] for aluminum. Here, the shape of the indents and the pileups are affected by the orientation of the indentation axis relative to the crystal axes. However, we will see that this is a relatively small effect compared to what happens in magnesium since the high symmetry of the face centred cubic aluminum provides a large number of equivalent slip systems. The situation in magnesium is very different due to its low symmetry and the large differences in the CRSS of different slip/twin systems as was noted in the introduction.

5.5.1 Proposed Sequence of events during loading and unloading

The sequence of how plasticity initiates and spreads under the indent can be rationalized based on the analysis of the indentation load-displacement curves, the observations made by 3D EBSD, and the results obtained from CPFEM. Figure 5.36 presents a set of schematic diagrams to illustrate the proposed sequence of events under the indenter. Figure 5.36a shows the initial situation when the contact is elastic, i.e. the situation shown in Figure 5.5a where the initial load-displacement curve follows the Hertz elastic solution closely. In the background of the figure the contour plot for the resolved shear stress (RSS) on the basal slip plane is shown. Although there is considerable uncertainty in the value of the CRSS between basal and 2nd order pyramidal $\langle c+a \rangle$ slip as was noted in the literature review, it is generally accepted that $\langle c+a \rangle$ slip is at least 5 times larger than that for basal $\langle a \rangle$ slip, i.e. the higher CRSS makes 2nd order pyramidal slip less favourable than basal slip, even though the RSS is somewhat higher, i.e. 0.45 vs. 0.375, respectively. As such, it is predicted that basal slip will be activated first in the area of highest RSS (see Figure 5.36b) and in order to satisfy the required material flux as indicated by the blue arrows. The deviation between the experiments and the Hertz solution for the load-displacement data that is observed in Figure

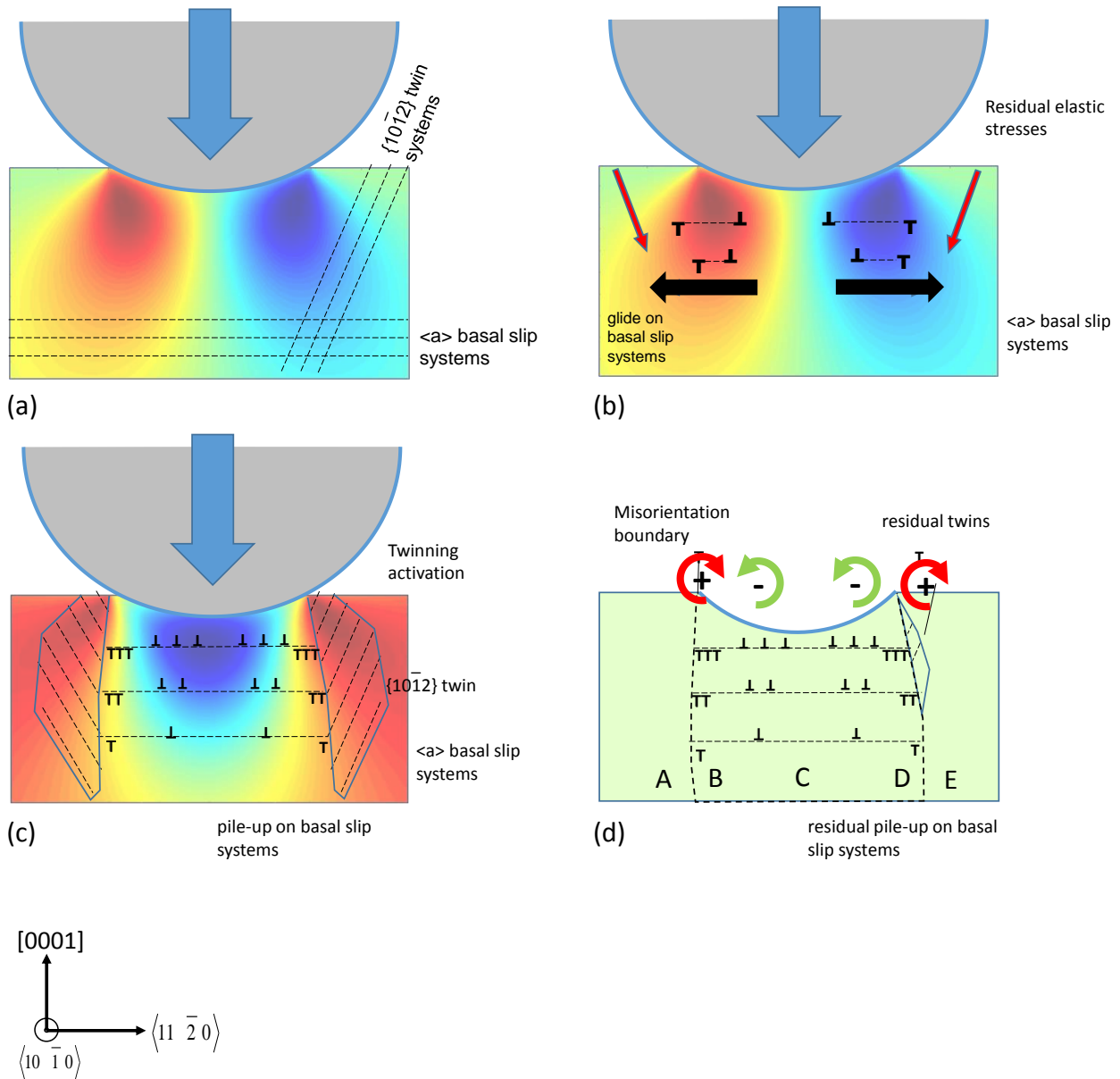


Figure 5.36: A set of schematic diagrams to illustrate the proposed sequence of events under the indenter. (a) The contact is elastic at this point. In the background of the figure the contour plot for the resolved shear stress (RSS) on the basal slip plane is shown. (b) The RSS on the basal slip plane reaches the CRSS for basal slip and plastic deformation is initiated. (c) The twins will form at those places where the RSS exceeds the CRSS for twinning. The distribution of the resolved shear stress on the extension twin habit planes derived from the Hertzian stress field is plotted as a background image. (d) The sample is unloaded and most of the twins will de-twin due to the elastic forces acting in their surrounding and due to the ease of movement of extension twin boundaries.

5.5b at a displacement of ≈ 32 nm can, thus, be rationalized as the point when plastic deformation is initiated by basal slip as shown schematically in Figure 5.36b. As the movement of $\langle a \rangle$ dislocations is not sufficient to accommodate the deformation upwards around the indent (i.e. in $\langle c \rangle$ direction), high residual elastic stresses will be built up as indicated in Figure 5.36b by the red arrows. The distribution of the resolved shear stress on the extension twin plane may be approximated with the Hertzian solution (although strictly speaking this solution does not allow any plastic deformation to occur) and is plotted as a background image in Figure 5.36c. As the indenter is pushed deeper into the material, twins will form at those locations indicated in Figure 5.36c. At this point, a discontinuity occurs in the load displacement curve from the formation of the $\{10\bar{1}2\}$ extension twin as shown in Figure 5.5c. Subsequently, the other 5 potential variants of extension twins will form. Indeed, this is what one observes in the data of Figure 5.4 where one sees 6 discontinuities, one for each of the $\{10\bar{1}2\}$ extension twin variants. The spacing of the discontinuities can be rationalized if one uses the Hertz solution as a qualitative guide to predict stress at which the different variants of $\{10\bar{1}2\}$ extension twin systems would operate. In Table 5.1, it can be observed that the normalized RSS on the six different twin variants ranges from 0.16 to 0.08 due to the fact that the loading axis was 9.3° away from the c-axis. This would suggest that the activation of the different variants would occur sequentially during indentation as observed in Figure 5.4 (there is probably also a stochastic aspect to the initiation stress for twinning and the possible local relaxation of stresses when a twin forms).

It is worth considering whether such discontinuities could be a result of dislocation pop-ins which have been observed by Pathak and Kalidindi [102]. In reference [102], they studied dislocation pop-ins during indentation of carefully prepared samples of aluminum (i.e. a material that does not exhibit deformation twinning under normal loading conditions) using a spherical indenter with radius of $13.3 \mu\text{m}$ (i.e. the same as used in the current study). They found that the magnitude of the displacement jump was 4-6 nm. This is much smaller than the 32 nm measured for the first discontinuity in the current work (see Figure 5.5c). The larger discontinuity in the current work would be consistent with the large shear strain associated with the formation of a twin. It is, therefore, unlikely that the large displacement steps observed in the current work are produced by dislocation pop-ins. In addition, it is worth noting that tests conducted on high purity aluminum (99.995) using the same indentation machine by the current researchers showed no evidence of discontinuities in the load-displacement curves (see Figure 5.15).

The formation of these twins can be explained as follows. As the indenter is pushed into the sample, material moves to the left and right by basal slip and then can flow to the surface by the operation of $\{10\bar{1}2\}$ extension twins. Indeed, it is observed that the location of the twins in the larger indents on the surface and in volume below the indent (Figures 5.3 and 5.9, respectively) corresponds to the region beside the indent.

Further, it is proposed that when the indenter is removed and the sample unloaded, most of the twins will retreat due to the elastic forces acting in their surrounding and the ease of movement of extension twin boundaries as shown schematically in Figure 5.36d. Evidence for de-twinning can be found by the observations of discontinuities in the unloading curves for the 100 and 500 nm indentations, see Figure 5.6. As discussed in the literature review, direct observations exist for twinning and de-twinning after loading and then unloading in uniaxial tension and compression tests [51-56] so it seems reasonable that the same effect will be found for indentation. Further, it is interesting to note that for an indent depth of 100 nm (Figure 5.5c), there is one discontinuity during loading and one during unloading (Figure 5.6c and 5.6d) while for an indent depth of 500 nm (Figure 5.4) one can observe six discontinuities in the loading curve and six discontinuities in the unloading curve (Figures 5.6e and 5.6f). It was found that for all cases of indent depths less than 500 nm, the number of discontinuities in the loading curves and unloading curves matched. If it is assumed that the discontinuities during loading correspond to twinning and those occurring during unloading correspond to de-twinning, it would suggest that no twins are left around the indent after the load is removed for the 500 nm indents. This would be consistent with the observation in Figure 5.3a and 5.7a that no twins could be observed on the surface or in the volume under the indenter. Thus, we propose that the absence of twins on the surface and below the indenter from the current study and previous studies [104,105,107] for some cases (e.g. the 500 nm deep indent shown in Figure 5.3a) does not necessarily mean that the twins were not present under load. Twins may have been present under load and then retreated during unloading as evidenced by the discontinuities in the unloading curves. Thus, one must be aware that post indentation examination does not always provide a complete picture of what happened. On the other hand, it appears there is a critical size above which, the de-twinning process is not completely reversible (Figure 5.3b and 5.3c). Thus, one must be careful about making conclusions on the deformation mechanism activated during indentation when making observations after the indenter is removed.

Finally, Figure 5.36d schematically illustrates an array of dislocations that would be consistent with the misorientation profiles. Here, it is envisioned that a series of dislocation loops (here seen in cross-section) have expanded under the indent to accommodate the removal of material as the indenter pushes into the sample. It can be seen that the number of dislocations “piled up” near a line extending from the edge of the contact surface would be inversely proportional to the distance from the surface, i.e. the misorientation along horizontal lines would decrease as a function of depth as seen in Figures 5.7, 5.8 and 5.12 from the experiments and CPFEM simulations, respectively. An additional insight that can be derived from this schematic diagram would be that the arrays of dislocations could form low energy dislocation boundaries under the edge of the contact point. Further, the GND calculations (Figure 5.10c) provide evidence of prismatic slip, presumably due to high stresses in this region. This may lead to the formation of sessile entanglements that keep the dislocation boundary at its place, even when the twins have retracted. This could explain why these boundaries are so readily observed in the unloaded samples, i.e. the low energy boundaries are maintained even when the load is removed. In contrast, the CPFEM simulations which do not take the local dislocation-dislocation interactions into account predicts that the boundaries would almost completely disappear when the load was removed.

However, for the case of indentation precisely parallel to the c-axis, the normalized RSS on the six different twin variants will be the same, i.e. 0.16. An example where the indentation direction only has a small deviation from the c-axis is shown in Figure 5.37. The inverse pole figure map (Figure 5.37a), and its corresponding $\{0001\}$ pole figure (Figure 5.37b) of a grain in Mg-1 wt% Zn- 0.5 wt% Nd (ZE10) alloy loaded precisely parallel to the c-axis can be observed. Six variants of $\{10\bar{1}2\}$ extension twins can be observed around the indent in the IPF map. Also, the indentation load-depth data for this grain can be seen in Figure 5.38. Figure 5.38b shows the enlarged view of the indentation load-depth curve. In comparison with the case that the loading axis was 9.3° away from the c-axis (Figure 5.4), here the magnitude of the displacement for all six discontinuities are similar. Also, the discontinuity events spread out over a narrower range of displacement.

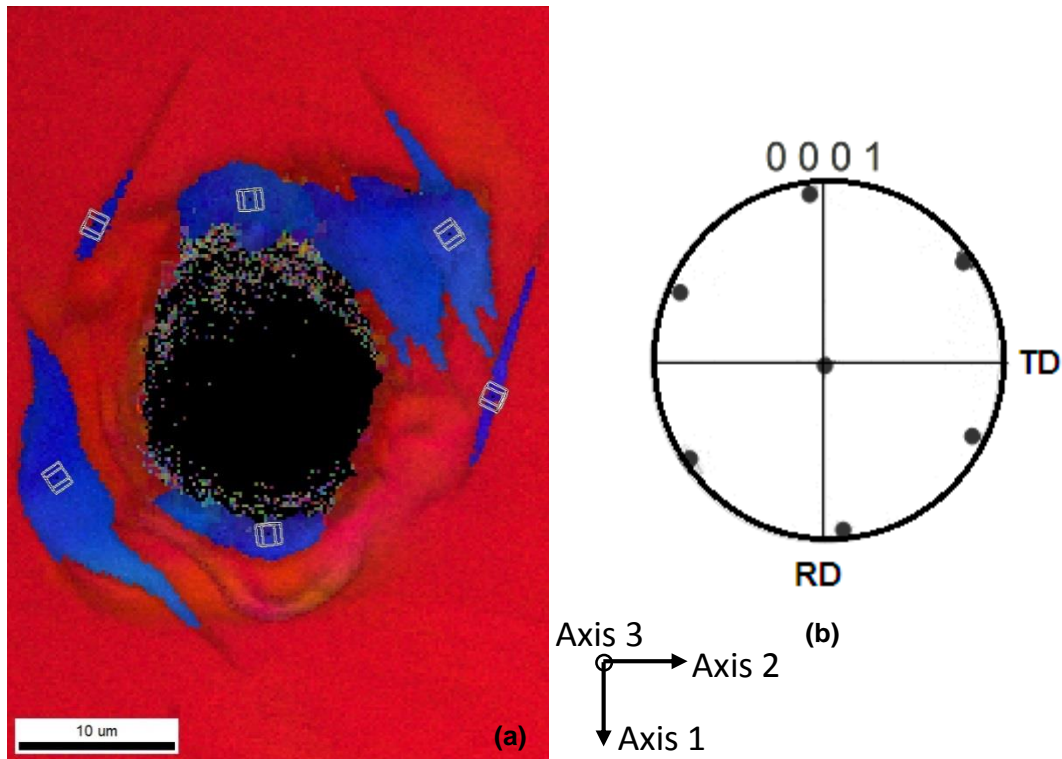


Figure 5.37: (a) Inverse pole figures (IPF) map and (b) its corresponding $\{0001\}$ pole figure map after indentation tests on Mg-1 wt% Zn- 0.5 wt% Nd (ZE10) alloy. Six variants of $\{10\bar{1}2\}$ extension twins can be observed around the indent. Note, the sample reference direction for A1 is close to $[\bar{1}2\bar{1}0]$, A2 is close to $[10\bar{1}0]$, and A3 is perpendicular to the surface (parallel to indentation direction).

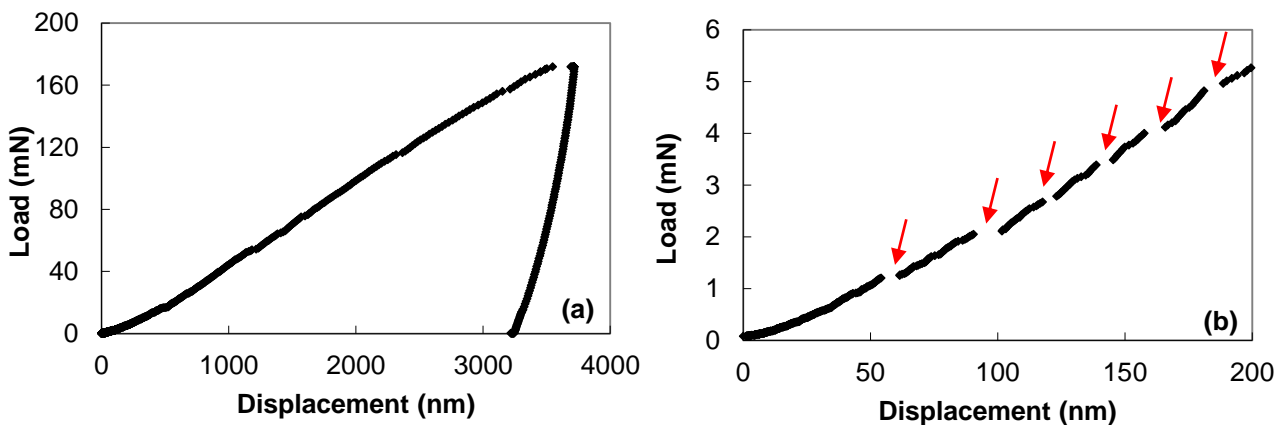


Figure 5.38: (a) Load-displacement curve of indentation test for on Mg-1 wt% Zn- 0.5 wt% Nd (ZE10), for indent depth of 3500 nm, and (b) An enlarged view of the loading curve, showing the occurrence of six similar.

5.5.2 Detailed observations on the residual deformation zone

Having sketched out a simple view of how the material flows under the indenter for this orientation of loading, it is worth exploring the residual deformation pattern in more detail by returning to the EBSD observations and the CPFEM simulations. In both cases of experiments (Figures 5.7 and 5.8) and CPFEM simulations (Figure 5.12), a boundary of large misorientation is observed near the edge of the indenter-material boundary and gradually changing misorientation angle as one moves from one side of the indent to the other. Good agreement between the experiments and the CPFEM simulations was observed between the magnitude of the maximum misorientation at different depths (Figure 5.13) for the 500 nm indent but the agreement was less satisfactory for the larger indents. Presumably, this relates to the larger effects of the extension twins on the deformation field as the indents become deeper which was not accounted for the CPFEM simulations. The other difference between the experiments and the CPFEM simulations was the gradient of misorientation outside the indent contact radius, i.e. this was much steeper in the experiments. Again, the presence of the extension twins in the experiments may explain this difference. Further, the twins would act to block the motion of basal dislocations creating a steeper gradient as seen in the experimental results shown in Figure 5.7 and 5.8.

The GND measurements from the 3D misorientation data suggest that it is primarily basal edge dislocations that are left behind in cylinder-shaped volume below the indenter after the indenter is removed (see Figure 5.10). There is also evidence of a smaller density of 2nd order pyramidal $\langle c+a \rangle$ dislocations (less than 10% the density of basal edge) inside of this volume. Additionally, a thin layer around this cylinder shows a high density of basal screw dislocations, together with a significantly lower density of $\langle a \rangle$ dislocations on prism planes. The dislocations in this volume most likely correspond to those that piled up and entangled in front of the deformation twins.

For the cylindrical volume below the indenter the analysis of the pole figures shown in Figure 5.7c and 5.8c demonstrates that the rotation axis is $\langle 11 \bar{2} 0 \rangle$. A look into the 3-dimensional results, however, reveals that the situation is less simple: Figure 5.39a shows a schematic view looking down on a plane parallel to the surface of the sample. The lateral flow of material under the indent can be accommodated by the expansion of dislocation loops with the 3 different $\langle a \rangle$ Burgers vectors as it is shown in the figure (note that there are 3 different Burgers vectors of type $\langle 11 \bar{2} 0 \rangle$). The result of this dislocation activity is that there are 3 different sectors centred around the 3 $\langle 11 \bar{2} 0 \rangle$

directions where plasticity is dominated by expansion of one type of dislocation loop. In these sectors, the rotations from the array of dislocations will be perpendicular to the Burgers vectors, i.e. the rotation axis should be $\langle 10 \bar{1} 0 \rangle$. On the other hand, as the schematic suggests, there are 3 sectors where a combination of dislocations with 2 Burgers vectors would be active. These sectors are parallel to the 3 $\langle 10 \bar{1} 0 \rangle$ directions. In the limiting case of equal numbers of the two different dislocations, the net Burgers vector would be one of the $\langle 10 \bar{1} 0 \rangle$ directions, e.g. $-b_1 + b_2 =$ would give an effective Burgers vector of $[1 \bar{1} 0 0]$ which is parallel to the black horizontal line in Figure 5.39a. In this case, the rotation axis would be expected to be perpendicular to one of the effective $\langle 10 \bar{1} 0 \rangle$ Burgers vectors, i.e. one of the $\langle 11 \bar{2} 0 \rangle$ directions.

Returning to the EBSD maps shown in Figure 5.7 and 5.8, recall that the A2 direction was close to $\langle 11 \bar{1} 0 0 \rangle$ and the A1 direction was close to $\langle 11 \bar{2} 0 \rangle$, i.e. this corresponds to a section cut through the centre of the indent parallel to the $\langle 11 \bar{1} 0 0 \rangle$ direction (the blue line in Figure 5.39a). The rotation axis determined from the pole figures was the $\langle 11 \bar{2} 0 \rangle$ exactly as expected from Figure 5.39a. In order to further examine this geometric prediction, the 3D data obtained from the 1500 nm indent experiment were used to generate a map indicating the direction of the rotation axes for a plane parallel to the sample surface at a depth of 4 μm below the surface ($z/a = 0.4$). This map is shown in Figure 5.39b. Here it can be seen that the experimentally determined rotation axis changes from $\langle 11 \bar{2} 0 \rangle$ (green) to $\langle 10 \bar{1} 0 \rangle$ (blue) with the rotation axis corresponding to the direction perpendicular to the effective Burgers vector, e.g. $\langle 10 \bar{1} 0 \rangle$ (blue) for directions parallel to the b_1, b_2 or b_3 and $\langle 11 \bar{2} 0 \rangle$ green for equal combinations of two different Burgers vectors. Further, Figure 5.39c shows the magnitude of the misorientation in the selected plane. It can be observed that the magnitude of the misorientation is maximum at the surface of the cylinder volume below the indent described above. The misorientation profiles shown in Figure 5.7b and 5.8b correspond to lines across the section close to the $\langle 11 \bar{1} 0 0 \rangle$ direction. Finally, based on this discussion, it is now worth

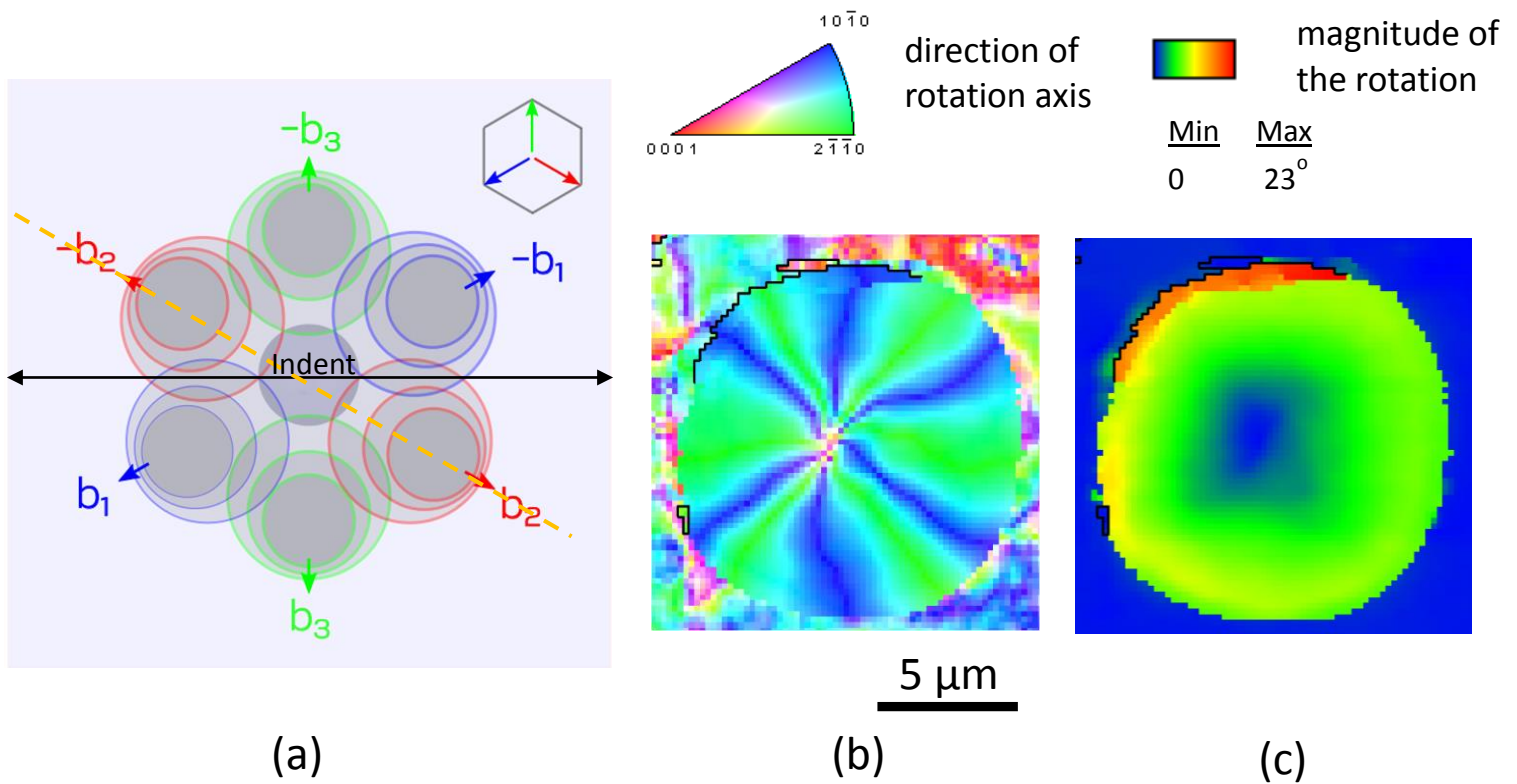


Figure 5.39: Characterization of rotations under the 1500 nm indenter, a) schematic diagram of dislocation loops for different basal slip systems. Note, the black arrow is $[10\bar{1}0]$, and the orange dashed line is $[11\bar{2}0]$. b) experimental observation on rotation axis the of crystal with respect to the original orientation for a horizontal slice, $4\mu\text{m}$ below the surface and c) magnitude of the misorientation angle on the same slice as shown in b). Note, solid black lines in b) and c) are misorientations greater than 15° .

clarifying that the schematic diagram shown in Figure 5.36 displays the situation occurring on a cross section through the indenter containing the $[0001]$ and one of the $\langle 11\bar{2}0 \rangle$ directions, indicated by the orange dashed line in Figure 5.39a.

This analysis shows that formation of the deformation pattern under the indenter is driven by a combination of the geometric requirement that the penetration of the indenter must be accommodated and the evolution of resolved shear stresses on the various slip systems (noting that there are very different CRSS values for basal and non-basal slip). Further, the plastic flow predominantly occurs by motion of $\langle a \rangle$ basal dislocations. The remnants of this deformation can be clearly observed from the post indentation observations of GNDs (Figure 5.10) and the

associated rotation axes (Figure 5.39b). The hypothesis that extension twins were present under load is consistent with the fact that the misorientation change at the edge of the projected contact surface is much sharper in the experiments than for the CPFEM, i.e. the twins blocked the motion of basal dislocations after they formed. Though our experiments provide strong evidence, direct proof that twins existed under load is challenging for high purity magnesium. Future experiments on magnesium alloys where detwinning is more difficult may provide evidence to support this hypothesis.

Returning to the second examined crystallographic orientation, i.e. spherical indentation approximately perpendicular to the c-axis, Figure 5.24 illustrates the load-displacement behavior of indentation on this studied orientation. According to Figure 5.24b the load-displacement curve initially follows the Hertz elastic solution. However, the deviation from elasticity occurs at a very small load, i.e. ~ 1.37 mN. As was explained earlier in Section 2.2, in magnesium, for uniaxial compression perpendicular to the c-axis, $\{10\bar{1}2\}$ extension twins are expected to operate. Let's first consider the relationship between the six extension twin variants under the spherical indent, i.e. $(01\bar{1}2)$, $(0\bar{1}12)$, $(\bar{1}012)$, $(10\bar{1}2)$, $(1\bar{1}20)$ and $(1\bar{1}02)$ planes. As the indenter is pushed into the sample, material moves down along the indenting axis, as a result four types of extension twins, $(01\bar{1}2)$, $(0\bar{1}12)$, $(\bar{1}012)$, and $(10\bar{1}2)$ activate, Figure 5.22a. However, for the case of two other shear planes of variants $(1\bar{1}20)$ and $(1\bar{1}02)$, the loading direction $[11\bar{2}0]$ is parallel to the shear planes, Figure 5.22b. Thus, these two shear planes require larger stresses to operate under the indent.

Figure 5.40a illustrates a schematic diagram of the distribution of twin and basal slip regions under the spherical indenter for the studied orientation. Figure 5.40b shows a combined image quality/ IPF map after indentation nearly perpendicular to the c-axis, for an indentation of 3500 nm. As can be seen from Figure 5.40a, the loading direction right under the indent can be considered as an uniaxial compression, which is favorable for extension twin operation. Therefore, extension twinning would operate in this region and expands along the z direction within the x-z plane. However, according to the Hertz solution, Figure 5.23c, the maximum normalized RSS on the basal plane occurs below the surface near the boundary between the contact region of the indent and the free surface, and its value is similar to the maximum RSS on the extension twin plane (Table 5.5). Therefore, as explained before (Section 5.3.2), there is a competition between basal slip and extension twin operation.

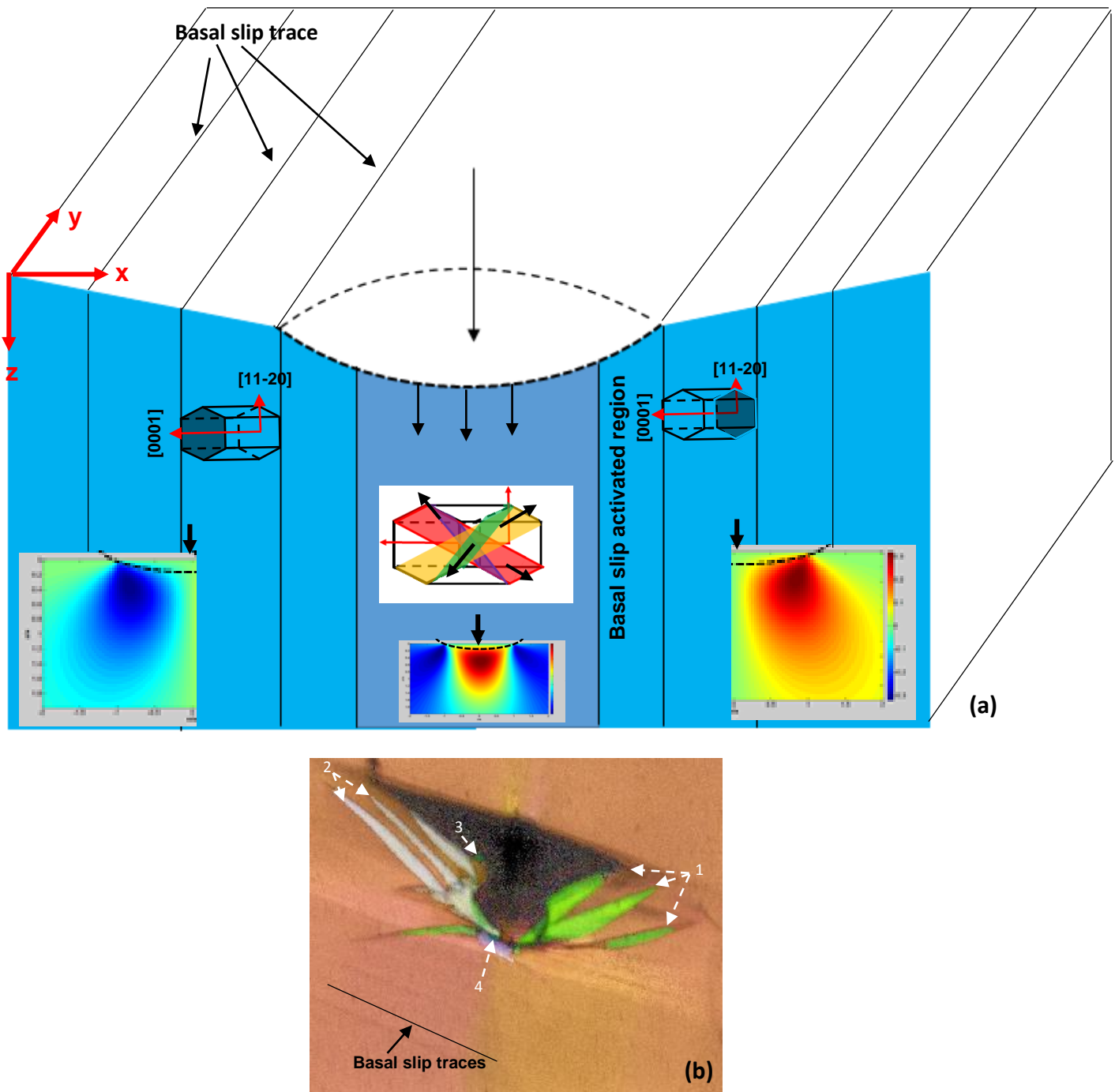


Figure 5.40: (a) Schematic figure of indentation perpendicular to the c-axis, and (b) IPF EBSD image after indentation nearly perpendicular to the c-axis, for indentation of 3500 nm.

However, the result from the indentation stress-strain curve (Figure 5.26) illustrated that the basal slip would operate first for this studied orientation, and presumably right after that four extension twin would operate sequentially. Table 5.6 and 5.7 also show the $RSS_{0.1\% \text{ offset}}$ values obtained for basal slip and the first extension twin plane. As can be observed the $RSS_{0.1\% \text{ offset}}$ for basal slip (67 MPa) is lower than extension twin plane (79 MPa), and thus it is suggested that the plasticity initiates by basal slip operation for this studied orientation. The presence of both basal slip traces and four extension twin variants can be seen around the indent (Figure 5.40b), which is in good agreement with the schematic figure.

One more interesting observation is the presence of two more extension twins (i.e. $(1\bar{1}20)$, and $(1\bar{1}02)$ extension twin planes) under the indent for indentions of up to 1500 nm. This is in contrast with the results from Hertz calculation which suggests the operation of only four extension twins under the indent (Figure 5.23). One possible explanation is that, when the indenter is pushed into the material, first the initial extension twins operate under the indent and tried to move the material to the left and right side. On the other hand, the flow of material to the left and right of the indent will be highly constrained by the surrounding elastic material. The constraint from the surrounding elastic material raises the local RSS on the (i.e. $(1\bar{1}20)$, and $(1\bar{1}02)$ extension twin variants. The formation of these twins would relieve the stress under the indent.

A further interesting observation for this studied orientation is that, the unloading segments of the indentation load-displacement curves and their derivatives confirm the occurrence of no discontinuities during unloading (Figure 5.25). Therefore, we do not expect reverse plasticity of the material during unloading as a result of no or at least very limited de-twinning. If we compare EBSD maps obtained from 3D-EBSD tests from the center cross-section slices of both studied orientations, i.e. indentation approximately parallel to the c-axis with the case in which the indentation direction is nearly perpendicular to the c-axis (Figures 5.7b, and 5.7f compared with Figures 5.27c, and 5.28c), we might conclude that the extension twins extended deeper into the material in the latter case. For example, for the case of indentation nearly parallel to the c-axis (Figure 5.7f), the deformation twins extended up to the depth of 4.5 μm . However, looking at the second condition (Figure 5.28c), one might see that the extension twins extended much deeper distances under the indent than can be practically obtained (limited by FIB time). The sample extracted by FIB had a thickness of 10 micron, and presumably the deformation twins propagated

much deeper than the sample thickness. Therefore, it may be more difficult to observe these twins completely after load removal.

For the third crystallographic orientation, i.e. indentation with a direction 54° away from c-axis, Hertz's elastic contact analysis confirms that the plasticity should be initiated when the RSS on the basal slip plane reaches the $RSS_{0.1\% \text{ offset}}$ for basal slip (Table 5.8). For this orientation, basal slip is the most favorable deformation system under the indent. Here again we have used the Hertz solution to qualitatively predict when other deformation systems would operate. According to Hertz (Table 5.8), the maximum normalized RSS on four different extension twin variants, i.e. $(01\bar{1}2)$, $(0\bar{1}12)$, $(\bar{1}012)$, and $(10\bar{1}2)$ twin variants, ranges from 0.32 to 0.27. However, for the two other extension twins, i.e. $(1\bar{1}20)$ and $(1\bar{1}02)$ extension twins, the normalized RSS are much lower (0.13). Therefore, the four most favorable extension twins are expected to be seen around and under the indent. Similar to the previous orientation, in order to have a better understanding of operation of slip/twinning deformation systems, the $RSS_{0.1\% \text{ offset}}$ values for basal and extension twin planes were studied. Table 5.9 and 5.10 show the $RSS_{0.1\% \text{ offset}}$ values obtained for basal slip and the apparent CRSS for the first extension twin plane. According to this Table, the $RSS_{0.1\% \text{ offset}}$ for basal slip (63 MPa) is lower than the $(01\bar{1}2)$ extension twin plane (76 MPa). So, it is expected that basal slip would operate first and then four extension twins, i.e. $(01\bar{1}2)$, $(0\bar{1}12)$, $(\bar{1}012)$, and $(10\bar{1}2)$ twin variants, would activate under the indent sequentially.

However, as shown in Figure 5.30, and 5.35, the existence of another deformation twin can be observed under and around the indent after the load removal. Also, looking at the $\{0001\}$ pole figures (Figure 5.30h, and 5.35d) confirms that this deformation twin formed 86° away from the primary twin (twin number 3). As mentioned in Chapter 2, besides twinning, double twinning (re-twinning inside a primary twin) was also observed as a mechanism of plasticity. Based on previous experimental results [32,49,50], double twins of $\{10\bar{1}1\}$ - $\{10\bar{1}2\}$ and $\{10\bar{1}3\}$ - $\{10\bar{1}2\}$ types, have been detected in magnesium. However, in our experiment, we have not observed either contraction twinning (i.e. twinning on $\{10\bar{1}1\}$ or $\{10\bar{1}3\}$ planes) or double contraction extension twinning. However, Jain [46] has previously observed the presence of double extension twin (i.e. extension twins formed within extension twins) in AZ80 material, compressed along the $\langle 10\bar{1}2 \rangle$ direction. Jain [46] explained the occurrence of the secondary twins as an accommodation mechanism to help maintain strain compatibility caused due to twinning. He found the presence of 6 extension

twin and 1 double extension twin in his experiment. He concluded that the double-extension twin, had a misorientation of 86° with one of the primary extension twins. In our experiment, one might see from Figures 5.30, and 5.35 that the secondary twin (twin number 4) has a misorientation of 86° with the primary extension twin (twin number 3). It is suggested that this secondary extension twin formed in response to the local stress field associated with the primary twins.

Figure 5.41 is a summary of the load-displacement curves from the three different studied orientations. It can be observed that magnesium is elastically quite isotropic, although it shows high plastic anisotropy. This is clear in Figure 5.41 by overlapping of the initial elastic region of the load-displacement curves for three different orientations. Also for all three cases some well-defined and large discontinuities can be seen in the load-displacement curves. For the case of indentation with loading directions 10° and 54° away from c-axis (red curve, and light green curve), there is a well-defined deviation from Hertz contact which is argued to correspond to the basal slip operation. This deviation occurs on the load-displacement curve prior to the first discontinuity.

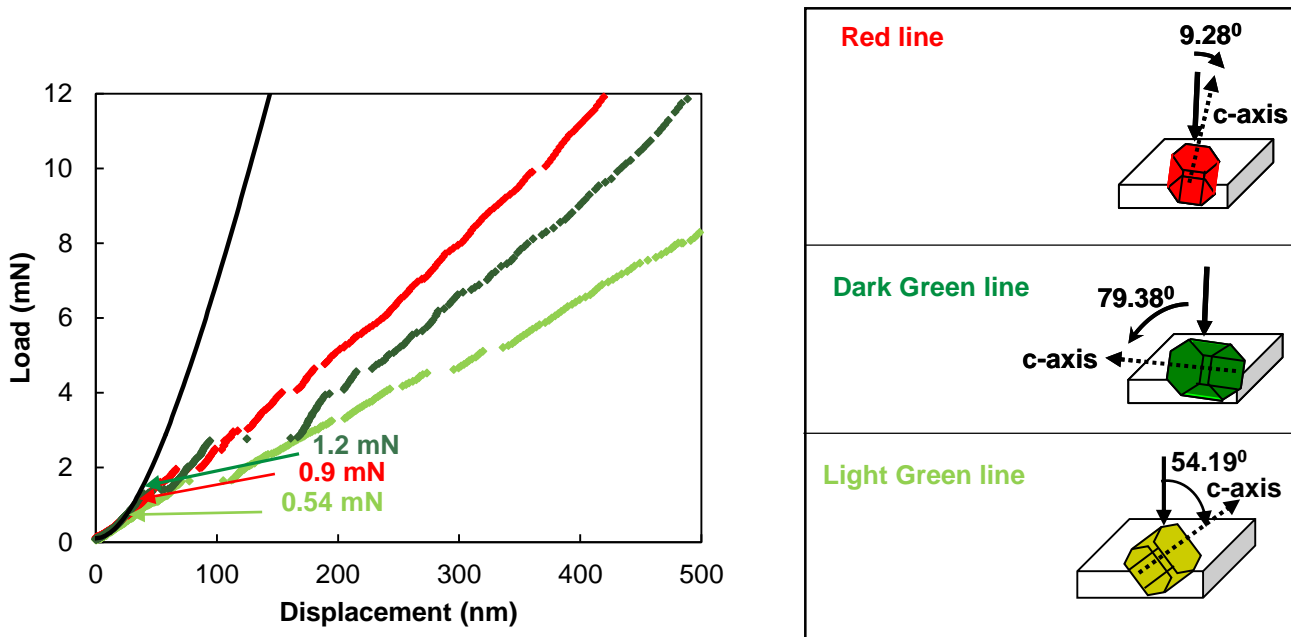


Figure 5.41: Comparison between the indentation load-displacement curves for three orientations.

However, for the case of indentation nearly perpendicular to the c-axis (dark green curve), the indentation load-displacement behavior is different from those arising from the two other

orientations. For this case, the deviation from elasticity occurs close to the load at which the first large discontinuity happens in indentation load-displacement curve. In order to clearly define the exact yield point (i.e. the point at which the indentation curve deviates from elasticity), the indentation stress-strain curve was calculated from the load-displacement data.

Figure 5.42 is a summary of the indentation stress-strain curves of all three examined orientations. It can be observed that the deviation from elasticity occurs at stress of 135, 178, and 181 MPa for light green, dark green, and red curves, respectively. Table 5.11 is a summary of $RSS_{0.1\% \text{ offset}}$ values obtained for basal slip, and the extension twin plane on all three examined orientations, based on the measurement of 20 spherical indentation tests. According to Figure 5.42, and Table 5.11, it can be summarized that the plastic deformation occurs first on a grain which is 54 degrees off from c-axis (light green line in Figure 5.42) and last on a grain which is nearly parallel to the c-axis. Among all three studied orientations, extension twinning appears at lower load, and consequently at lower stress on a grain which is nearly perpendicular to the c-axis (Figures 5.41 and 5.42), which is a favorable orientation for extension twin operation.

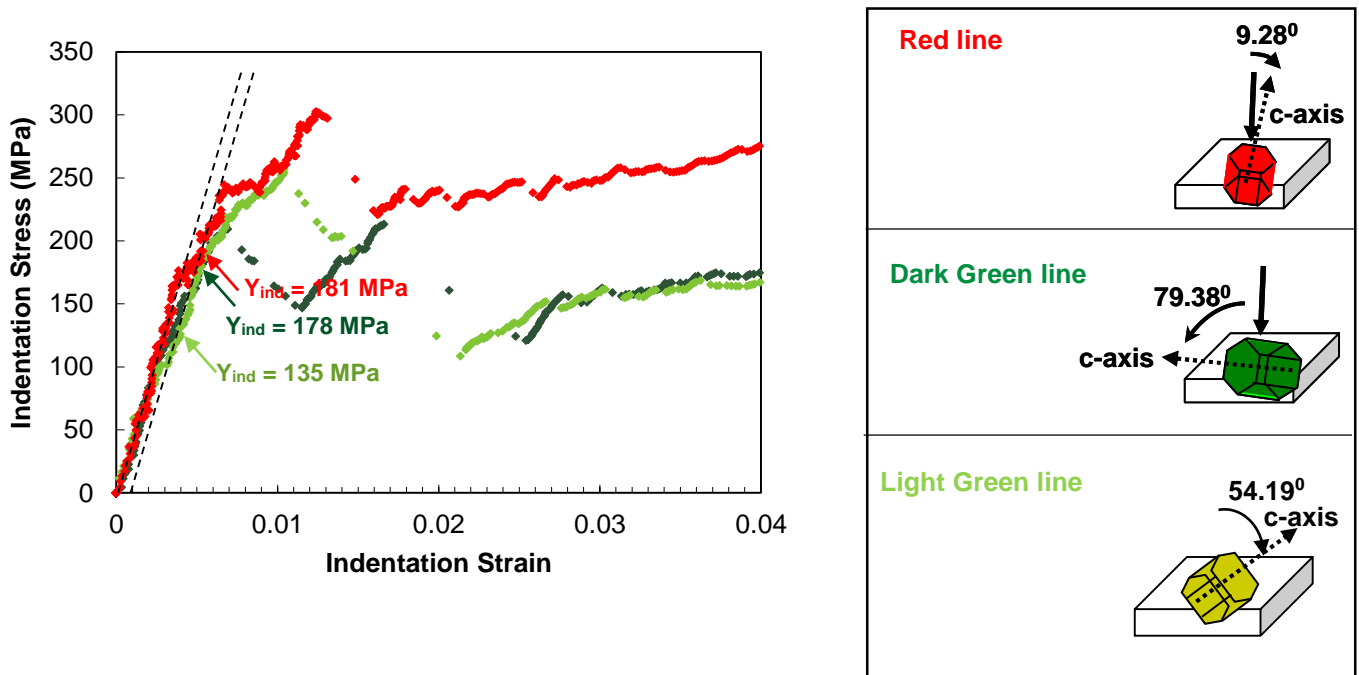


Figure 5.42: Comparison between the indentation stress-strain curves for three orientations.

Table 5.11: Summary of the $RSS_{0.1\% \text{ offset}}$ for basal slip and the apparent CRSS for 6 extension twins for three different studied orientations

	Critical resolved shear stress (MPa)		
	9.3 degrees rotated from [0001]	80 degrees rotated from [0001]	54 degrees rotated from [0001]
Basal Slip	68 ± 3	66 ± 3	63 ± 3
First twin	48 ± 3	79 ± 4	81 ± 5

Also, looking at Table 5.11, one might conclude that for the case where the indentation is almost parallel to the c-axis, the apparent CRSS value for extension twinning is relatively lower than the other two cases (i.e. indentation is nearly perpendicular to the c-axis, 79 MPa, and indentation is at loading direction of 54 degrees away from the c-axis, 81 MPa). It can be observed from Table 5.2 that for the case of indentation almost parallel to the c-axis, the normalized RSS value for activation of extension twinning (0.16) is relatively low compared to the normalized RSS for basal slip operation (0.38). As previously explained, when the plasticity is initiated in this studied orientation, first basal slip operates and causes the material to flow to the right and left sides under the indenter. However, the flow of the material is constrained by the surrounding elastic materials and that raises the local RSS on the extension twinning variants. As a result, extension twinning operates under the indent. Therefore, one possibility here is that after the activation of basal slip, the Hertz solution will no longer be valid for this studied orientation, and thus the apparent CRSS obtained in Table 5.11 is not quantitatively reliable. On the other hand, for the other two cases, the difference between the normalized RSS values for basal slip and extension twinning are relatively low. For example, looking at Tables 5.6 and 5.7, one might see that the normalized RSS for basal slip and the first extension twin are 0.37, and 0.39, respectively. Therefore, there would be competition between basal slip and extension twinning to operate under the indent. Consequently, the elastic solution from Hertz is relatively more valid for extension twinning operation, and thus, it is expected that the apparent CRSS values obtained in Table 5.11 for these two cases are more quantitatively reasonable.

5.6 Summary

In this chapter, it has been shown that, the indentation behaviour for near c-axis oriented grains of magnesium has been found to be accommodated by a combination of (predominantly) basal slip

and $\{10\bar{1}2\}$ extension twinning. A consequence of the confinement of basal slip into a cylindrical volume below the indenter by extension twins is the formation of a cylindrical low angle boundary under the indent coinciding with the contact area of the indenter on the sample surface. The misorientation associated with this boundary increases as the indentation depth is increased but decreases with depth into the crystal.

The initial deviation of load-displacement data from Hertz's elastic prediction is associated with onset of basal slip and the subsequent discontinuities are due to extension twinning. The appearance of discontinuities in the unloading curves and the 3D-EBSD microstructure observations following indentation suggest that twins retreat during unloading. For the smallest indents all the twins retreat when the load is removed. This offers an explanation for contradictory observations in the literature where post indentation microstructure examination have sometimes shown extensions twins and other results have not.

For the case of indentation perpendicular to the c -axis, it was shown that the favorable location for twin nucleation is underneath the indenter. That is different with the case of indentation parallel to c -axis, in which the extension twins nucleate near the edge of the indenter-material boundary.

CHAPTER 6 The Effect of Tip Radius on the Local Mechanical Properties of Magnesium

6.1 Introduction

In this chapter the indentation size effect will be studied in spherical indentation for commercially pure magnesium. The size effect in plasticity at small length scales was reported for a range of FCC and BCC metals [124,165,166]. Here, we present experimental data on indentation size effect obtained in commercially pure magnesium for indentation approximately parallel to the [0001] direction. First, the results of the indentation load-displacement of five different spherical indenters with tip radii of $R= 1 \mu\text{m}$, $3.69 \mu\text{m}$, $13.3 \mu\text{m}$, $50.0 \mu\text{m}$, and $250.0 \mu\text{m}$ will be presented. Then, the indentation stress-strain curves will be derived from the load-displacement data, the initial yield strength of magnesium will be shown to increase linearly with inverse square root of indentation radius. This enables us to measure the uniaxial yield strength and consequently the critical resolved shear stress (CRSS) of bulk magnesium.

6.2 Load-depth curve

In this study, a grain having an angle of 9.3° between the indentation loading direction and the c-axis was used. A number of indentation tests with two different depths (500nm, and 3500nm) were made on the selected grain. Figure 6.1 presents the results of spherical indentation experiments using a range of spherical indenter tip radii of $R= 1 \mu\text{m}$, $3.69 \mu\text{m}$, $13.3 \mu\text{m}$, $50.0 \mu\text{m}$, and $250.0 \mu\text{m}$. The maximum loads for the five indents are $1.7 \text{ mN} \pm 0.02 \text{ mN}$, $7.1 \text{ mN} \pm 0.1 \text{ mN}$, $13.6 \text{ mN} \pm 0.2 \text{ mN}$, $34.2 \text{ mN} \pm 0.5 \text{ mN}$, and $80.9 \text{ mN} \pm 1 \text{ mN}$, from the smallest indenter ($R= 1 \mu\text{m}$) to the largest one ($250.0 \mu\text{m}$), for indent depth of 500 nm. As can be observed, the maximum load increases with increasing tip radius.

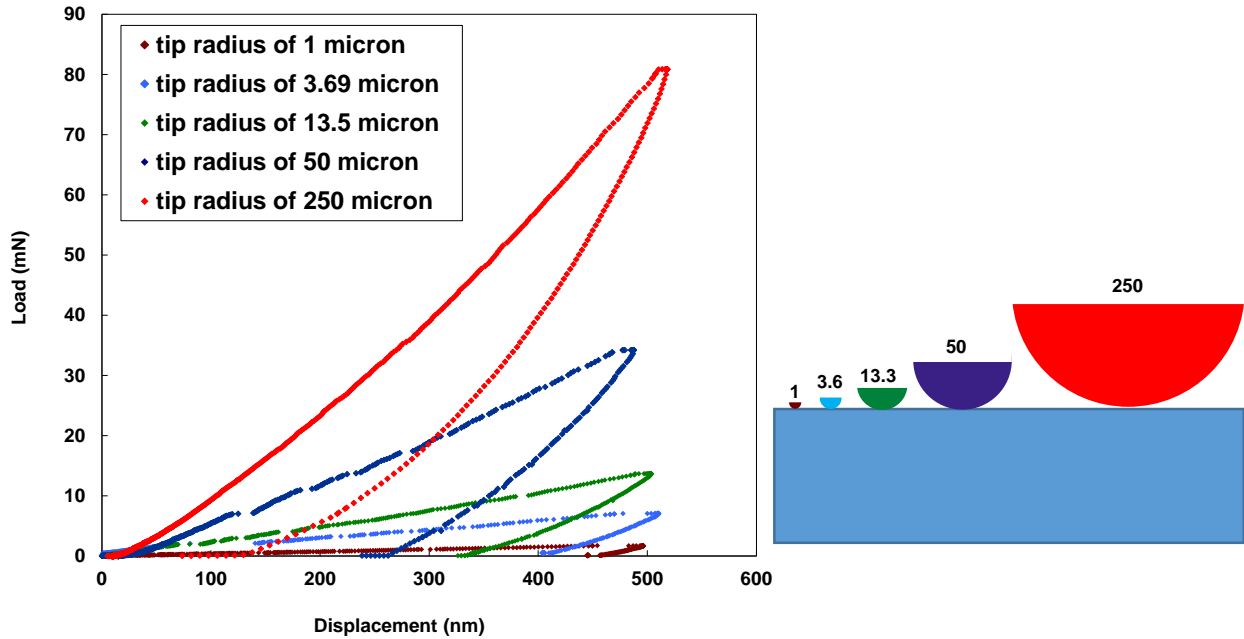


Figure 6.1: Effect of tip radius on the load-displacement curves for commercial purity magnesium, (spherical indentation performed using spherical indenter tip radii of $R= 1 \mu\text{m}$, $3.69 \mu\text{m}$, $13.3 \mu\text{m}$, $50.0 \mu\text{m}$, and $250.0 \mu\text{m}$).

Figure 6.2 shows EBSD inverse pole figure (IPF) maps of the sample surface after indentation and their corresponding $\{0001\}$ pole figures for indentations using a range of spherical indenter tip radii of $R = 1 \mu\text{m}$ to $250.0 \mu\text{m}$. The indentation tests were conducted for 500 nm , and 3500 nm displacements. Figures 6.2a, and 6.2b show the IPF maps obtained after the indentation tests for indent depths of 500 nm and 3500 nm , respectively, using the indenter with a tip radius of $250 \mu\text{m}$. Figure 6.2c shows the corresponding pole figure from these two maps. For these two indents, it can be seen that only one crystal orientation, i.e. the matrix, was found. Looking at the IPF maps of the smaller indenter, i.e. the indenter with a tip radius of $50 \mu\text{m}$, for the case of indentation depth of 500 nm (Figure 6.2d), one might conclude that only one crystal orientation, which is the matrix, was observed after the indentation. However, indentation to a larger depth, i.e. 3500 nm indentation depth, lead to the formation of two variants of extension twins (twin numbers 1 and 2 in the IPF map (Figure 6.2e, and its corresponding pole figure (Figure 6.2f)). Figures 6.2g, and 6.2h, show the IPF maps obtained after indentation using the indenter tip with a radius of $13.3 \mu\text{m}$, for indent depths of 500 nm , and 3500 nm , respectively. Figure 6.2i shows the corresponding pole figure map from these two IPF maps.

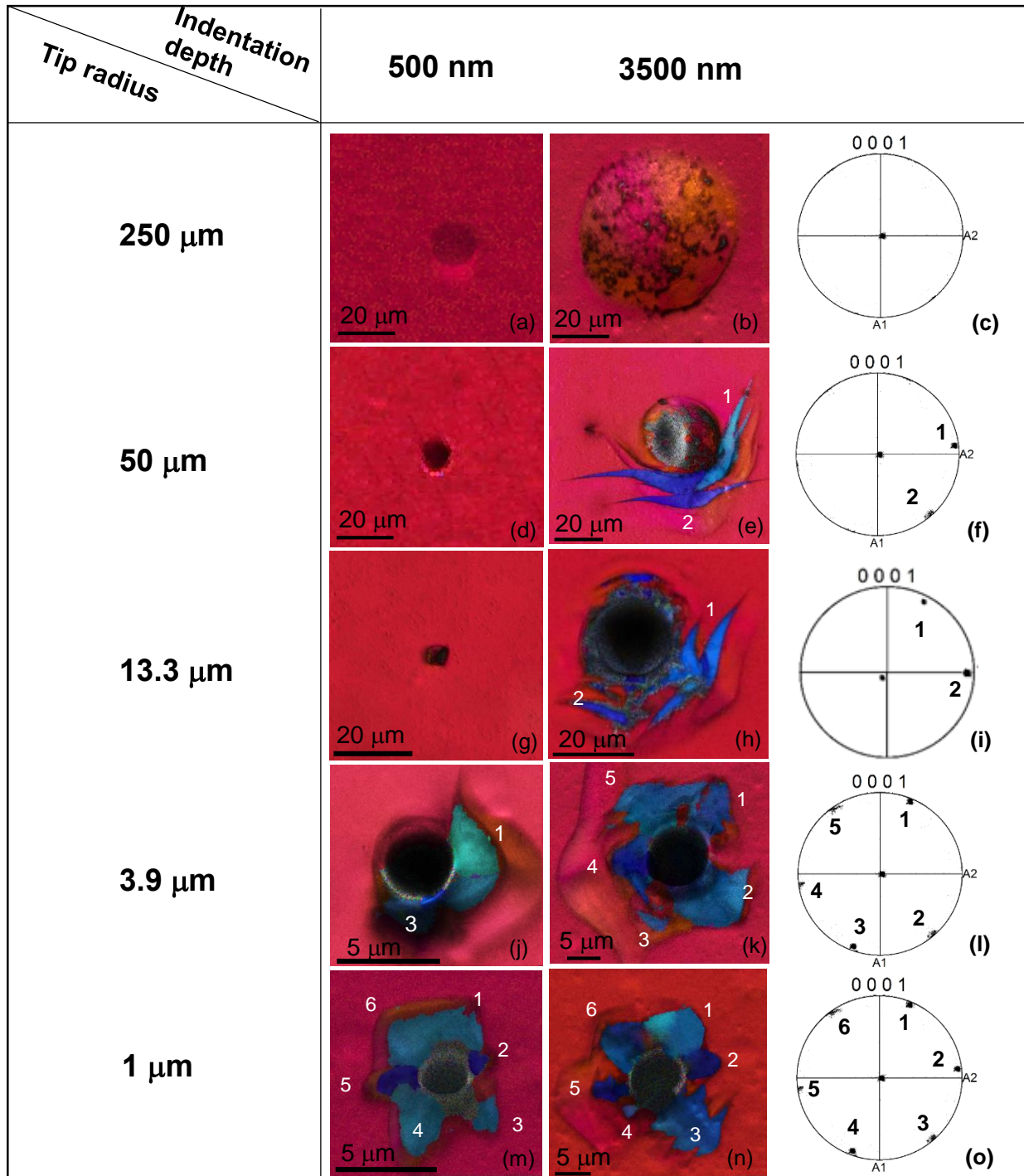
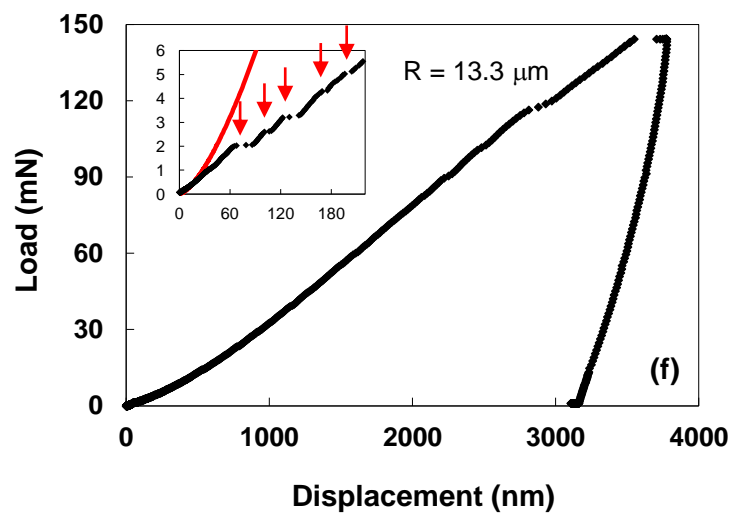
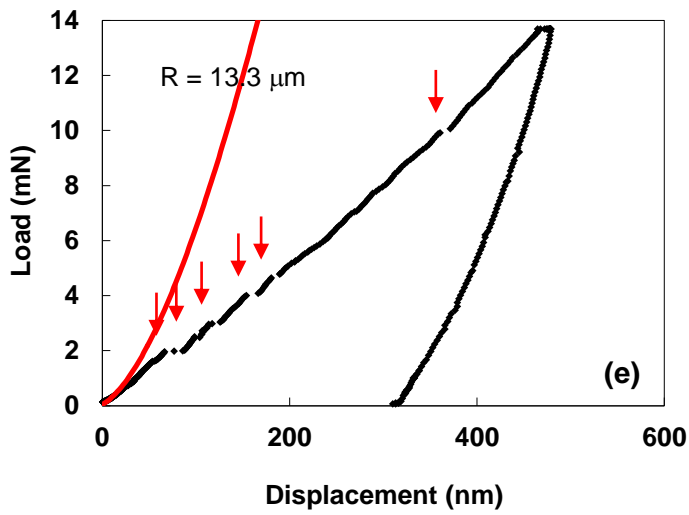
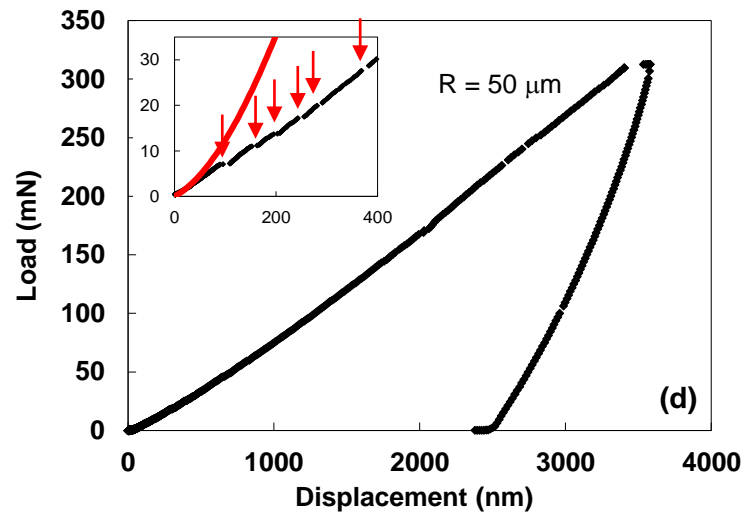
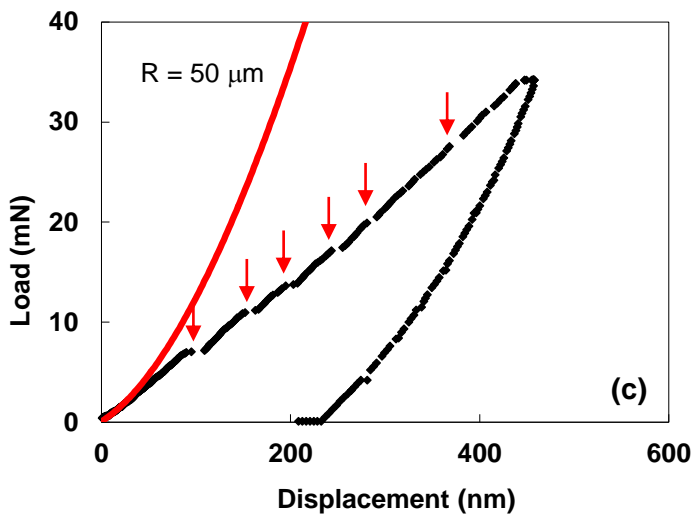
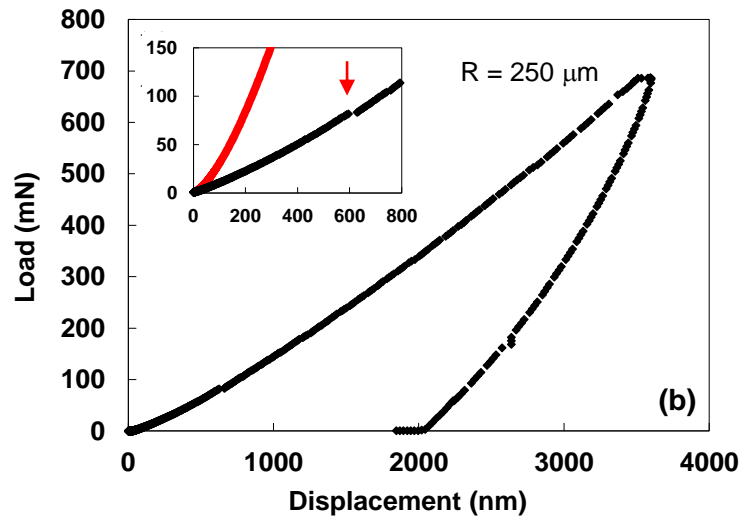
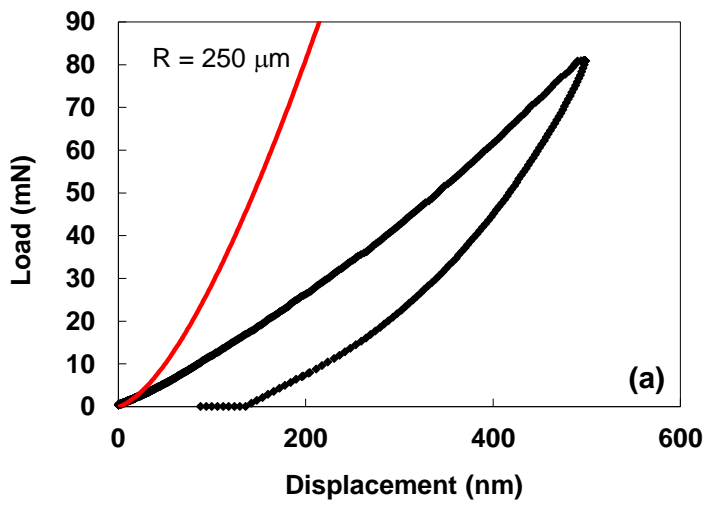


Figure 6.2: Inverse pole figures (IPF) maps and their corresponding $\{0001\}$ pole figure maps after indentation tests using five different indenter tips (a, b, and c) $R= 250 \mu\text{m}$, and (d, e, and f) $R= 50 \mu\text{m}$, (g, h, and i) $R= 13.3 \mu\text{m}$, (j, k, and l) $R= 3.9 \mu\text{m}$, and (m, n, and o) $R= 1 \mu\text{m}$ for two indentation depths; (a, d, g, j, and m) 500 nm indent depth, (b, e, h, k, and n) 3500 nm indent depth.

For the 500 nm indentation depth (Figure 6.2g), there is no evidence of the existence of twins around the indent. However, looking at Figure 6.2h, one can see the existence of two extension twins around the indent. Note: the 3D-EBSD observation illustrated the presence of three extension twin variants under the indent (Appendix 1). Finally, the IPF maps obtained after the indentation using smaller indents, i.e. 3.9 μm tip radius and 1 μm tip radius, illustrate the presence of extension twins even around the 500 nm indent depth. For example, Figures 6.2j show the IPF maps of the indents using the indenter tip with a radius of 3.5 μm , for indent depths of 500 nm. The existence of two twin variants can be observed around the indent (twins number 1 and 3). Looking at the indent with a larger depth, i.e. 3500 nm indent depth (Figure 6.2k), 5 twin variants can be seen. Also, with 1 μm indenter tip, 6 extension twin variants can be observed around the indent for both cases of 500 nm and 3500 nm indent depth, Figures 6.2m and 6.2n, respectively. This illustrates that the presence of deformation twins on the surface after unloading depends not only on indent depth, which was previously illustrated in Chapter 5, but also on the indenter tip size.

Figure 6.3 shows the load-displacement curves for indent depths of 500 nm, and 3500 nm using all five indenters, i.e. within the range of $R=1\ \mu\text{m}$ to 250.0 μm . Also, the prediction from Hertzian contact theory [65] (red line) for comparison, can be seen in these figures. For each curve, a significant deviation from Hertzian occurs at a specific load and displacement. Here, it can be clearly seen that the residual plastic deformation increases by decreasing tip radius. For example, the residual plastic deformations for indenters with tip radii of $R = 1\ \mu\text{m}$, 3.69 μm , 13.3 μm , 50.0 μm , and 250 μm , are 3500 nm, 3444 nm, 3170 nm, 2500 nm, and 2000 nm, respectively, for the case of indent depth of 3500nm. Figures 6.3a, and 6.3b, show the load-displacement curves for indentation depths of 500nm, and 3500nm, respectively, for the case of indentation using an indenter with tip radius of 250 μm . According to Figure 6.3a, no discontinuity was observed during loading. However, looking at Figure 6.3b, one might see the occurrence of one discontinuity during loading. In fact, the enlarged view of the loading segment shows that this discontinuity occurs at a displacement of 650 nm. However, using smaller indenters, i.e. within the range of 50 μm to 1 μm radius, leads to the occurrence of six discontinuities during loading for both indent depths of 500nm, and 3500nm, Figures 6.3c to 6.3j. It should be noted that all six discontinuities occurs prior to 500 nm displacements.



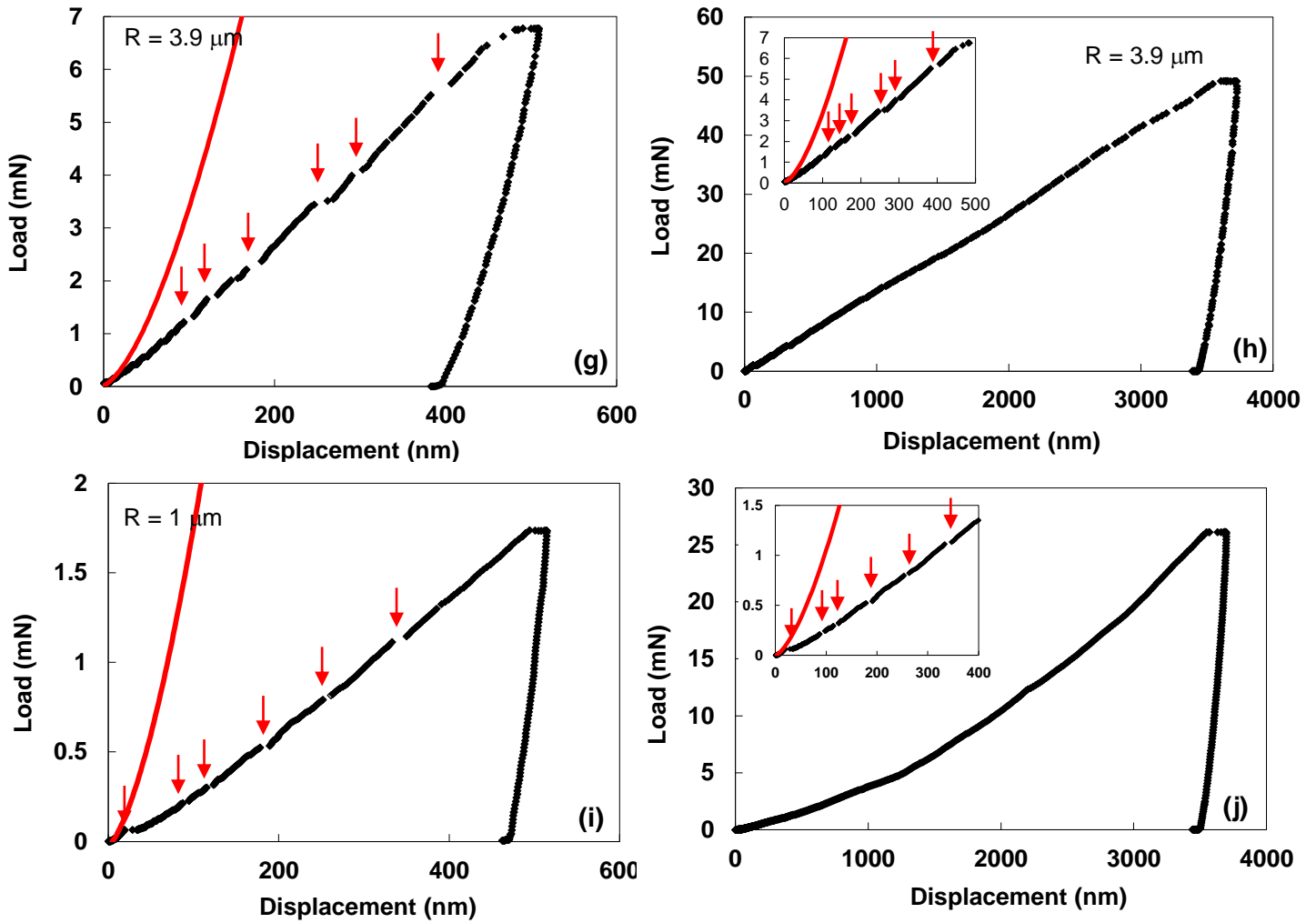
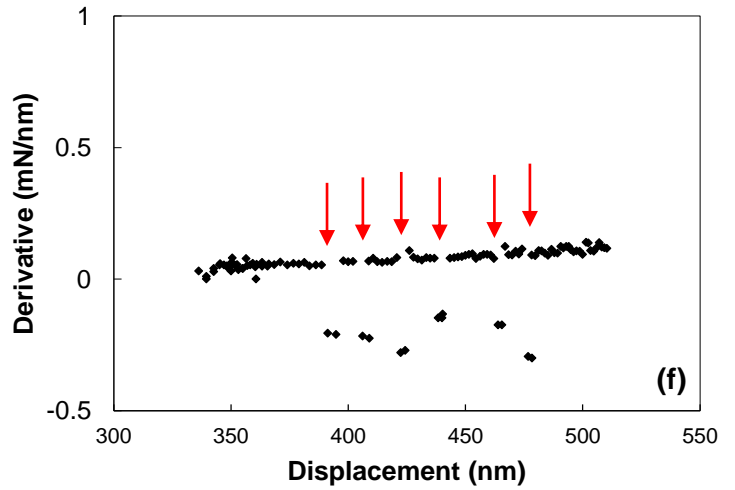
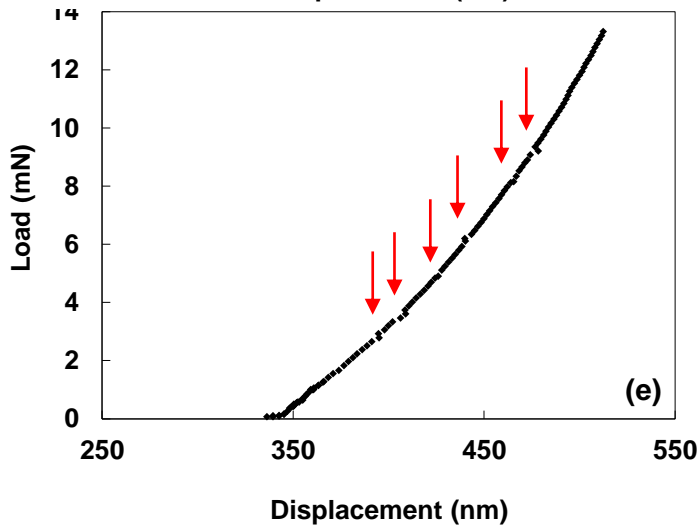
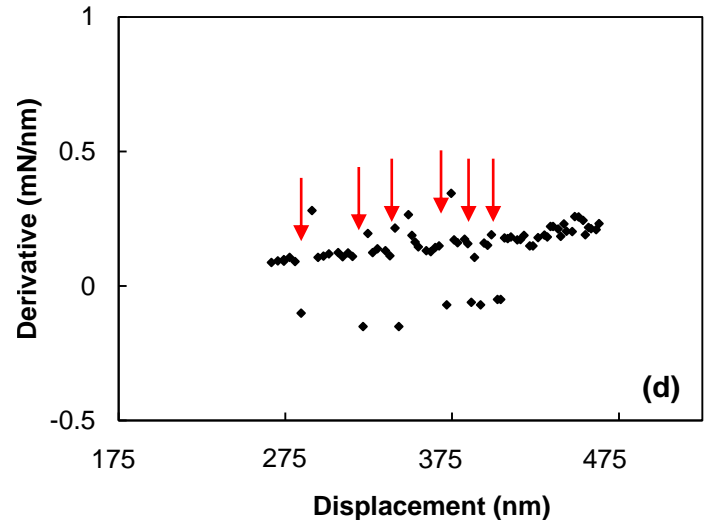
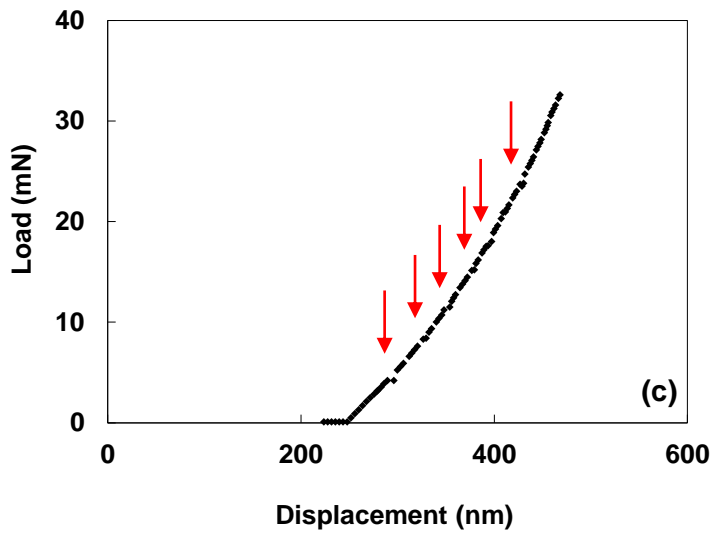
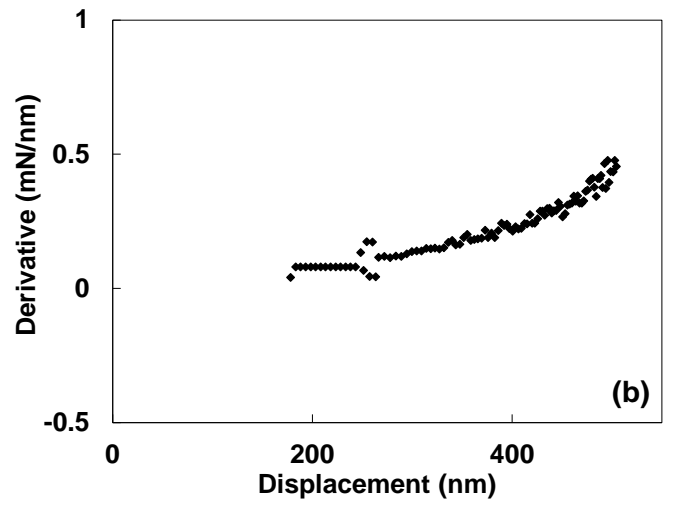
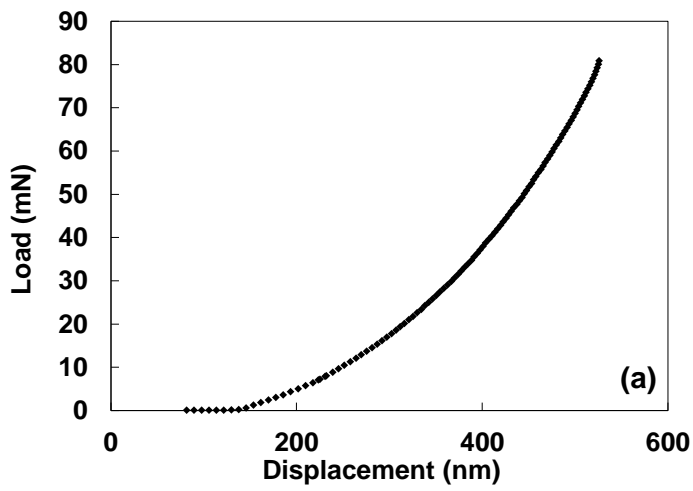


Figure 6.3: Load-displacement curves for commercial purity magnesium using different spherical diamond tips, (a and b) $R = 250 \mu\text{m}$, (c and d) $R = 50 \mu\text{m}$, (e and f) $R = 13.3 \mu\text{m}$, (g and h) $R = 3.6 \mu\text{m}$, and (i and j) $R = 1 \mu\text{m}$, for 500 nm, and 3500 nm displacements.

Figure 6.4 shows enlarged views of the unloading segments of the indentation curves (Figures 6.4.a, 6.4.c, 6.4.e, 6.4.g, and 6.4.i), and their corresponding derivatives (Figures 6.4.b, 6.4.d, 6.4.f, 6.4.h, and 6.4.j) for displacements of 500 nm, using indenters with tip radii of $R = 250 \mu\text{m}$, $50 \mu\text{m}$, $13.3 \mu\text{m}$, $3.5 \mu\text{m}$, and $1 \mu\text{m}$, respectively. Figures 6.4a and 6.4b show the unloading curve and its corresponding derivative, respectively, using the spherical indenter with a tip radius of $250 \mu\text{m}$. In this case, there is no evidence of any detectable discontinuities during unloading. Also, for this case, no discontinuities were observed during loading (Figure 6.3a). If it is assumed that the



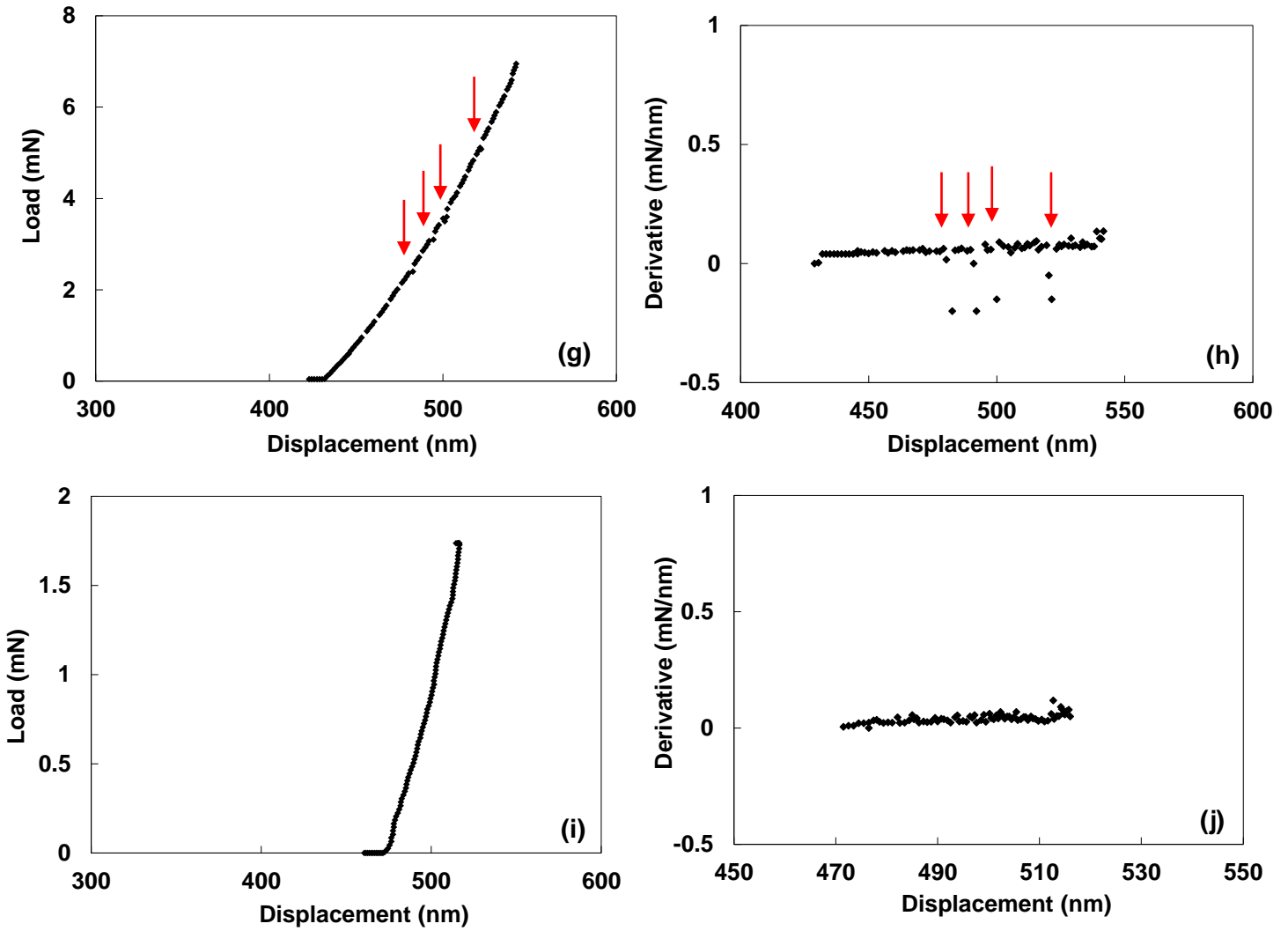


Figure 6.4: Magnified view of unloading curves, and Magnified view of the derivative curves for 500 nm depth using different spherical diamond tips, (a, b) $R = 250\mu\text{m}$, (c, d) $R = 50\mu\text{m}$, (e, f) $R = 13.3\mu\text{m}$, (g, h) $R = 3.6\mu\text{m}$, and (i, j) $R = 1\mu\text{m}$.

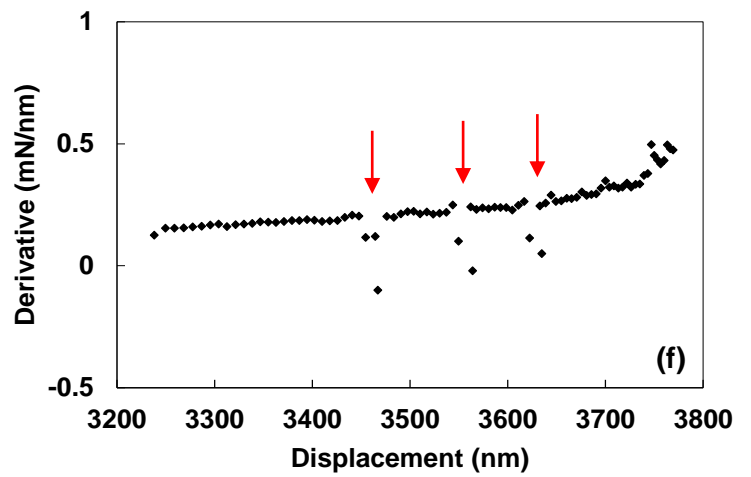
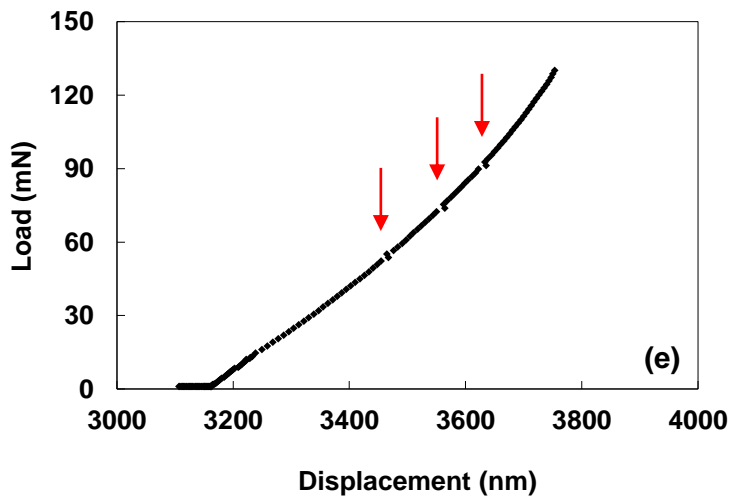
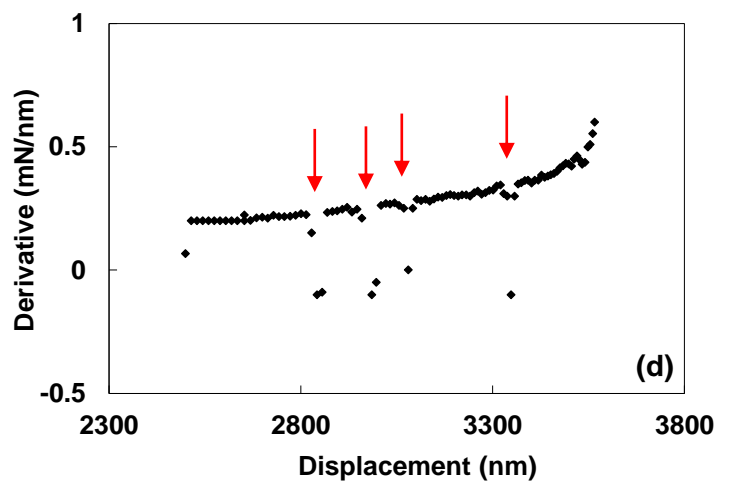
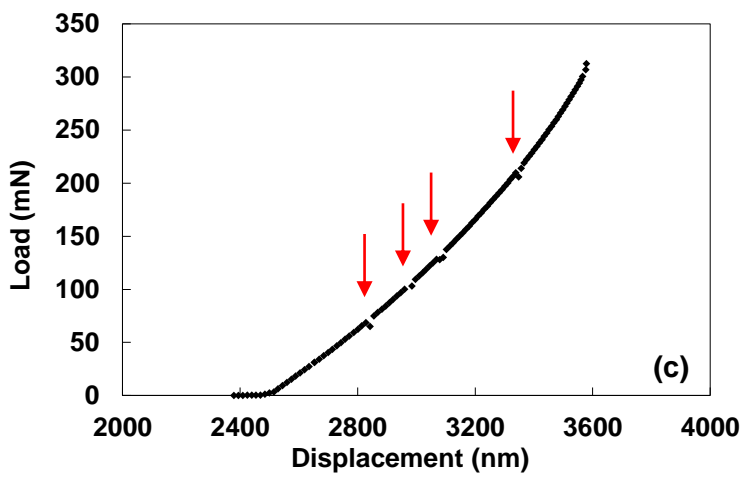
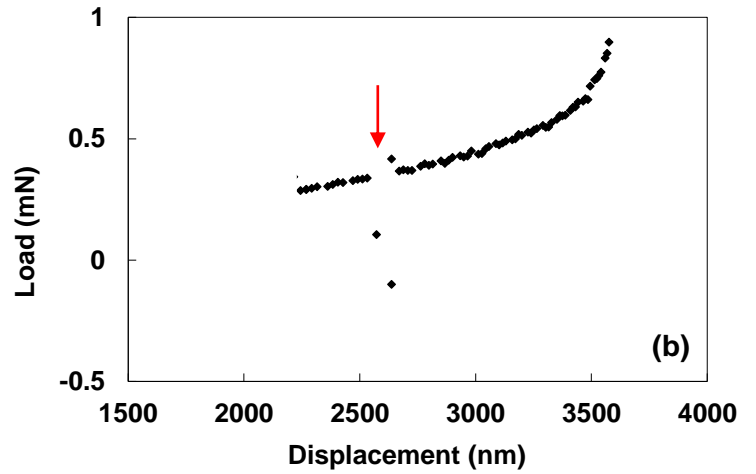
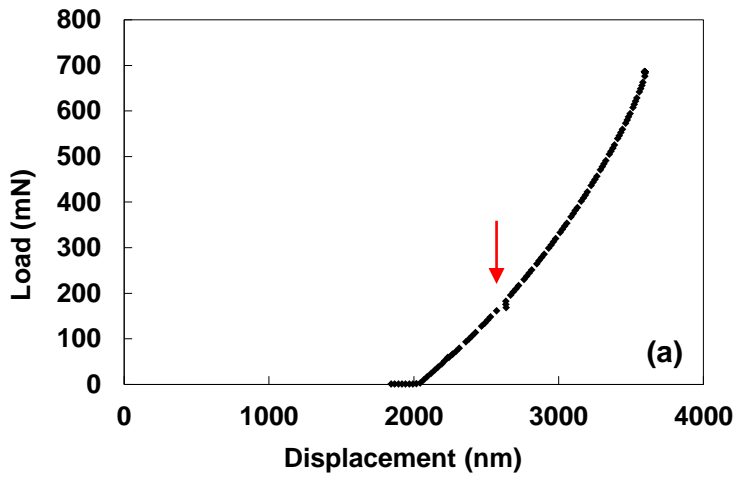
discontinuities during loading correspond to twinning and those occurring during unloading correspond to de-twinning, as was explained in details in Chapter 5, it would suggest that no twinning occurs in this case. This result is consistent with the EBSD observation, i.e. Figure 6.2a.

However, in the case of the smaller indenters, i.e. indenters with radii of $R = 50$ and $13.3\mu\text{m}$, the occurrence of six discontinuities is observed in the unloading segments (Figures 6.4b and 6.4e) and their corresponding derivatives (Figures 6.4d and 6.4f). As explained before, for these two studied cases, the occurrence of six discontinuities were observed during loading, Figure 6.3d and

6.3g. Therefore, it would suggest that six extension twins operate during loading, and all twins retreat during unloading. Consequently, it would be expected that no twins are left around the indents after the unloading. This is consistent with the EBSD observations, Figures 6.2d, and 6.2g. For the indenter with tip radius of 3.5 micron, the occurrence of 4 discontinuities can be observed during unloading (Figures 6.4g and 6.4h). For this indent, during loading six discontinuities were observed (Figure 6.4g), and consequently, two extension twins are expected to remain after unloading. The EBSD observation (Figure 6.2j) confirms this conjecture. Finally, for the case of indentation using the tip with radius of 1 μm , no detectable discontinuities can be observed during unloading in both the unloading segment and its corresponding derivative (Figures 6.4i and 6.4j, respectively). For this indent, there were six discontinuities during loading (Figure 6.3j), and thus this would suggest that all six twins remain after the load is removed. The EBSD observation (Figure 6.2m) shows the existence of six extension twins around the indent.

Figure 6.5 shows an enlarged view of the unloading segment of the indentation curves (Figures 6.5a, 6.5c, 6.5e, 6.5g, and 6.5i), and their corresponding derivatives (Figures 6.5b, 6.5d, 6.5f, 6.5h, and 6.5j) for indent depth of 3500 nm, using all five indenters. Similar to 500 nm indent depth (Figure 6.4), for this studied indentation case, it can also be seen that the number of discontinuities in the unloading curve depends on the indenter tip size.

Tables 6.1 and 6.2 summarize the number of discontinuities that appears during loading and unloading for the cases of indent depth of 500 nm and 3500 nm, respectively. It can be observed that the number of discontinuities in the unloading curves, decreases with decreasing the indenter tip radius. However, for the case of indentation using the tip radius 250 μm , the scenario is different. For this case, the maximum selected indent depth, i.e. 3500 nm, is still not deep enough to operate the extension twins. As can be observed in Figure 6.3j, only one discontinuity occurs during loading for 3500 nm indent depth. Unfortunately, it was not feasible to apply further displacement, due to the upper force limit of the indentation machine.



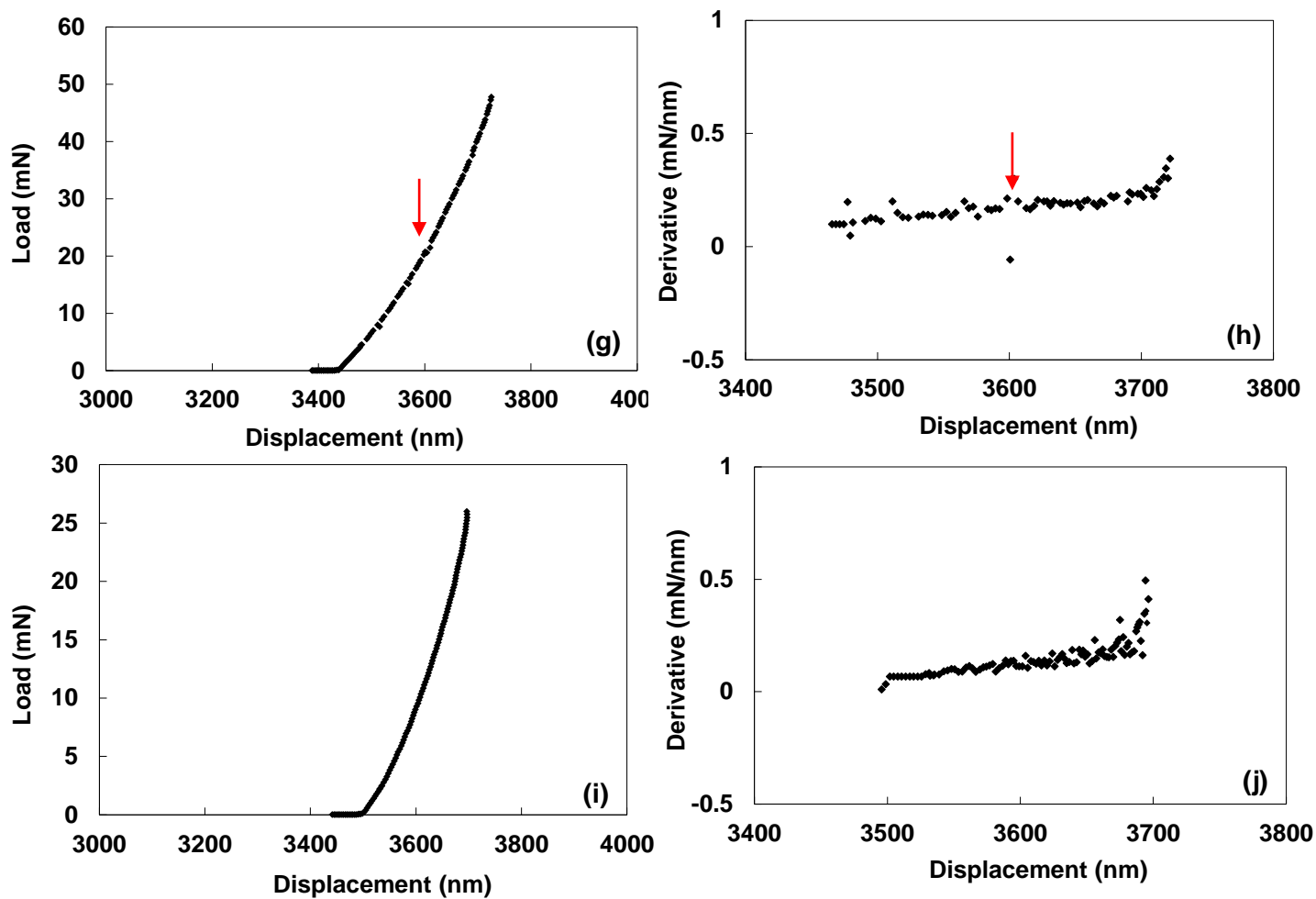


Figure 6.5: Magnified view of unloading curves, and Magnified view of the derivative curves for 3500 nm depth using different spherical diamond tips, (a, b) $R = 250 \mu\text{m}$, (c, d) $R = 50 \mu\text{m}$, (e, f) $R = 13.3 \mu\text{m}$, (g, h) $R = 3.6 \mu\text{m}$, and (i, j) $R = 1 \mu\text{m}$.

Table 6.1: Summary of EBSD and indentation tests results for indent depth of 500 nm

	250 μm	50 μm	13.3 μm	3.5 μm	1 μm
Number of discontinuities during loading	0	6	6	6	6
Number of discontinuities during unloading	0	6	6	4	0
Number of twins expected to be seen around the indent, based on the number of discontinuities during loading and unloading	0	0	0	2	6
Number of twins detected by EBSD observation around the indent	0	0	0	2	6

Table 6.2: Summary of EBSD and indentation tests results for indent depth of 3500 nm

	250 μm	50 μm	13.3 μm	3.5 μm	1 μm
Number of discontinuities during loading	1	6	6	6	6
Number of discontinuities during unloading	1	4	3	1	0
Number of twins expected to be seen around the indent, based on the number of discontinuities during loading and unloading	0	2	3	5	6
Number of twins detected by EBSD observation around the indent	0	2	3 ¹	5	6

Based on the number of discontinuities that occurs during loading and unloading, the number of twins that operates during loading and then retreats during unloading, can be predicted. Table 6.1 and 6.2 show the number of twins expected to be observed around the indent, which is in good agreement with the EBSD observations.

Figure 6.6 shows a graph which summarizes the number of twins left around the indent after the load is removed using four different indenters, i.e. indenters with radii of $R = 50 \mu\text{m}$, $13.3 \mu\text{m}$, $3.6 \mu\text{m}$, and $1 \mu\text{m}$. Three indent depths (500nm, 1500nm, and 3500nm) were also selected (note: the first number in each parenthesis shows the number of discontinuities observed during loading and the second number shows the number of discontinuities occurring during unloading for each test indent). It can be concluded from this graph that by decreasing the tip radius or increasing the indent depth, the number of twins which de-twins would decrease, and consequently the number of twins left after unloading increases. Returning to Section 5.2.4, the Hertz calculation predicted the operation of six extension twins around the indent for the case of indentation on a grain nearly parallel to the c-axis. Also, the load-displacement curves (e.g. Figure 6.2), illustrated the presence of six discontinuities, one for each of the $\{10\bar{1}2\}$ extension twin variants, during the loading. Thus, as mentioned before, six different twin variants of $\{10\bar{1}2\}$ operate during loading. However, depending on the indenter tip size and the indent depth, the number of twins that retreats during unloading changes.

¹ The number of twins for the indenter with tip radii of $13.3 \mu\text{m}$ reported based on the 3D-EBSD observations (Appendix 1).

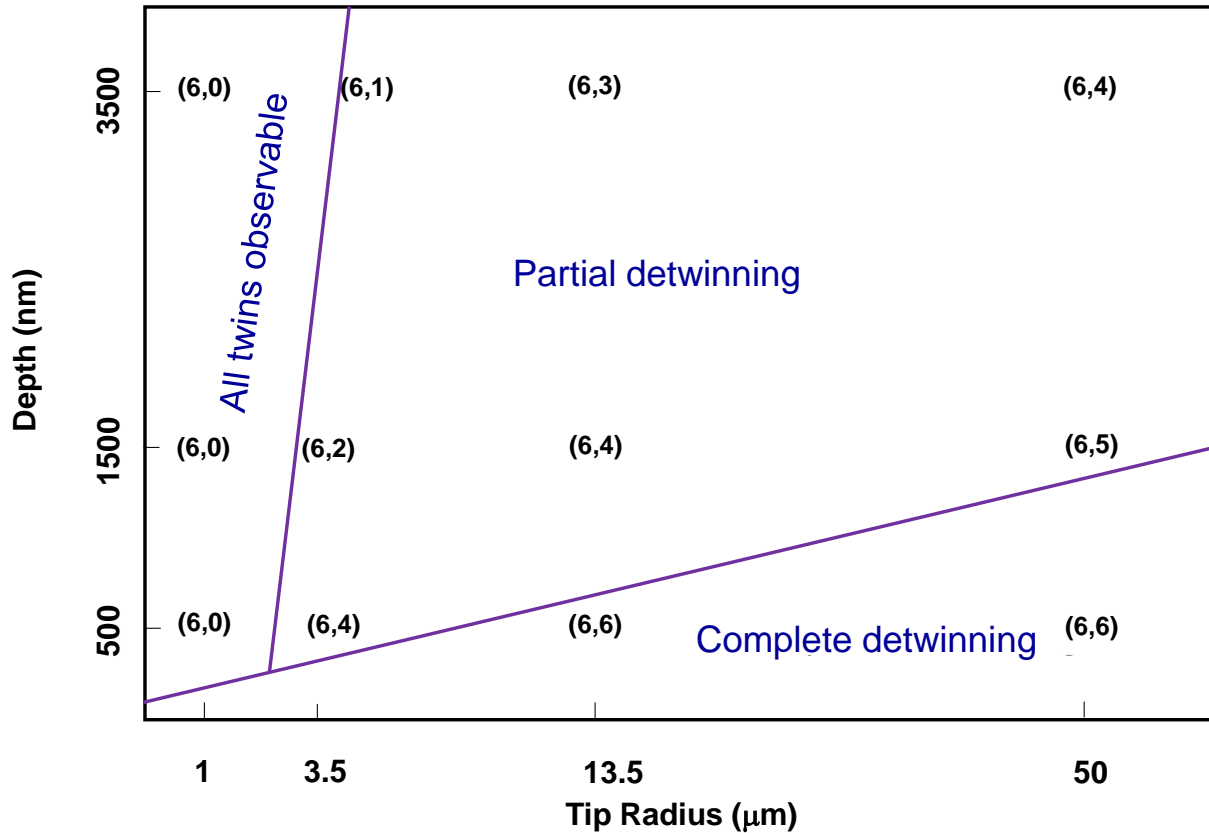


Figure 6.6: Summary of number of twins appearing around the indent for three different indentation depths, (i.e. 500, 1500, and 3500 nm) using four indenters with radii of $R = 50 \mu\text{m}$, $13.3 \mu\text{m}$, $3.5 \mu\text{m}$, and $1 \mu\text{m}$. the first number in each parenthesis shows the number of discontinuities observed during loading and the second number shows the number of discontinuities occurring during unloading for each test indent.

6.3 Indentation stress-strain curve

Figure 6.7 shows the indentation stress-strain curves obtained from the load-displacement data from the spherical indentation tests using the Pathak method [68] for 5 different indenters. The dashed line shows the Hertzian elastic response. The Young's modulus obtained is 45 GPa which is in good agreement with the theoretical values [160]. The 0.1% offset was chosen to define the yield stress in the indentation stress-strain curve. It can be clearly observed that the yield value increased with decreasing the tip size. Table 6.3 summarizes the yield stress obtained for all 5 spherical tests. It should be mentioned that for each tip radius, the test was performed for at least 10 times to check the reproducibility and repeatability.

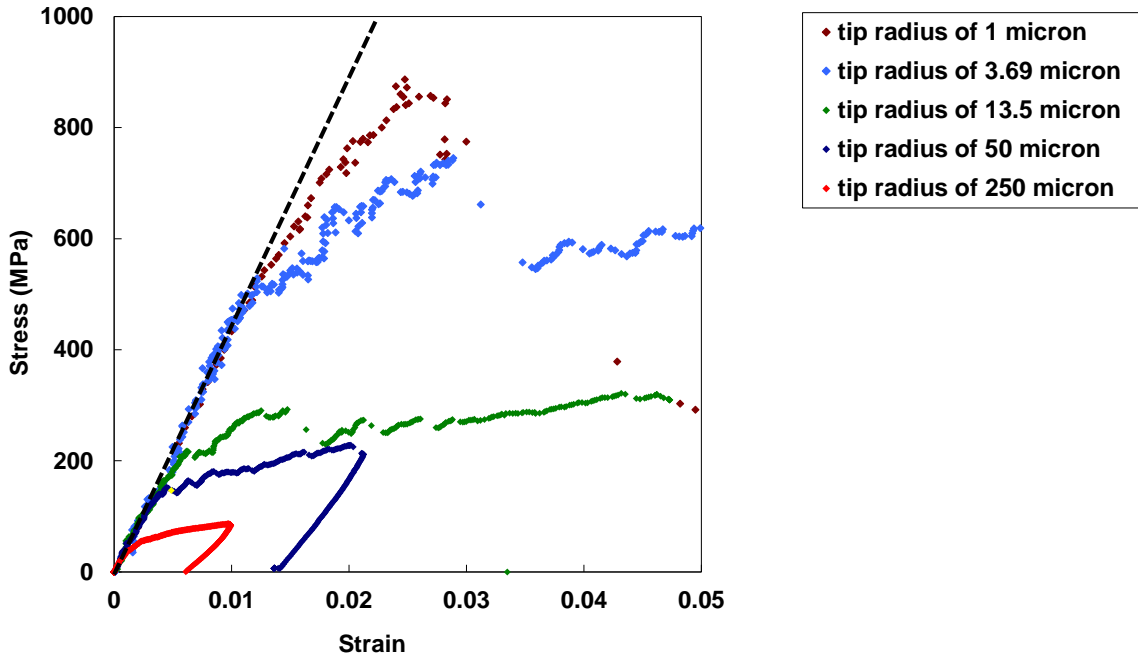


Figure 6.7: Effect of tip radius on the stress-strain curves for commercial purity magnesium, spherical indentation was performed using a range of spherical indenter tip radius of $R= 1, 3.69, 13.3, 50.0,$ and $250.0 \mu\text{m}$.

The normalized resolved shear stress value for this specific crystal orientation was calculated in Chapter 5.1 and is used to estimate the critical resolved shear stress ($\text{RSS}_{0.1\% \text{ offset}}$) for all five studied conditions; Table 6.3 shows the summary of this result. Also, the apparent CRSS values for the extension twinning for all five different conditions were calculated and the result is shown in Table 6.4. It can be seen that the apparent CRSS value decreases noticeably by increasing the tip radius.

Table 6.3: List of normalized RSS, yield stress, and $\text{RSS}_{0.1\% \text{ offset}}$ of the basal slip for five indenters

	Basal slip plane (τ_{RSS}/p_m)	Yield stress (MPa)	$\text{RSS}_{0.1\% \text{ offset}}$ (MPa)
Tip radius of $250.0 \mu\text{m}$	0.37	55 ± 3	21 ± 2
Tip radius of $50.0 \mu\text{m}$	0.37	140 ± 5	52 ± 2
Tip radius of $13.3 \mu\text{m}$	0.37	181 ± 5	69 ± 2
Tip radius of $3.69 \mu\text{m}$	0.37	510 ± 10	193 ± 4
Tip radius of $1.0 \mu\text{m}$	0.37	715 ± 10	250 ± 4

Table 6.4: List of normalized RSS (τ_{RSS}/ρ_m), yield strength, and the apparent CRSS of the extension twin plane for five indenters

	Extension twin plane(τ_{RSS}/ρ_m)	Pop-in stress (MPa)	Apparent CRSS (MPa)
Tip radius of 250.0 μm	0.13	87 ± 2	11 ± 2
Tip radius of 50.0 μm	0.13	168 ± 5	22 ± 2
Tip radius of 13.3 μm	0.13	295 ± 4	39 ± 2
Tip radius of 3.69 μm	0.13	744 ± 10	97 ± 4
Tip radius of 1.0 μm	0.13	853 ± 8	111 ± 4

Figure 6.8 and 6.9 show how the apparent CRSS for basal slip and extension twinning changes with increasing the tip size.

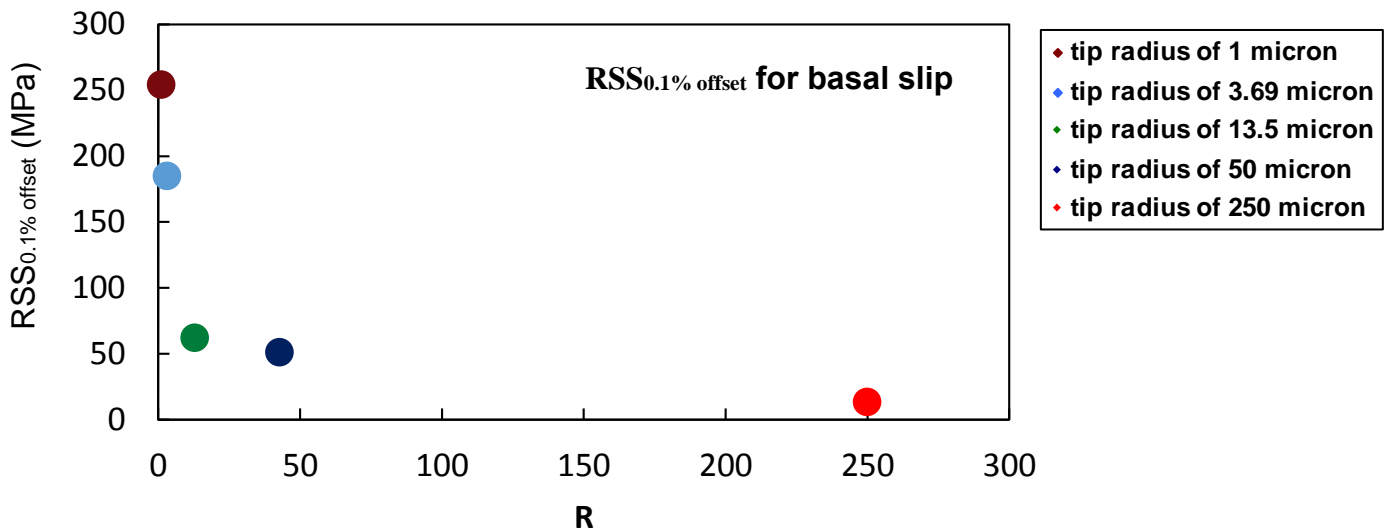


Figure 6.8: Effects of tip radius on the RSS_{0.1% offset} for (a) basal slip for pure magnesium.

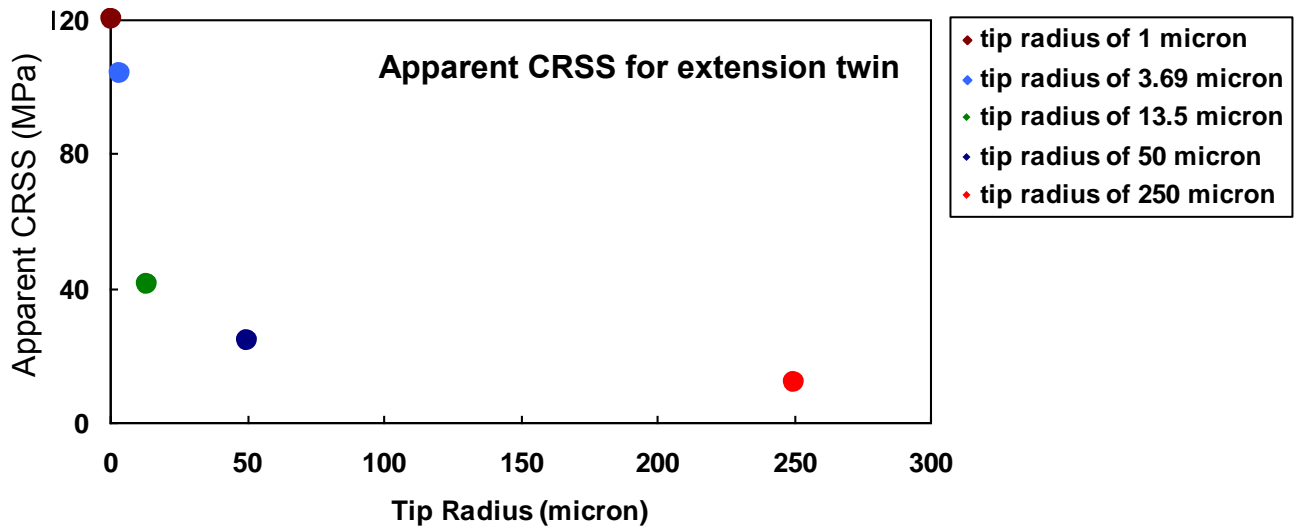


Figure 6.9: Effects of tip radius on the apparent CRSS for extension twin for pure magnesium.

6.4 Discussion

The indentation size effect (ISE) is a widely discussed phenomenon, wherein the hardness of a crystalline material increases with decreasing indentation size [108-112]. This phenomenon becomes more noticeable in the micron or sub-micron depth regime [126,167]. Although the size effect was investigated in plasticity for a range of FCC and BCC metals [124,166,167], there is a one study in literature on magnesium [101]. Recently, Guo [101] has studied the indentation size effect in AZ31 magnesium alloy for indentation perpendicular to the [0001] direction. The apparent CRSS for the initiation of basal slip in AZ31 shows a range of (200 MPa to 450 MPa). Using three different indenters with radii of 5 μm , 10 μm , and 50 μm , it was illustrated that the apparent CRSS decreases by increasing the indenter radius. Guo plotted the apparent CRSS of basal slip in the AZ31 alloy as a function of the indenter radius, and she found a linear relationship between these two variables. Fitting a line through the obtained data points, she predicted that if the indenter radius would extend to greater than 60 μm , the CRSS values decrease to (15-30 MPa). However, a more detailed and systematic study based on the physical concepts is required to have a more rigorous prediction of the CRSS value for an infinitely large diameter indenter.

The physical description of the ISE is associated with the large strain gradients produced beneath the indenter in small indentation leading to geometrically necessary dislocations (GND) [116,117-121,126]. Ashby [168] showed that the density of these GNDs can be expressed as:

$$\rho^G = \frac{1}{b} \frac{\partial \gamma}{\partial x_1} \quad (6.1)$$

where b is the Burgers vector, and $\partial\gamma/\partial x$ is the gradient of the shear strain. The density is large if the gradient is steep. It has also been shown by Ashby that the lattice is rotated by a gradient of simple shear and the misorientation gradient, given by $\partial\theta/\partial x$ can be measured by using Equation (6.2).

$$\rho^G = \frac{1}{b} \frac{\partial \theta}{\partial x} \quad (6.2)$$

On the other hand, it was illustrated that the yield strength of a material increases with its dislocation density based on the following equation [169]:

$$\sigma = \sigma_0 + \frac{\alpha M \mu b}{L} \quad (6.3)$$

where σ_0 is the friction stress, the, α is the material constant, M the Taylor factor, μ the shear modulus, L is the spacing between the dislocations, and σ is the yield strength. Also, L is a function of dislocation density and can be expressed as $L = \rho^{-1/2}$ [169]. By combining equations 6.2 and 6.3, it can be concluded that the yield strength of a material can be varied as a function of the square root of the misorientation gradient under the indent, and is expressed as,

$$\sigma = \sigma_0 + \alpha M \mu b^{1/2} \sqrt{\frac{d\theta}{dx}} \quad (6.4)$$

Returning to Figure 5.13a, one can see the maximum amplitude of the misorientation as a function of normalized indenter depth (h/a). An arbitrary maximum misorientation was chosen, which was 8.9° . The corresponding normalized indenter depth (h/a) for this specific misorientation

angle is 0.145. Figure 6.10 shows the misorientation profile under the indent for 1500 nm indent depth for the case of $z/a = 0.75$ in which 8.9° maximum misorientation can be obtained. It can be concluded that the slope of the misorientation profile ($d\theta/dx$) can be calculated by dividing the maximum misorientation (θ_{\max}), which is 8.9° in this case, over half of the contact radius ($a/2$). Following this approach, the misorientation gradient ($d\theta/dx$) was derived for all five indenters, and is shown in Table 6.5.

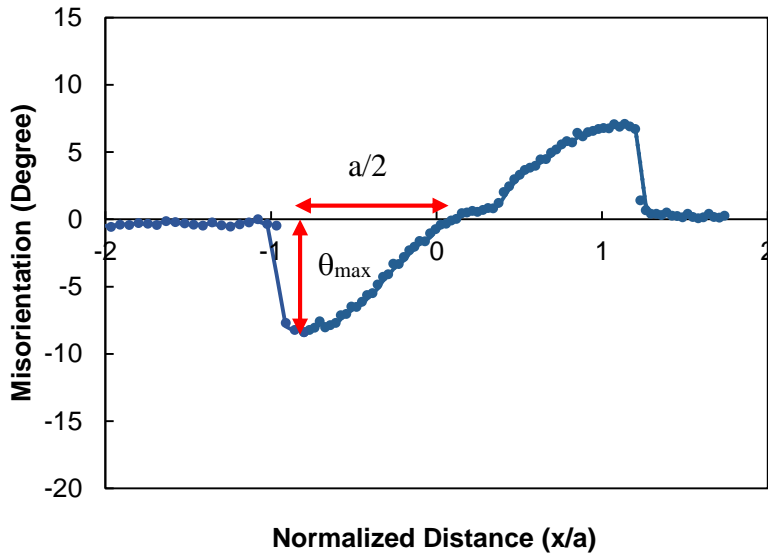


Figure 6.10: The misorientation profile under the indent for 1500 nm indentation depth. The slope of the misorientation profile can be obtained by dividing θ_{\max} over half of the contact radius ($a/2$).

Table: 6.5: The misorientation gradient ($d\theta/dx$) for all five indenters

Radius (μm)	1	3	13.3	50	250
$d\theta/dx$	68.9	22.9	5.1	1.4	0.27

Finally, the $\text{RSS}_{0.1\% \text{ offset}}$ (from Table 6.3), is plotted as a function of the square root of the misorientation gradient, Figure 6.11. It can be observed that a linear regression $ax + b$ can be used to fit the data. Vertical error bars represent the standard deviation measured in the $\text{RSS}_{0.1\% \text{ offset}}$ results. If the line is extrapolated to the ordinate, the y-intercept, i.e. b , would correspond to the CRSS of a zero misorientation gradient. This is consistent with the case of the absence of the size

effect/geometrically necessary dislocations. Using the least-square fit method, the optimum values of a and b were obtained as follow: $a = 33.01 \pm 0.79$ and $b = 1.72 \pm 3.42$. The standard errors for the slope and y-intercept are obtained using the fitting algorithms available in the Gnuplot software [170]. Therefore, the measurement of the CRSS for basal slip from instrumented indentation lies between 0 and 5.1 MPa (i.e. for one standard deviation). This compares to results in the literature from tests on single crystals which estimate the CRSS to be 0.5-0.8 MPa [7,14].

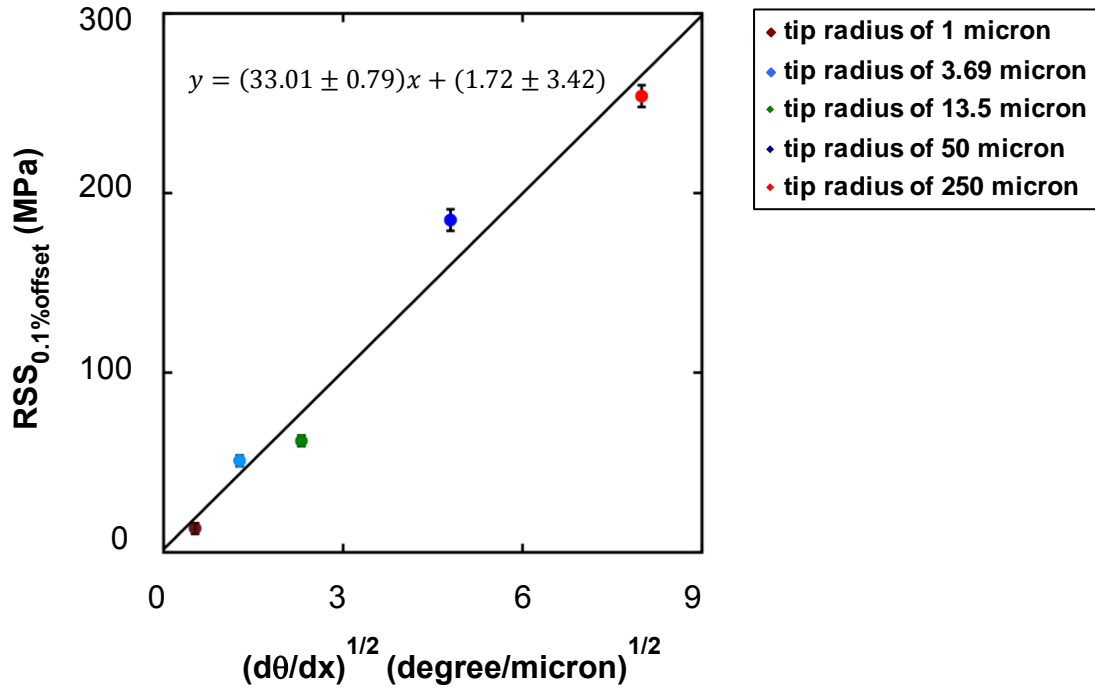


Figure 6.11: The $RSS_{0.1\% \text{ offset}}$ as a function of square root of misorientation gradient. A linear regression was used to fit to the data.

However, it can also be shown that $d\theta/dx$ can be expressed as a function $1/R$. Based on Figure 6.10, it can be observed:

$$\frac{d\theta}{dx} = \frac{\theta_{\max}}{a} \quad (6.5)$$

Where, θ_{\max} can be related to h/a according to Figure 5.13, i.e. $\theta_{\max} = Kh/a$, where K is a constant. Thus, $d\theta/dx$ can be expressed as follows:

$$\frac{d\theta}{dx} = K \frac{h/a}{a} = K \frac{h}{a^2} = K \frac{h}{2Rh} = \frac{K'}{R} \quad (6.6)$$

where $K' = K / 2$. Combining Equation 6.4 with Equation 6.6, it can be concluded that the σ_{CRSS} can be expressed as a function of $1/R$:

$$\sigma = \sigma_0 + \alpha M \mu b^{1/2} \sqrt{\frac{K'}{R}} \quad (6.7)$$

Figure 6.12 shows the $RSS_{0.1\% \text{ offset}}$ (from Table 6.3) as a function of the inverse square root of the indenter radius. Vertical error bars represent the standard deviation measured in the $RSS_{0.1\% \text{ offset}}$ results. Here, the optimum parameters obtained from the least-square fitting are $a = 274.18 \pm 6.56$ and $b = 1.72 \pm 3.42$. This result is consistent with results shown in Figure 6.11.

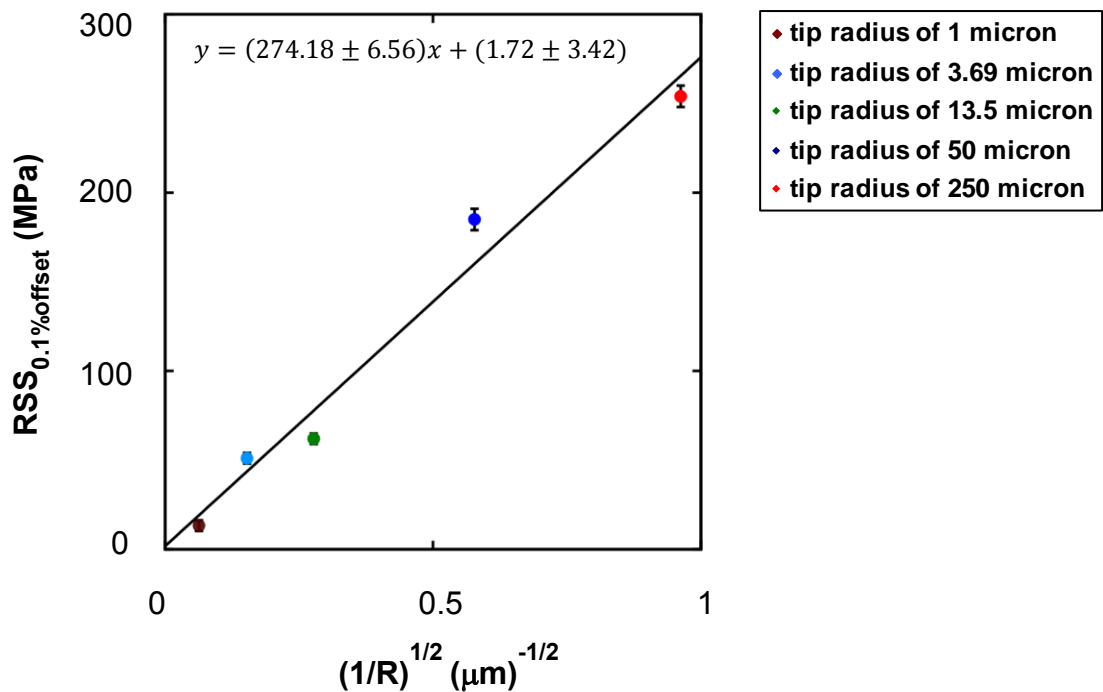


Figure 6.12: The $RSS_{0.1\% \text{ offset}}$ as a function of inverse square root of indenter radius. A linear regression was used to fit to the data.

6.5 Conclusion

This chapter shows spherical indentation was successfully used for a systematic study on ISE on pure Mg. The previous research on ISE of Mg [101] showed the trend of changes of $RSS_{0.1\% \text{ offset}}$ with the indenter size. However, the results presented in this chapter show that using spherical indentation with different indenter radii, enables us to have a reasonable prediction of CRSS for basal slip for the case of using infinitely large indenters.

CHAPTER 7 The Effect of Composition on the Local Mechanical Properties of Commercially Pure Magnesium

7.1 Introduction

This chapter addresses the effect of alloying additions on the local mechanical properties of commercially pure Mg using the instrumented indentation technique. In order to pursue this study, spherical indentation tests were conducted on AZ31B (Mg-2.5 wt% Al-0.7 wt%Zn-0.2 wt.% Mn), and AZ80 (Mg-8 wt% Al-0.5 wt%Zn-0.2 wt.% Mn) alloys approximately parallel to the [0001] direction. The tests were performed using an indenter with a tip radius of 13.3 micron. First, the indentation load-displacement data will be presented for all three investigated materials. Then, the indentation stress-strain curves will be derived from the load-displacement data. Finally, it will be concluded that increasing the aluminum levels results in an increase in yield strength in commercially pure magnesium. Using the simple model from the previous Chapter, the basal slip CRSS value for an infinitely large diameter indenter will be calculated. Also, higher aluminum content results in a decrease in the detwinning phenomenon. It will be shown that detwinning is less significant in AZ magnesium alloys compared to commercially pure magnesium.

7.2 Load-depth curves

In this study, grains having an angle in a range of 9° to 11° between the indentation loading direction and the c-axis in pure Mg, AZ31B (Mg-2.5 wt% Al-0.7 wt%Zn-0.2 wt.% Mn), and AZ80 (Mg-8 wt% Al-0.5 wt%Zn-0.2 wt.% Mn) alloys were selected. A number of indentation tests with three different depths (500nm, 1500nm, and 3500nm) were conducted on the selected grains. Figure 7.1 presents the results of spherical indentation experiments on the three investigated materials for indent depth of 500nm. As can be observed, the maximum load increases with increasing aluminum content, i.e. the maximum load for pure Mg, AZ31B, and AZ80 alloys are 13.6 mN, 18.5 mN, and 26 mN, respectively. Also, the prediction from Hertzian contact theory [65] (black line) for comparison, i.e. equation (2.5), can be seen in these figures. For each curve, a significant deviation from Hertzian behaviour occurs at a specific load and displacement. For all three curves, the occurrence of six discontinuities during loading can be seen.

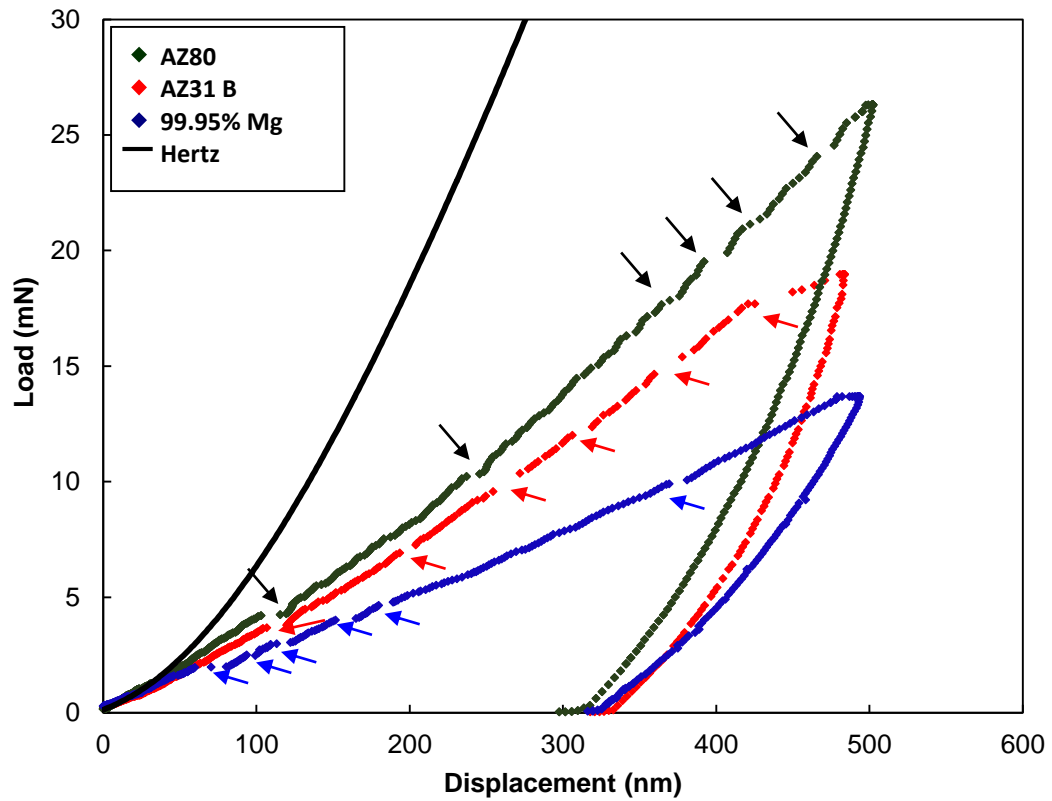


Figure 7.1: Effect of composition on the load-displacement curves for commercial purity magnesium.

According to Chapter 5, these discontinuities are related to extension twinning.

Figure 7.2a shows the load-displacement data for all three investigated materials at indent depth of 3500 nm. Figure 7.2 also shows the enlarged views of the unloading segments of the indentation curves (Figures 7.2.b and 7.2d) and their corresponding derivatives (Figures 7.2c and 7.2e) for AZ31B, and AZ80 alloys. For these two alloys, there is no evidence of detectable discontinuities during unloading. If it is accepted that the occurrence of the discontinuities during unloading correspond to de-twinning as explained in Chapter 5, it would suggest that no or very little detwinning should be observed after unloading for the case of AZ31B, and AZ80 alloys.

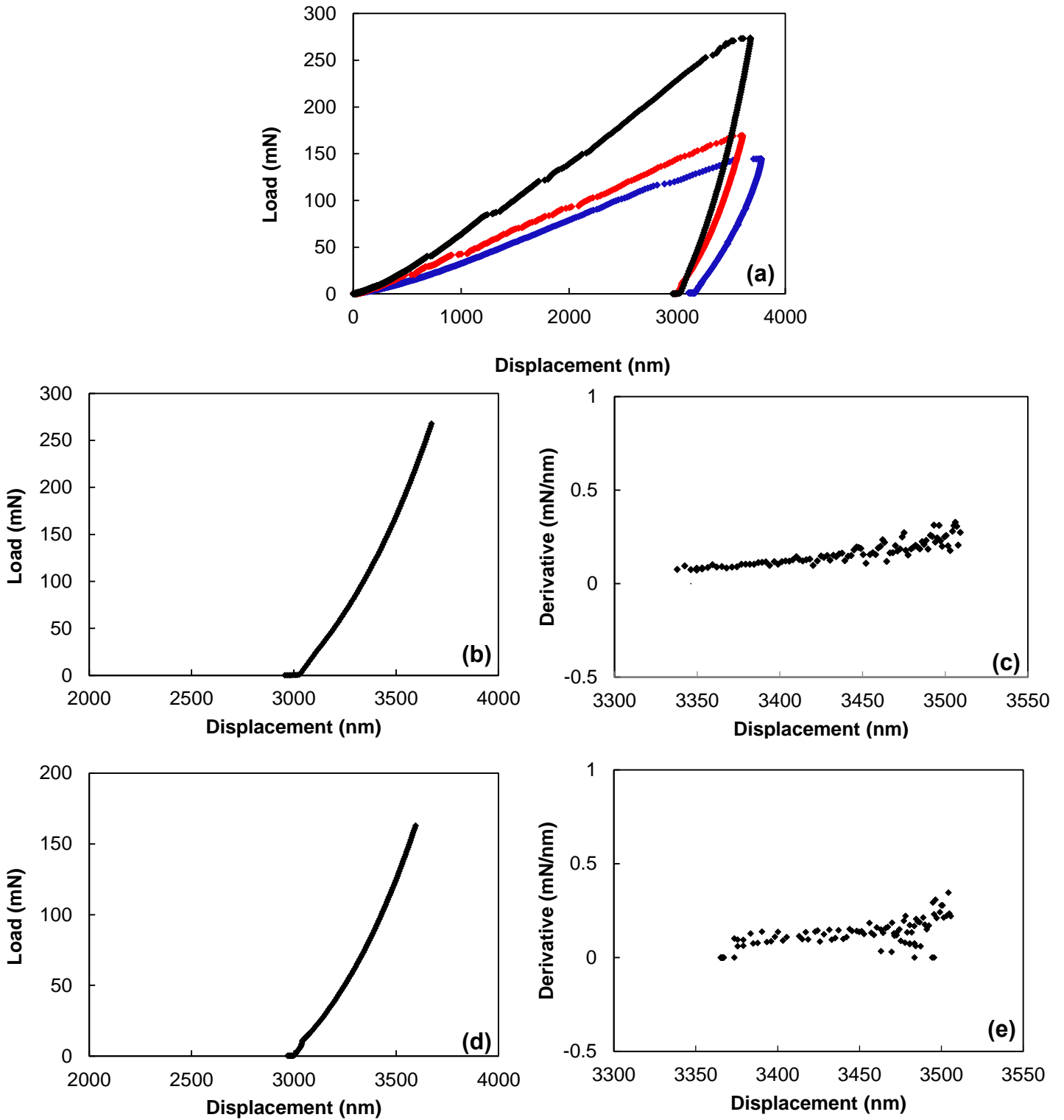


Figure 7.2: (a) Indentation load-depth curve for pure Mg, AZ31B, and AZ80 alloys for 3500 nm displacement, and magnified view of unloading curves, and Magnified view of the derivative curves for (b and c) AZ31B, and (d and e) AZ80 alloys.

Figure 7.3 shows the image quality and EBSD inverse pole figure (IPF) maps of the sample surface after indentation and their corresponding $\{0001\}$ pole figures for indentation on AZ80 alloy. The indentation tests were conducted for 3500 nm displacements. The residual impression from the indent (i.e. black circles) are indicated by white arrows on the EBSD maps. These are regions where the orientation could not be easily indexed with the EBSD software. In this case, six different areas of large misorientation can be observed. The pole figure (Figure 7.3c) confirms that this would be consistent with six variants of $\{10\bar{1}2\}$ extension twins. This result is in good agreement with the results from the indentation tests, which showed the occurrence of six discontinuities during loading and none during unloading (Figures 7.1 and 7.2). Therefore, 6 extension twins occur during loading and all of them remain after the unloading. Li and Enoki [171] claimed that in the AZ31 alloy, detwinning occurrence was not observed compared with pure magnesium in which this phenomenon was detected. The result of the current work also suggests that detwinning occurs more in commercially pure Mg in comparison with the AZ magnesium alloy.

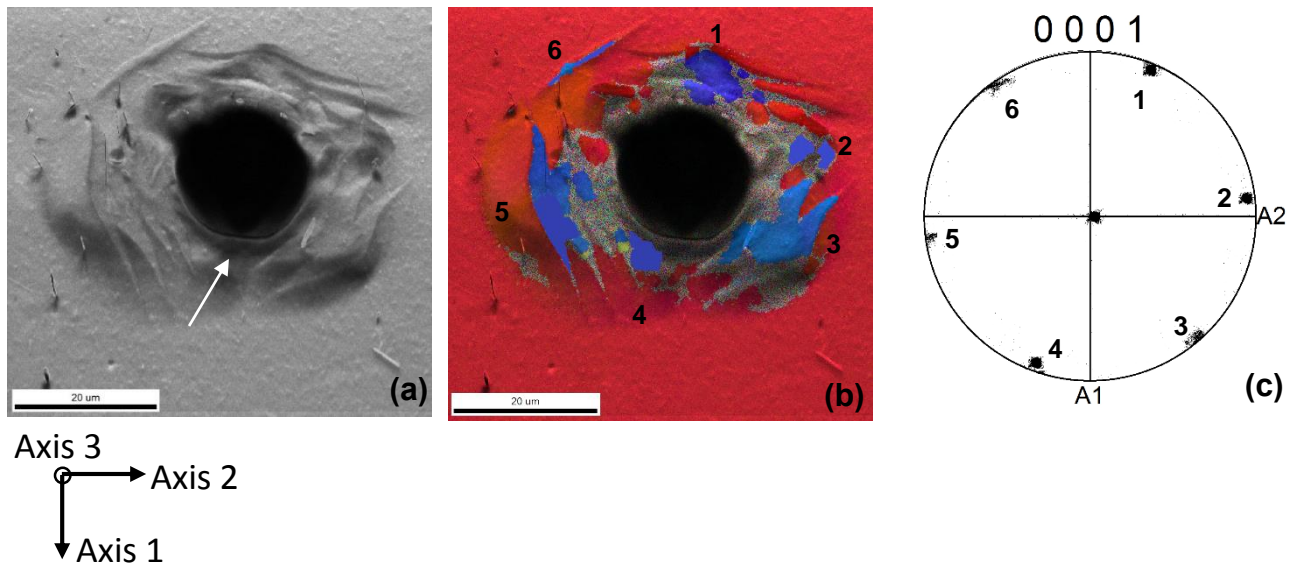


Figure 7.3: (a) SEM image, (b) inverse pole figures (IPF) map and (c) its corresponding $\{0001\}$ pole figure map after indentation tests on AZ80 alloy. The indent depth is 3500 nm, and the indenter diameter is 13.3 μm . Six variants of $\{10\bar{1}2\}$ extension twins can be observed around the indent. Note, the sample reference direction for A1 is close to $[\bar{1}2\bar{1}0]$, A2 is close to $[10\bar{1}0]$, and A3 is perpendicular to the surface (parallel to indentation direction).

7.3 Stress-strain curve

Figure 7.4 shows the indentation stress-strain curves obtained from the load-displacement data from the spherical indentation test using the Pathak method [68] on commercially pure Mg, AZ31B, and AZ80 alloys. The Young's Modulus obtained is 46 GPa which is in good agreement with the theoretical values [160]. The 0.1% offset was chosen to define the yield stress in the indentation stress-strain curve. It can be clearly observed that the yield value increased by increasing the aluminum content. Table 7.1 summarizes the yield stress and consequently the $RSS_{0.1\% \text{ offset}}$ obtained for all three studied materials. Note: The normalized resolved shear stress value for this specific crystal orientation was calculated in chapter 5.1 and is used here to estimate the critical resolved shear stress (CRSS).

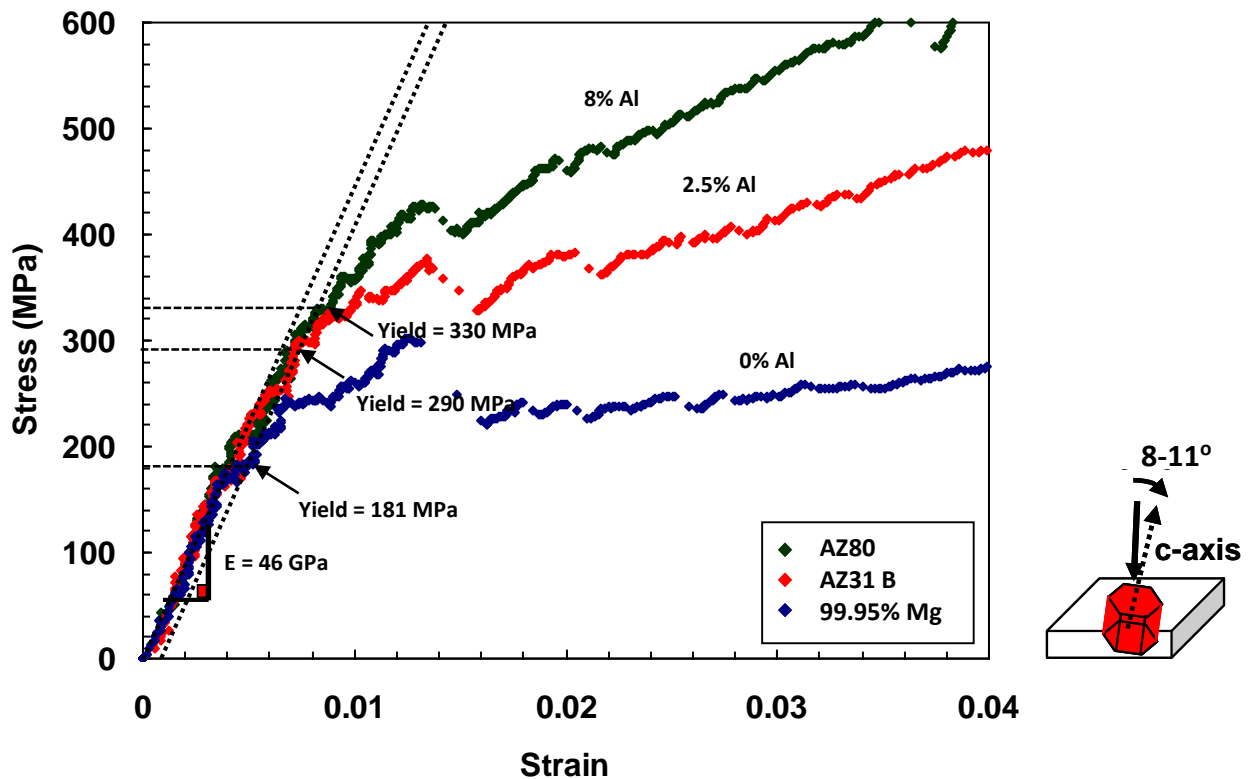


Figure 7.4: Effect of aluminum additions on the stress-strain curves for commercial purity magnesium alloys.

Table 7.1: List of normalized RSS (τ_{RSS}/ρ_m), yield strength, and the $RSS_{0.1\% \text{ offset}}$ for the basal slip using 13.3 micron indent

	Basal slip plane (τ_{RSS}/ρ_m)	Yield stress (MPa)	$RSS_{0.1\% \text{ offset}}$ (MPa)
Commercially pure Mg	0.38	181 ± 5	69 ± 2
AZ31B	0.38	290 ± 5	110 ± 2
AZ80	0.38	330 ± 5	125 ± 2

7.4 Discussion

Solid solution strengthening is one of the strengthening mechanisms in polycrystalline materials. The relationship between shear stress and the alloying concentration is expressed as $\tau_{ss}=kc^n$, where k, and n are constants, and c is the alloying concentration [172,173]. Based on previous models, n value could be 1/2, 2/3, or 1 [139-140]. Aktar and Teghtsoonian studied the effects of Zn [14] and Al [174] additions on the CRSS of basal slip and prismatic slip of Mg using conventional tensile tests. They showed that the CRSS of basal slip in a single crystal of magnesium increases linearly with $c^{1/2}$, where c is the concentration of alloying elements. Later Caceres et al [139] investigated the solid solution strengthening on Mg-Al alloy. They have shown that for Mg-Al alloys, with Al contents ranging from 1 to 8 wt%, the hardness increases linearly with c^n , where $n = 1/2$. They proposed that the solid solution strengthening in polycrystals of Mg-Al alloys is controlled by basal slip.

In order to compare our experimental results with the previous work on aluminum-containing magnesium alloys [174], n value was selected to be 1/2 in this work. The $RSS_{0.1\% \text{ offset}}$ values obtained for AZ31B, and AZ80 alloys in this study (Table 7.1) are higher than what would be expected for magnesium based on the literature [46]. As explained in Chapter 6, the high values of $RSS_{0.1\% \text{ offset}}$ is due to the indentation size effect. In Chapter 6, it was shown how it would be feasible to predict the CRSS values for basal slip activation of bulk magnesium with a high degree

of accuracy. By combining equation 6.2 and 6.3, it can be shown that the $RSS_{0.1\% \text{ offset}}$ can be expressed as a function of the square root of the misorientation gradient (equation 7.1),

$$\sigma = \sigma_0 + C \sqrt{\frac{d\theta}{dx}} \quad (7.1)$$

where C is $\alpha M \mu b^{1/2}$. Based on Figure 6.11, C equals 33.

Having the value of C from the high purity magnesium case and assuming that the misorientation gradient is only geometrically driven, one can calculate the σ_0 for the case of AZ31B, and AZ80 alloys from equation 7.1. According to this equation, for indentation using a tip with radius of 13.3 micron, σ_0 of AZ31B, and AZ80 are 33 MPa and 45 MPa, respectively. Table 7.2 summarizes the CRSS values obtained for commercially pure Mg, AZ31B, and AZ80 alloys. Jain [46] utilized the crystal plasticity simulations to interpret slip and twinning activity based on a systematic set of deformation experiments on AZ80 and AZ31B (note: he used the experimental results for AZ31B from Agnew's work [175]). For each slip or twin system, the Voce hardening law (Equation 4.13) was used in the crystal plasticity model. With careful use of experimental results, he was able to back calculate the CRSS for each slip and twinning systems. He found that using a CRSS for basal slip in AZ80 and AZ31B alloys of 29 MPa and 39 MPa, respectively, gave a good fit to the macroscopic stress-strain response of the polycrystal. Note: this also required CRSS value for non-basal slip and extension twinning.

Table 7.2: List of normalized CRSS for the basal slip for commercially pure Mg, AZ31B, and AZ80 alloys

	CRSS (MPa)
Commercially pure Mg	1.5
AZ31B	33
AZ80	45

The Δ CRSS is plotted as a function of $c^{1/2}$ (Figure 7.5). It can be observed that a linear regression, with a slope of 15, can be used to fit the data. Data from previous studies by Jain [46] is also displayed (blue symbols). It can be seen that these two sets of data are in good agreement. In addition the data from Akhtar and Teghtsoonian [176] obtained for binary Mg-Al alloys single crystals is shown in Figure 7.5 by red symbols. As can be observed, the current work shows a deviation from their work on Mg-Al alloys. However, it should be mentioned that in the current study, the investigated alloys are AZ31B (Mg-2.5 wt% Al-0.7 wt% Zn-0.2 wt.% Mn) and AZ80 (Mg-8 wt% Al-0.5 wt% Zn-0.2 wt.% Mn), which contain 0.7 wt% Zn and 0.5 wt% Zn, respectively. On the other hand, the study on Mg-Al alloys, with different percentage of Al, does not include the effect of zinc addition on the CRSS of basal slip. Similar to Mg-Al, it has been shown that the CRSS for basal slip in Mg-Zn alloy increases with the square root of the zinc concentration [176]. In order to have a better comparison of Akhtar's work with the current work, the effect of Zn addition on the CRSS of Mg-Al alloy should be considered. According to Kocks [177], the different contributions to the CRSS is the sum of the squares of each contributors. For the case of Mg-Al and Mg-Zn alloys, the CRSS of Mg-0.7Zn-xAl (x: different amount of aluminum) can be expressed by the equation below. Note: 0.7 wt% Zn was selected in order to compare Akhtar's result [176] with the current work result on AZ31B (Mg-2.5 wt% Al-0.7 wt% Zn-0.2 wt.% Mn) alloy.

$$\tau_{(Mg-0.7Zn-xAl)} = \sqrt{\tau_{Mg-xAl}^2 + \tau_{Mg-0.7Zn}^2} \quad (7.2)$$

where $\tau_{ss(Mg-0.7Zn)}$ and $\tau_{ss(Mg-xAl)}$ can be obtained from Akhtar's work [176]. In Figure 7.5 the green symbols show values of CRSS for basal slip after including the contribution of zinc. Still, after this modification, some discrepancy exists between the current work and Akhtar's work [176]. One of the reasons of this discrepancy may be due to the fact that it is assumed that the gradient effect (i.e. the magnitude of C in Equation 7.1) is independent of composition. For future work, it is suggested that the CRSS be measured directly for the studied alloys by performing the spherical indentation tests on AZ31B and AZ80 using all five different indenters to test this hypothesis. Also, in this study the yield strength obtained based on the 0.1% offset method. As mentioned before in Chapter 5.2.6, this offset value was selected in order to be consistent with literature [68]. However, changing the offset value may also have some effect on the yield strength and consequently on the CRSS of basal slip.

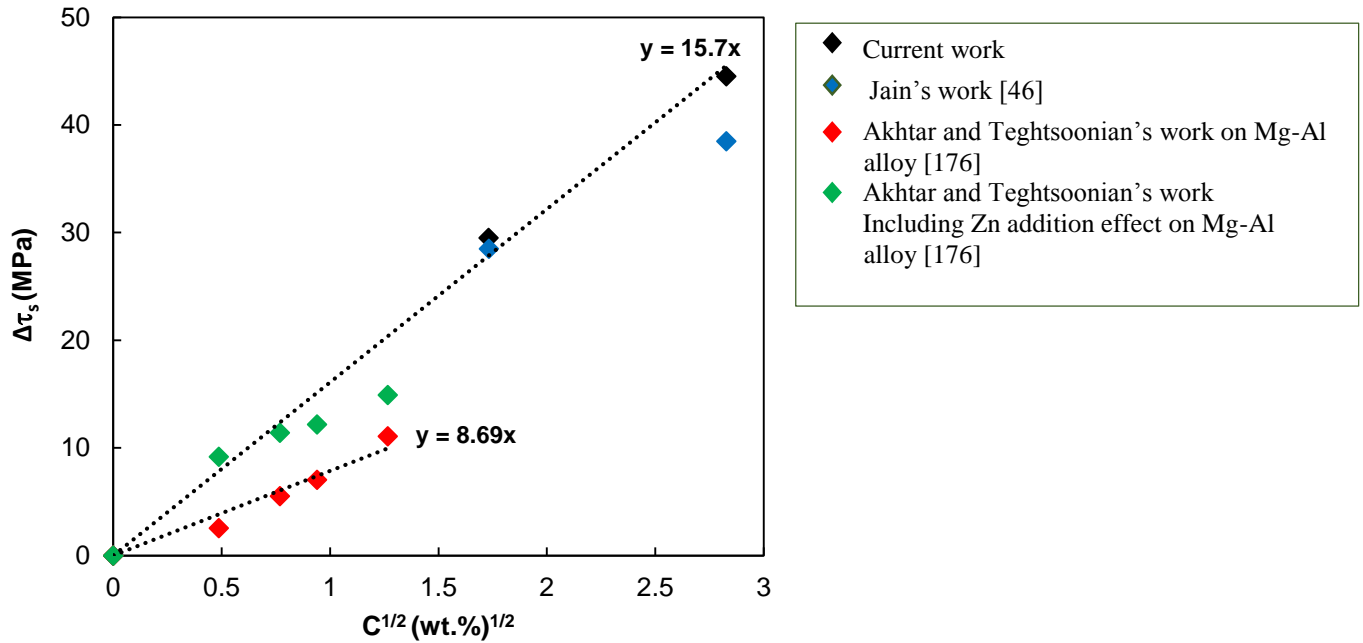


Figure 7.5: ΔCRSS for basal slip activation vs. $c^{1/2}$ for Mg-(0, 3, and 8 wt.%)Al. Data by Jain [46] and Akhtar and Teghtsoonian [176] are included for comparison.

7.5 Summary

It was shown that by using a simple model from the previous chapter, the CRSS of basal slip for an infinitely large diameter indenter can be measured for AZ31B (Mg-2.5 wt% Al-0.7 wt% Zn-0.2 wt% Mn) and AZ80 (Mg-8 wt% Al-0.5 wt% Zn-0.2 wt% Mn) alloys. Although there is still some discrepancy between the results from the indentation test and the conventional testing method [176], the instrumented indentation test can be considered as a promising method to predict the CRSS of basal slip in magnesium alloys.

CHAPTER 8 Conclusions and Future Work

8.1 Conclusion

In this work, the instrumented indentation technique was employed to study the initiation of plasticity in commercially pure Mg, AZ31B (Mg-2.5 wt% Al-0.7 wt%Zn-0.2 wt.% Mn) and AZ80 (Mg-8 wt% Al-0.5 wt%Zn-0.2 wt.% Mn) alloys.

The key, new contributions that this work has made are summarized below along with their impacts and significance.

- i) The technique used in this work successfully differentiated the basal slip and extension twinning from the load-displacement curves. It has been proposed that the initial deviation of the load-depth data from the elastic solution of Hertz is caused by the activation of pre-existing dislocations and the subsequent large discontinuity is associated with the onset of $\{10\bar{1}2\}$ extension twinning.
- ii) It was also found that the quantitative values for the $RSS_{0.1\% \text{ offset}}$ for basal slip of magnesium obtained from the indentation test and Hertzian contact theory is indentation size dependent and it increases linearly with the inverse square root of the misorientation gradient under the indent. This opens the door to quantify CRSS for basal slip and possibly extension twinning from indentation tests on polycrystalline samples.
- iii) The Effect of chemistry on the CRSS for basal slip was also successfully measured by conducting the indentation tests on Al-containing magnesium alloys (AZ magnesium alloys). Using spherical indentation test, it was shown that the CRSS of basal slip in a single crystal of magnesium increases linearly with $c^{1/2}$, where c is the concentration of Al. Understanding of alloying effects on the CRSS for basal slip in magnesium could be used to develop new alloys where basic knowledge on the chemistry dependence of the CRSS is unknown.

8.2 Future work

There are some interesting areas for further studies including:

- i) TEM analysis can be performed on slices which are underneath the indenter and perpendicular to the surface of the sample. TEM measurements will help us to confirm the presence of basal dislocations under the indent. Also, it can be helpful to support the idea that there are no other dislocations such as prism or 2nd order pyramidal slip dislocations under the indent.
- ii) In-situ indentation systems will help us to confirm the occurrence of twinning and subsequent detwinning during loading and unloading. Therefore, coupling the nanoindentation system with the EBSD machine will help to support the present assumption.
- iii) Study the indentation size effect on commercially pure magnesium and AZ magnesium alloys on the grain which is perpendicular to the c-axis to help us see how the CRSS varies as a function of tip radius for this crystallographic orientation.
- iv) The relationship between the indentation deformation zone (size and orientation) and the initiation of recrystallization in commercially pure magnesium, and AZ magnesium alloys can be investigated. This study will help us to elucidate how the recrystallization behaviour varies as a function of grain orientation, indentation size, and alloying addition in magnesium.
- v) Finally, it would be interesting to measure the heterogeneity/stored energy of deformation as a function of the grain orientation with respect to the tensile axis using instrumented indentation testing. This can be done by conducting indentation tests in fully annealed and deformed conditions in polycrystalline, commercially pure magnesium on grains with different crystallographic orientations.

References:

1. I.J. Polmear, Light alloys. metallurgy of light metals, 3rd edition. Arnold, London 1995.
2. A.A. Luo, M.O. Pekguleryuz, "Review-cast magnesium alloys for elevated temperature application," J. Mater. Sci., Vol. 29, 1994, p. 5259.
3. G. S. Cole, "Summary of magnesium vision 2020: A North American automotive strategic vision for Magnesium," Magnesium Technology 2007 (Minerals, Metals, and Materials Society, Warrendale, PA, 2007, p. 35.
4. E. Aghion, B. Bronfin, "Magnesium alloys development towards the 21st century," Mater. Sci. Forum, Vol. 350–351, 2000, p. 19.
5. International Magnesium Association. IMA 2014 Awards of Excellence and Environmental Responsibility Award Highlight Advances in Magnesium Technology, Processes and Products. [http://www.magnet.ubc.ca/assets/pdf/NewsAccessed January 30th, 2015](http://www.magnet.ubc.ca/assets/pdf/NewsAccessed%20January%2030th,%202015).
6. R. von. Mises, Z. Agnew, "Mechanics of plastic deformation in. crystals," Math. Mech., Vol. 6, 1928, p. 85.
7. R. E. Reed-Hill, W. D. Robertson, "Deformation of magnesium single crystals by non-basal slip," Trans. TMS-AIME., Vol. 220, 1957, p. 496.
8. R. E. Reed-Hill, W. D. Robertson, "Pyramidal slip in magnesium," Trans. TMS-AIME., Vol. 221, 1958, p. 256.
9. AC. Fischer-Cripps, Nanoindentation. Berlin. Springer, 2004.
10. W. F. Sheely, R. R. Nash, "Solid-solution strengthening of Magnesium single crystals at room temperature," Transaction Metallurgical Society AIME, Vol. 218, 1960, p. 416.
11. Y.W. F. Hosford, "The machanics of crystals and textured polycrystals," Oxford University press, Newyork, Oxford, 1993, p. 9.
12. J.P. Hirth and J. Lothe, "Theory of dislocations," 1982, New York: Wiley.
13. A. Akhtar, E. Teghtsoonian, "Solid solution strengthening of magnesium single crystals—II the effect of solute on the ease of prismatic slip," Acta Metallurgica., Vol. 17, 1969, p. 1339.
14. A. Akhtar, E. Teghtsoonian, "Solid solution strengthening of magnesium single crystals I—alloying behavior in basal slip," Acta Metallurgica, Vol. 17, 1969, p. 1351.

15. N. Stanford, M.R. Barnett, "The origin of "rare earth" texture development in extruded Mg-based alloys and its effect on tensile ductility," *Material Science and Engineering A*, Vol. 496, 2008, p. 399.
16. J. Bohlen, M.R. Nurnberg, J.W. Senn, D. Letzig, S.R. Agnew, "The texture and anisotropy of magnesium–zinc–rare earth alloy sheets," *Acta Materialia*, Vol. 55, 2007, p. 2101.
17. D. Tabor, *The hardness of metals*. Oxford: Oxford University Press, 1951.
18. T. Obara, H. Yoshinga, S. Morozumi, $\{11\bar{2}2\} \langle 1\bar{1}23 \rangle$ slip system in magnesium," *Acta Metallurgica*, Vol. 21, 1973, p. 845.
19. S. Ando, K. Namamura, K. Takashima, H. Tonda, *Journal of Japan Institute of Light Metals*, 1992, Vol. 42, p. 765.
20. B. Bhattacharya, PhD Thesis, McMaster University, 2006, Hamilton, Ontario, Canada.
21. J.H. Shin, I.S. Choi, B. Selvarajou, S. P. Joshi, T. K. Ha, K. H. Oh, H.N. Han, "Orientation-dependent indentation response of magnesium single crystals: experiments and modelling", The 10th International Conference on Magnesium alloys and Their Applications, 2015, Korea, Jeju Island.
22. F. E. Hauser, P. R. Landon, J. E. Dorn, "Deformation and fracture mechanisms of polycrystalline magnesium at low temperatures," *Trans. ASM.*, Vol. 48, 1956, p. 986.
23. Z. Keshavarz, M. R. Barnett, "EBSD analysis of deformation modes in Mg-3Al-1Zn," *Scripta Metallurgica*, Vol. 55, 2006, p. 915.
24. B. Bhattacharya, M. Niewczasa, "Work-hardening behaviour of Mg single crystals oriented for basal slip," *Philosophical Magazine*, Vol. 91, 2011, p. 2227.
25. J. Koike, T. Kobayashi, T. Mukai, H. Watanabe, M. Suzuki, K. Maruyama, K. Higashi, "The activity of non-basal slip systems and dynamic recovery at room temperature in fine-grained AZ31B magnesium alloys," *Acta Materialia*, Vol. 51, 2003, p. 2055.
26. J. Koike, "Enhanced deformation mechanisms by anisotropic plasticity in polycrystalline Mg alloys at room temperature," *Metallurgical and Materials Transaction A*, Vol. 36A, 2005, p. 1689.
27. S.R. Agnew and O. Duygulu, "Plastic anisotropy and the role of non-basal slip in magnesium at room temperature in fine-grained AZ31B magnesium alloys," *Acta Materialia*, Vol. 51, 2005, p. 1161.
28. H. Yoshinaga, T. Obara and S. Morozumi, "Twinning deformation in magnesium compressed along the C-axis," *Materials Science and Engineering A*, Vol. 12, 1973, p. 255.

29. M.R. Barnett, "Twinning and the ductility of magnesium alloys. Part I: "Tension" twins," *Materials Science and Engineering A*, Vol. 464, 2007, p. 1.
30. M.R. Barnett, "Twinning and the ductility of magnesium alloys Part II. "Contraction" twins," *Materials Science and Engineering A*, Vol. 464, 2007, p. 8.
31. J. Koike, Y. Sato, D. Ando, "Origin of the anomalous $\{10\bar{1}2\}$ twinning during tensile deformation of Mg alloy sheet," *Materials Transactions*, Vol. 48, 2008, p. 2792.
32. S. H. Park, S. G. Hong, C. S. Lee, "Activation mode dependent $\{10\bar{1}2\}$ twinning characteristics in a polycrystalline magnesium alloy," *Scripta Materialia*, Vol. 62, 2010, p. 202.
33. S. R. Agnew, M. H. Yoo, and C. N. Tome, "Application of texture simulation to understand mechanical behavior of Mg and solid solution alloys containing Li or Y", *Acta Materialia*, 2001, Vol. 49, p. 4277.
34. A. Jain, S.R. Agnew, "Modeling the temperature dependent effect of twinning on the behavior of magnesium alloy AZ31B sheet", *Materials Science and Engineering A*, 2007, Vol. 462, p. 29.
35. S. B. Yi, C.H.J. Davies, H.-G. Brokmeier, R.E. Bolmaro, K.U. Kainer, J. Homeyer, "Deformation and texture evolution in AZ31 magnesium alloy during uniaxial loading", *Acta Materialia*, 2006, Vol. 54, p. 549.
36. R. S. Agnew and O. Duygulu, "Plastic anisotropy and the role of non-basal slip in magnesium alloy E.W. Kelley, and Jr. W.F. Hosford, "Plane-strain compression of magnesium and magnesium alloy crystals", *Transactions of the Metallurgical Society of AIME*, Vol. 242, 1968, p. 1422.
37. B. Selvarajou, J.H. Shin, T.K Ha, I.S. Choi, S.P. Joshi, and H.N. Han, "Orientation-dependent indentation response of magnesium single crystals: Modeling and experiments" *Acta Materialia*, Vol. 81, 2014, p. 358.
38. A. Chapuis and J. H. Driver, "Temperature dependency of slip and twinning in plane strain compressed magnesium single crystals", *Acta Mater*, Vol. 59, 2011, p. 1986.
39. H. Yoshinaga, R. Horiuchi, "Deformation mechanisms in magnesium single crystals compressed in the direction parallel to the hexagonal axis" *Trans. JIM*, Vol. 4, 1963, p. 1.
40. M. A. Gharghouri, G. C. Weatherly, J. D. Embury, J. Root, "Study of the mechanical properties of Mg-7.7at.% Al by in-situ neutron diffraction", *Philosophical Magazine A*, Vol. 79, 1999, p. 1671
41. S. Godet, L. Jiang, A. A. Luo, J. J. Jonas, "Use of Schmid factors to select extension twin variants in extruded magnesium alloy tubes", *Scripta Materialia*, Vol. 55, 2006, p. 1055.

42. L. Jiang, J. J. Jonas, R. K. Mishra, A. A. Luo, A. K. Sachdev and S. Godet, “Twinning and texture development in two Mg alloys subjected to loading along three different strain paths”, *Acta Materialia*, Vol. 55, 2007, p. 3899.
43. I. J. Beyerlein, L. Capolungo, P. E. Marshall, R. J. McCabe, C. N. Tomé, “Statistical analyses of deformation twinning in magnesium”, *Philosophical Magazine*, Vol. 90, 2010, p. 2161.
44. J. Jiang, A. Godfrey, W. Liu, Q. Liu, “Identification and analysis of twinning variants during compression of a Mg–Al–Zn alloy”, *Scripta Materialia*, Vol. 58, 2008, p. 122.
45. M. R. Barnett, Z. Kechavarz and M. D. Nave, “Microstructural features of rolled Mg-3Al-1Zn”, *Metallurgical and Materials Transactions A*, Vol. 36A, 2005, p. 1697.
46. J. Jain, “The deformation behaviour of a Mg-8Al-0.5Zn alloy”, PhD thesis, The University of British Columbia, Canada, 2010.
47. Beyerlein, L. Capolungo, P. E. Marshall, R. J. McCabe, C. N. Tomé, *Proc. R. Soc. A*, Vol. 466, 2010, p. 2517.
48. L. Jiang, J.J. Jonas, A.A. Luo, A.K. Sachdev and S. Godet, “Twinning-induced softening in polycrystalline AM30 Mg alloy at moderate temperatures,” *Scripta Materialia*, Vol. 54, 2006, p. 771.
49. W. H. Hartt, R. E. Reed-Hill, “The irrational habit of second-order $\{10\bar{1}1\}$ - $\{10\bar{1}2\}$ twins in magnesium,” *Transactions of the Metallurgical Society of AIME*, Vol. 239, 1967, p. 1511.
50. R. E. Reed-Hill, “A study of the $\{10\bar{1}1\}$ and $\{10\bar{1}3\}$ twinning modes in magnesium,” *Transactions of the Metallurgical Society of AIME*, Vol. 218, 1960, p. 554.
51. C. H. Cáceres, T. Sumitomo, and M. Veidt, “Pseudoelastic behaviour of cast magnesium AZ91 alloy under cyclic loading–unloading”, *Acta Materialia*, Vol. 51, 2003, p. 6211.
52. G.E. Mann, T.Sumitomo, C.H.Cáceres, J.R.Griffiths, “Reversible plastic strain during cyclic loading–unloading of Mg and Mg–Zn alloys”, *Materials Science and Engineering A*, Vol. 456, 2007, p. 138.
53. X. Y. Lou, M. Li, R. K. Boger, S. R. Agnew, and R. H. Wagoner, “Hardening evolution of AZ31B Mg sheet” *International Journal of Plasticity*, Vol. 23, 2007, p. 44.
54. T. Yasutomi and M. Enoki, “In-Situ Evaluation of Detwinning Behavior in Extruded AZ31 Mg Alloy by AE”, *Mater Trans*, Vol. 53, 2012, p. 1611.
55. L. Wua, A. Jain, D.W. Brown, G.M. Stoica, S.R. Agnew, B. Clausen, D.E. Fielden, P.K. Liaw, “Twinning–detwinning behavior during the strain-controlled low-cycle

- fatigue testing of a wrought magnesium alloy, ZK60A”, *Acta Materialia*, Vol. 56, 2008, p. 688.
56. C. Fischer-Cripps, “Introduction to contact mechanics”, 2000, Springer, p. 96.
 57. A. Kelly and N.H. Macmillan, *Strong Solids*, Oxford Science Publication, 1986, p. 145.
 58. H. Hertz, “On the contact of elastic solids,” *J. R. Angew. Math.* 92, 1881, pp.156–171. Translated and reprinted in English in *Hertz’s Miscellaneous Papers*, Macmillan & Co., London, 1896, Chapter 5.
 59. H. Hertz, “On hardness,” *Verh. Ver. Beförderung Gewerbe Fleisses*, Vol. 61, 1882, p. 410, Translated and reprinted in English in “Hertz’s Miscellaneous Paper”, Macmillan and Co, London, 1986.
 60. W.C. Oliver, G.M. Pharr, “An improved technique for determining hardness and elastic modulus using load and displacement sensing indentation experiment,”. *Journal of Materials Research*, Vol. 7, 1992, p. 1564.
 61. C.A. Schuh, (2006) “Nanoindentation studies of materials,” *Materials Today*, Vol. 9, 2006, p. 32.
 62. A.C. Fischer-Cripps, “The use of combined elastic modulus in the analysis of depth sensing indentation data,” *Journal of Materials Research*, Vol. 16, 2001, p. 3050.
 63. I.N. Sneddon, “Boussinesq’s problem for a rigid cone,” *Proceedings of the Cambridge Philosophical Society*, Vol. 44, 1948, p. 492.
 64. G.M. Pharr, W.C. Oliver, and F.R. Brotzen, “On the generality of the relationship among contact stiffness, contact area, and the elastic modulus during indentation, ” *Journal of Materials Research*, Vol. 7, 1992, p. 613.
 65. K.L. Johnson, *Contact mechanics*. Cambridge: Cambridge University Press, 1987.
 66. G.M. Pharr, W.C. Oliver, “Measurement of hardness and elastic modulus by instrumented indentation. Advances in understanding and refinements to methodology,” *Journal of Materials Research*, Vol. 19, 2004, p. 3.
 67. B. Bhushan, X. Li, (2003) “Nanomechanical characterisation of solid surfaces and thin films,” *International Materials Reviews*, Vol. 48 , 2003, p. 125.
 68. S.R. Kalidindi, S. Pathak “Determination of the effective zero-point and the extraction of spherical nanoindentation stress–strain curves,” *Acta Materialia*, Vol. 56, 2008, p. 3523.
 69. S. Pathak, S.R.Kalidindi, C.Klemenz, N.Orlovskaya, “Analyzing indentation stress–strain response of LaGaO₃ single crystals using spherical indenters,” *Journal of the European Ceramic Society*, Vol. 28, 2008, p. 2213.

70. S.Pathak, J. Shafferer, S.R. Kalidindi, "Effective zero-point and extraction of indentation stress-strain curves without the Continuous Stiffness Measurement signal," *Scripta Materialia*, Vol. 60, 2009, p. 439.
71. S. Pathak, D. Stojakovic, S.R. Kalidindi, "Measurement of the local mechanical properties in polycrystalline samples using spherical nanoindentation and orientation imaging microscopy," *Acta Materialia*, Vol. 57, 2009, p. 3020.
72. M.F. Doerner and W.D. Nix, "A method for interpreting the data from depth-sensing indentation instruments," *Journal of Materials Research*, Vol.1 4, 1986, p. 601.
73. B. Bhushan, *Springer Handbook of Nanotechnology: Edition 2*, , March 27, 2007, p. 1148.
74. J.S. Field and M.V. Swain, "A simple predictive model for spherical indentation," *Journal of Materials Research*, Vol. 8, 1993, p. 297.
75. J.S. Field, M.V. Swain, "A simple predictive model for spherical indentation," *Journal of Materials Research*, Vol. 10, 1995, p. 101.
76. M.V. Swain, "Mechanical property characterisation of small volumes of brittle materials with spherical tipped indenters," *Materials Science and Engineering A*, Vol. 253, 1998, p. 160.
77. S. Basu, A. Moseson and M. W. Barsoum, "On the determination of spherical nanoindentation stress-strain curves," *Journal of Materials Research*, Vol. 21, 2006, p. 2628.
78. B. Taljat, T. Zacharia, F. Kosel, "New analytical procedure to determine stress-strain curve from spherical indentation data," *International Journal of Solid Structure*, Vol. 35, 1998, p. 4411.
79. Beghini M, Bertini L, Fontanari V., "Evaluation of the stress–strain curve of metallic materials by spherical indentation," *International Journal of Solid Structure*, Vol. 43, 2006, p. 2441.
80. S. Pathak, S.R. Kalidindi, C. Klemenz, N. Orlovskaya, "Analyzing indentation stress–strain response of LaGaO₃ single crystals using spherical indenters," *Journal of the European Ceramic and Society*, Vol. 28, 2008, p. 2213.
81. A.C. Fischer-Cripps, "Critical review of analysis and interpretation of nanoindentation test data," *Surface and Coating Technology*, Vol. 200, 2006, p. 4153.
82. J. Deuschle, S. Enders, E. Arzt, "Surface detection in nanoindentation of soft polymers," *Journal of Materials Research*, 2007, Vol. 22, p. 3107.
83. T. Chudoba, M. Griepentrog, A. Duck, D. Schneider, F. Richter, "Young's modulus measurements on ultra-thin coatings," *Journal of Materials Research*, Vol. 19, 2004, p. 301.

84. T. Chudoba, N. Schwarzer, F. Richter, "Determination of elastic properties of thin films by indentation measurements with a spherical indenter," *Surface and Coating Technology*, Vol. 127, 2000, p. 9.
85. L. Ma, L. Levine, R. Dixson, D. Smith and D. Bahr, "Effect of the Spherical Indenter Tip Assumption on the Initial Plastic Yield Stress", *Nanoindentation in Materials Science*, Chapter 2, 2012, p. 25.
86. N. Gane, and F. P. Bowden, "Microdeformation of solids", *Journal of Applied Physics*, Vol. 39, No. 3, 1968, p. 1432.
87. T. F. Page, W. C. Oliver, and C. J. McHargue, "The deformation behavior of ceramic crystals subjected to very low load (nano) indentations", *Journal of Materials Research*, Vol. 7, No. 2, 1992, pp.450.
88. J. E. Bradby, J. S. Williams, J.Wong-Leung, M. V. Swain, and P. R. Munroe, "Nanoindentation-induced deformation of Ge", *Applied Physics Letters*, Vol. 80, No. 15, 2002, p. 2651.
89. R. D. K. Misra, Z. Zhang, Z. Jia, M.C. Somani, and L.P. Karjalainen, (2010) "Probing deformation processes in near-defect free volume in high strength–high ductility nanograined/ultrafine-grained (NG/UFG) metastable austenitic stainless steels", *Scripta Materialia*, Vol. 63, No. 11, 2010, p. 1057.
90. V. Domnich, Y. Gogotsi, and S. Dub, "Effect of phase transformations on the shape of the unloading curve in the nanoindentation of silicon", *Applied Physics Letter*, Vol. 76, 2000, p. 2214.
91. J.E. Bradby, J.S. Williams, and M.V. Swain, "In situ electrical characterization of phase transformations in Si during indentation" *Physical Review B*, Vol. 67, 2003, p. 85.
92. T. Juliano, V. Domnich, and Y. Gogotsi, "The effect of indentation loading conditions on the phase transformation induced events in silicon", *Journal of Materials Research*, Vol. 18, 2003, p. 1192.
93. A. Kailer, Y.G. Gogotsi, and K.G. Nickel, "Phase transformations of silicon caused by contact loading", *Journal of Applied Physics*, Vol. 81, 1997, p. 3057.
94. J.S. Williams, Y. Chen, J. Wong-Leung, A. Kerr, and M.V. Swain, "Ultra-micro-indentation of silicon and compound semiconductors with spherical indenters", *Journal of Materials Research*, Vol. 14, 1999, p. 2338.
95. I. Zarudi and L.C. Zhang, "Structure changes in mono-crystalline silicon subjected to indentation-experimental findings", *Tribology International*, Vol. 32, 1999, p. 701.
96. A.B. Mann, D. Van Heerden, J.B. Pethica, and T.P. Weihs, "Sizedependent phase transformations during point loading of silicon", *Journal of Materials Research*, Vol. 15, 2000, p. 1754.

97. J.E. Bradby, J.S. Williams, J. Wong-Leung, M.V. Swain, and P. Munroe, "Transmission electron microscopy observation of deformation microstructure under spherical indentation in silicon", *Applied Physics Letter*, Vol. 77, 2000, p. 3749.
98. G. L. Cross, W.A. Schirmeisen, P. Grutter, and U.T. Durig, "Plasticity, healing and shakedown in sharp-asperity nanoindentation", *Nature Materials*, Vol. 5, 2006. No. 5, p. 370.
99. T. Juliano, V. Domnich, T. Buchheit, and Y. Gogotsi, "Numerical derivative analysis of load-displacement curves in depth-sensing indentation", *Materials Research Society*, Vol. 791, 2004, p. 10.
100. D. Catoor, Y.F. Gao, J. Geng, M.J.N.V. Prasad, E.G. Herbert, K.S. Kumar, G.M. Pharr, E.P. George, "Incipient plasticity and deformation mechanisms in single-crystal Mg during spherical nanoindentation" *Acta Materialia*, Vol. 61, 2013, p. 2953.
101. T. Guo, "Initiation of plasticity by nanoindentation in Mg alloys", PhD thesis, Deakin University, October 2015, Australia.
102. S. Pathak, D. Stojakovic, R. Doherty, and S. R. Kalidindi, "Importance of surface preparation on the nano-indentation stress-strain curves measured in metals", *Journal of Materials Research*, Vol. 24, 2009, p. 1142.
103. J.H. Shin, S.H. Kim, T.K. Ha, K.H. Oh, I.S. Choi, and H.N. Han, "Nanoindentation study for deformation twinning of magnesium single crystal", *Scripta Materialia*, Vol. 68, 2013, p. 483.
104. H. Kitahara, T. Mayama, K. Okumura, Y. Tadano, M. Tsushida, S. Ando, "Anisotropic deformation induced by spherical indentation of pure Mg single crystals", *Acta Materialia*, Vol. 78, 2014, p. 290.
105. R. Sanchez-Martin, M.T. Perez-Prado, J. Segurado, J. Bohlen, I. Gutierrez-Urrutia, J. Llorca, J.M. Molina-Aldareguia, "Measuring the critical resolved shear stresses in Mg alloys by instrumented nanoindentation", *Acta Materialia*, Vol. 71, 2014, p. 283.
106. C. Zambaldi, C. Zehnder, and D. Raabe, "Orientation dependent deformation by slip and twinning in magnesium during single crystal indentation", *Acta Materialia*, Vol. 91, 2015, No. 1, p. 267
107. R. Sanchez-Martin, M.T. Perez-Prado, J. Segurado, and J.M. Molina-Aldareguia, "Effect of indentation size on the nucleation and propagation of tensile twinning in pure magnesium", *Acta Materialia*, Vol. 93, 2015, p. 114.
108. B. Backes, K. Durst, and M. Goken, "Determination of plastic properties of polycrystalline metallic materials by nanoindentation: Experiments and finite element simulations." *Philosophical Magazine*, Vol. 86, p. 5541.

109. K. Durst, B. Backes, O. Franke, and M. Goken, "Indentation size effect in metallic materials: Modeling strength from pop-in to macroscopic hardness using geometrically necessary dislocations", *Acta Materialia*, Vol. 54, 2006, p. 2547.
110. A.A. Elmustafa, J.A. Eastman, M.N. Rittner, J.R. Weertman, and D.S. Stone, "Indentation size effect: large grained aluminum versus nanocrystalline aluminum-zirconium alloys", *Scripta Materialia*, Vol. 43, 2000, p. 951.
111. W.D. Nix, and H. Gao, "Indentation size effects in crystalline materials: A law for strain gradient plasticity" *Journal of the Mechanics and Physics of Solids*, Vol. 46, 1998, p. 411.
112. M. Rester, C. Motz, and R. Pippan, "Indentation across size scales - A survey of indentation-induced plastic zones in copper {1 1 1} single crystals", *Scripta Materialia*, Vol. 59, 2008, p. 742.
113. W.J. Poole, M.F. Ashby and N.A. Fleck, "Micro-hardness of annealed and work-hardened copper polycrystals", *Scripta Materialia*, Vol. 34, 1996, No. 4, p. 559.
114. Z. Wang, "Influences of sample preparation on the indentation size effect and nanoindentation pop-in on nickel", PhD thesis, University of Tennessee, Knoxville, 2012.
115. Y. Liu, and A.H.W. Ngan, "Depth dependence of hardness in copper single crystals measured by nanoindentation", *Scripta Materialia*, Vol. 44, 2001, p. 237.
116. W.D. Nix, and H. Gao, "Indentation size effects in crystalline materials: A law for strain gradient plasticity", *Journal of the Mechanics and Physics of Solids*, Vol. 46, 1998, p. 411.
117. Y. Huang, H. Gao, W.D. Nix, and J.W. Hutchinson, "Mechanical-based strain gradient-II. Analysis", *Journal of the Mechanics and Physics of Solids*, Vol. 48, 2000, p. 99.
118. N.A. Fleck, J.W. Hutchinson, "A reformulation of strain gradient plasticity", *Journal of the Mechanics and Physics of Solids*, Vol. 49, 2001, p. 2245.
119. N.A. Fleck, G.M. Muller, M.F. Ashby, and J.W. Hutchinson, "Strain gradient plasticity: Theory and experiment", *Acta Metallurgica et Materialia*, Vol 42, 1994, p. 475.
120. H. Gao, Y. Huang, W.D. Nix, and J.W. Hutchinson, "Mechanism-based strain gradient plasticity-- I. Theory", *Journal of the Mechanics and Physics of Solids*, Vol. 47, 1999, p. 1239.

121. W.C. Oliver, and G.M. Pharr, "An improved technique for determining hardness and elastic modulus using load and displacement sensing indentation experiments", *Journal of Materials Research*, Vol. 7, 1992, p. 1564.
122. G. I. Taylor, "Plastic strain in metals", *Journal of the Institute of Metals*, 1938, p. 62.
123. D. Tabor, "The hardness of Metals", 1951, Clarendon Press, Oxford.
124. J.G. Swadener; E.P. Georgea, G.M. Pharr, "The correlation of the indentation size effect measured with indenters of various shapes", *Journal of the Mechanics and Physics of Solids*, Vol 50, 2002, p. 681.
125. K. W. McElhaney, J. J. Vlassak, and W. D. Nix, "Determination of indenter tip geometry and indentation contact area for depth-sensing indentation experiments", *Journal of Materials Research*, Vol. 13, 1998, p. 1300
126. Q. Ma and D. R. Clarke, "Size-dependant hardness of silver single crystal", *Journal of Materials Research*, Vol. 10, 1995, p. 853.
127. K. Durst, B. Backes, O. Franke, and M. Goken, "Indentation size effect in metallic materials: Modeling strength from pop-in to macroscopic hardness using geometrically necessary dislocations", *Acta Materialia*, Vol. 54, 2006, p. 2547.
128. K. Durst, B. Backes, and M. Goken, "Indentation size effect in metallic materials: Correcting for the size of the plastic zone", *Scripta Materialia*, Vol. 52, 2005, p. 1093.
129. K. Durst, O. Franke, A. Bohner, and M. Goken, "Indentation size effect in Ni-Fe solid solutions", *Acta Materialia*, 2007, Vol. 55, p. 6825.
130. A. Akhtar, "Solid solution strengthening of magnesium", PhD thesis, The University of British Columbia, Canada, July 1968.
131. B.S. Suh, M.S. Shin, K.S. Shin, and N. J. Kim, "Current issues in magnesium sheet alloys: Where do we go from here?" *Script Mater*, Vol. 84-85, 2014, p. 1-6.
132. Y. Xue, Z. Zhang, L. Lang, and H. Yang, "Influence of aging on microstructure and Mechanical Properties of wrought magnesium alloys", *Adv. Mater. Res*, Vol. 152-153, 2010, p. 560.
133. D.G.J. Griffiths, "Understanding texture weakening in magnesium rare earth alloys", PhD Thesis, The University of Manchester, 2014.
134. K. Oh-ishi, K. Hono and K. Shin, "Effect of pre-aging and Al addition on age-hardening and microstructure in Mg-6 wt% Zn alloys", *Materials Science and Engineering: A*, Vol. 496, 2008, p. 425.
135. J.F. Nie, B.C. Muddle, "Characterisation of strengthening precipitate phases in a Mg-Y-Nd alloy", *Acta Materialia*, Vol. 48, 2000, p. 1691.

136. C. Antion, P. Donnadieu, F. Perrard, A. Deschamps, C. Tassin, A. Pisch, "Hardening precipitation in a Mg–4Y–3RE alloy", *Acta Materialia*, Vol. 51, 2003, p. 5335.
137. J. A. Yasi, L. G. Hector Jr., D. R. Trinkle, "First-principles data for solid-solution strengthening of magnesium: From geometry and chemistry to properties", *Acta Materialia*, Vol. 58, 2010, p. 5704.
138. N. Stanford and M. R. Barnett, "Solute strengthening of prismatic slip, basal slip and $\{1\ 0\ \bar{1}\ 2\}$ twinning in Mg and Mg–Zn binary alloys", *International Journal of Plasticity*, Vol. 47, 2013, p. 165.
139. C. Caceres and D. Rovera, "Solid-solution strengthening in concentrated Mg–Al alloys", *Journal of Light Metals*, Vol 1, 2001, p. 151.
140. R.L. Fleischer, in: D. Peckner (Ed.), *Strengthening of Metals*, Reinhold, New York, 1964, pp. 114–117.
141. R. Labusch, *Phys. Status Solidi A* 41 (1970) 659–664.
142. G. Martin, C.W. Sinclair, W.J. Poole, and H. Azizi-Alizamini, "Local plastic-strain heterogeneities and their impact on the ductility of Mg", *Journal of the Minerals, Metals and Materials Society*, Vol. 67, 2015, p. 1761.
143. G. Petzow, "Metallographic etching: techniques for metallography, ceramography, plastography", ASM International, 2nd ed. 1999, New York.
144. C. W. Bale, E. Bélisle, P. Chartrand, S. A. Deckerov, G. Eriksson, K. Hack, I. H. Jung, Y. B. Kang, J. Melançon, A. D. Pelton, C. Robelin and S. Petersen, *FactSage thermochemical software and databases - recent developments*, *Calphad*, Vol. 33, 2009, p. 295, www.factsage.com.
145. B.R. Lawn, T.R. Wilshaw, and N.E.W. Hartley, "A computer simulation study of hertzian cone crack growth," *International Journal of Fracture*, Vol 101, 1974, p. 1.
146. S. Zaefferer, S.I. Wright, and D. Raabe, "Three-dimensional orientation microscopy in a focused ion beam–scanning electron microscope: A new dimension of microstructure characterization", *Metallurgical and Materials Transactions A*, Vol. 39A, 2008, p. 374.
147. L.A. Giannuzzi, B.W. Kempshall, S.M. Schwarz, J.K. Lomness, B.I. Prenitzer, and F.A. Stevie, "Introduction to focused ion beams, instrumentation, theory, techniques, and practice, In: Lucille A. Giannuzzi and Fred A. Stevie, *Introduction to Focused Ion Beams, Instrumentation, Theory, Techniques, and Practice*", North Carolina State University, 2005, Springer, p. 201.
148. P.J. Konijnenberg, S. Zaefferer, S.-B. Lee, A.D. Rollett, G.S. Rohrer, and D. Raabe, "Advanced methods and tools for reconstruction and analysis of grain boundaries from 3D-EBSD data sets", *Materials Science Forum*, Vols. 702-703, 2012, p. 475.

149. E. Demir, D. Raabe, N. Zaafarani, and S. Zaeferrer, "Investigation of the indentation size effect through the measurement of the geometrically necessary dislocations beneath small indents of different depths using EBSD tomography" *Acta Materialia*, Vol. 57, 2009, p. 559.
150. P.J. Konijnenberg, S. Zaeferrer, D. Raabe, "Assessment of geometrically necessary dislocation levels derived by 3D EBSD", *Acta Materialia*, Vol. 99, 2015, p. 402.
151. F. Roters, P. Eisenlohr, L. Hantcherli, D.D.Tjahjanto, T.R Bieler, and D. Raabe. "Overview of constitutive laws, kinematics, homogenization and multiscale methods in crystal plasticity finite-element modeling: Theory, experiments, applications", *Acta Materialia*, Vol. 58, 2010, p. 1152.
152. R.S. Kalidindi, A.C. Bronkhorst, and L. Anand, "Crystallographic texture evolution in bulk deformation processing of FCC metals," *Journal of Mechanics and Physics of Solids*, Vol. 40, 1992, p. 537.
153. C. Zambaldi Y. Yang, T.R. Bieler, and D. Raabe, "Orientation informed nanoindentation of alpha-titanium: Indentation pileup in hexagonal metals deforming by prismatic slip", *Journal of Materials Research*, Vol. 27, 2012, p. 356.
154. C. Zambaldi, F. Roters, and D. Raabe, "Quantifying the plastic anisotropy of gamma-TiAl by axisymmetric indentation", *Acta Materialia*, Vol. 58, 2010, p. 3516.
155. F. Roters, P. Eisenlohr, C. Kords, D. Tjahjanto, M. Diehl, and D. Raabe, *Procedia IUTAM*, Vol. 3, 2012, P. 10.
156. F. Roters et al. *Düsseldorf Advanced Materials Simulation Kit -DAMASK.mpie.de*. 2011.
157. G. Simmons, and H. Wang, *Single Crystal Elastic Constants and Calculated Aggregate Properties: A Handbook*. MIT Press, Cambridge MA, 1971.
158. C.N. Tomé, G.R. Canova, U.F. Kocks, N. Christodoulou, and J.J. Jonas, "The relation between macroscopic and microscopic strain hardening in FCC polycrystals", *Acta Metallurgica*, Vol. 32, 1984, p. 1637.
159. G.M. Pharr, A. Bolshakov, "Understanding nanoindentation unloading curves" *Journal of Materials Research*, Vol. 17, 2002, p. 2660.
160. W. F. Hosford, "Mechanical Behaviour of Materials," Oxford University press, Newyork, Oxford, 2005, p. 27.
161. A.C. Reardon, "Metallurgy for the non-metallurgist", ASM International, Materials Park, Ohio, 2011, p. 54.
162. P. W. Bakarian, and C. H. Mathewson, "Slip and twinning in magnesium single crystals at elevated temperatures." *Transactions of the Metallurgical Society of AIME*, 1943, Vol. 152, p. 226.

163. E. C. Burke, and W. R. Hibbard, "Plastic deformation of magnesium single crystals", Transactions of the Metallurgical Society of AIME, Vol. 194, 1952, p. 295.
164. S. J. Vachhani, and S. R. Kalidindi, "Grain-scale measurement of slip resistances in Aluminum polycrystals using spherical nanoindentation" Acta Materialia, Vol. 90, 2015, p. 27.
165. Y.Y. Lim and M.M. Chaudhri, "The effect of the indenter load on the nanohardness of ductile metals: an experimental study on polycrystalline work-hardened and annealed oxygen-free copper", Philosophical Magazine A, 1999, Vol. 79, p. 2979.
166. J. Spray, A. J. Bushby and N. M. Jennett, "On the indentation size effect in spherical indentation", Philosophical Magazine, 2006, Vol. 86, p. 5581.
167. N.A. Stelmashenko, M.G. Walls, L.M. Brown, Y.V. Milman, "Microindentation on W and Mo oriented single crystals: an STM study", Acta Metallurgica et Materialia, Vol. 41, 1993, p. 2855.
168. M.F. Ashby, "The deformation of plastically non-homogenous alloys", in: Strengthening Methods in Crystals (A. Kelly and R.B. Nicholson, eds.), Applied Science Publication, London, 1971, p. 137.
169. G.E. Dieter, "Mechanical Metallurgy", Third edition, New York, McGraw-Hill, 2001, p. 190.
170. T. Williams and C. Kelley, Gnuplot 4.6: An Interactive Plotting Program, 2014.
171. Y. Li and M. Enoki, "Deformation and anelastic recovery of pure magnesium and AZ31B alloy investigated by acoustic emission", Materials Transactions, Vol. 48, 2007, No. 9, p. 2343.
172. R.L. Fleischer, "Solution hardening", Acta Metallurgica, Vol. 9, 1961, p. 996.
173. R.L. Fleischer, "Substitutional solution hardening", Acta Metallurgica, Vol. 11, 1963, p. 203.
174. A. Akhtar and E. Teghtsoonian, "Substitutional solution hardening of magnesium single crystals", Philosophical Magazine, Vol. 25, 1972, p. 906.
175. S.R. Agnew, C.N. Tomé, D.W. Brown, T.M. Holden, S.C. Vogel, "Study of slip mechanisms in a magnesium alloy by neutron diffraction and modeling", Scripta Materialia, Vol 48, 2003, p. 1003.
176. A.E. Teghtsoonian, "Substitutional solution hardening of magnesium single crystals", Philosophical Magazine, Vol. 25, 1972, p. 897.
177. U.F. Kocks, A. S. Argon, and M.F. Ashby, "Thermodynamics and kinetics of slip", Progress in Materials Science, Pergamon press, third edition, 1975, Oxford.

APPENDIX A1: 3D-EBSD Measurements of Commercially Pure Magnesium

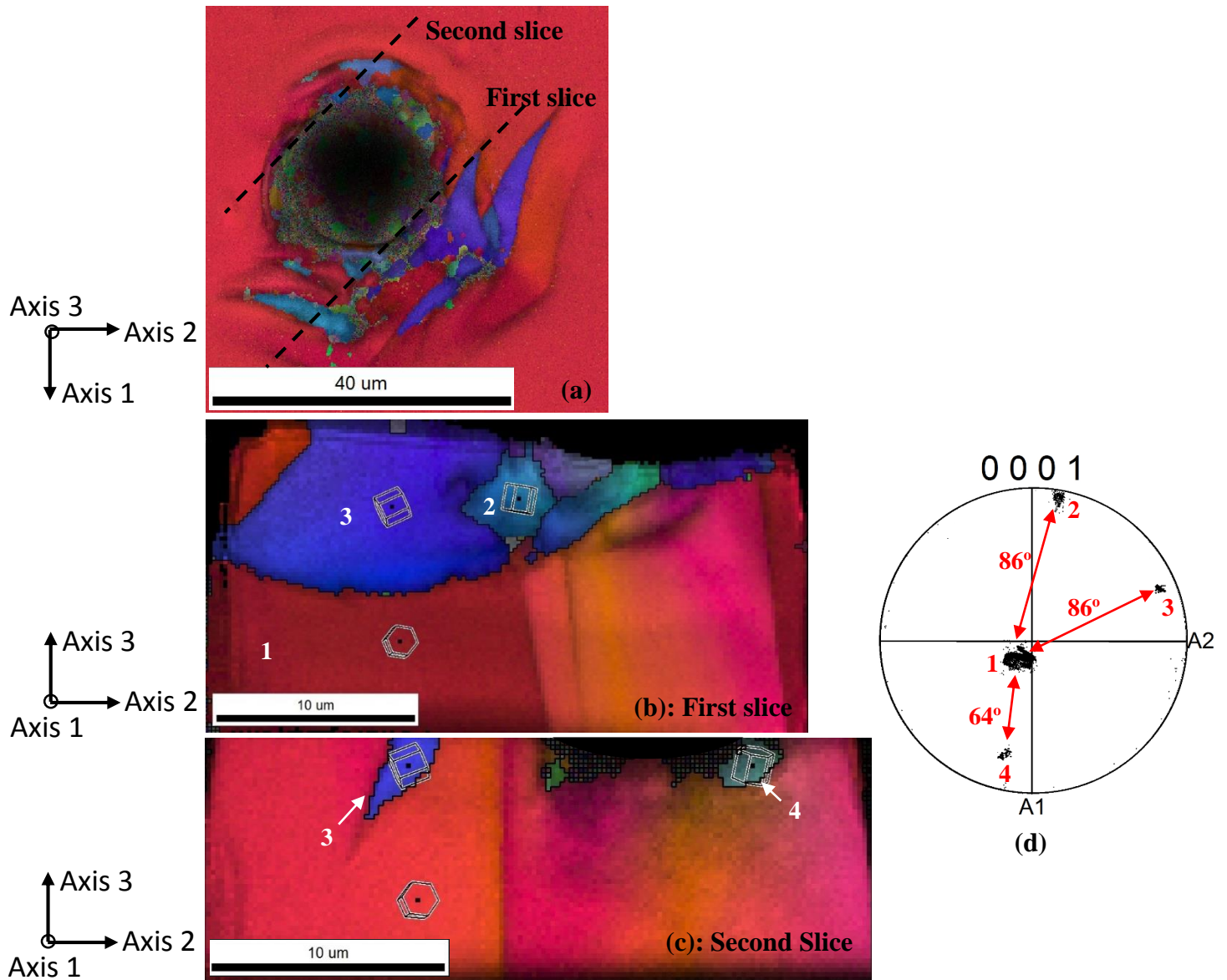


Figure A1: (a) The combined image quality/IPF map of the indentation area for indentation almost parallel to the c -axis, (b) and (c) the combined image quality/IPF maps of the first slice and the second slice, respectively, for commercially pure magnesium. The sections shown are perpendicular to the surface of the sample and the locations of them are shown by dashed lines in (a). (d) The corresponding $\{0001\}$ pole figures of IPF maps. In this pole figure, three extension twins can be observed (i.e. twins number 2, 3, and 4). Note: twin number 4 is a double extension twin which has a misorientation of 64° with the parent grain. Note, the detail explanation of double extension twinning can be found in Chapter 5.5.2. The sample reference direction for A1 is close to $[11\bar{2}0]$, A2 is close to $[10\bar{1}0]$, and A3 is perpendicular to the surface (parallel to indentation direction).